

SEISMICITY AND TECTONICS OF THE PAMIR-HINDU KUSH

REGION OF CENTRAL ASIA

by

STEVEN WILLIAM ROECKER

B.S., Georgia Institute of Technology
(1975)

SUBMITTED IN PARTIAL FULFILLMENT
OF THE REQUIREMENTS FOR THE
DEGREE OF

DOCTOR OF PHILOSOPHY

at the

MASSACHUSETTS INSTITUTE OF TECHNOLOGY

February 1981

© Massachusetts Institute of Technology 1981

Signature of Author

Department of Earth and Planetary Sciences

Certified by

Thesis Supervisor

Accepted by

Chairman, Department Committee

WITHDRAWN
FROM
MIT LIBRARIES
APR 2 1981
LIBRARIES

SEISMICITY AND TECTONICS OF THE PAMIR-HINDU KUSH
REGION OF CENTRAL ASIA

Steven W. Roecker

Submitted to the Department of Earth and Planetary Sciences on January 15, 1981, in partial fulfillment of the requirement for the degree of Doctor of Philosophy at the Massachusetts Institute of Technology.

Abstract

Along the 3000 kilometer suture between India and Eurasia, only the Pamir-Hindu Kush region of central Asia frequently experiences intermediate depth earthquakes. During the years 1967-1968 and during two months in each of 1976 and 1977, Soviet, French, and American seismologists carried out microearthquake investigations of the seismic activity in the Pamir-Hindu Kush and related regions. The data collected in these investigations is used in this thesis to determine the spatial distribution of the seismic activity, as well as the variations of the attenuation factor (Q) and the velocity in the region.

The locations of events recorded during the 1977 investigation reveal a broad, aseismic region centered at about 37°N , 71.7°E that separates the seismicity of the Pamir-Hindu Kush into two zones: a northward-dipping zone in the south, and a southeastward-dipping zone in the north. The gap is approximately 50 kilometers wide and curves laterally with depth. The earthquakes occurring in the southern zone and at depths shallower than 170 kilometers are located in a broad (~30 kilometer) zone which dips at progressively steeper angles from west to east. The fault plane solutions in this region do not reveal any consistent pattern. The earthquakes above and below 170 kilometers are separated by an aseismic region of approximately 30 kilometers thickness. In contrast to the shallow zone, the seismicity deeper than 170 kilometers occurs in a narrow (15-20 kilometer) zone, and the associated fault plane solutions consistently show T axes lying in the plane of seismicity.

Except for the seismicity associated with surface faults, the upper 70 kilometers of the Pamir-Hindu Kush is

almost completely aseismic. The seismic zone begins abruptly below 70 kilometers, which is approximately the depth of the Moho in this region.

Although the trends of the seismic zone are determined with data from a short term array, there is evidence that these trends persist for times longer than one month. First, the differences in dip and breadth of the seismic zones on either side of the gaps, as well as the differences in the associated fault plane solutions, attest to the roles of the gaps as real discontinuities. Second, the trends in seismicity inferred from the microearthquake investigations of 1966-1967 and 1976 mirror those determined by the 1977 investigation, which suggests the longevity of these features.

Along with other evidence, the earthquake locations suggest that subduction in the Pamir-Hindu Kush has taken place in two isolated regions. Subduction in the regions north of 37° probably occurred along the Darvaz-Karakul fault, and in the south either along or between the Panjer and Kunar faults. Seismicity is scattered throughout the region between the Panjer and Kunar faults and does not define any singularly active fault. Finally, subduction in the Pamir-Hindu Kush was probably a relatively recent event, initiating within the last 20 million years, and perhaps continuing to the present.

Several tests designed to estimate the accuracy of the earthquake locations in the Pamir-Hindu Kush resulted in the formulation of several empirical rules for location reliability. For instance, it was found that the inclusion of S wave arrivals significantly stabilizes a location, as does an arrival at a station within one focal depth of the event. It can be shown theoretically that such arrivals have a dramatic effect on the linearly estimated covariance of the solution, as well as on the impact or "sensitivity" of a given observation.

Using data from four digital recorders operated as part of the 1977 investigation, values of Q were determined for coda (Q_c) and for S waves (Q_s). Q in the Pamir-Hindu Kush increases with both frequency and depth. Q_c is approximately equal to Q_s in the crust, which lends credence to the basic assumption that coda is primarily composed of scattered S waves. When compared to the Q_c of other areas, the Q_c in the Pamir-Hindu Kush is found to reflect the relatively strong heterogeneity of the region.

The outstanding result of the inversion for three-dimensional velocity structures in the Pamir-Hindu Kush is the revelation of a low velocity region enveloping the seismic zone. The low velocity region has 8% to 10% lower velocities than the surrounding regions and extends from the

lower crust down to at least 150 kilometers depth. This result suggests that a substantial amount of continental crust has been subducted in the Pamir-Hindu Kush, and therefore that continental, rather than only oceanic, lithosphere has been subducted. Oceanic lithosphere may exist at approximately 160 to 200 kilometers depth.

Thesis Supervisor: Peter H. Molnar

Title: Associate Professor of Geophysics

TABLE OF CONTENTS

	Page
TITLE PAGE	1
ABSTRACT	2
TABLE OF CONTENTS	5
ACKNOWLEDGEMENTS	6
PREFACE	8
I. MICROEARTHQUAKE SEISMICITY AND FAULT PLANE SOLUTIONS IN THE HINDU KUSH REGION AND THEIR TECTONIC IMPLICATIONS	12
II. SEISMICITY AND FAULT PLANE SOLUTIONS OF INTERMEDIATE DEPTH EARTHQUAKES IN THE PAMIR-HINDU KUSH	36
III. SHALLOW EARTHQUAKES AND ACTIVE TECTONICS IN EASTERN AFGHANISTAN	44
IV. SENSITIVITY OF THE EARTHQUAKE LOCATION PROBLEM TO NETWORK GEOMETRY	56
V. ESTIMATES OF Q IN CENTRAL ASIA AS A FUNCTION OF FREQUENCY AND DEPTH USING THE CODA OF LOCALLY RECORDED EARTHQUAKES	94
VI. THE VELOCITY STRUCTURE OF THE PAMIR-HINDU KUSH REGION: POSSIBLE EVIDENCE OF SUBDUCTED CRUST	159
BIOGRAPHICAL NOTE	297
MICROFICHE OF APPENDIX A TO CHAPTER I	REAR FLAP

ACKNOWLEDGEMENTS

It's a good life.

- Peter Molnar, over a yogurt
in Paramethia, Greece.

I have been a graduate student at M.I.T. for nearly five and one half years, and in each of those years I was fortunate enough to be engaged in field work in some part of the world. Accordingly, I have accumulated a sizeable list of people to whom I owe thanks. Faced with such a horde of benefactors, I have the choice of writing either a terse statement or a drawn-out tome. Since acknowledgements and biographical notes are often the most widely read parts of a thesis, I choose the latter option.

My friend and advisor, Peter Molnar, managed (in order of increasing difficulty) to guide this thesis, introduce me to the world, and teach me the English language. I thank him for his accessibility both academically and socially.

I received encouragement over the years from several faculty members, and I would particularly like to thank Keiiti Aki for his patience and advice while I accosted him with several hare-brained ideas. Ted Madden also provided much useful discussion, but still needs to learn the difference between basketball and hockey.

Of the research associates at M.I.T., I am grateful to Brian Tucker for his long hours and his apple-cider philosophies, and to Bernard Chouet for starting me on the coda study.

A great percentage of the total effort that went into this thesis was spent in the field, and Denis Hatzfeld (Le Chef) is to be credited with much of the success of the investigations. Jerry King designed and built much of the digital equipment used in Afghanistan, and somehow managed to keep it running in the field. In addition to those already mentioned, others who ably assisted in the field were Tanya Atwater, Jean-Luc Chatelain, Julian Freschet, Michele Frogneux, Xavier Goula, Robert Giguet, Mark Grosenbaugh, Lucy Jones, Kandari, Jean Maurer, Osman, Richard Prevot, Rabi, Sharrif, and my favorite Mexican, Gerardo Suarez.

J.P. Carbonnel, Jon Summers, H.Hafiz, and R.S. Saleem are also to be thanked for their logistical help in each of the three investigations.

Jean-Luc Chatelain suffered with me through the Herculean task of reading 50,000 arrival times, and, in our travels together, provided me with the kind of experiences that one probably sits around a fireplace and relates to his grandchildren.

I extend my appreciation to all my good friends in the other Cambridge, with special thanks to Dave Gubbins and Carl Spencer for their help and advice. I also appreciate the perpetually effervescent James Jackson and Geoff King for being what they are.

A.A. Lukk, I.L. Nersesov, and O.V. Soboleva contributed a lot of hard earned data to this work, and the times I spent with V.I. Khalturin made my trips to the Soviet Union a truly educational experience.

Of all the factors which affected my development at M.I.T., none was so great as the atmosphere of camaraderie generated by my peers. Of the many graduate students I was fortunate to associate with, I would especially like to thank Ken Anderson, Yves Caristan, Wang Ping Chen, Arthur Cheng, Bill Ellsworth, Mike Fehler, Gerry LaTorraca, Dale Morgan, Jon Nabelek, Jim Scheimer, Bob Siegfried, Steve Taylor, Cliff Thurber and George Zandt for their various and sundry personalities. Particular thanks goes to Bill Ellsworth, who provides advice and encouragement even after his flight to the west coast.

Much of the computation in this thesis, including the nifty right-justified margins in several of the chapters, was made possible through the generosity of M. Chinnery and R.T. Lacoss, who allowed me to use the facilities of the Applied Seismology Group of Lincoln Laboratory. I would also like to thank Tom Fitch and Bob North of Lincoln Lab for helping locate events and for a lot of useful discussion.

Finally, Deborah Gillett provided a great deal of nourishment and encouragement during these difficult times. I thank her for her patience and I hope she never has to put up with anything like this again.

I'm sure I forgot someone. Please forgive me.

Preface

Approximately 40 million years ago, the last remnant of the Tethys sea between India and Eurasia disappeared into the mantle, and the collision of the two continents ensued. In addition to building a mountain range which has become a haven for Buddhist monks, starstruck geophysicists, and other seekers of the good life, the India-Eurasia collision has created fodder for a considerable amount of scientific research. Several fundamental aspects of this archtypical collision remain an enigma, however, largely because of the hardships involved in gathering data. Seismologists, in particular, are faced with a relative paucity of data from large earthquakes in the region, and must brave the inevitable contact metamorphism associated with the operation of delicate instruments in a harsh environment.

Along the ca. 3000 km length of the collision, the only region with an exceptionally high level of seismic activity is the Pamir-Hindu Kush region of central Asia. Located at the western edge of the collision zone, the Pamir-Hindu Kush region was probably the Tethys' closing scene, the final stage of eons of subduction of oceanic lithosphere.

The six papers which make up the chapters of this thesis generally concern the seismicity and tectonics of the Pamir-Hindu Kush. Chapter 1 uses 600 of the best located earthquakes recorded by short term arrays in 1976 and 1977 to describe the seismic zone and, with fault plane solutions, its state of stress. Chapter 2 addresses similar

questions with arrival time data from an array managed by Soviet scientists in 1966-1967, and with fault plane solutions accumulated over a number of years by O.V. Soboleva. Chapter 3 examines the shallow seismicity to the south of the Hindu Kush, defining the activity on several faults in the area.

A great deal of effort was spent in trying to estimate the reliability of the locations of the events discussed in the first three chapters. This effort inspired a search for a more theoretical approach to the problem of evaluating location accuracy, the fruits of which appear in Chapter 4. While this chapter has no direct bearing on the tectonics of the Pamir-Hindu Kush, the results of this analysis verify many of the suggestions put forward in Chapter 1 concerning the factors governing the accuracy of earthquake locations.

Four digital recorders were operated during the 1977 investigation, and in Chapter 5 this data is used to deduce the average Q structure for central Asia. Finally, all of the data in Chapter 1 which could not be explained by earthquake locations are used in Chapter 6 to deduce one- and three-dimensional velocity structures of the Pamir-Hindu Kush region.

Only one name appears on the cover of this anthology of multi-authored papers. Since these works are presented in the context of a Ph.D. thesis, it is necessary to give some account of how much effort was spent by the candidate. In the following the contributions of the various authors of

the papers are discussed primarily. The contributions of other persons are mentioned in the acknowledgements at the end of each paper.

Chapter 1. The organization and operation of the field programs in which the data was gathered involved many persons from M.I.T. and I.R.I.G.M. in Grenoble. The reading of the arrival times, the location of the events, and the initial evaluation of the results were performed by J.L. Chatelain and S.W. Roecker. J.L. Chatelain and D. Hatzfeld drew most of the illustrations. S.W. Roecker wrote most of the article.

Chapter 2. The data was gathered by Soviet workers and the arrival times were read by A.A. Lukk and I.L. Nersesov. O.V. Soboleva contributed the fault plane solutions. S.W. Roecker located the events and shared the writing with P. Molnar. J.L. Chatelain and D. Hatzfeld drew most of the illustrations.

Chapter 3. R. Prevot did most of the work, and P. Molnar wrote the English version of the paper. S.W. Roecker relocated the events using a master event technique, the results of which appear in R. Prevot's thesis. This paper is included strictly for completeness.

Chapter 4. The original idea of investigating the sensitivity matrix was W.L. Ellsworth's. S.W. Roecker developed most of the analytical forms used in the approach.

Each did an equal share of the writing and illustrating.

Chapter 5. B. Tucker, J. King and D. Hatzfeld were instrumental in the design and maintenance of the digital equipment as well as in the organization of the investigation. In addition, B. Tucker sacrificed many hours in the initial processing of the digital data, and carefully reviewed the manuscript. S.W. Roecker did the rest.

Chapter 6. S.W. Roecker is the only author listed on this paper, but J.L. Chatelain must again be credited with sharing in the reading of arrival times and analysing the initial locations, both of which represent a significant percentage of the total work involved.

CHAPTER I

... the field is the only reality.

- *Albert Einstein*

*Quoted in "The Philosophical Impact
of Contemporary Physics" by*

M. Capek

MICROEARTHQUAKE SEISMICITY AND FAULT PLANE SOLUTIONS IN THE HINDU KUSH REGION
AND THEIR TECTONIC IMPLICATIONS

J. L. Chatelain,¹ S. W. Roecker,² D. Hatzfeld,¹ and P. Molnar²

Abstract. The nature of the Hindu Kush intermediate seismic zone was studied in two microearthquake investigations in 1976 and 1977. By testing several sources of uncertainty the precision of about 600 earthquake locations was estimated to be about 5 km in epicenter and 10 km in depth. Projections of the earthquake locations from several perspectives reveal several regions of aseismicity as well as a highly contorted nature of the active regions. Very little seismicity was recorded in the crust from 0- to 70-km depth. The part of the zone southwest of about 37°N, 71.5°E and shallower than about 160 km is broad and seems to dip north at progressively steeper angles from west to east. Fault plane solutions for this region do not reveal a simple consistent pattern. This region is separated from another active region to the northeast by a curved gap that is nearly 50 km wide. Northeast of this gap the zone dips to the southeast. In the western portion there is an aseismic region around 160-km depth that separates the contorted shallower zone from a narrow (15-20 km wide), consistently steep, deeper zone. As in island arcs, the fault plane solutions for the deeper events show T axes generally lying within the plane of seismicity and P axes perpendicular to the plane. In contrast to island arcs the T axes in general are not parallel to the dip direction, and there seems to be greater variation in the orientation of these axes. The entire western zone plunges to the west at about 20°, and most of the T axes plunge steeply to the west. In detail, the earthquakes tend to occur in clusters that leave aseismic gaps between the clusters. There is a distinct gap of about 15-km width near 70.7°E. This gap seems to separate events with fault plane solutions that in the west have westward plunging T axes and in the east have eastward or vertically plunging T axes. Although many of these features were not detected in previous studies of this region, the data from those studies are consistent with the dips, changes in dip, gaps, and breadth of the seismic zone. Both the variations in dip and breadth of the active zones and, for one gap, the difference in fault plane solutions of earthquakes on either side of it, make the role of the gaps as boundaries clear and suggest their long-term existence. We infer that the configuration of the Hindu Kush seismic zone could possibly be the result of the subduction of oceanic litho-

sphere from two separate, small basins in opposite directions. The age of the subducted lithosphere is probably greater than 70 m.y., and subduction probably has occurred over a relatively short duration. The rate of subduction probably has been between 20 mm/yr and 48 mm/yr. Correlations of seismic trends with surficial features suggest that in the south the Hindu Kush suture zone lies along or somewhere between the Panjer and Kunar faults and that in the north the Pamir suture zone lies near the Darvaz-Karakul fault. Finally, it seems that the protrusion of India into Eurasia has been a major factor in developing the present configuration of the zone.

Introduction

The upper mantle beneath the mountainous Hindu Kush region of northeastern Afghanistan is the site of a tectonically complex area. Although it is not clearly associated with any island arc system, this region is perhaps the most active zone of intermediate depth (70-300 km) earthquakes in the world. The region is therefore interesting, since it provides a setting for examining deep-seated tectonic processes in a collision zone as well as allowing a study of intermediate depth seismicity as a phenomenon in itself.

Because of its proximity to the Eurasian-Indian plate boundary the Hindu-Kush seismic zone is believed to be grossly related to the convergence of the Indian and Eurasian subcontinents. The scenarios offered by various authors for the existence of the zone, however, cover a wide spectrum. Many authors [Billington et al., 1977; Isacks and Molnar, 1971; Khalaturin et al., 1977; Nowroozi, 1971, 1972; Santo, 1969] have suggested that the zone is evidence of subducted oceanic lithosphere, possibly remnants either of the Tethys Sea or of a marginal interarc basin. Explanations of this type are complicated by the unusual configuration of the zone, which seems to be much more contorted than is typical of island arcs, and other interpretations have been given. Santo [1969], for example, on the basis of what he interpreted to be a V-shaped zone of seismicity, suggested that two lithospheric layers had been underthrust from different directions in the same place. Alternatively, Vinnik et al. [1977] and Vinnik and Lukk [1973, 1974] interpret the activity as the result of a downward extension of a Paleozoic shieldlike structure. In their scenario this structure defines a 300-km-thick tectosphere that is being stressed by compressive forces somehow associated with the Himalayan fold belt. The wide range of explanations is indicative of a lack of conclusive evidence, such as large numbers of precisely determined earthquake locations or compatible relations to surficial geology.

¹Laboratoire de Geophysique Interne, Institute de Recherches Interdisciplinaires de Geologie et de Mechanique, B.P. 53, 38041 Grenoble, France.

²Department of Earth and Planetary Sciences, Massachusetts Institute of Technology, Cambridge, Massachusetts 02139.

To help resolve the origin of the intermediate seismic zone, we carried out investigations of microearthquakes in the Hindu Kush region in both 1976 and 1977. Our immediate objectives were to define accurately the configuration of the seismic zone and to determine more fault plane solutions of earthquakes of the region over a larger portion than has been possible using data from the World-Wide Standardized Seismic Network (WWSSN) alone. Despite the short duration of these studies - 2 weeks in 1976 and 1 month in 1977, the high activity of the area (40 locatable events per day) made these objectives feasible. In order to infer the long-term nature of some of the features in the seismicity we compare the results of these investigations with those from previous studies made of the Hindu Kush region. These include the results of a 2-year microearthquake study by Soviet scientists in 1966-1967 [Roecker et al., 1980] as well as the teleseismic studies of Billington et al. [1977] and Santo [1969].

Data

Recording Procedure

From June 11 to July 13, 1977, we operated 11 Sprengnether MEQ-800 smoked paper recording systems circling the Hindu Kush in north-eastern Afghanistan (Figure 1). In addition, we obtained copies of short-period records from the Seismic Research Observatory (KBL) in Kabul. The stations were distributed to allow precise locations of intermediate depth (70-300 km) events. However, owing to various geographical and political limitations (e.g., bad roads and proximity to borders with neighboring countries) we were unable to put stations further east or north of the zone. Nevertheless, the wide range of takeoff angles along with adequate recording of the other azimuths seems to compensate for lack of coverage on the north and east.

The Sprengnether stations operated

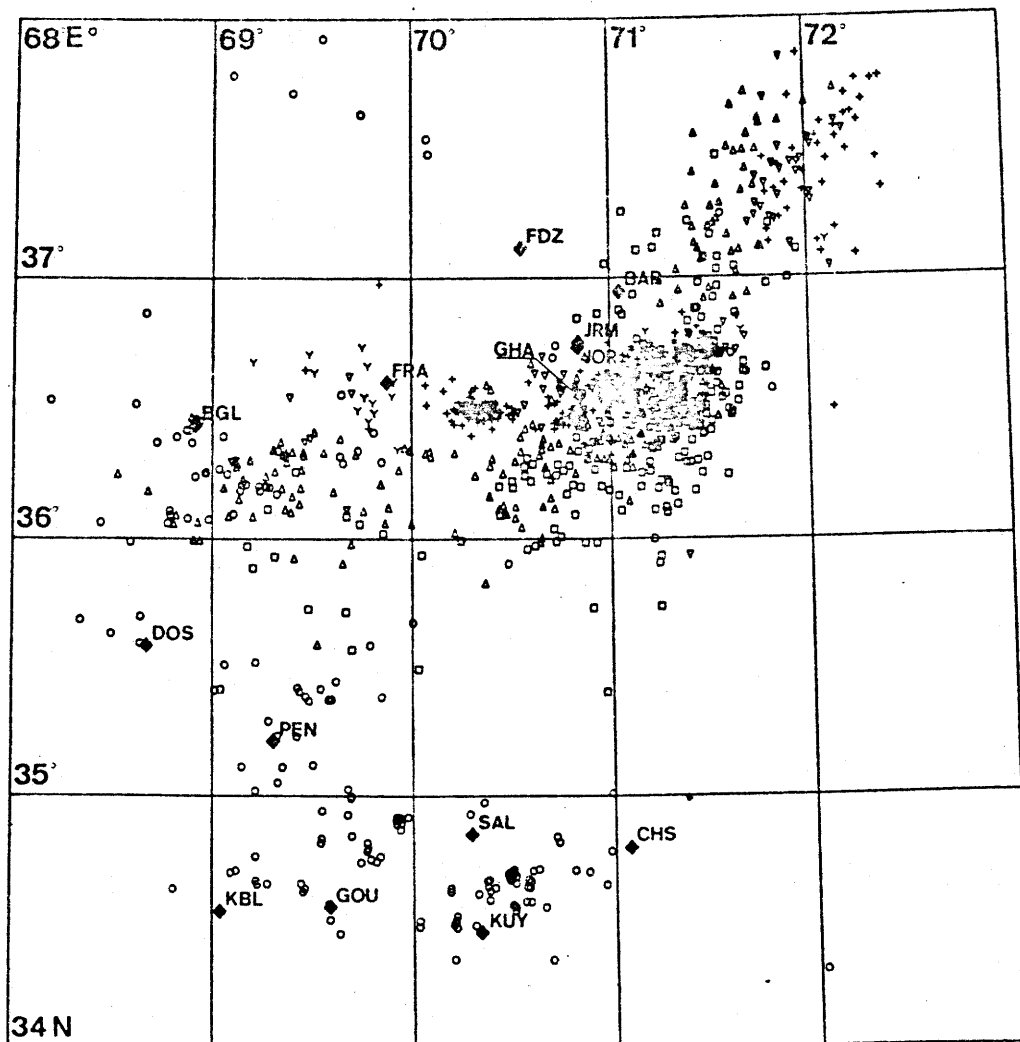


Fig. 1. Arrangement of seismographs and location of epicenters during the 1977 investigation. Station locations are indicated by solid diamonds. The epicenters are plotted with symbols corresponding to depth (z) intervals as follows: open circles, $0 \leq z \leq 50$ km; squares, $50 \leq z \leq 100$ km; triangles, $100 \leq z \leq 150$ km; inverted triangles, $150 \leq z \leq 200$ km; pluses, $z \geq 250$ km.

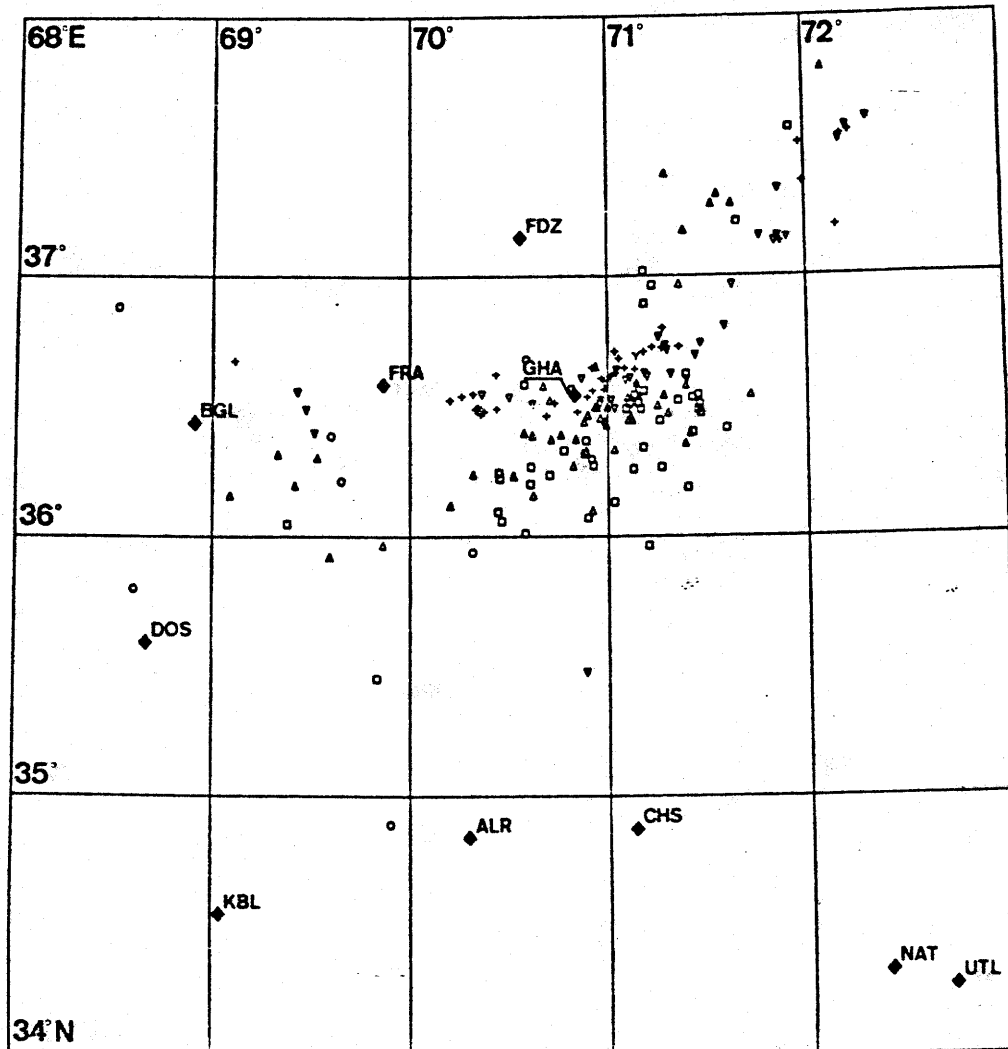


Fig 2. Arrangement of seismographs and location of epicenters during the 1976 investigation. Symbols for stations and epicenters are the same as in Figure 1.

continuously throughout the duration of the investigation. All of the stations were equipped with 1-Hz L4-C vertical seismometers. The filters on the instruments were set to allow a flat velocity response to frequencies between 0.3 and 30 Hz, and the amplifier gains were set at either 78 or 84 dB. The amplification of the signal from the ground motion to the trace on the record is about 500,000 at 84 dB and 250,000 at 78 dB. Traces were recorded by a fine stylus on kerosene smoked paper fixed to a rotating drum. The drum rotated at 60 mm/min at most stations and 120 mm/min at KUY. The records were changed every 2 days at all stations except KUY (which was maintained daily) and the clock drift was checked by recording a time signal transmitted by the ATA station in New Delhi. Station locations were determined using topographic maps with a scale of 1:250,000. The short-period records obtained from KBL were in ink and were recorded at 120 mm/min. Maintenance on these instruments was performed daily by members of Kabul University. The data accumulated during this investigation will be the primary topic in the discussion below.

A preliminary field study for the work in

1977 was made between August 18 and 31, 1976 [Chatelain et al., 1977]. During that time we operated seven stations in a configuration similar to that in 1977 (Figure 2). The field procedure was essentially the same as that in 1977. These data were supplemented by recordings from short- (and sometimes long) period instruments in Kabul and from the Lamont-Doherty array near Tarbella Dam [Armbruster et al., 1978].

Analysis of Data

In Appendix A¹ we give an extended discussion of the procedures used to analyze the seismograms, the reasoning behind our estimates of the uncertainties in the arrival times, a long discussion of the tests made to evaluate errors in locating the events, and the logic behind the criteria used to assign uncertainties

¹Appendix is available with entire article on microfiche. Order from the American Geophysical Union, 2000 Florida Ave., N. W., Washington, DC 20009. Document J80-002; \$01.00. Payment must accompany order.

TABLE 1. Velocities of Layered Model Used to Locate Events

Depth to Top of Layer, km	Velocity of P Wave, km/s
0	6.0
45	8.0
85	8.2
110	8.4
150	8.6
200	8.8

to the location. Here we summarize the results described in Appendix A.

To analyze the 170 seismograms with nearly 45,000 arrivals, we digitized, on a tabletop digitizer, the phases of interest and relevant minute marks. A computer program then computed arrival times. We estimate the uncertainty of impulsive P arrivals to be about 0.1 s and emergent ones to be about 0.2 s, after clock corrections have been added. We used S phases whenever we could confidently pick the onset with an uncertainty of less than 1 s.

To evaluate the uncertainties in the locations, a series of tests were made, using both synthetic and real data. The first test was designed to examine whether or not the program HYP071 [Lee and Lahr, 1975], which assumes a flat layered structure, could locate events well in a region as large as the Hindu Kush (dimensions 300 km). Travel times to stations from hypothetical events at different locations were calculated for a spherical earth, and the events were relocated with HYP071. Epicenter had errors less than 0.5 km, and depths were wrong by about 1 km (Table A1). We conclude that the dimensions of the Hindu Kush region pose no obstacle to HYP071.

The second test explored the effects of random errors on the location. Travel times were calculated to stations for 58 events throughout the zone, and the events were relocated after random errors of 0.1 s for P and 0.6 s for S were added to the synthetic data. The mean mislocation is about 2 km but increases toward the edge of the array to 3 km (Table A2). When standard errors were increased to 0.2 and 1.0 s for P and S, the mislocation increased by about 1 km throughout the array (Table A3).

We then made tests with subsets of the array to determine the precision of the location and to gain insight into which data were redundant. We first selected 15 well-recorded events throughout the array and relocated them with subsets of the stations used initially (Table A4). Provided S waves were used, and provided 8 or more arrivals were used, locations were generally within 2-3 km of one another. Without an S wave the locations were much less reliable. Similar results were found by Buland [1976] and James et al. [1969]. The geometry of the network also is very important. To insure reliable depths, the distance of one station to the epicenter should be less than the depth. Moreover, when the azimuths to all

stations are within 60° of one another, more than eight arrivals are needed. As a second method we calculated uncertainties in location using the covariance matrix relating the data and location (see Appendix A and Figure A1). Results of this analysis agree with those described above and suggest that eight phases, including at least one S phase, are adequate to give a precision of 2-3 km in the locations in most of the region.

Because there are likely to be large lateral heterogeneities in the deep structure of the Hindu Kush while HYP071 requires a flat layered structure, we also calculated travel times from hypothetical events in a laterally heterogeneous structure and relocated them with HYP071. The heterogeneous structure was intended to imitate a slab of high-velocity material with maximum velocity contrast of 10%, surrounding the earthquake zone (Figure A2). This was imbedded in the uniform structure used by HYP071 (Table 1), a modification of that given by Lukk and Nersisov [1970]. The results show that relocations (Table A5) are in error by less than 5 km. When an incorrect choice of the ratio V_p/V_s was assumed (1.70 or 1.76 instead of 1.74), however, the relocated depths were systematically in error by about 10 km (too deep for $V_p/V_s = 1.70$ and too shallow for 1.76). These errors are systematic, so in terms of the precision of the locations the effect of the lateral heterogeneity introduces an error of about 5 km.

All of the results discussed above apply to events in the center of the array. For the deeper events in the western portion, however, the uncertainties could be twice as large.

From these tests we considered as reliable only locations based on at least eight arrivals, with at least one S phase and with at least one station at a distance from the epicenter less

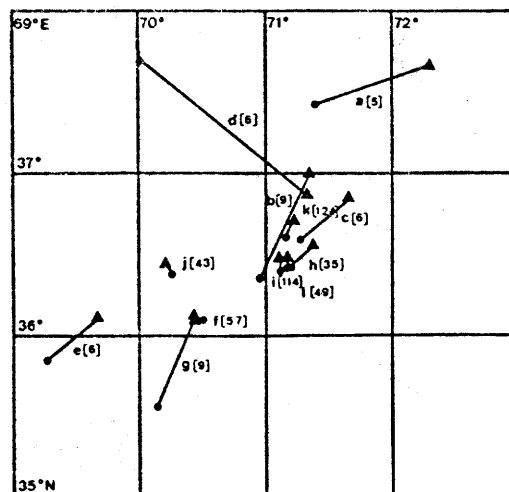


Fig. 3. A comparison of event epicenters located by both the USGS and the 1977 local array. Solid circles are epicenters reported by the USGS, and solid triangles are epicenters located by the local array. Letters near the epicenters specify the events in Table A7. Numbers in brackets refer to the number of stations used by the USGS in locating the events.

than the depth of focus. In addition, when the azimuths to all the stations were within only 60° , only those locations based on 10 or more such stations were considered reliable. Finally, acceptable locations included only those with root-mean-square residuals (Rms) greater than 0.1 s but less than 0.55 s. Among 1200 initial locations we used only 600. They are listed in Table A6.

We estimate the uncertainties in the epicenter to be about 5-10 km, increasing with a decreasing number of arrivals and decreasing depth. Similarly, depths are uncertain by

5-15 km. For comparison we plotted the locations of events in 1976 and 1977 that were also located by the United States Geological Survey (USGS) (Figure 3 and Table A7). The locations given by USGS for events recorded at more than 40 stations differ by about 10 km in depth and about 5 km in epicentral coordinates from those obtained by the local arrays. USGS locations with less than 40 stations disagree with ours considerably. Agreement in location suggests that both locations are good and that many stations are required to locate an event well teleseismically.

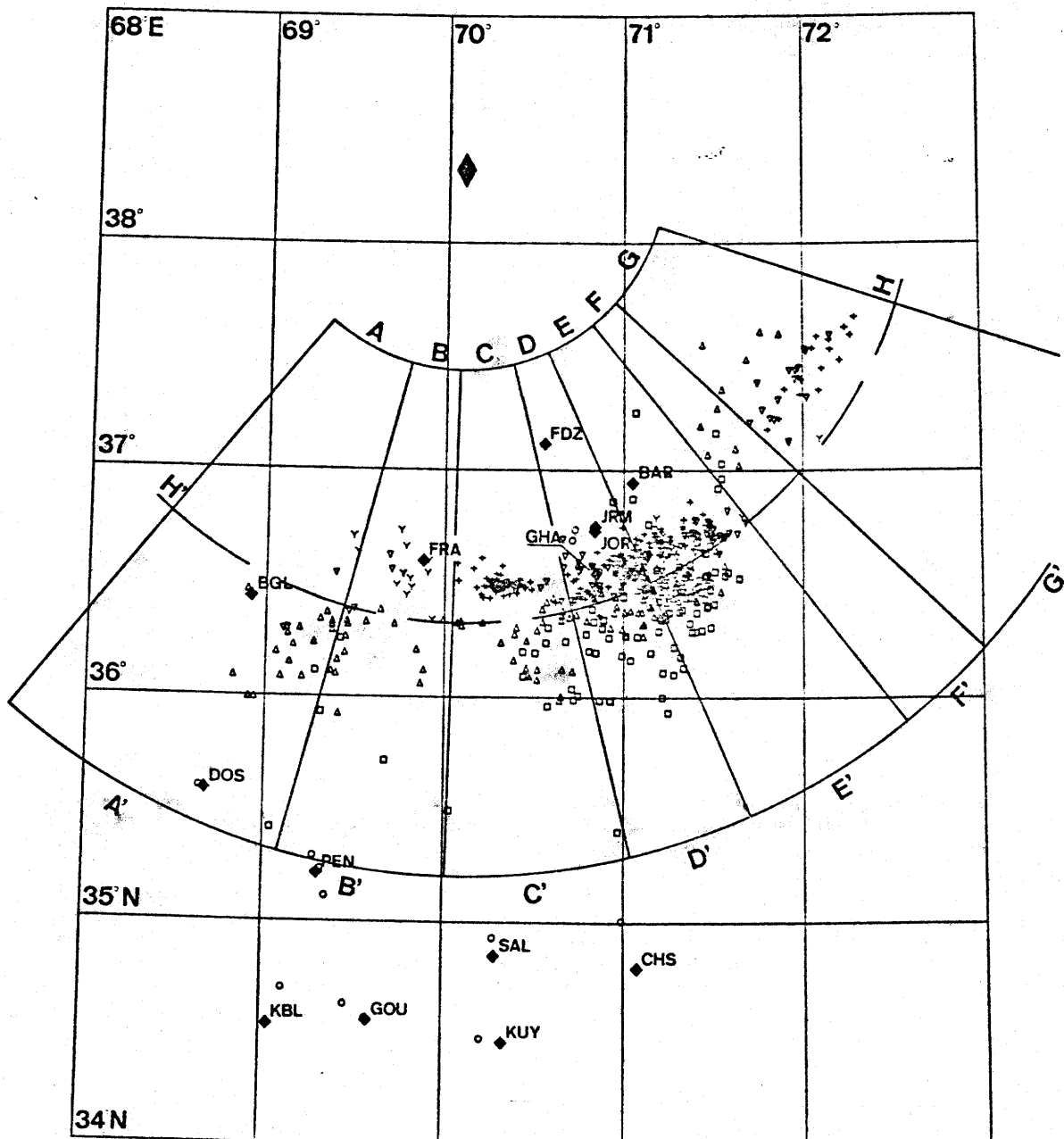


Fig. 4. Map view of the earthquake locations which passed all the quality criteria, along with the plotting scheme for cross sections. In plotting cross sections perpendicular to the trend of the zone, hypocenters are projected onto planes which bisect the sections. The lateral cross section is made by radially projecting hypocenters onto a vertical cylinder, the intersection of which with the map is denoted by the line H'H.

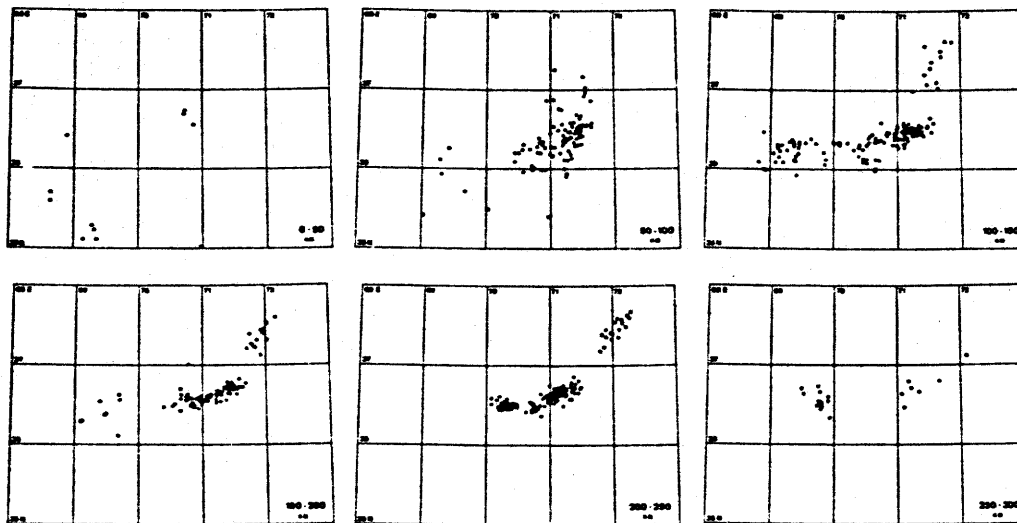


Fig. 5. Map views of the best locations of 1977. Events are divided into 50-km depth intervals.

Results

Mapping Techniques

The configuration of the zone, as revealed in each microseismic study, is displayed by plotting the recorded events in three orthogonal projections. The first consists of a series of plan views which divide the events into intervals of 50-km depth (Figures 5 and 7). The second is a series of vertical cross sections. Because of the basically accurate trend in the seismicity, we chose to divide the zone into several circular sections (Figure 4) and project the events onto planes bisecting the sections (Figures 6 and 8). Such projections are everywhere nearly perpendicular to the trend of the zone. In the third perspective the events are projected radially onto a vertical cylinder (H'H in Figure 4), resulting in a lateral section that is approximately parallel to the trend of the zone (H'H in Figures 6 and 8).

The events that met all the quality criteria established above are plotted as solid circles in these diagrams. While it is advantageous not to consider poor locations when describing the seismic trends of an area, it is important to insure that the criteria are not overly biasing the results. Therefore some events that did not meet all the criteria are included in the plots as open circles. First, shallow events with depths less than the distance to the nearest station but otherwise meeting the quality criteria are included in the plots for 1977. This is because this criterion would prohibit nearly all shallow seismicity regardless of how well recorded it is and would thus give a false impression of complete shallow aseismicity. Second, since all the tests described above were based on the 1977 array, the strict application of the criteria to the results of previous studies may be questionable. The configuration of the 1966-1967 [Roecker et al., 1980] array, for example, is somewhat different from that of 1977. Also, while the configuration of the 1976 array is

similar to that in 1977, the uncertainty in the arrival times is somewhat greater owing to the reading techniques used. Therefore in plotting the events from these other studies, the only restriction was that the Rms be less than 0.7.

Description of the Zone

Because of our greater confidence in the 1977 results they provide the basis for our conclusions. Nevertheless, some of the conclusions from this study arise from defining regions of aseismicity. While considerable effort was spent verifying where events actually occur, the task of defining where they do not is more difficult. One can easily argue that 1 month of recording is not sufficient to sample the seismicity adequately. Fortunately, despite both the greater uncertainties and the fewer events in the other investigations of Hindu Kush seismicity, many of the gross aspects of the zone defined by the data from 1977 are apparent in the data from 1976, from 1966-1967, and from the teleseismic studies of Billington et al. [1977] and Santo [1969]. The agreement of all these results verifies the existence of features in the zone for at least 10 years.

In general, the intermediate depth seismicity of the Hindu Kush is confined to a small isolated area, roughly 700 km in extent and bounded on the west at about 69°E (Figure 1). The eastern boundary is beyond the limits of the local arrays, but teleseismic results show the intermediate seismicity ceases at about 75°E [Billington et al., 1977, Figures 2 and 8]. On the whole, the zone is grossly planar and steeply dipping, but several unusual features can be resolved with the 1977 data.

With the exception of some activity in the westernmost part of the zone, there is very little seismicity between 0- and 70-km depth (Figures 6 and 8, Roecker et al. [1980, Figures 2 and 3], Billington et al. [1977, Figures 2, 3, and 4], and Santo [1969, Figure 9]). Krestnikov and Nersesov [1964] inferred that the depth of the Moho is about 65-70 km for at least parts of this region. Therefore the

relatively aseismic region seems to correspond to the crust, with activity beginning abruptly in the mantle below.

The entire zone can be separated into two

regions of activity: one north of 37°N trending to the northeast and another south of 37°N aligned approximately east-west (Figure 5). At depths greater than about 100 km there is a

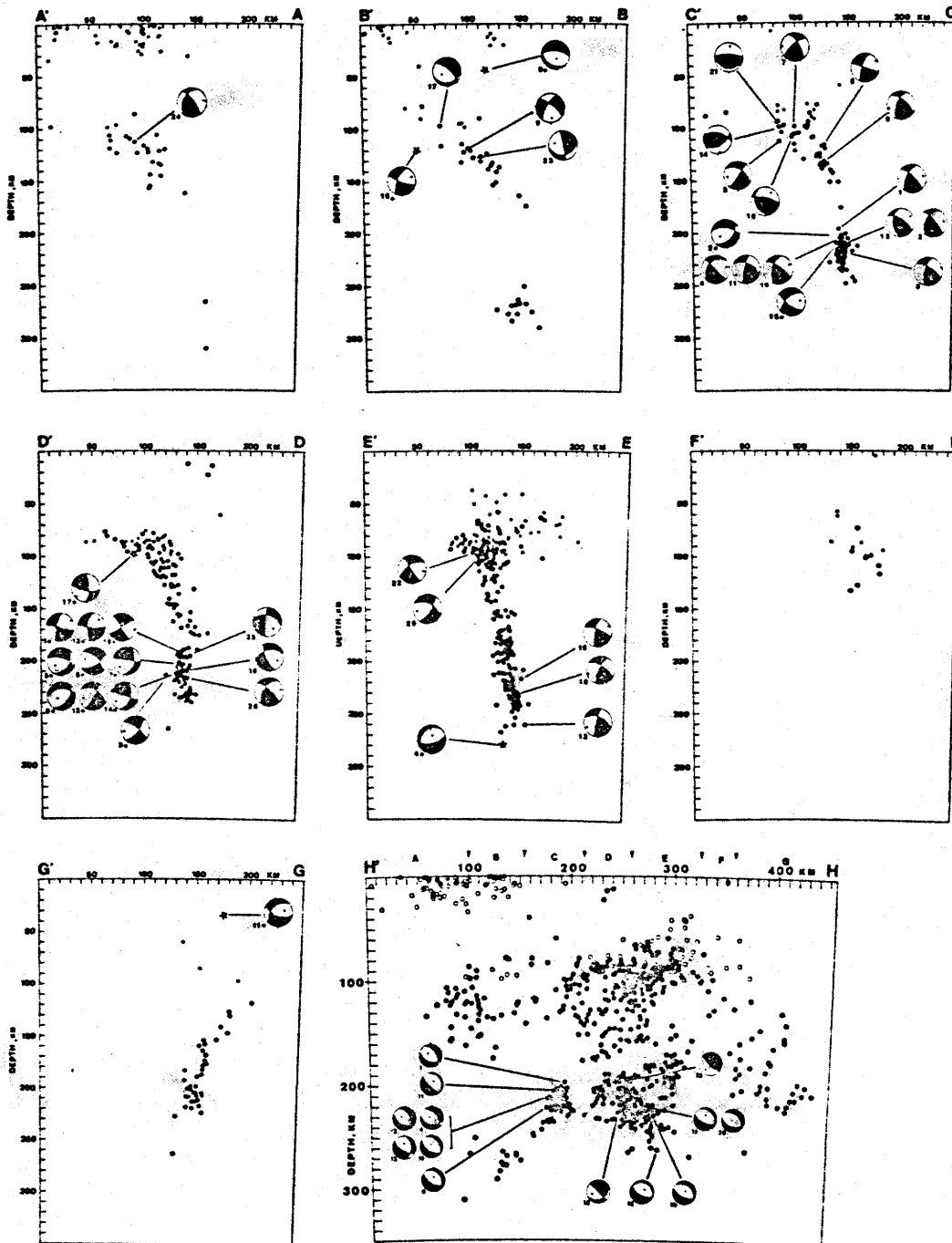


Fig. 6. Projections of 1977 hypocenters and fault plane solutions onto planes perpendicular to the zone (A'A - G'G) and onto a cylindrical surface parallel to the zone (H'H). In each of the sections perpendicular to the zone the northernmost side is marked by the unprimed letter. In the parallel section H'H, H marks the easternmost point, and the boundaries of the perpendicular sections are plotted above the figure. Solid circles represent locations which passed all of the quality criteria. Open circles represent events which passed all of the criteria with the exception of being recorded by a station whose epicentral distance was less than the depth of the event. Fault plane solutions are plotted in back sphere projections. Dark quadrants include compressional first motions, and white dilatational. T axes are plotted as open circles, and P axes as solid circles. Starred solutions are those determined with data from the WWSSN. All others were determined with local data.

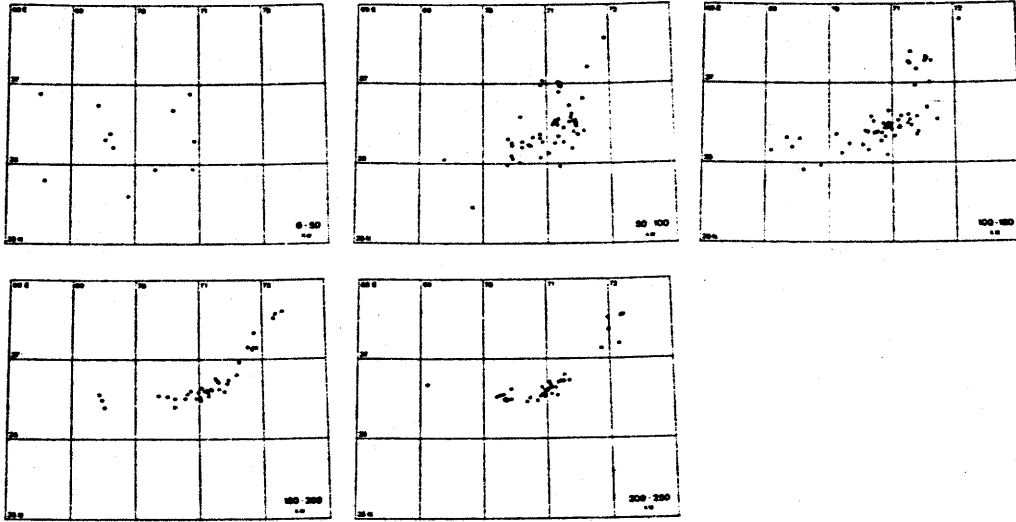


Fig. 7. Map of the best locations of 1976. Events are divided into 50-km depth intervals.

rather wide (~50 km) gap between these seismic regions, which appears in all of the local results (Figures 5, 7, and 9). The FF' cross section in Figures 6 and 8 and Figure 3 of Roecker et al. [1980] shows that this gap is well defined at depths greater than 150 km. The lateral projections show some curvature in this gap above 150 km and suggest that it extends down from as shallow as 100 km depth (Figure 9, H'H in Figures 6 and 8, and Roecker et al. [1980, Figure 3]). The seismicity shallower than 100 km that connects these two active regions north and south of 37°N seems to occur in a restricted area roughly 70 km long and 30 km in both width and depth.

The seismic zone south of 37°N can be further divided into two regions: a shallower one between 70- and 170-km depth and a deeper one between 180- and 300-km depth. Only one microearthquake was located deeper than 300 km for the entire zone. The gap between them is about 70 km wide in the west and narrows in the east to about 15-20 km near 70.7°E (Figure 9, H'H in Figure 6 and 8, and Roecker et al. [1980, Figure 3]). This gap is evident in Figures 3 and 4 in Billington et al. [1977], but unfortunately, the entire southern region was plotted on one projection, and identification of this gap in the west is impossible. Santo [1969, Figure 9] shows no real aseismic gap, but he notes a pronounced minimum of events at 160-km depth. We note that when viewed on lateral sections (HH' in Figure 6), the entire southern region seems to plunge west at roughly 20°. This observation is based on the apparent trends of the aseismic boundaries which define the shallower and deeper regions.

In cross section the shallower seismicity defines in the southwestern region a broad zone about 40 km in width (particularly CC', DD', and EE' in Figures 6 and 10). Even with the estimated errors for the locations this shallower region must be at least 30 km thick. In the far west the zone dips north at about 45° and becomes progressively steeper to the east. Although the seismicity appears to be continuous in the shallower region, there seems to be

a relative sparseness in activity roughly 30 km wide centered at about 70.2°E.

The deeper seismicity defines a consistently narrow zone (15-20 km wide) which has a nearly vertical dip (Figures 6 and 8, Roecker et al. [1980, Figure 3], and Billington et al. [1977, Figure 3]). Given the errors in locations, however, this zone could be somewhat thinner. In cross section the deeper events in the west seem to be more scattered than in the center of the zone, but as discussed above, the locations there are less precise.

In all of the local results a gap in the seismicity, which is about 15 km wide, appears at 70.6°E at about 200 km depth (Figs. 5, 7, and 9 and Roecker et al. [1980, Figure 2]). This gap also appears in Figure 6 of Billington et al., but the low density of events to the west of the gap makes its appearance less dramatic. The events east of 200- and 250-km depth near this gap between 70.8°E seem to concentrate (Fig. 5), but the possible gap between these and the events further east is too small to resolve with the present data. This concentration is especially important because it contains most of the events with fault plane solutions determined with the WSSN.

Perhaps the most curious trend in the seismicity of the deeper region is the trail of events that extends downward and to the west of the concentration at 70.3°E (HH' in Figures 6 and 8). The narrowness of this trend when viewed from any angle suggests that the events are confined to a tube of activity which branches off from the concentration to the east.

Because the region to the north of 37°N is outside the 1977 array, any fine details of this seismic zone are more difficult to resolve. However, the gross trend of the zone shows a dip of about 45° to the southeast at 150-km depth that becomes almost vertical at 200-km depth (G'G in Figures 6 and 8, and Roecker et al. 1980, Figure 3). Therefore this zone dips in nearly the opposite direction from that in the southern zone. This reversal in dip is also evident in Figure 5 of Billington et al., but they showed no reliably located events at

depths greater than about 170 km. By contrast, the 1977 results show microearthquakes to depths of about 240 km, with one event as deep as 260 km.

Although the Hindu Kush seismic zone is grossly planar and steeply dipping, in detail it is highly contorted and consists of several zones separated by gaps of aseismicity. Two of the most prominent gaps - one that separates the regions north and south of 37°N (Figures 5 and 9) and another that separates events deeper and shallower than about 160 km depth (Figure 9

and AA', BB' and HH' in Figure 6) - serve as boundaries between regions distinctly different in dip and breadth. A third gap, in the deeper region at 70.7°E (Figures 5, HH' and Figures 6 and 9) does not separate zones which show distinct qualities in spatial distribution of events but, as discussed below, seems to separate regions with different fault plane solutions. The consistency of the patterns obtained from studies made in the last few years, with both locally and teleseismically recorded data, confirms that these gaps have

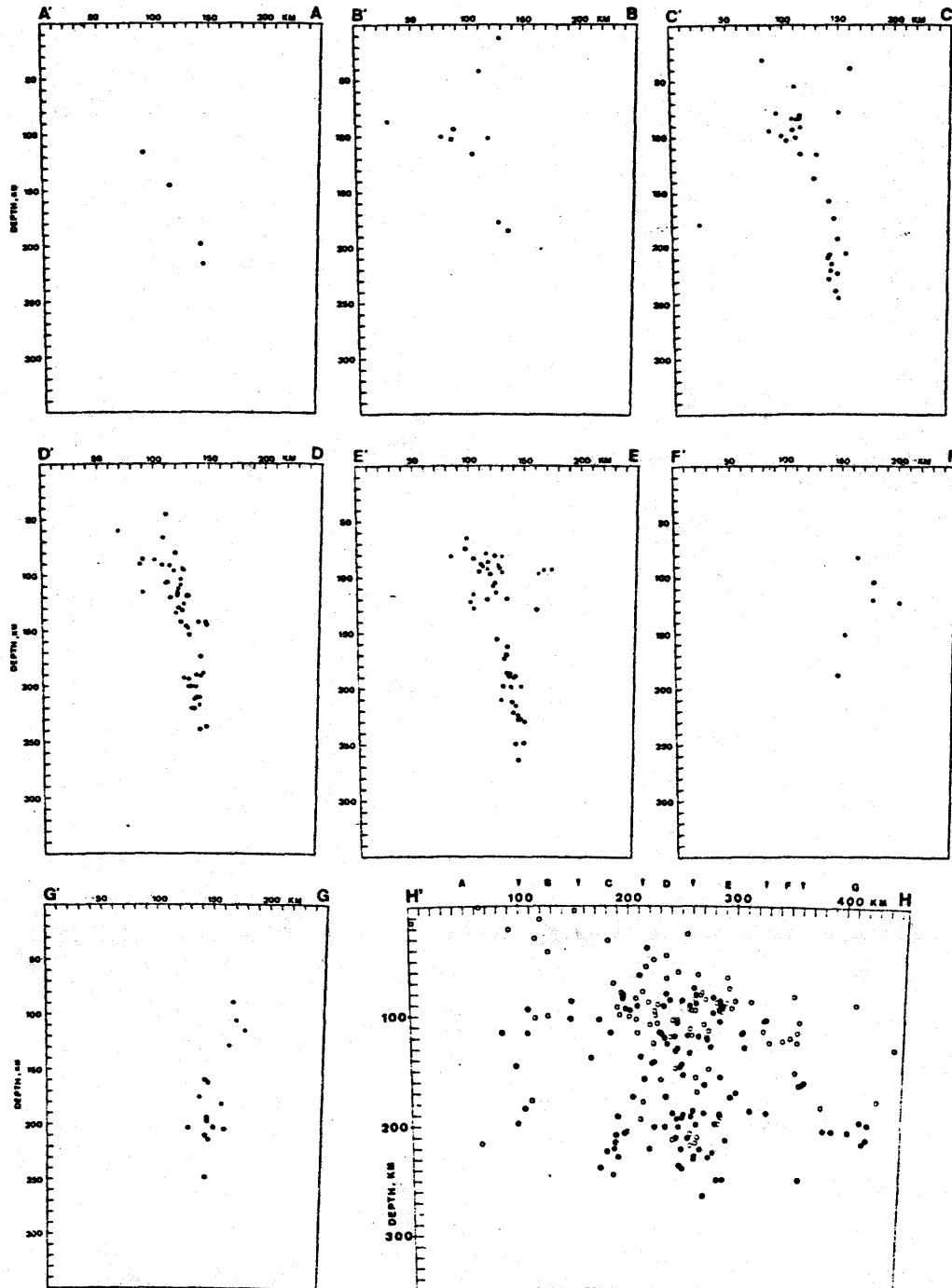


Fig. 8. Projections of the 1976 locations onto planes perpendicular and a cylinder parallel to the trend of the zone. The sections are the same as those used for the 1977 data (Figure 6). Hypocenters which passed all the quality criteria are plotted as solid circles. Open circles represent all of the events which have Rms residuals less than 0.7 but did not pass all the criteria.

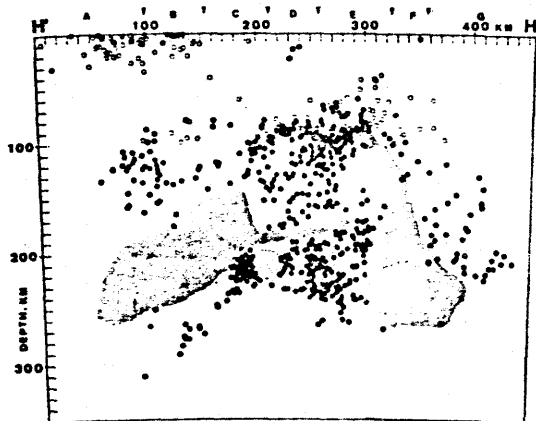


Fig. 9. Gaps in activity. HH' from Figure 6 is plotted without fault plane solutions but with gaps discussed in text shaded.

been real features in the Hindu Kush for at least the past 10 years. Moreover, their clear role as boundaries between regions of distinct qualities provides an argument for claiming that they may have existed for thousands of years and perhaps longer.

Fault Plane Solutions

Although the distribution of stations in 1977 proved adequate for determining locations over a wide area, the hypocentral regions for which well-constrained fault plane solutions could be determined were more restricted. Nevertheless, because of the large number of events recorded with data from the local stations, we were able to determine 26 relatively well constrained solutions for individual earthquakes in various places in the zone (Figure 10 and Table 2). The data were supplemented by first-motion readings from the Soviet station at Khorog [see Roecker et al., 1980]. Two composite solutions were made for events in regions where we could not obtain a solution for an individual earthquake (B and C in Figure 10 and Table 3). The purpose of these solutions is to show that the earthquakes of these regions have radiation patterns grossly consistent with those observed with WWSSN stations rather than implying the orientation of any axis or nodal plane. Composite fault plane solutions were, as a rule, avoided in this study. There are large variations among the well-constrained individual solutions for events in relatively small regions within the Hindu Kush, so that a composite solution will most likely misrepresent the patterns that exist. Fault plane solutions were also determined for 17 events using teleseismic recordings at WWSSN stations (Figure 10 and Table 4). While the addition of these solutions extends the regions represented by fault plane solutions, there are unfortunately few places where solutions based on local and teleseismic data overlap.

Giving a quantitative description of how well constrained a certain fault plane solution is or estimating the exact errors involved in the orientations of the nodal planes and axes requires several subjective decisions. Rather

than attach uncertainties to the parameters for each solution given in Tables 2 and 4, we present all the data used in determining the fault plane solutions in lower hemisphere plots (Figure 10).

As in previous investigations of fault plane solutions of the Hindu Kush [Billington et al., 1977; Isacks and Molnar, 1971; Ritsema, 1966; Shirokova, 1959; Soboleva, 1968a,b, 1972; Stevens, 1966], the solutions generally indicate thrust faulting with nearly vertical T axes. This type of solution is similar to that for intermediate depth earthquakes at island arcs [Isacks and Molnar, 1971]. There are, however, some significant variations that we explore by plotting the fault plane solutions in various orientations on the seismicity maps and profiles (Figures 6, 8, and 11-14).

Local solutions. Plotted in plan view (Figure 11), the solutions for events with depths less than 170 km show considerable scatter, much more scatter than is typical of island arcs. Although most display thrust faulting, solutions 23 and 24 have large strike slip components, and solutions 9, 21, and 14 indicate normal faulting. One might expect some scatter in these solutions because of the highly contorted nature of the shallow region. When plotted on the cross sections (Figure 6), many of the solutions seem to have either one nodal plane or the T axis parallel to the dip of the zone. One possible explanation for this duality is that events with nodal planes parallel to the zone occur along the boundary between two plates of lithosphere, while those with downdip T axes occur within a subducted slab of lithosphere. This observation is not consistent for all events, however, and the lack of sufficient data makes the explanation arguable. In any case the stress field in the shallow region appears to be too complex to be explained in a simple manner.

In contrast to the shallower region, solutions for events in the region below 170 km are much more consistent with one another. The solutions for the seven events (1, 2, 4, 8, 11, 13, and 19) in the concentration west of 70.6°E are essentially the same (Figure 12). The T axes lie within the plane of the zone and plunge to the west at an angle of about 45° . There appear to be some exceptions to this pattern, shown by the composite solution A (Figure 10), made using events in this region, for which there are some apparently inconsistent first motions.

Most of the solutions for events east of 71°E have similar solutions to those west of 70.6°E , but two of them (18 and 25) indicate more southward plunging T axes (Figure 12). The composite solution B (Figure 10), made from events in this area, generally shows compressional first motions in the center and is consistent with reverse faulting. There are unfortunately no solutions for the concentration of events near 70.3°E (Figure 12), which is where several events with solutions using the WWSSN are located. A composite solution (C in Figure 10) made from locally recorded events in this area shows compressional first motions in the center of the diagram, but the nodal planes are poorly constrained.

Viewed on the cross sections (Figure 6), the nodal planes for the deeper events, although regular, do not seem to align with any trend in seismicity, and so are not obviously related to any deep major faulting. A plot of the solutions on the lateral section (HH' in Figure 6) shows the P axes generally perpendicular to the seismic zone, and the T axes are consistently within it as at island arcs. The T axes, however, deviate from the downdip vertical direction by 20° - 40° . The T axes for events in the cluster at 70.4° E seem to be parallel to the tube of seismicity that plunges to the west (HH' in Figure 6).

WWSSN solutions. As with the local solutions the T axes for most of the WWSSN solutions plunge steeply and lie within the zone. Similarly also, there is considerable variation in the solutions.

Most of the events for which WWSSN solutions are available are located in clusters (Figure 13). The radiation patterns for events within each cluster are generally similar to one another, but differ from cluster to cluster. In particular events near 36.4° N, 70.7° E and 210 km-depth (2, 5, 7, 8, and 14) all radiated compressional first motions to stations to the northwest and southeast, with some dilatations to the south and southwest (Figure 10). The solutions for events near 35.5° N, 70.9° E and 180-km depth indicate two trends. The events farther to the west (6 and 16) radiated compressions more to the south, and the quadrant with compressional first motion is aligned more east-west than for the solutions for events at 70.7° E. Events 1 and 13, at the eastern end of the cluster at 70.9° E, radiated dilatations to the southeast, and the zone of compressions tends to be aligned in a northeast-southwest direction. Events 3 and 12 radiated compressions to the east and west, and dilatations to the south. We note that these two events were located by the International Seismological Center in an area where we recorded no events. Solution 15, which is the only solution that overlaps with the local solutions at 70.4° E, generally has compressional first motions in the center of the diagram, but the nodal planes are poorly constrained. It is, in fact, possible to redraw this solution to look more like the local solutions (Figure 10). Event 4 radiated compressional first motions to the west, which are separated from dilatations to the east by a nodal plane that trends north-south. As mentioned above, this event is deep (~ 280 km) and is somewhat isolated from the rest of the events. Plotted in plan view (Figure 13), a pattern emerges where the P axes for the solutions rotate smoothly from a northeast-southwest orientation in the west to one that is more northwest-southeast in the east.

Viewed on the cross sections (Figure 6), two of the solutions (1 and 13) seem to have nodal planes aligned with the dip of the deeper zone. However, as in the local solutions, this observation is not applicable for most of the solutions. On the lateral section (Figure 14), there appears to be a systematic change in the plunge of the T axes from east to west. T axes for the five events (2, 5, 7, 8, and 14) at 70.7° E plunge about 70° to the north or north-

east. This cluster is just to the east of the gap at 70.6° E and contrasts with the westward plunging T axes of the local solutions west of the gap (HH' in Figure 6). East of 70.7° E, solutions 6 and 16 show nearly vertical T axes, and further east the T axes for events 1 and 13 plunge to the west, following the same pattern as the local solutions. The solution for event 12 also has a westward dipping T axis, while that for solution 3 is more vertical, but again there is no seismicity in this area to which these solutions can be related.

The four solutions for events shallower than 150 km (9, 10, 11, and 17) indicate large components of reverse faulting. These earthquakes are scattered throughout the zone, and events 9 and 11 apparently occurred in the crust. When plotted in plan view (Figure 11) or in cross section (Figure 6), the solutions for these events show no apparent consistency either among themselves or with the deeper events and seem to accentuate the variability of solutions for events shallower than 150 km, which were noted in the local solutions.

Fault plane solutions throughout the Hindu Kush are reminiscent of those for island arcs but show significantly more variation. When correlated with seismic trends, some patterns in the solutions emerge, but the stresses governing their orientations do not appear to be simple. Nodal planes of the solutions generally do not align with the dip of the zone, so there is apparently no major deep-seated faulting. The T axes for the deeper events lie in the plane of seismicity but do not plunge downdip. Instead, many plunge about 70° to the west, and align with the plunge of the tube of seismicity west of 70.5° E (HH' in Figure 6). As discussed below, there is some evidence that the aseismic gap at about 160-km depth indicates that the lower part of the slab has broken off from the upper part, at least in the west. The westward dipping T axes would then support the idea that the partially detached slab is hanging from the shallower region in a hingelike fashion. Resistance to subduction caused either by a pull from an eastern connection to the shallower zone or by some frictional drag due to flow of mantle material around an obliquely sinking lithosphere could cause the T axes to deviate from vertical. The exceptions to the westward plunging T axes that occur east of the gap at 70.6° E, where the T axes plunge to the east, is also evidence of a local perturbation in the stress field. This perturbation could indicate that the slab in this area is being torn apart by competing stresses. The origin of these stresses is uncertain, but the change in orientation of the axes about a relatively small gap suggests that the subducted lithosphere is discontinuous here.

Tectonic Interpretation

To discuss the Hindu Kush seismicity in the context of the India-Eurasia collision, we make some correlations between the trends of the zone and regional tectonics. In Figure 15 the projection of the seismic zone to the surface is drawn on a map depicting the major faults and some pertinent geology of the region.

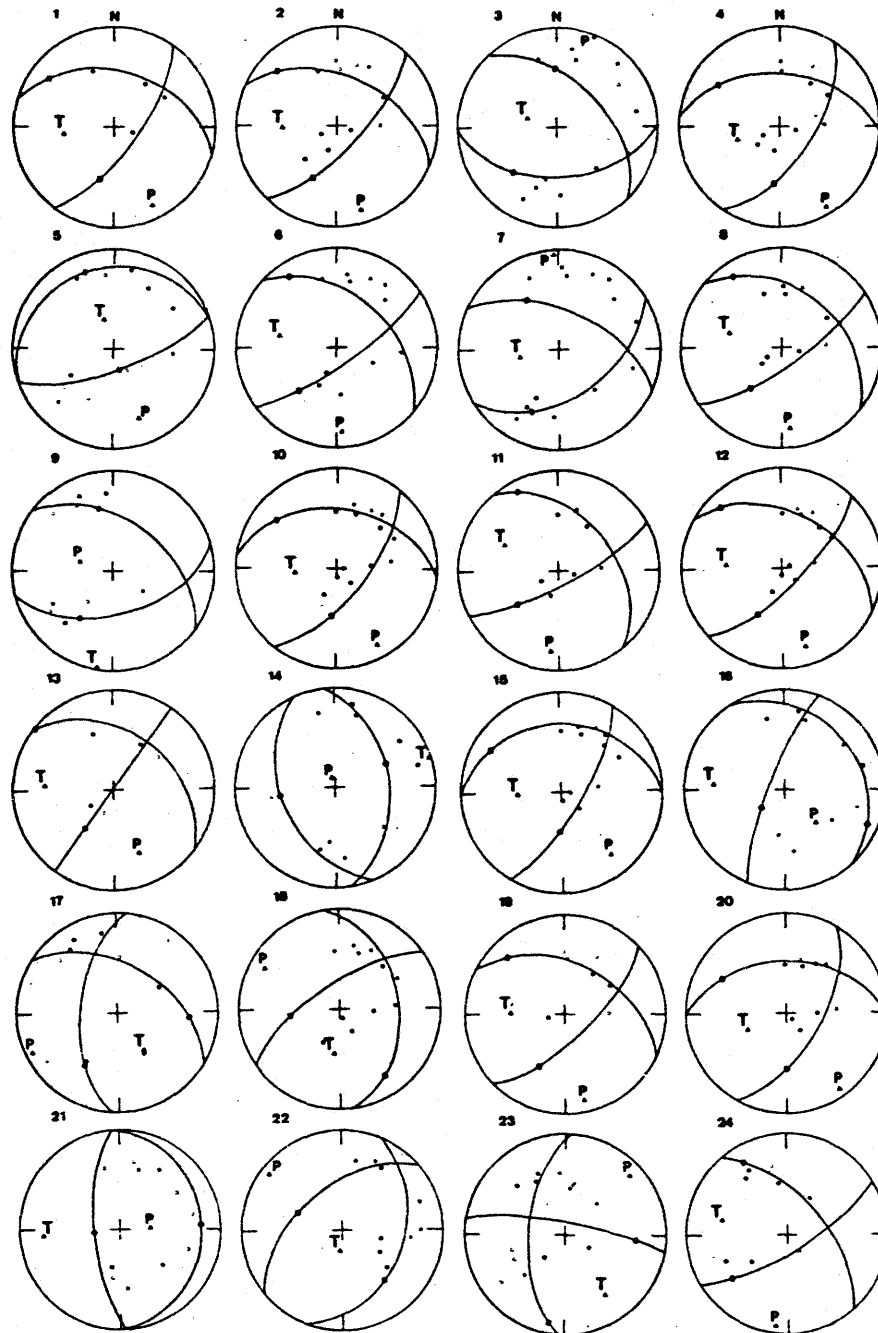


Fig. 10. Lower hemisphere fault plane solutions of all data used in this study. Solid circles represent compressional first motion, and open circles dilatations. Starred solutions are those using data from the WSSN. Arrows on the WSSN plots indicate S wave polarities, and crosses represent nodal readings. Solutions A, B, and C are composite solutions using local data.

Tectonic Overview

As India approached Eurasia, subduction of the Tethys ocean beneath Eurasia apparently occurred along the Indus-Tsangpo suture zone [e.g., Dewey and Bird, 1970; Gansser, 1964, 1966]. The location of this suture east of 76°E is generally assumed to be quite simple with only a single belt of ophiolites [Gansser, 1966, 1977]. To the west, however, the location of the Indus suture is evidently not as simple. One candidate for the westward extension of the

Indus suture is the Dras volcanics that are found in the Ladakh region and can be traced westward almost continuously into Afghanistan [e.g., Gansser, 1977]. Mafic sequences in the Kohistan Himalaya south of the Dras volcanics, however, have been interpreted by Tahirkeli et al. [1977] as being suggestive of island arc crust. According to this interpretation, India would have been subducted at this island arc, and the Dras volcanics would mark the zone where a marginal basin between the arc and the rest of Asia was subducted (see also Burke et al. [1977]). In this region the Indus suture would be a broad

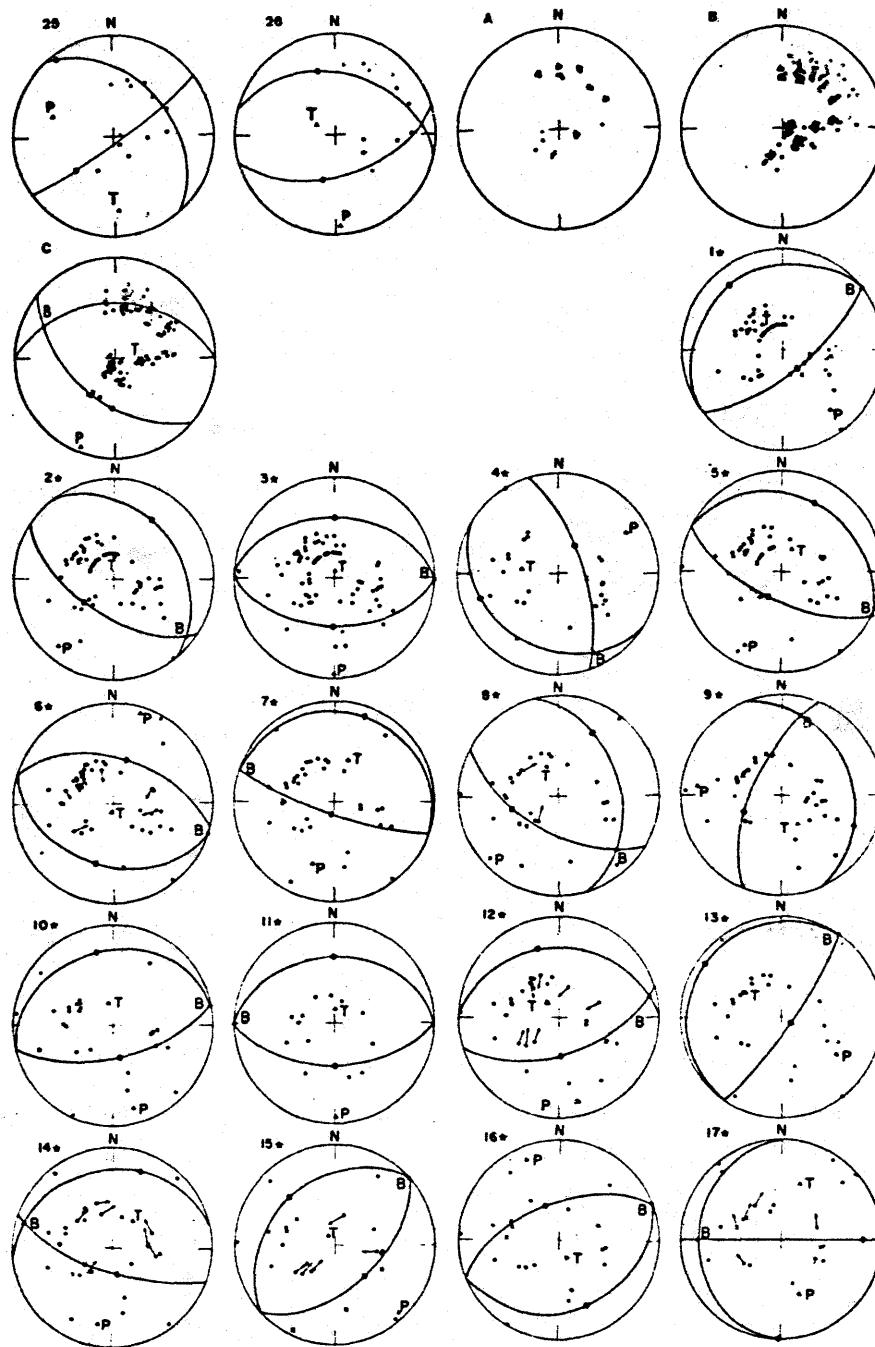


Fig. 10. (continued)

zone that includes both the arc terrain and the Dras volcanics.

The Dras volcanics seem to reach as far west as the Kunar fault, an active fault that is very clear on the Landsat imagery [Prevot et al., 1980]. The Kunar fault seems to terminate in the west near the Sarubi fault, an active right lateral strike slip fault [Prevot et al., 1980; Wellman, 1966]. Ophiolites have been found south and west of the Sarubi, and a mapping of them suggests that they were emplaced during the late Cretaceous or early Tertiary [Cassaigneau, 1979]. These ophiolites seem to be bordered on the west by the Chaman fault, an active left lateral fault than can be traced almost to the Gulf of Oman. West of the Chaman fault there have not seemed to be

ophiolites or other evidence of subduction since the mid-Cretaceous. At present, the Chaman fault appears to accommodate a substantial fraction of the slip between India and Eurasia [Auden, 1974; Chatelain et al., 1977; de Lapparent, 1972; Wellman, 1966]. Both the Chaman and Sarubi faults seem to terminate at the Panjer valley, through which, according to Wellman [1966], the east-west, right lateral Herat fault continues. The Panjer fault trends in a direction approximately parallel to the Kunar fault and is itself associated with ophiolite bodies [Gansser, 1977; Stöcklin, 1977].

In the north, crustal deformation, apparently due to the protrusion of India into Eurasia, essentially follows an arclike pattern

centered symmetrically at about 73°E. This region is laced with a series of southward dipping thrust faults. At least one of them, the Darvaz-Karakul fault, becomes a left lateral strike slip fault to the west [Kuchai and Trifonov, 1977]. To the east, most of the thrust faults abut against right lateral strike slip faults (e.g., the Karakorum fault) [Burtman et al., 1963; Peive et al., 1964; Ruzhentsev, 1963]. Some of these faults were active as early as in the Paleogene, while others appeared in more recent times [Peive et al., 1964]. The trend of the faults generally conforms to that of the Pamir mountain range. The Pamir, however, appears to be a westward continuation of the Kunlun, a late Paleozoic-early Mesozoic orogenic belt along the northern margin of Tibet [Morin [1979], and quoted by Molnar and Burke [1977]; Peive et al. [1964]]. Subsequent right lateral faulting along the Karakorum and other faults seems to have displaced the Pamir 250 km north in relation to the Kunlun [Morin, 1979; Peive et al., 1964].

Inferences Derived From the Configuration of the Seismic Zone

The most general inference that one can make about the Hindu Kush seismic zone is that subduction has taken place. The narrow width and approximately planar character of the zone, along with its essential continuity to depths of 300 km, are indicative of anomalously low temperatures confined to a narrow, planar zone. Presumably, subduction of cold oceanic lithosphere into the warmer asthenosphere has occurred. For the rest of this discussion we take the general scenario of subduction as a starting point and elaborate on it as the additional complexities of the zone require. In particular, we are concerned with the rate and duration of subduction, the influence of the collision on the seismic zone, the possible

locations of sutures, and scenarios for emplacement.

Evidence For Times and Amounts of Subduction

With the exception of seismic activity beneath Burma, the Hindu Kush seismic zone is the only zone of intermediate depth activity near the boundary between India and Eurasia. This observation implies that the Hindu Kush was the scene of final subduction of oceanic lithosphere between India and Eurasia. If the subduction beneath the Hindu Kush was initiated prior to the collision, which occurred 45±10 m.y. ago [Gansser, 1966; Molnar and Tapponnier, 1975; Powell and Conaghan, 1973], the occurrence of earthquakes suggests that it has continued for some time after the collision as well.

Unlike most subduction zones, however, there are no active volcanoes and not even any known recent volcanic material above the seismic zone. Although a full understanding of calc-alkaline volcanism at island arcs is lacking, we note that such volcanism occurs at nearly every known actively subducting region. In western North America, volcanism and subduction seemed to have ceased at essentially the same time [Cross and Pilger, 1973; Snyder et al., 1976]. Although there are no active volcanoes in some portions of the Andes, beneath which subduction has taken place for a long time, most of the Andes experienced Pliocene or Quaternary volcanoes. Therefore we infer that since no volcanic rocks of late Cenozoic age have been reported anywhere along the Hindu Kush, subduction probably occurred only for a short duration.

One implication of a short duration is that if subduction was initiated a long time ago, for instance, 50 m.y. ago, cessation of subduction must also have occurred a long time ago. The existence of intermediate depth events would, however, seem to disallow that.

Table 2. Fault plane solutions determined with the local array data of 1977.

NO	DATE	ORIGIN TIME	LATITUDE (°N)	LONGITUDE (°E)	DEPTH (KM)	P AXIS		T AXIS		B AXIS		POLE OF FIRST NODAL PLANE		POLE OF SECOND NODAL PLANE	
						AZ	PL	AZ	PL	AZ	PL	AZ	PL	AZ	PL
1	77/06/17	15:29	36°28'	70°24'	197	155	14	263	48	52	38	195	46	307	20
2	77/06/18	21:32	36°29'	70°19'	212	154	14	268	46	62	40	204	42	313	20
3	77/06/18	23:20	35°59'	70°38'	112	22	3	286	64	114	26	276	37	358	41
4	77/06/19	05:49	36°29'	70°23'	209	152	7	252	54	56	35	186	42	304	28
5	77/06/19	13:40	36°20'	70°04'	117	160	26	340	65	70	0	340	20	164	72
6	77/06/19	22:50	35°20'	70°39'	135	177	14	282	42	70	42	220	42	326	14
7	77/06/20	01:48	36°05'	70°26'	99	358	5	260	56	90	34	204	32	325	40
8	77/06/20	15:55	36°30'	70°23'	220	174	20	286	44	66	38	326	14	219	48
9	77/06/20	18:16	36°10'	69°24'	119	285	62	189	2	98	26	217	42	347	36
10	77/06/20	20:00	36°41'	71°05'	233	152	14	264	56	52	30	186	50	308	24
11	77/06/22	02:16	36°29'	70°20'	209	186	21	296	40	74	42	232	46	334	12
12	77/06/23	15:37	36°48'	71°11'	260	154	18	274	44	60	39	305	15	208	46
13	77/06/23	15:48	36°33'	70°17'	212	159	32	273	32	36	42	216	50	315	0
14	77/06/23	22:30	36°02'	70°43'	97	340	82	63	1	164	8	66	44	262	44
15	77/06/24	02:45	36°43'	71°07'	217	144	22	270	54	40	26	181	58	302	20
16	77/06/24	20:12	36°07'	70°43'	107	136	52	275	30	18	20	112	12	234	66
17	77/06/26	09:26	35°56'	69°19'	97	246	8	146	52	330	36	94	29	213	39
18	77/06/26	15:05	36°33'	70°57'	212	299	16	188	52	40	32	146	20	262	50
19	77/06/27	16:28	36°28'	70°20'	209	168	14	272	46	64	40	208	44	316	20
20	77/07/01	05:43	36°32'	71°00'	221	145	8	248	56	51	34	180	44	300	28
21	77/07/02	21:11	35°59'	70°43'	94	86	65	266	25	175	0	266	70	36	20
22	77/07/03	14:21	36°24'	71°30'	96	308	8	188	73	40	15	141	35	291	51
23	77/07/04	20:41	36°12'	69°26'	128	48	14	146	28	296	58	139	10	94	30
24	77/07/07	16:48	36°08'	69°08'	112	138	9	282	34	82	56	230	30	329	16
25	77/07/09	17:22	36°33'	71°02'	197	288	37	177	26	60	41	229	48	324	6
26	77/07/11	11:02	36°26'	71°20'	104	178	8	297	72	84	16	345	34	136	50

Table 3. Events used in determining composite fault plane solutions.

Sol.	Date	Origin time	Latitude (°N)	Longitude (°E)	Depth (km)
A	77/06/18	10:03	36°31'	70°24'	221
	77/06/20	00:25	36°31'	70°18'	210
	77/06/22	03:30	36°28'	70°20'	208
	77/06/26	11:03	36°27'	70°22'	216
B	77/06/17	17:14	36°33'	70°57'	197
	77/06/19	01:47	36°44'	71°29'	194
	77/06/20	20:00	36°42'	71°06'	233
	77/06/21	21:33	36°33'	71°22'	160
	77/06/23	23:32	36°42'	71°22'	167
	77/06/26	15:05	36°33'	70°57'	212
	77/07/02	04:09	36°41'	71°04'	242
	77/07/02	14:21	36°28'	70°59'	231
	77/07/03	01:55	36°43'	71°14'	254
	77/07/06	04:54	36°33'	71°01'	204
	77/07/08	01:30	36°38'	71°09'	212
	77/07/08	05:25	36°40'	71°10'	224
	77/07/08	09:50	36°42'	71°14'	235
	77/07/10	08:05	36°40'	71°09'	226
C	77/06/21	05:33	36°29'	70°46'	204
	77/06/23	03:22	36°27'	70°46'	214
	77/06/23	12:14	36°33'	70°41'	205
	77/06/23	20:40	36°38'	70°46'	190
	77/06/25	12:40	36°36'	70°45'	168
	77/07/01	01:39	36°25'	70°43'	219
	77/07/01	15:39	36°37'	70°59'	230
	77/07/02	03:30	36°34'	70°40'	174
	77/07/07	06:20	36°25'	70°38'	229
	77/07/08	03:22	36°27'	70°57'	163
	77/07/12	08:05	36°28'	70°48'	203

In active subduction zones, such as the Japanese arc, the limit in the depth of seismicity occurs in lithosphere that has resided in the mantle for about 15 m.y. or less. We suspect therefore that if subduction of lithosphere beneath the Hindu Kush has ceased, it probably could not have done so earlier than 20 m.y. ago. In fact, since the upper boundary of the seismicity seems to coincide with the depth of the Moho, it is possible that subduction has ceased very recently or is continuing aseismically through a relatively weak lower crust. The continuation of subduction would require that continental lithosphere is being subducted, a situation which might account for the broader zone of seismicity at depths shallower than 170 km.

Although it is difficult to place a precise limit on the duration or on the times of subduction, we can place lower bounds on values associated with these parameters. First the above observations taken together suggest that subduction beneath the Hindu Kush most likely completely postdates the collision about 45 m.y. ago and was probably much more

recent. Since the trend of the seismic zone is approximately perpendicular to the direction of convergence between India and Eurasia, it is unlikely that subduction occurred at a rate exceeding the rate of convergence between these two continents, about 43 mm/yr [Minster and Jordan, 1978]. From the depth of the seismic zone we know that at least 300 km of lithosphere have been subducted. Therefore while the lack of volcanics suggests a short duration of subduction, the depth of seismicity indicates it must be at least 7 m.y.

If all of the convergence did not take place in the region of subduction, the subduction rate could perhaps have been slower, which would in turn result in a longer duration. It is unlikely that the rate of subduction could be very much less, however, because, for lower rates, subduction to such depths probably could not occur. From a study of seismic zones where the rates of subduction and age of subducted oceanic lithosphere is known, Molnar et al. [1979] deduced that the length of the seismic zone is approximately proportional to the rate of subduction times the square of the thickness of subducted lithosphere. If the age of the subducted lithosphere is less than about 100 m.y., the thickness of the lithosphere is proportional to the square root of the age, so that, approximately, length = rate \times age^{1/2} [Molnar et al., 1979]. For oceanic lithosphere older than about 120 m.y., however, the thickness of the lithosphere is essentially constant (\approx 125 km, Parsons and Sclater [1977]), so that the length of the seismic zone is proportional to the rate of subduction. Thus for a length of 300 km the rate of subduction of old lithosphere should be at least 20 mm/yr [Molnar et al., 1979]. For a maximum rate of 43 mm/yr the age of the lithosphere at the time it was subducted beneath the Hindu Kush should have been greater than about 70 m.y.

We conclude that relatively old, and therefore cold and thick, oceanic lithosphere was subducted beneath the Hindu Kush for a short duration in the late Tertiary.

Influence of the Collision

Locations of the earthquakes indicate that at least in the south the lithosphere is sharply bent, going from a horizontal to a vertical disposition in a very short distance. Assuming that the upper seismic zone defines an approximately circular transition region between these dispositions, the radius of curvature for this region is about 100 km. For most subduction zones the radius of curvature is about 200 km [Isacks and Barazangi, 1977]. From the discussion above we suggest that the subducted lithosphere was relatively thick. Therefore if the lithosphere is continuous, a large bending moment, significantly greater than is evident in island arcs, must be applied to it to bend it so sharply. The gap between the events shallower and deeper than about 170 km may in fact represent a discontinuity in the lithosphere, so that at shallower depths the lithosphere does not necessarily curve significantly with increasing depth. The vertically dipping lower region would then have

broken off recently and would be sinking somewhat independently of the shallower region. In addition, there is a considerable change in the dip of this shallower region from east to west. Since the length of the slab is much shorter than at island arcs, where the slab seems to be continuous, the gravitational body force associated with such a short slab is probably inadequate to bend the plate or to break it off. We suspect that the protrusion of the Indian subcontinent has provided a dynamic push that has bent the underthrust slab and straightened up the eastern end of the zone. This conjecture is supported by the fact that the top of the seismic zone near 70 km extends to shallower depths as the zone becomes more vertical, as one might expect if the entire slab were being rotated to a vertical direction without sinking. Moreover, the projection of the seismic zone to the surface (Figure 15) is parallel to trends of folds and faults such as those in the Panjer and Kunar valleys, which apparently were also deformed by the protrusion.

Emplacement Scenarios

An implication of a short duration of subduction is that it is unlikely that the lithosphere beneath the Hindu Kush was once part of the Tethys ocean that was attached to India and subducted beneath Eurasia, unless we have overestimated the date of the collision. Subduction that postdates the collision and occurs over a short duration suggests that independent pieces of oceanic lithosphere, such as intracontinental or interarc basins, have recently been subducted beneath the Hindu Kush north of the Tethys suture [Khalturin et al., 1977]. In examining this proposal we discuss the implications of a spectrum of possible emplacement scenarios.

The problem of trying to determine where and from which direction subduction took place is complicated by the fact that two parts of the zone dip in nearly opposite directions. Any explanation that assumes subduction in only one direction must account for the complete overturn of some part of the downgoing slab, presumably by the underthrusting lithosphere dragging it through the asthenosphere [e.g., Billington et al., 1977]. Such a phenomenon may have occurred north of New Guinea, where the intermediate depth zone dips south under the

island, not northward beneath the volcanoes [Johnson and Molnar, 1972].

The observation that Eurasia moves slowly with respect to frames of reference in which either the relative motion of the hot spots or the net rotation of the lithosphere is minimized [Minster et al., 1974] suggests that Eurasia has not overridden a slab attached to it. Since any slab originally dipping to the south probably would at most be forced to a vertical position, and since the southern zone dips northward, subduction from the north alone is unlikely.

In contrast, India moves rapidly with respect to such frames. As noted above, we infer that the protrusion of a northward moving Indian lithosphere is probably responsible for the partial straightening of the southern zone of subducted lithosphere. If one assumes that subduction occurred entirely from the south, this line of reasoning could be extrapolated to explain the overturning of the northeastern portion of the downgoing slab beneath the Pamirs [e.g., Billington et al., 1977]. Some evidence for this scenario is suggested by the trend of the seismic zone in this area, which conforms to the arc of deformation as defined by the southward dipping thrust faults in the Pamir. One consequence of such a scenario is that if the lithosphere were displaced northward sufficiently to overturn the slab, then the suture that formed when the last part of the basin was subducted, the Pamir suture, would be presently northwest of the seismic zone. The India-Eurasia suture zone is thought to be at or just south of the Kunar fault [Tahirkeili et al., 1977], which is nearly 300 km south of the seismic zone. The Kunar fault therefore could not have been the Pamir suture, and the oceanic lithosphere beneath the Pamir was not originally from the Tethys. Therefore regardless of whether or not subduction occurred entirely from the south, the existence of the intermediate depth events beneath the Pamir requires that an intracontinental (possibly interarc) basin originally lay north of the Kunar fault. Although we are aware of no evidence that disallows northward subduction beneath the Pamir and subsequent overturning of the zone, we think that the geologic evidence is more easily accommodated by a southward subduction beneath the Pamir.

Hence we think that a more likely scenario is

Table 4. Fault plane solutions determined with data from the WSSN.

No	DATE	LATITUDE (*N)	LONGITUDE (*E)	DEPTH (KM)	P AXIS		T AXIS		B AXIS		POLE OF FIRST NODAL PLANE		POLE OF SECOND NODAL PLANE	
					PL	AZ	PL	AZ	PL	AZ	PL	AZ	PL	AZ
1	64/01/28	36.48	70.95	197	26	140	64	320	0	50	22	320	72	140
2	65/03/14	36.42	70.65	205	15	219	72	2	8	127	30	32	58	241
3	66/06/06	36.43	71.12	221	5	180	85	0	0	90	40	0	50	180
4	67/01/25	36.71	71.60	281	24	60	60	276	17	155	64	32	22	252
5	69/03/05	36.41	70.73	208	20	205	70	25	0	115	25	25	65	205
6	69/08/08	36.44	70.86	196	7	16	83	196	0	106	52	16	38	196
7	71/08/06	36.42	70.73	207	35	198	55	18	0	108	10	18	80	198
8	72/01/20	36.39	70.72	214	10	228	64	339	22	134	30	28	50	256
9	72/06/24	36.28	69.69	47	17	276	62	152	23	14	22	112	56	248
10	72/11/16	35.67	69.91	120	18	166	72	346	0	76	27	346	63	166
11	73/10/12	37.68	71.88	35	10	180	80	0	0	90	35	0	55	180
12	73/10/17	36.38	71.11	211	15	168	75	322	13	76	30	342	60	176
13	74/05/13	36.54	70.96	197	35	124	55	304	0	34	10	304	80	124
14	74/07/30	36.42	70.76	209	24	190	63	35	10	285	20	19	67	168
15	74/12/10	36.48	70.47	213	10	137	80	317	0	47	35	317	55	137
16	75/03/03	36.45	70.92	187	15	337	75	157	0	67	30	157	60	337
17	75/05/14	36.08	70.90	97	42	161	42	18	20	270	0	0	70	90

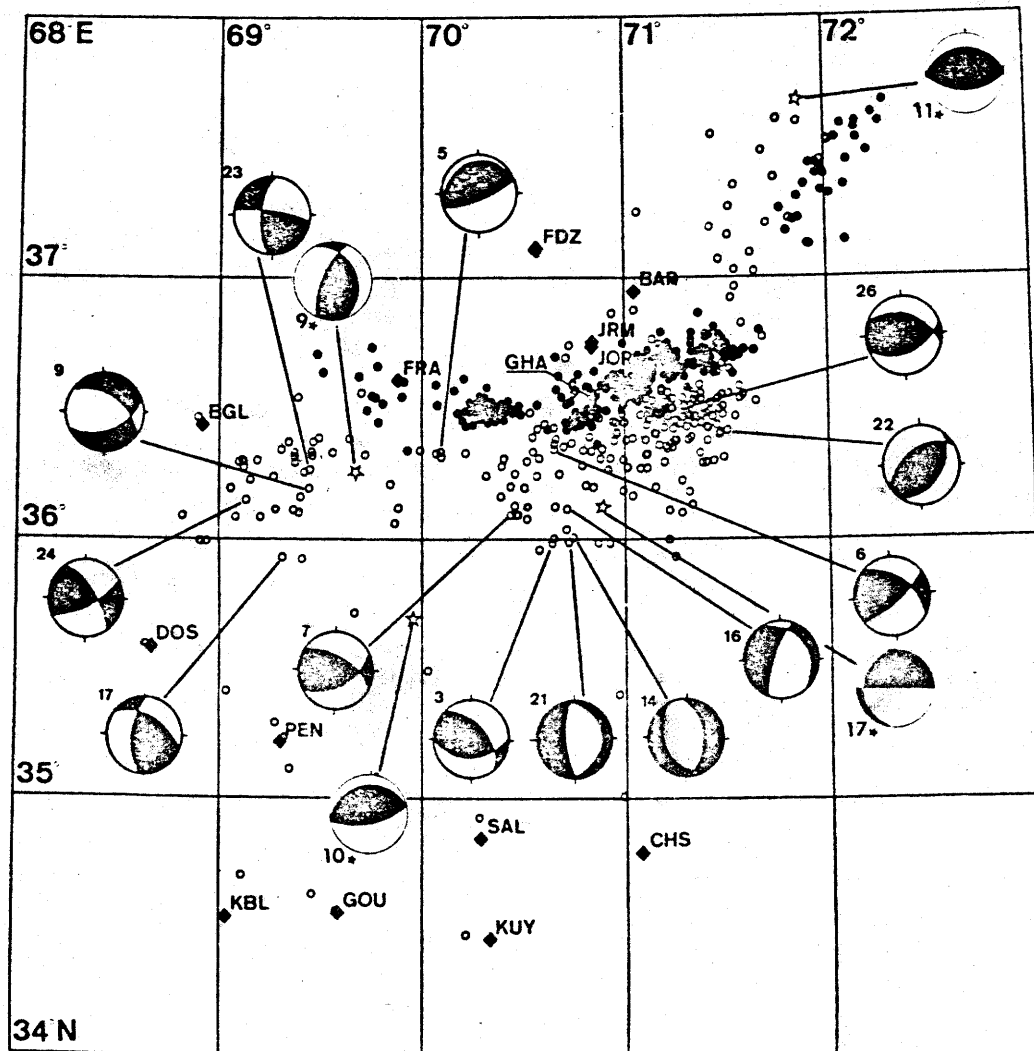


Fig. 11. Lower hemisphere projections in abbreviated balloon format of fault plane solutions for events shallower than 170-km depth using data from local and WSSN stations. Locations of events using WSSN data are plotted as stars. Dark quadrants represent compressional first motions, and white quadrants dilatations.

that two small ocean basins were subducted separately in opposite directions, one to the north beneath the Hindu Kush, and one to the south beneath the Pamir (see also Billington, et al. [1977], Malamud [1973] and Vinnik and Lukk [1974]). Evidence for subduction from the north beneath the Pamir consists of the following observations: first, the zone dips to the south. Second, almost all of the faults north of the zone indicate underthrusting to the south. By examining repeated facies of Cretaceous and Paleogene sediments, Peive et al. [1964] infer that at least 100 km of northward overthrusting has occurred along these faults. In the Garm region, just east of the Vakhsh overthrust, geodetic observations indicate active convergence of about 2 cm/yr [Konopoltsev, 1971] and an uplift of the south wall of a thrust fault at about 1 cm/yr [Finko and Enman, 1971; Mersesov et al., 1976]. A projection of the seismic zone to the surface lies near the Darvaz-Karakul fault, which changes from a southward dipping thrust in the north to a left lateral strike slip fault in the west [Kuchai and Trifonov, 1977]. Displace-

ment along the western part of Darvaz-Karakul seems to occur at about 1 cm/yr [Kuchai and Trifonov, 1977], and the accumulated displacement could be as much as 200 km [Zakharov, 1969]. Right lateral displacement of 250 km seems to have occurred along northeast trending faults east of the Pamir [Norin, 1979; Peive et al., 1964]. All of these data are consistent with a northward overthrusting of the Pamir onto the rest of the Eurasian landmass. Finally, thick marine sediments were deposited in the Tadjik depression north and west of the zone during the upper Cretaceous and Paleogene [Peive et al., 1964]. The Darvaz-Karakul fault seems to separate these sediments from Paleozoic deposits to the south and east. We note that subduction from the north requires a Pamir suture which lies far to the north of the India-Eurasia suture, and this in turn would imply that a marginal ocean basin, isolated within the Eurasian continent, once existed north of the Pamir.

The northward dip of the Hindu Kush seismic zone strongly implies that it formed by subduction from the south. Some geological

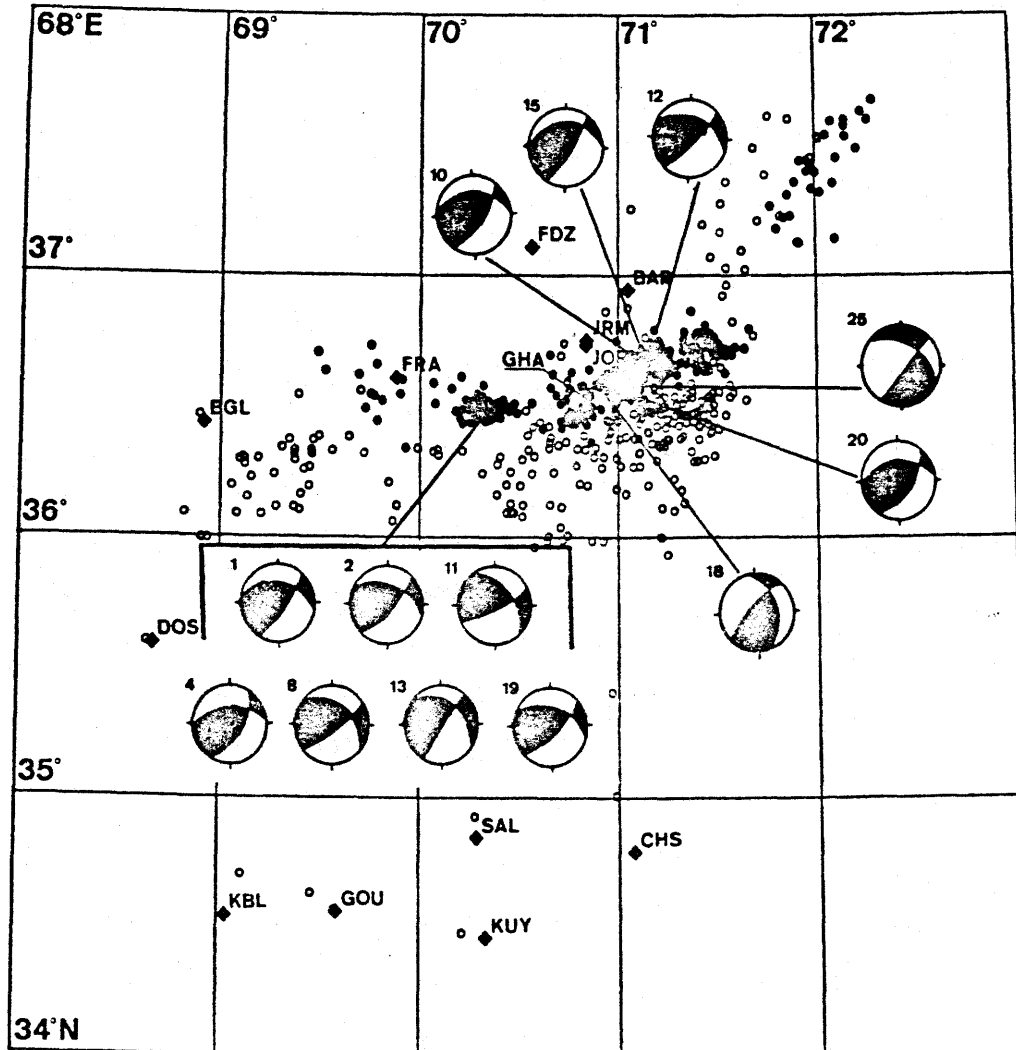


Fig. 12. Fault plane solutions using local data for events deeper than 170 km. Symbols as in Figure 11.

evidence exists that supports this direction of subduction, but the details of the emplacement are difficult to resolve. The surficial projection of the zone intersects the surface just south of the Panjer fault, making it a likely candidate for a suture zone. Ophiolites have been identified both on the Panjer and at least as far as 300 km to the south of the Panjer [Cassaigneau, 1979; Gansser, 1977; Stöcklin, 1977]. These latter ophiolites are bordered on the west by the Chaman fault, which apparently terminates at its intersection with the Herat fault in the Panjer valley. Such a geometry is suggestive of a system analogous to a trench-transform system. The Chaman fault has been active at least since some time in the Tertiary, and although the data are not conclusive, there may have been as much as 300-500 km of left lateral displacement along it [Auden, 1974; de Lapparent, 1973; Wellman, 1966]. A hypothetical extension of the fault past its termination aligns approximately with the western edge of the intermediate depth seismicity.

These observations, however, do not prove that subduction took place at the Panjer fault. The ophiolites south of the Panjer were apparently emplaced in the late Cretaceous or

early Tertiary [Cassaigneau, 1979; Gansser, 1977; Mattauer et al., 1978], which is too early to be associated with the final closure of a basin whose lithosphere now contains the Hindu Kush seismicity. Moreover, the ophiolites in the Panjer valley are of uncertain age and not well studied.

A second possibility for the suture zone is the Kunar fault and its extension east into the Hazara region north of the Kohistan Himalaya. From the geology of the region further north, Tahirkeli et al. [1977] suggested that an interarc basin was subducted at the Kunar fault after the collision with India. The projection of the seismic zone is approximately parallel to the trend of the Kunar fault but would imply that thrusting occurred on a plane dipping at about 20° between 0- and 70-km depth. Fault plane solutions of large events in the Himalaya are consistent with such a dip [e.g., Molnar et al., 1977], but a study of microearthquakes near the Kunar fault does not reveal a simple fault dipping northward [Prevot et al., 1980]. Again, this evidence is inadequate to prove that the lithosphere in which the Hindu Kush earthquakes occur was subducted here.

In any event, subduction beneath the Hindu Kush from the south seems likely, even if the suture zone cannot as yet be recognized with certainty.

Although the possibility of oppositely subducting lithosphere has been proposed before from other studies of seismicity, differences in the data resulted in different interpretations. In the teleseismic study of Billington et al. [1977], such a scenario was partially dismissed because the results implied that the two zones would somehow become contiguous after the collision. The microearthquake results, however, show a considerable gap between the regions. Therefore even though the simultaneous subduction of lithosphere in different directions within a relatively small area may seem unusual, the gap between them indicates that some spatial independence between the neighboring basins could have existed.

The earthquake locations also suggest that the sutures associated with subduction of the two basins lie on opposite sides of the Pamir-Hindu Kush orogenic belt. Since this belt formed in the late Paleozoic or early Mesozoic and therefore predates subduction, there must have been two oceanic basins separated by the Pamir-Hindu Kush belt regardless of the direction of subduction. On the basis of these

observations we suggest that the subduction of two oceanic basins in opposite directions beneath the Hindu Kush and Pamir is both plausible and likely.

Subduction of isolated basins probably has been quite common in the tectonic evolution of orogenic belts. As Arabia and Africa continue to converge with Eurasia, isolated basins such as those beneath the Black Sea and Caspian Sea probably will eventually be subducted. They could well be future analogues for the kind of subduction beneath the Hindu Kush and Pamir. For a brief time they will give rise to intermediate and possibly deep earthquakes in isolated areas far from the main suture zones, where thousands of kilometers of oceanic lithosphere were subducted. Clearly, the existence in the past of such basins and their subsequent subduction will cause complexity that will make the unraveling of geologic history of orogenic belts much more complicated than standard two-dimensional cartoons imply.

Summary

Owing to the high activity of the Hindu Kush seismic zone the microearthquake investigations of 1976 and 1977 recorded a substantial number of earthquakes. From a series of tests designed

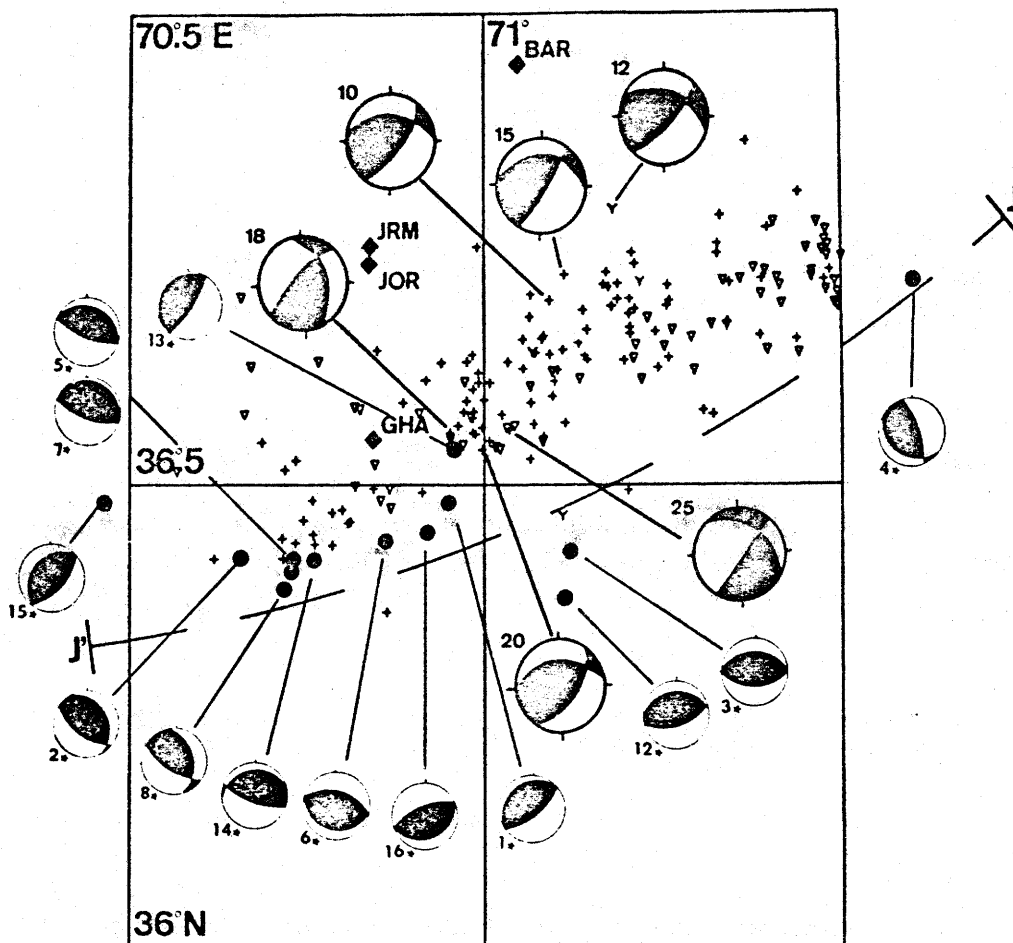


Fig. 13. Fault plane solutions using WSSN data for events deeper than 170 km. Solutions for locally recorded events occurring in the area are plotted as well. The line J'J is a section of H'H used to plot the solutions in a lateral projection parallel to the zone. Symbols as in Figure 11.

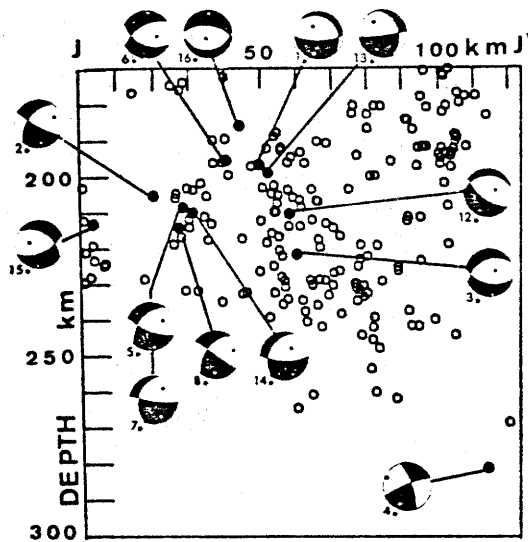


Fig. 14. Back hemisphere projections of fault plane solutions using WSSN data onto a lateral section parallel to the zone. Location of the J'J' section is given in Figure 13.

to evaluate different sources of uncertainty, quality criteria were developed for estimating the precision of the location of these events. From the 1200 events for which locations could be obtained, application of the criteria allowed us to cull out 600 well-located events, with uncertainties in epicenter of about 5 km and in depth of 10 km. These 600 events were used to define the seismic zone in some detail. While the definition of a seismic zone with data from a temporary network carries the stigma of inadequate sampling, many of the features revealed by the 1977 study are reflected in the microearthquake studies of 1976 and 1967-68 [Roecker et al., 1980] and in the teleseismic results of Billington et al. [1977] and Santo [1969]. In fact, the large number of earthquakes in the 1977 study accentuated many features such as a bend in the zone at shallower depths and aseismic gaps, which went largely unnoticed in previous studies.

We find that the crust from 0- to 70-km depth is essentially aseismic. Below the crust the seismic zone in the upper mantle is separated into three regions by two prominent aseismic gaps. A 70-km gap separates a southward dipping region beneath the Pamir from a northward dipping one beneath the Hindu Kush. A gap in seismicity beneath the Hindu Kush further separates seismic regions deeper and shallower than about 170 km from one another. The deeper region is characterized as a narrow (15-20 km) vertically dipping zone, while the shallower region is broad and dips at progressively steeper angles from west to east. The differences in dip and breadth of these regions makes the long-term role of the aseismic gaps as boundaries viable.

Fault plane solutions for the ocean events, determined with both local and WSSN data, reveal T axes generally lying in the plane of seismicity and P axes generally perpendicular to the plane, which is similar to solutions in island arcs. In contrast to island arcs the T

axes are not always parallel to the dip of the zone, and there seems to be substantial variation in their orientation. Much of this variation occurs on opposite sides of a resolvable gap in activity of about 15-km width in the deeper region at about 70.6°E. To the west of this gap, T axes plunge to the west. On the other side of the gap, T axes plunge to the east and, further east, become progressively more westward plunging. In the western end of the deeper seismic zone, activity seems to be confined to a tube which dips to the west, and the T axes west of the 70.7°E gap are roughly parallel with this trend.

In contrast to the smooth variation of the solutions for deeper events, the fault plane solutions for shallower events show a great deal of scatter. A larger data set than is presently available may perhaps resolve a pattern in these solutions, but no consistent behavior is evident in the 1977 solutions.

On the basis of the essentially narrow and planar definition at the seismic zone to depths of 300 km, we infer that subduction of oceanic lithosphere has taken place beneath the Hindu Kush. Some bounds on parameters associated with this subduction can be made by considering the extent of the seismic zone and its relation to the tectonic environment. From the isolated nature of the seismic zone, from the occurrence of earthquakes at depths of 300 km, and from the absence of volcanic rocks above the zone it is likely that subduction occurred over a short duration and did not begin much before 20 m.y. ago. Subduction may actually be occurring today through a relatively weak lower crust. A recent history of subduction places an upper bound on the rate of subduction of about 43 mm/yr, while the depth of activity restricts this rate to be at least about 20 mm/yr. We infer that the oceanic lithosphere was probably greater than 70 m.y. old when subducted and therefore relatively thick. A comparison of the dips of the shallower and deeper zones suggests that the gaps between them near 170-km depth actually may represent a discontinuity in the lithosphere, and the change in dip of the shallower zone is most likely a result of the penetration of the Indian subcontinent into Eurasia.

By correlating the trend of the seismic zone with surficial geology we draw some inferences regarding the tectonic evolution of the region. Although the scenario given is not exclusive, we think that the available evidence is most easily accommodated by subduction of two separate basins in opposite directions. A projection of the seismic zone to the surface reveals some possible candidates for Hindu Kush - Pamir suture zones. North of the Pamir the seismic projection lies south of the Darvaz-Karakul thrust fault, which separates the thick Cenozoic marine deposits of the Tadjik depression in the west and north from Paleozoic deposits to the south and east. South of the Hindu Kush the projection lies just south of the Panjer fault, but the role of this fault as a suture is uncertain. Another candidate for Hindu Kush suture is the Kunar fault and its extension to the east, north of the Kohistan Himalaya, since it may have at one time been

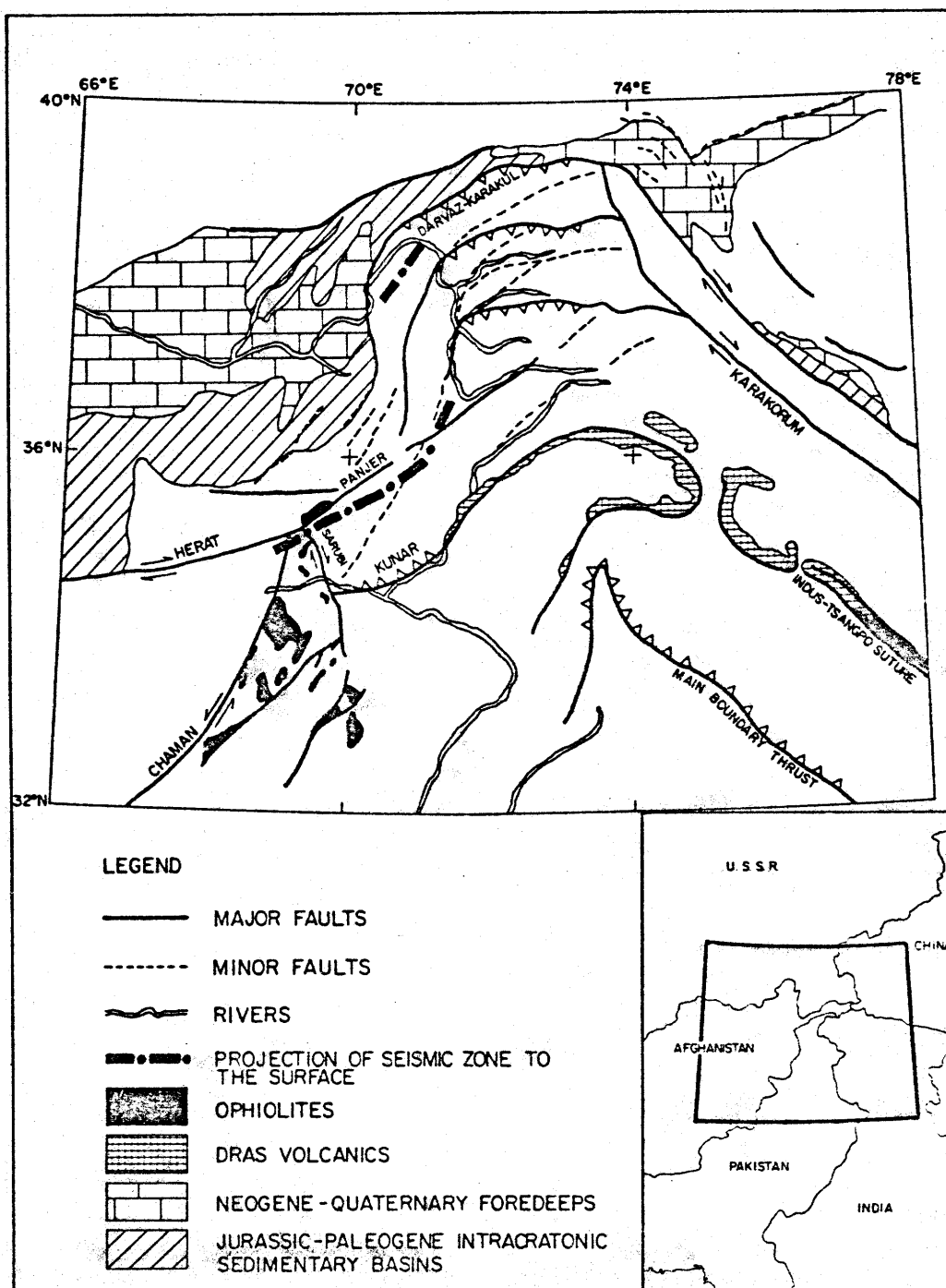


Figure 15. Map of major tectonic features of the Pamir-Hindu Kush region and their relation to a projection of the seismic zone to the surface. The projection of the zone was made by fitting a line to the trend of the shallower side of the zone above 170 km. Faults and geologic features are taken from maps compiled by Desio [1975], Gansser [1977], Peive et al. [1964], and Stöcklin [1977].

associated with subduction of a marginal basin [Burke et al., 1977; Tahirkeli et al., 1977].

While the unraveling of the history of the Pamir-Hindu Kush is rather complicated, we suggest that the geology and seismicity in this area may actually be a prototype of a type of complexity that will exist after basins such as those beneath the Black and Caspian seas are subducted and that has probably been common in collision zones.

Acknowledgements. We thank J. P. Carbonnel for assistance in both logistics and technical matters. We were ably assisted in the field by J. Frechet, M. Frogneux, X. Goula, M. Grosenbaugh, L. Jones, J. King, J. Maurer, R. Prevot, G. Suarez, and B. Tucker and Afghan engineers Kandari, Osman, Rabi, and Sharif. We appreciated the assistance and hospitality of J. Summers of the Afghan American Educational Commission and R. E. Gibson, H. Hafiz, A. S.

Saleem, and others of Kabul University. We thank Woodward Clyde Consultants and, in particular, W. Savage and D. Tocher for loaning us two Sprengnether instruments for the work in 1977. We thank D. Gubbins for assisting us in preparing the test made with a laterally heterogeneous structure. We also benefitted from discussion and encouragement from K. H. Jacob, V. I. Khalturin, A. A. Lukk, M. Mattauer, I. L. Nersesov, G. Perrier, F. Proust, T. G. Rautian, L. Seeber, O. V. Soboleva, and P. Tapponnier. We thank Kabul University for copies of seismograms from the station in Kabul, the Applied Seismology Group of the Lincoln Laboratory and Lamont-Doherty Geological Observatory for the use of the WWSSN data and facilities, Lamont also for the use of data from the Tarbella Array, and the Institute of Physics of the Earth of the Academy of Sciences of the USSR for allowing us to examine records from Soviet stations in Tadzhikistan. Finally we thank two anonymous referees for constructive criticism. This research was supported primarily by contract ATP No. 35-06 of IMAG (Grenoble) and NSF grants EAR76-13367A01 and EAR78-13673 (MIT). The MIT group's part, however, was made possible by an H. O. Wood award from the Carnegie Institution in Washington and by an Alfred P. Sloan Fellowship.

References

- Armbruster, J., L. Seeber, and K. H. Jacob, The northwestern termination of the Himalayan mountain front: Active tectonics from micro-earthquakes, *J. Geophys. Res.*, **83**, 269-282, 1978.
- Auden, J. B., Afghanistan-West Pakistan, Mesozoic-Cenozoic Orogenic Belts: Data for Orogenic Studies; Alpine-Himalayan Orogens, *Geol. Soc. London Spec. Publ.*, **4**, 365-378, 1974.
- Billington, S., B. L. Isacks, and M. Barazangi, Spatial distribution and focal mechanisms of mantle earthquakes in the Hindu-Kush-Pamir region: A contorted Benioff zone, *Geology*, **5**, 699-704, 1977.
- Buland, R., The mechanics of locating earthquakes, *Bull. Seismol. Soc. Amer.*, **66**, 173-188, 1976.
- Burke, K., J. F. Dewey, and W. S. F. Kidd, World distribution of sutures: The sites of former oceans, *Tectonophysics*, **40**, 69-99, 1977.
- Burtman, V. S., A. V. Peive, and S. V. Ruzhentsev, Main lateral faults of Tien Shan and Pamir, in *Faults and Horizontal Movements of the Earth's Crust* (in Russian), Academy of Sciences of the USSR, Institute of Geology, pp. 152-172, 1963.
- Cassaigneau, C., Contribution a l'étude des suture Inde-Eurasie; la zone de suture de Khost dans le Sud-Est de l'Afghanistan l'abduction Paleogene et la tectonic tertiaire, these de Docteur de 3^{ème} cycle, Univ. des Sci. et Tech. du Languedoc, Montpellier, France, 1979.
- Chatelain, J. L., S. Roecker, D. Hatzfeld, P. Molnar, and G. Perrier, Etude seismologique en Afghanistan, Premiers resultats, *C. R. Somm. Soc. Geol. Fr.*, **5**, 260-262, 1977.
- Cross, T. A., and R. H. Pilger, Constrains on absolute plate motions and plate interaction inferred from Cenozoic igneous activity in the western United States, *Amer. J. Sci.*, 1978.
- de Lapparent, A. F., Esquisse géologique de l'Afghanistan, *Rev. Geogr. Phys. Geol. Dyn.*, **14**, (2), 327-344, 1972.
- Desio, H. (ed.), *Italian Expeditions to the Karakorum (K2) and Hindu Kush*, vol. 3, *Geology of Central Badakhstan (Northeast Afghanistan) and Surrounding Countries*, 628 pp., E. J. Brill, Leiden, Netherlands, 1975.
- Dewey, J. F., and J. M. Bird, Mountain belts and the new global tectonics, *J. Geophys. Res.*, **75**, (14), 2625-2647, 1970.
- Finko, Ye. A., and V. B. Enman, Present surface movements in the Surkhob fault zone (in Russian), *Geotectonika*, **5**, 117-125, 1971.
- Gansser, A., *Geology of the Himalayas*, 289 pp., Interscience, New York, 1964.
- Gansser, A., The Indian Ocean and the Himalayas A geological interpretation, *Eclogae Geol. Helv.*, **59**, 831-848, 1966.
- Gansser, A., The great suture zone between Himalaya and Tibet - A preliminary account, in *Himalaya: Sciences de la Terre*, pp. 209-212, Centre National de la Recherche Scientifique, Paris, 1977.
- Isacks, B. L., and M. Barazangi, Geometry of Benioff zones: Lateral segmentation and downwards bending of the subducted lithosphere *Island Arcs, Deep-Sea Trenches, and Back-Arc Basins*, Maurice Ewing Ser., Vol. 1, edited by M. Talwani and W. C. Pitman, III, pp. 99-114, AGU, Washington, DC, 1977.
- Isacks, B. L., and P. Molnar, Distribution of stresses in the descending lithosphere from a global survey of focal mechanism solutions of mantle earthquakes, *Rev. Geophys. Space Phys.*, **9**, 103-174, 1971.
- James, D. E., I. S. Sacks, E. Lazo L., and P. Araricio G., On locating local earthquakes using small networks, *Bull. Seismol. Soc. Amer.*, **59**, 1201-1212, 1969.
- Johnson, T., and P. Molnar, Focal mechanisms and plate tectonics of the southwest Pacific, *J. Geophys. Res.*, **77**, 1433-1438, 1972.
- Khalturin, V. V., T. G. Rautian, and P. Molnar, The spectral content of Pamir-Hindu Kush intermediate depth earthquakes, evidence for a high Q zone in the upper mantle, *J. Geophys. Res.*, **82**, 2931-2943, 1977.
- Konopaltsev, I. M., Crustal movements in the Garm area, from the 1948-1970 measurements (in Russian), *Geotectonika*, **5**, 111-116, 1971.
- Krestnikov, V. V., and I. L. Nersesov, Relations of the deep structure of the Pamirs and Tien Shan to their tectonics, *Tectonophysics*, **1**, 183-191, 1964.
- Kuchai, V. K., and V. G. Trifonov, Young sinistral shearing along the Darvaz-Karakul fault zone, (in Russian), *Geotectonika*, **3**, 91-105, 1977.
- Lee, W. H. K., and J. C. Lahr, HYP071 (revised): A computer program for determining hypocenter, magnitude, and first motion pattern of local earthquakes, *Open File Rep.*, **75-311**, U. S. Geol. Surv., Reston, VA, 1975.
- Lukk, A. A., and I. L. Nersesov, The deep Pamir-Hindu Kush earthquakes, in *Earthquakes in the USSR in 1966* (in Russian), pp. 118-136, Nauka, Moscow, 1970.
- Malamud, A. S., Several regularities of the spatial distribution of the Pamir-Hindu Kush

- deep focus earthquakes (in Russian), Izv. Akad. Nauk Tadzh. SSR Otd. Fiz. Matematicheskikh Geol. Khim. Nauk, 4, 70-73, 1973.
- Mattauer, M., F. Proust, P. Tapponnier, and C. Cassaigneau, Ophiolites, obductions et tectonique global dans l'Est de l'Afghanistan, C. R. Acad. Sci., 287, 983-985, 1978.
- Minster, J. B., and T. H. Jordan, Present day plate motions, J. Geophys. Res., 83, 5331-5354, 1978.
- Minster, J. B., T. H. Jordan, P. Molnar, and E. Haines, Numerical modeling of instantaneous plate tectonics, Geophys. J. Roy. Astron. Soc., 36, 547-576, 1974.
- Molnar, P., and K. Burke, Penrose conference report: Erik Norin Penrose Conference on Tibet, Geology, 5, 461-463, 1977.
- Molnar, P., W. P. Chen, T. J. Fitch, P. Tapponnier, W. E. K. Warsi, and F. T. Wu, Structure and tectonics of the Himalaya: A brief summary of relevant geophysical observations, Colloques Internationaux du C.N.R.S., No. 268, Ecologie et Geologie de l'Himalaya, 269-293, 1977.
- Molnar, P., and P. Tapponnier, Cenozoic tectonics of Asia: Effects of a continental collision, Science, 189, 419-426, 1975.
- Molnar, P., D. Freedman, and J. S. F. Shih, Lengths of intermediate and deep seismic zones and temperatures in downgoing slabs of lithosphere, Geophys. J. Roy. Astron. Soc., 56, 41-54, 1979.
- Nersesov, I. L., T. V. Latynina, T. V. Guseva, N. Zharinev, and A. A. Khobotko, On the deformation of the earth's crust in the Surkhob fault zone (in Russian), Izv. Acad. Sci. USSR, Phys. Solid Earth, 12, 26-37, 1976.
- Norin, E., The relation between the Tibetan platform and the Tarim Basin, Submitted to Geol. Soc. Amer. Bull., 1979.
- Nowroozi, A. A., Seismo-tectonics of the Persian plateau, eastern Turkey, Caucasus, and Hindu Kush regions, Bull. Seismol. Soc. Amer., 61, 317-321, 1971.
- Nowroozi, A. A., Focal mechanism of earthquakes in Persia, Turkey, West Pakistan, and Afghanistan and plate tectonics of the Middle East, Bull. Seismol. Soc. Amer., 62, 823-850, 1972.
- Parsons, B., and J. Sclater, An analysis of ocean floor bathymetry and heat flow with age, J. Geophys. Res., 82, 803-827, 1977.
- Peive, A. V., V. S. Burtman, S. V. Ruzhentsev, and A. I. Suvorov, Tectonics of the Pamir-Himalayan sector of Asia, in Report of the Twenty Second Session, India, International Geological Congress, part XI, Himalayan and Alpine Orogeny, pp. 441-464, International Geological Congress, New Delhi, 1964.
- Powell, C. McA., and P. J. Conaghan, Plate tectonics and the Himalayas, Earth Planet. Sci. Lett., 20, 1-12, 1973.
- Prevot, R., D. Hatzfeld, S. W. Roecker, and P. Molnar, Shallow earthquakes and active tectonics in eastern Afghanistan, J. Geophys. Res., 85, this issue, 1980.
- Ritsema, A. R., The fault plane solutions of earthquakes of the Hindu Kush Centre, Tectonophysics, 3, 147-163, 1966.
- Roecker, S. W., O. V. Soboleva, D. Hatzfeld, J. L. Chatelain, and P. Molnar, Seismicity and fault plane solutions of intermediate depth earthquakes in the Pamir-Hindu Kush region, J. Geophys. Res., 85, this issue, 1980.
- Ruzhentsev, S. V., Transcurrent faults in the southeastern Pamir, in Faults and Horizontal Movements of the Earth's Crust (in Russian), pp. 115-127, Academy of Sciences of the USSR, Institute of Geology, Moscow, 1963.
- Santo, T., Regional study on the characteristic seismicity of the world, I, Hindu Kush region, Bull. Earthquake Res. Inst., Tokyo Univ., 47, 1035-1049, 1969.
- Shirokova, E. I., Determination of the stresses effective in the foci of the Hindu Kush earthquakes (in Russian), Izv. Akad. Nauk SSSR, Ser. Geofiz., 12, 1739-1745, 1959.
- Snyder, W. S., W. R. Dickinson, and M. L. Silberman, Tectonic implications of space-time patterns of Cenozoic magmatism in the western United States, Earth Planet. Sci. Lett., 32, 91-106, 1976.
- Soboleva, O. V., Special features of the directions of the principal stress axes in the foci of Hindu Kush earthquakes (in Russian), Izv. Acad. Sci. USSR, Phys. Solid Earth, 1, 71-78, 1968a.
- Soboleva, O. V., Effect of the asymmetry of the focal radiation upon the distribution of the displacements around the epicenter of a deep earthquake (in Russian), Izv. Acad. Sci. USSR, Phys. Solid Earth, 10, 45-56, 1968b.
- Soboleva, O. V., Method for unambiguous determination of the fault plane in the source using the Hindu-Kush zone as an example, (in Russian), Izv. Acad. Sci. USSR, Phys. Solid Earth, 1, 50-59, 1972.
- Stevens, A. E., S-wave focal mechanism studies of the Hindu Kush Earthquake of 6 July 1962, Can. J. Earth Sci., 3, 367-384, 1966.
- Stöcklin, J., Structural correlation of the Alpine ranges between Iran and Central Asia, in Livre a la Memoire de Albert F. de Lapparent, pp. 333-353, Société Géologique de France, Paris, 1977.
- Tahirkeili, R. A. K., M. Mattauer, F. Proust, and P. Tapponnier, Données nouvelles sur la suture Inde-Eurasie au Pakistan, in Himalaya; Sciences de la Terre, pp. 209-212, Centre National de la Recherche Scientifique, Paris, 1977.
- Vinnik, L. P., and A. A. Lukk, Velocity inhomogeneities of the upper mantle of Central Asia (in Russian), Dok. Akad. Sci. USSR, 213, 580-583, 1973.
- Vinnik, L. P., and A. A. Lukk, Lateral inhomogeneities in the upper mantle under the Pamir-Hindu Kush (in Russian), Izv. Acad. Sci. USSR, Phys. Solid Earth, 1, 9-22, 1974.
- Vinnik, L. P., A. A. Lukk, and I. L. Nersesov, Nature of the intermediate seismic zone in the mantle of Pamir-Hindu Kush, Tectonophysics, 38, T9-T14, 1977.
- Wellman, H. N., Active wrench faults of Iran, Afghanistan, and Pakistan, Geol. Rundschau, 55, 716-735, 1966.
- Zakharov, S. A., On the characteristic features of the geotectonics of the Tadjik depression, in Neotectonics and Seismo-tectonics of Tadjikistan (in Russian), pp. 3-19, Donish, USSR, 1969.

(Received April 23, 1979;
revised November 1, 1979;
accepted November 7, 1979.)

CHAPTER II

Aureliano not only understood by then, he also lived his brother's experiences as something of his own, for on one occasion when the latter was explaining in great detail the mechanisms of love, he interrupted him to ask: "What does it feel like?" José Arcadio gave his immediate reply:

"It's like an earthquake."

- Gabriel Garcia Marquez

One Hundred Years of Solitude

SEISMICITY AND FAULT PLANE SOLUTIONS OF INTERMEDIATE
DEPTH EARTHQUAKES IN THE PAMIR-HINDU KUSH REGIONS. W. Roecker,¹ O. V. Soboleva,² I. L. Nersesov,³ A. A. Lukk,³
D. Hatzfeld,⁴ J. L. Chatelain,⁴ and P. Molnar¹

Abstract. Relocations of earthquakes, recorded by a local network of stations in Afghanistan and Tadjikistan in 1966 and 1967, indicate a narrow seismic zone (width \lesssim 30 km) dipping steeply into the mantle to a depth of 300 km beneath the Pamir and Hindu Kush ranges. Very low seismicity was observed at depths less than about 70 km, the approximate depth of the Moho. Clear gaps in activity exist also within the zone of intermediate depth seismicity. One gap, about 50 km wide near 37°N and at depths greater than 100 km, separates a steeply northward dipping zone to the southwest from a steeply southeastward dipping zone to the northeast. This gap probably marks either a tear in the downgoing slab or a gap between two oppositely dipping slabs. Fault plane solutions, determined by Soboleva for events between 1960 and 1967, generally show steeply plunging T axes approximately within the planar seismic zone. They therefore are grossly similar to those at island arcs where no deep earthquakes occur and presumably result from gravitational body forces acting on a relatively dense slab of lithosphere. At the same time there is a very large variation in the fault plane solutions, much larger than is common at island arcs.

Introduction

Although it does not have an island arc structure, the Pamir-Hindu Kush region is the source of very high intermediate depth seismicity. This region is one of the most active sources of earthquakes felt within the USSR, even though most of it lies outside of the USSR, in Afghanistan. Accordingly, Soviet seismologists have devoted considerable attention to its study. An extensive network of stations has been operated in Tadjikistan for 20 years by the Tadjik Institute of Seismo-Resistant Construction and Seismology (TISSS) of the Academy of Sciences of the Tadjik SSR and by the Institute of Physics of the Earth (IFZ) of the Academy of Sciences of the USSR (in Moscow). Moreover, in 1966 and 1967 a special network was installed in Afghanistan and along the Soviet-Afghan boundary by the IFZ to study the seismicity and structure of this region. The data in

1966 and 1967 allowed the most precise determinations of hypocenter that were possible at that time [Lukk and Nersesov, 1970]. These hypocenters defined an approximately planar zone that dips steeply into upper mantle and extends in an east-west direction for nearly 700 km. With careful analytical and graphical techniques, but without the aid of high-speed computers, Lukk and Nersesov [1970] simultaneously determined a velocity structure for the crust and upper mantle and located the earthquakes. In the present paper we extend their study and present relocations of these same events using a computer.

The data obtained with this network were also used to infer a high-velocity zone surrounding the seismic zone [Vinnik and Lukk, 1973, 1974; Vinnik et al., 1977], and subsequent studies suggested a corresponding high Q zone [Khalturin et al., 1977; Molnar et al., 1976]. These studies and others [Billington et al., 1977; Chatelain et al., 1977, 1980; Malamud, 1973; Nowroozi, 1971, 1972] suggested a variety of possible configurations of slabs of oceanic or continental lithosphere that had been subducted in the region.

In addition, the longer-term recording in Tadjikistan has allowed the determination of numerous fault plane solutions of earthquakes with magnitudes ranging from about $4\frac{3}{4}$ to 7 [Soboleva, 1968a,b, 1972]. Because of the close proximity of many stations, much smaller events were studied than was ordinarily possible with data from the World-Wide Standardized Seismograph Network (WWSSN) alone. Soboleva [1968a] discussed the orientations of the P, T, and B axes and their relationships to the seismic zone, but her interpretation preceded the recognition of plate tectonics and more modern ideas about such relationships [Isacks et al., 1968, 1969; Isacks and Molnar, 1969, 1971]. Moreover, locations of these events which occurred between 1960 and 1967 were sufficiently imprecise to reveal systematic relationships between solution and location, such as those observed by Chatelain et al. [1980]. In the present paper we use either Nowroozi's 1971 relocations of the events or hypocentral determinations given by the International Seismological Center (ISC) to relate the solutions to the seismic zone defined by the well-located earthquakes determined here for smaller events in 1966 and 1967. We then discuss the results in light of the ideas given by Isacks et al. [1968, 1969] and Isacks and Molnar [1969, 1971]. (Nersesov and Lukk take no responsibility for the interpretation given in that discussion.)

Seismicity

Three-component short-period seismograph stations, equipped with Soviet S5S seismometers,

¹Department of Earth and Planetary Sciences, Massachusetts Institute of Technology, Cambridge, Massachusetts 02139.

²Tadjik Institute of Seismo-Resistant Construction and Seismology, Tadjik Academy of Sciences, Dushanbe, Tadjik SSSR, USSR.

³Institute of Physics of the Earth, Academy of Sciences of the USSR, Moscow, USSR.

⁴Laboratoire de Geophysique Interne, Institute de Recherches Interdisciplinaires de Geologie et de Mécanique, B.P. 53, 38041 Grenoble, France.

were operated at locations shown in Figure 1 (and at other sites not used in this study). These instruments have a flat frequency response for displacement between about 5 and 30 Hz. Recording speeds were typically 120 mm/min, and signals were usually impulsive. Consequently, P wave arrival times could be determined with uncertainties less than a few tenths of a second, and S waves arrival times could be identified with somewhat larger uncertainties, about 1 s. These times were measured by A. A. Lukk and I. L. Nersesov. When possible, the data were supplemented by published arrival times from stations at Warsak Dam, Pakistan (WRK), and Kabul, Afghanistan (KBL).

We relocated the earthquakes recorded by this network in 1966 and 1967 using the computer program HYP071, written by Lee and Lahr [1975], assuming a modification of the velocity structure determined by Lukk and Nersesov [1970]. A more complete discussion of the velocity structure,

of the location procedure, and of the various uncertainties is given in the companion paper [Chatelain et al., 1980]. Much of the analysis given in that study deals with networks with some stations in approximately the same places as Soviet stations were in 1966 and 1967. Therefore the precision of the locations is probably comparable. The Soviet network, however, is concentrated to the north of the seismic zone, and the temporary networks employed by Chatelain et al. [1980] in 1976 and 1977 were largely south of the zone. We found a systematic northward displacement (of about 10 km) of the seismic zone using the Soviet data compared with the data from 1976 and 1977, and we infer that pronounced lateral variation in velocity in the region may be the cause of systematic differences between the locations of events. Nevertheless, the uncertainties in the relative locations of events (their precision) are likely to be approximately the same for either

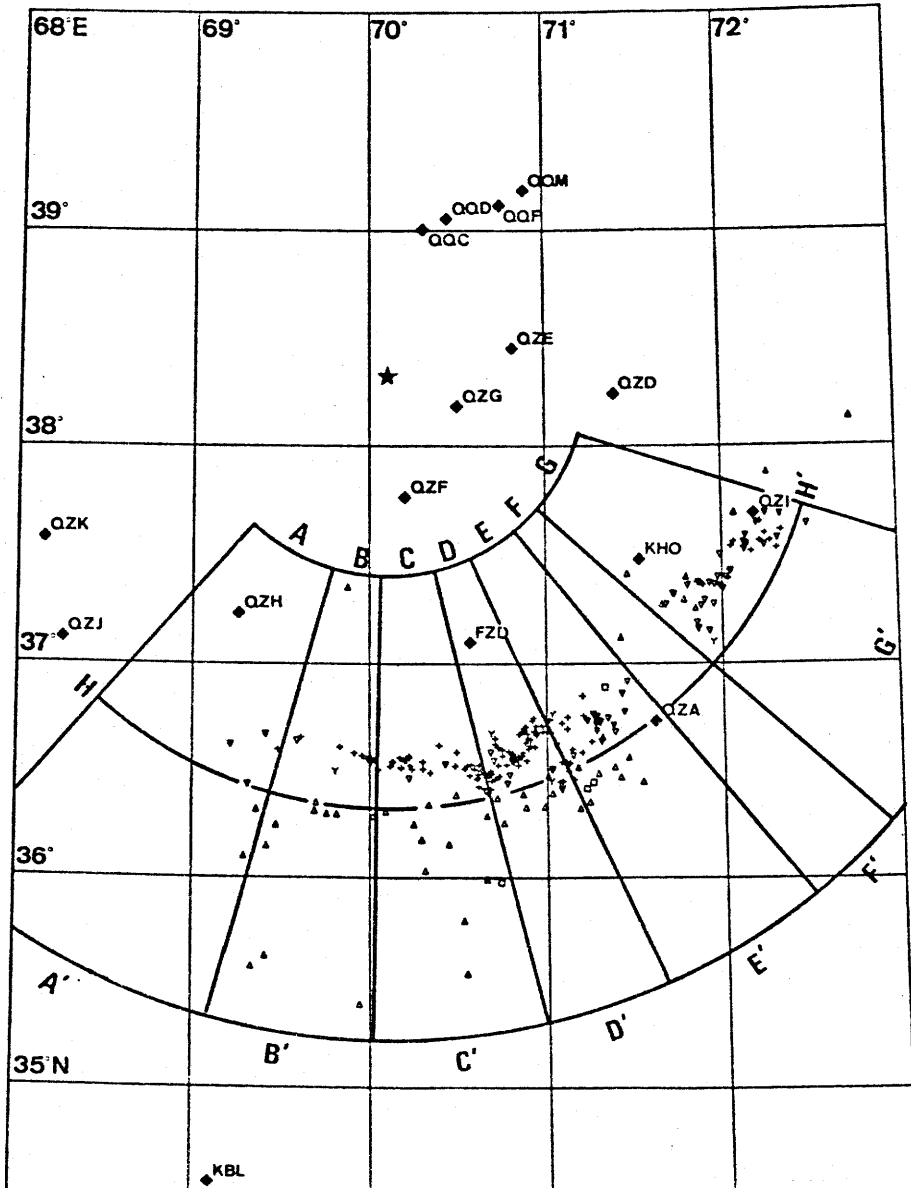


Fig. 1. Map of region showing position of stations (solid diamonds) and epicenter of earthquakes at various depths: solid triangles, 50-100 km; open triangles, 100-150 km; inverted triangles, 150-200 km; pluses, 200-250 km; and Y's, 250-300 km.

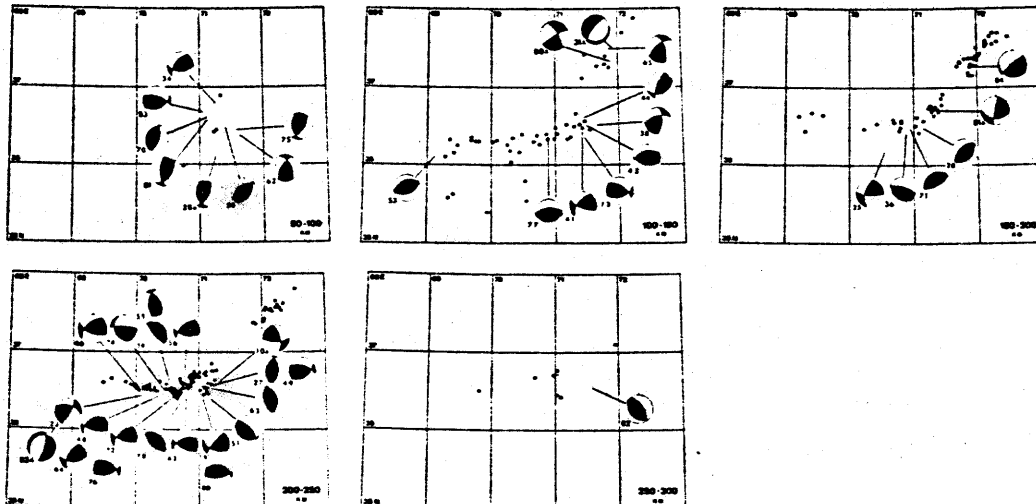


Fig. 2. Maps of 1966-1967 epicenters of events in different depth ranges and fault plane solutions in abbreviated balloon format. Lower hemisphere diagrams are shown with quadrants with compressional first motions in black, and locations of earthquakes with fault plane solutions are from Nowroozi [1971] or the ISC. Numbers correspond to events in Table 1 and Appendix A.

configuration of stations. For the majority of the events we estimate that uncertainties in the precision of the depths and hypocenters are about 10 km and that there could also be systematic errors of the same amount.

All locations with Rms residuals less than 0.7 sec [Chatelain et al., 1980] are plotted in Figure 1 and are listed in Table A1. Maps for separate depth ranges are given in Figure 2, and cross sections are shown in Figure 3. This arrangement of plots is the same as in Chatelain et al. [1980], and the general features of the seismicity are similar. As noted in other studies, the seismic zone dips steeply (Figure 3) and is oriented approximately east-west (Figures 1 and 2) [Billington et al., 1977; Chatelain et al., 1977; Lukk and Nersesov, 1970; Malamud, 1973; Nowroozi, 1971]. West of approximately 71°E the zone trends east-west, but to the east it trends more nearly northeast-southwest. As the data from the studies referenced above show, at depths greater than about 150 km, the east-west zone dips steeply to the north, and the northeast-southwest zone dips steeply to the southeast (Figure 3).

Because of the greater number of more precisely determined hypocenters than for the previous studies, there are also some features that were less clearly resolved in most of these earlier studies. At shallower depths (70-150 km), both zones appear to dip at shallower angles than at greater depths (Figure 3), a result also obtained by Billington et al. [1977]. At the same time there is a very low level of seismicity at depths shallower than about 70 km (Figure 3). This is not a consequence of inaccurate locations but reflects much lower seismicity in the crust than in the underlying mantle.

The seismic zone is not a continuous planar zone with uniformly distributed seismicity but instead contains pronounced gaps in activity and tight clusters of concentrated activity. One gap, near 37°N , is clear at all depths (Figure 2 and section FF' in Figure 3). This gap, approximately 50 km wide, seems to separate the zones that dip north and southeast (Figures 1 and 3), and it is tempting to suggest that the slab of lithosphere in which the earthquakes presumably occur is discontinuous there. This gap in activity is also clear in the data discussed by Chatelain et al. [1980].

A less well-defined gap in the western part of the zone between depths of about 150 and 180 km separates regions of shallower and deeper activity (profiles BB', CC', and HH' in Figure 3). Although there may not be enough events to convincingly demonstrate its existence here, this gap is particularly clear in the data described by Chatelain et al. [1980]. There is a suggestion also of a narrow gap in activity between 200 and 250 km at about 70.5°E (Figure 2 and profile HH' in Figure 3) which is very clear in the data from 1977 [Chatelain et al., 1980, Figure 5].

Along most of the zone and below about 150-km depth the width of the zone is about 30 km, a result similar to that of Billington et al. [1977] but much narrower than the data from most previous studies suggest [e.g., Lukk and Nersesov, 1970; Malamud, 1973; Nowroozi, 1971]. Given the uncertainties in the locations, the width could be narrower in most regions, except possibly near 71°E , and at depths greater than 200 km. There the zone seems to divide into two separate zones separated by a gap in activity about 20 km wide (Figure 2 and profile DD' in Figure 3). Events in both clusters were located with the same stations, and our estimation of the errors in locations suggests that this separation is real. Nevertheless, with a more favorable station distribution the southern branch is not apparent in the data of Chatelain et al. [1980].

Because most of the gaps and clusters in the

¹Appendix is available with entire article on microfiche. Order from the American Geophysical Union, 2000 Florida Ave., N. W., Washington, DC 20009. Document J80-003; \$01.00. Payment must accompany order.

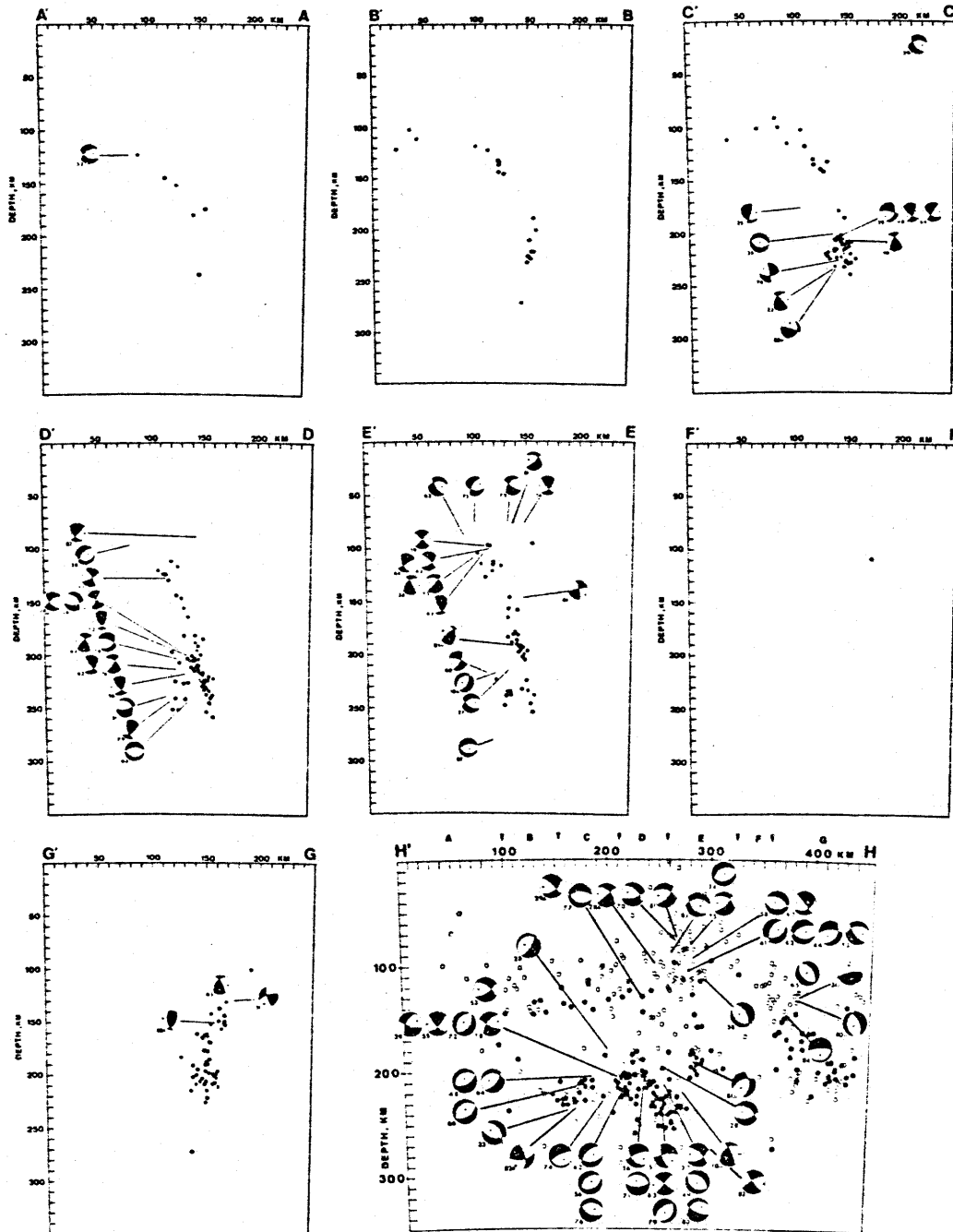


Fig. 3. Cross section of seismicity perpendicular to seismic zone (A'A to G'G) and parallel to zone (H'H) and fault plane solutions (see Figure 1). Back hemisphere of fault plane solutions shown. Solid symbols for earthquakes which met the quality constraint in Chatelain et al. [1980], and open symbols for those with most mean square residuals less than 0.7 s.

seismicity in 1966 and 1967 are evident in the data obtained in 1976 and 1977 [Chatelain et al., 1980], we do not consider them to be artifacts of short time periods of recording. At the same time the data are clearly inadequate to show that these features are representative of much longer periods of time. A close correlation of peculiarities in fault plane solutions with hypocentral positions [Chatelain et al., 1980], however, suggests that these clusters and gaps reflect variations in the state of stress and therefore may be representative of the seismicity for longer time periods than considered here.

Fault Plane Solutions

Since most of the data used to determine the fault plane solutions were radiated into the upper hemisphere of the focal sphere, upper hemisphere diagrams for all of the solutions are given in Appendix A. Pertinent parameters are listed in Table 1. To facilitate comparison with data in other studies, however, lower hemispheres given in abbreviated balloon format in Figure 2 for earthquakes at different depths, and back hemispheres are given in Figure 3 in the cross sections. These solutions were determined by Soboleva [1968a,b, 1972, new unpublished data,

1979], and among those discussed in her papers, these include only the ones to which she assigned the highest quality factor. They include essentially all events between 1960 and 1967 for which it was possible to determine a solution with Soviet data. The locations of these earthquakes were taken from Nowroozi's [1971] tabulation for events occurring in 1960-1963 and from the ISC listings for the more recent events. We assume that the uncertainty in the locations of some of these may be 10 km, but for most it is probably 20 km.

Probably the most obvious generality reflected in these data is that the T axes are nearly vertical in most cases, a result noted by Soboleva [1968a, 1972] and observed with solutions determined with other data [e.g., Billington et al., 1977; Chatelain et al., 1980; Isacks and Molnar, 1971; Nowroozi, 1972]. Among Soboleva's better constrained solutions, those used here, the T axis is in all but two cases more nearly vertical than the P axis.

Perhaps the most notable feature in Figure 2 is the wide variety of fault plane solutions. This contrasts markedly with island arc structures, where fault plane solutions of intermediate and of deep earthquakes are usually very similar to one another within the arc and in the same depth range [Isacks and Molnar, 1971]. Solutions for events 71, 78, 80, and 82 were obtained both from Soviet recordings, most of which were radiated into the upper hemisphere of the focal sphere (Appendix A), and from data of the WWSSN, which were radiated into the lower hemisphere [Chatelain et al., 1980, Table 1,

Appendix A]. In general, the parameters differ by less than 10° and always less than 15°, their approximate uncertainty. This suggests that locally heterogeneous velocity structures do not cause the large observed variation in the solutions and that there is a real variation in the orientation of the fault planes.

Variation in fault plane solutions was noted for the larger events ($M \geq 5.5$) in the Hindu Kush region, but much of this variation is systematic [Chatelain et al., 1980]. Near 70.6°E most of the P axes trend northeast-southwest, becoming more nearly north-south near 70.8°E and approximately northwest-southeast farther east near 71.0°E (Figure 2). Although many of the solutions presented here fit this general pattern, particularly the larger events, there is still a very large scatter. Although the solutions presented here are not as well constrained as those determined with the WWSSN, the variation in the observed first motions of the P waves requires large differences among the solutions (see Appendix A). We think that the variability within localized regions may not be real but is simply a consequence of large errors in the locations of the events. Chatelain et al. [1980] found very large differences in fault plane solutions of earthquakes only 20-30 km apart. Therefore errors in locations of this amount, which are difficult to eliminate, could introduce an apparently random scatter of solutions, whereas in fact there is a simple regional variation.

The fault plane solutions for the shallower events (70-150 km) include large components of

Table 1. FAULT PLANE SOLUTIONS

#	DATE	Origin Time	LAT (°N)	LONG (°E)	DEPTH (KM)	P AXIS		T AXIS		B AXIS		POLE OF FIRST NODAL PLANE		POLE OF SECOND NODAL PLANE	
						AZ	PL	AZ	PL	AZ	PL	AZ	PL	AZ	PL
23	60/01/9	07:24	36.43°	70.10°	234	150	15	260	50	49	36	300	20	190	40
25	60/02/8	18:54	36.19°	70.55°	175	143	10	46	33	247	55	100	30	0	15
27	60/02/19	10:36	36.56°	71.11°	211	95	5	195	80	4	10	260	40	105	45
28	60/02/23	02:09	36.51°	71.11°	194	310	5	135	80	40	1	130	40	320	50
34	61/03/20	03:30	36.78°	71.26°	75	335	0	65	60	245	30	130	35	0	40
10561	04/26	05:23	36.56°	71.30°	218	40	0	310	40	130	50	0	25	260	30
36	61/06/19	17:04	36.47°	70.88°	197	30	20	170	70	296	12	200	25	50	60
30561	07/20	00:40	39.40°	72.40°	120	15	61	126	12	223	24	98	50	326	11
31561	08/17	13:48	37.50°	71.70°	113	105	60	315	26	220	15	344	68	124	18
32861	08/18	07:56	39.70°	72.70°	110	142	2	234	79	52	10	154	46	311	42
38	61/08/21	07:00	36.49°	71.68°	108	130	0	220	45	40	45	275	30	165	30
39	61/09/6	13:35	36.52°	70.61°	204	225	30	45	60	135	0	45	15	225	75
41	62/01/5	04:27	36.46°	71.39°	104	166	9	67	40	266	48	125	35	20	20
42	62/01/8	22:25	36.41°	70.77°	212	182	6	84	54	276	35	150	40	30	30
43	62/02/27	05:40	36.53°	71.45°	101	355	0	90	75	265	15	160	40	10	40
44	62/03/28	00:51	36.58°	71.47°	102	307	22	78	59	208	21	110	20	340	60
48	62/07/6	23:05	36.46°	70.35°	208	172	14	59	58	270	29	140	50	15	25
49	62/08/3	18:02	36.52°	71.10°	203	340	5	245	60	73	30	315	40	185	35
51	62/10/9	15:59	36.41°	71.19°	238	40	25	235	65	133	6	25	65	225	20
53	63/01/12	06:20	36.09°	69.09°	122	155	0	345	85	245	1	330	45	160	50
55	63/02/17	05:38	36.46°	70.55°	201	255	0	160	65	345	25	100	40	230	40
56	63/02/18	14:25	36.46°	70.78°	219	165	5	70	55	258	35	140	40	15	35
58	63/03/7	21:49	36.47°	71.41°	96	135	0	235	80	45	10	300	40	145	45
28563	06/11	10:49	36.12°	71.24°	96	100	5	355	63	193	26	300	35	70	45
29563	07/11	03:25	37.11°	70.07°	24	295	5	185	70	27	19	280	50	130	35
62	63/07/10	02:12	36.37°	71.60°	87	275	5	180	55	9	35	125	30	240	40
63	63/08/13	07:03	36.55°	71.04°	245	255	10	80	85	344	1	75	40	255	60
64	63/09/29	10:39	36.46°	70.33°	205	145	0	55	54	235	36	115	35	355	35
65	63/10/14	21:12	37.46°	71.88°	113	107	0	197	43	17	47	145	30	250	30
66	63/12/28	01:40	36.55°	70.12°	209	170	8	68	53	266	35	136	42	19	27
70	64/01/23	15:19	36.58°	71.18°	76	110	15	270	75	19	5	280	30	120	60
71	64/01/28	14:09	36.48°	70.95°	197	150	20	335	70	241	2	150	65	330	25
72	64/02/18	17:58	36.47°	70.70°	202	162	9	69	40	264	44	130	40	15	25
72564	03/23	08:38	38.25°	73.63°	125	355	41	345	18	138	44	290	43	36	15
73	64/05/16	09:38	36.36°	71.43°	110	9	6	271	56	103	33	340	40	215	30
74	64/05/17	11:45	36.49°	70.47°	226	22	26	149	51	278	27	180	15	70	60
75	64/09/29	06:51	36.42°	71.51°	77	105	10	0	65	200	24	305	35	80	45
76	64/11/27	11:03	36.40°	70.73°	211	181	5	283	65	92	24	340	35	205	45
77	64/12/24	01:08	35.35°	70.89°	127	350	15	180	75	81	2	350	60	170	30
78	65/03/14	15:53	36.42°	70.73°	205	220	15	40	75	130	0	220	60	40	30
80565	04/10	21:21	37.33°	71.87°	129	290	16	195	18	58	65	244	23	152	2
81565	07/20	07:43	36.72°	71.32°	191	308	30	62	35	188	40	1	48	94	4
79	65/11/16	01:03	36.41°	71.11°	242	341	19	89	43	233	41	130	15	25	45
82565	05/30	11:28	36.42°	70.09°	234	268	58	116	28	20	14	149	68	286	15
80	66/06/6	07:46	36.43°	71.12°	214	178	18	322	68	86	13	350	25	200	60
81	66/07/07	19:00	36.58°	71.14°	79	286	8	30	59	192	34	80	31	318	43
82	67/01/25	01:50	36.71°	71.60°	281	48	11	265	76	138	7	36	55	234	33
83	67/02/11	08:05	36.66°	71.05°	88	2	9	249	62	96	25	202	30	334	48
84	67/12/28	20:15	37.28°	71.92°	147	330	35	123	54	230	12	138	11	13	76

thrust faulting, therefore with steeply dipping T axes, and with P axes oriented approximately northwest-southeast (Figure 2). The dip of the seismic zone is not well defined in this depth range (Figure 3) but seems to increase with depth. It is possible that for some of these events one of the nodal planes is parallel to the seismic zone (event 53 in AA'; event 77 in DD'; events 38, 41, 43, 44, 58, and 73 in EE'; and event 65 in GG' of Figure 3). In such a case the slip during earthquake might represent displacement along a fault parallel to the seismic zone [Vinnik and Lukk, 1973, 1974; Vinnik et al., 1977]. Such a phenomenon is unusual for earthquakes at these depths, but perhaps in Asia the plates are thicker than at island arcs [e.g., Vinnik et al., 1977]. These earthquakes would then result from relative plate motion, not internal deformation of the downgoing slab as at island arcs [Isacks and Molnar, 1971].

The approximately horizontal northwest-southeast P axes for these events (Figures 2 and 3) are similar to those of shallower, crustal events further south [Prevot et al., 1980]. At the same time the solutions in Figure 2 are sufficiently different that the slip vectors definitely differ from one another. Therefore only some, if any, of these events between 70 and 150 km could reflect slip of one plate past another. They might reflect more diffuse deformation resulting from northwest-southeast compressive stress due to the India-Eurasia collision.

Alternatively, the nearly vertical T axes for the deeper of these events (near 150-km depth) could indicate internal deformation of the downgoing slab, as is typical of intermediate depth events at island arcs. The uncertainties in the locations of these events and in the configuration of the seismic zone do not allow this to be resolved.

Summary

A study of earthquakes occurring in 1966 and 1967 in the Pamir-Hindu Kush region and recorded by a relatively dense network of local stations reveals several unusual patterns in the seismicity. Seismicity in the crust is very low so that the intermediate depth zone does not continue to the earth's surface along any clear zone. Two possible explanations are either that convergence between India and Eurasia continues, with deformation in the crust occurring aseismically, or that convergence is absorbed farther north (or south), with the intermediate depth earthquakes occurring in a slab of lithosphere hanging in the mantle. These two explanations are not mutually exclusive.

To a first approximation the seismicity is confined to a narrow (width <30 km) planar zone that dips steeply into the mantle. The data suggest a pronounced gap near 37°N that separates a steeply north dipping zone in the west from a steeply southeast dipping zone in the northeast. This gap in activity could represent a discontinuity in the downgoing slab of lithosphere or even a gap between two lithospheric slabs [see Chatelain et al., 1980]. There is a suggestion of a decrease in the dip

of the zones at shallower depths (~100 km), but because of the lack of continuity of seismicity to the surface, it is difficult to trace either inferred zone to a place at the earth's surface, where subduction of the slab would have occurred. The dips of the seismic zone suggest a southerly source of the western zone and a northerly source for the eastern zone, an idea expressed by others from the faulting and geologic structure along the northern margin of the Pamir [Khalturin et al., 1977; Malamud, 1973; Molnar et al., 1973; Ulomov, 1974; Vinnik and Lukk, 1973, 1974; Vinnik et al., 1977]. This interpretation is certainly not required by the data, and Billington et al. [1977] give other possible scenarios.

The gap in activity at 37° is not the only gap, and clusters of activity also occur. Since these gaps and clusters are evident in data obtained during short periods of recording 10 years later, we think that they are representative of the seismicity for at least tens of years. Perhaps they have persisted hundreds or thousands of years [Chatelain et al., 1980].

We used fault plane solutions of earthquakes in 1960-1967, determined by Soboleva [1968a, 1972], but assumed the locations given in Nowroozi [1971] and ISC. The T axes, in general, plunge at steep angles and lie approximately within the plane of the seismic zone. Thus they conform to the gross pattern for intermediate depth events at island arcs where there are no deep events or where there is a gap in seismicity between intermediate and deep events [Isacks and Molnar, 1969, 1971]. Therefore most of them presumably result from stress in a downgoing (or hanging) slab of lithosphere. The important parameters would be the orientation of the P, T, and B axes, not the nodal planes or slip vectors. The downdipping T axes imply that gravitational body forces tend to pull the slab down [Isacks and Molnar, 1969, 1971].

The only exception to this pattern might be for events at shallower depths (70-150 km), where the seismic zones seem to dip less steeply. Solutions for some but not all of these events show that one plane could be parallel to the seismic zone. If the plane of seismicity marks a fault, then the displacement might represent slip of one plate with respect to another. The data do not require this interpretation, however.

Fault plane solutions of deeper events (160-230 km) also show considerable variability. Although the regional variation in solutions discussed by Chatelain et al. [1980] describes much of the variation in the data presented here, the scatter is still very large. We suspect that the scatter is only apparent and is due to errors in the locations.

Acknowledgments. I. Nersesov and A. Lukk carried out the analysis of the travel times and determined preliminary locations. O. Soboleva determined the fault plane solutions. S. Roecker, D. Hatzfeld, and J. Chatelain redetermined the locations and carried out the analysis of the fault plane solutions in light of the seismicity. S. Roecker, D. Hatzfeld, and P. Molnar assembled the manuscript; they, O. Soboleva, and J. Chatelain made the

interpretations in terms of subduction of oceanic lithosphere. Much of the work was done at Applied Seismology Group in Lincoln Laboratories. We thank them for making their facilities available and for their help. We also thank V. I. Khalturin, R. North, G. Perrier, T. G. Rautian, and B. E. Tucker for help at various stages in this work and two anonymous referees for constructive criticism of the manuscript. This work was supported by NSF grants EAR76-13367 and EAR78-13673, by contract ATP No. 35-06, 35-25, and 35-58 of INAG from the Centre National de la Recherches de France, by an H. O. Wood Award, and by an Alfred P. Sloan Fellowship.

References

- Billington, S., B. L. Isacks, and M. Barazangi, Spatial distribution and focal mechanisms of mantle earthquakes in the Hindu-Kush-Pamir region: A contorted Benioff zone, Geology, 5, 699-704, 1977.
- Chatelain, J. L., S. Roecker, D. Hatzfeld, and P. Molnar, Microearthquake seismicity and fault plane solution in the Hindu Kush region and their tectonic implications, J. Geophys. Res., 85, this issue, 1980.
- Chatelain, J. C., S. Roecker, D. Hatzfeld, P. Molnar, and G. Perrier, Etude seismologique en Afghanistan, Premiers resultats, C. R. Somm. Soc. Geol. Fr., 2, 260-262, 1977.
- Isacks, B., and P. Molnar, Mantle earthquake mechanisms and the sinking of the lithosphere, Nature, 223, 1121-1124, 1969.
- Isacks, B., and P. Molnar, Distribution of stresses in the descending lithosphere from a global survey of focal mechanism solutions of mantle earthquakes, Rev. Geophys., Space Phys., 9, 103-174, 1971.
- Isacks, B., J. Oliver, L. R. Sykes, Seismology and the new global tectonics, J. Geophys. Res., 73, 5855-5899, 1968.
- Isacks, B., L. R. Sykes, and J. Oliver, Focal mechanisms of deep and shallow earthquakes in the Tonga Kermadec region and tectonics of island arcs, Geol. Soc. Amer. Bull., 80, 1443-1470, 1969.
- Khalturin, V. I., T. G. Rautian, and P. Molnar, The spectral content of Pamir-Hindu-Kush intermediate depth earthquakes, evidence for a high Q zone in the upper mantle, J. Geophys. Res., 82, 2931-2943, 1977.
- Lee, W. H. K., and J. C. Lahr, HYP071 (revised): A computer program for determining hypocenter, magnitude and first motion pattern of local earthquakes, Open File Rep. 75-311, U. S. Geol. Surv., Reston, VA, 1975.
- Lukk, A. A., and I. L. Nersesov, The deep Pamir Hindu-Kush earthquakes (in Russian), in Earthquakes in the USSR in 1966, pp. 118-136, Nauka, Moscow, 1970.
- Malamud, A. C., Several regularities of the spatial distribution of Pamir Hindu-Kush deep focus earthquakes, Izv. Akad. Nauk Tadzh. SSR Otd. Fiz. Matematicheskikh Geol. Khim. Nauk, 9, 70-73, 1973.
- Molnar, P., T. J. Fitch, and F. T. Wu, Fault plane solutions of shallow earthquakes and contemporary tectonics in Asia, Earth Planet. Sci. Lett., 19, 101-112, 1973.
- Molnar, P., T. G. Rautian, and V. I. Khalturin, Influence of the propagation path of waves and local registration of CHISS-spectra of local earthquakes of the Garm region, in Soviet-American Work on Earthquake Prediction, (in Russian), pp. 159-170, Donish, Dushanbe, Moscow, 1976.
- Nowroozi, A. A., Seismotectonics of the Persian plateau, eastern Turkey, Caucasus and Hindu-Kush regions, Bull. Seismol. Soc. Amer., 61, 317-321, 1971.
- Nowroozi, A. A., Focal mechanisms of earthquakes in Persia, Turkey, West Pakistan, and Afghanistan and plate tectonics of the Middle East, Bull. Seismol. Soc. Amer., 62, 833-850, 1972.
- Prevot, R., D. Hatzfeld, S. W. Roecker, and P. Molnar, Shallow earthquakes and active tectonics in eastern Afghanistan, J. Geophys. Res., 85, this issue, 1980.
- Soboleva, O. V., Special features of the directions of the principal stress axes in the foci of Hindu-Kush earthquakes, Izv. Acad. Sci. USSR, Phys. Solid Earth, 1, 71-78, 1968a.
- Soboleva, O. V., Effect of the asymmetry of the focal radiation upon the distribution of the displacements around the epicenter of a deep earthquake, Izv. Acad. Sci. USSR, Phys. Solid Earth, 10, 45-56, 1968b.
- Soboleva, O. V., Method for unambiguous determination of the fault plane in the source using the Hindu-Kush zone as an example, Izv. Acad. Sci. USSR, Phys. Solid Earth, 1, 50-59, 1972.
- Ulomov, V. I., Dynamics of the Earth's Crust and Prediction of Earthquakes (in Russian), 214 pp., Fan, Tashkent, USSR, 1974.
- Vinnik, L. P., and A. A. Lukk, Velocity inhomogeneities of the upper mantle of Central Asia (in Russian), Dokl. Akad. Sci. USSR, 213, 580-583, 1973.
- Vinnik, L. P., and A. A. Lukk, Lateral inhomogeneities in the upper mantle under the Pamir Hindu Kush, Izv. Acad. Sci. USSR, Phys. Solid Earth, 1, 9-22, 1974.
- Vinnik, L. P., A. A. Lukk, and I. L. Nersesov, Nature of the intermediate seismic zone in the mantle of the Pamir-Hindu-Kush, Tectonophysics, 38, 9-14, 1977.

(Received April 23, 1979;
revised November 1, 1979;
accepted November 6, 1979.)

CHAPTER III

Perhaps the closest one could approach an experience of travel in the old sense today would be to drive in an aged automobile with doubtful tires through Rumania or Afghanistan without hotel reservations and to get by on terrible French.

- Paul Fussel

*Abroad: British Literary traveling
between the Wars*

Shallow Earthquakes and Active Tectonics in Eastern Afghanistan

R. PREVOT AND D. HATZFELD

*Laboratoire de Geophysique Interne, Universite Scientifique et Medicale du Grenoble
38041 Grenoble Cedex, France*

S. W. ROECKER AND P. MOLNAR

*Department of Earth and Planetary Sciences, Massachusetts Institute of Technology
Cambridge, Massachusetts 02139*

Brief studies of microearthquakes in four separate parts of eastern Afghanistan reveal a high level of seismicity over a broad area. In general, the activity is not concentrated on well-defined faults, nor does it define new faults, but seismicity on or close to the Chaman and Sarubi faults attests to their activity. First motions of *P* waves are consistent with left- and right-lateral strike-slip motion, respectively, on these two faults. Fault plane solutions and composite solutions of events in different areas throughout the region differ from one another, but in general, the *P* axes are parallel to the north-northwest direction of relative motion between India and Eurasia. Several earthquakes beneath Kabul and its immediate surroundings emphasize a need for further study of its seismic hazard.

INTRODUCTION

The tectonic activity of the Himalayan belt, of which north-eastern Afghanistan is a part, is usually interpreted as a consequence of the collision between the Indian and Eurasian subcontinents [e.g., Dewey and Bird, 1970; Molnar and Tappanier, 1975]. This collision is thought to have occurred approximately 40–50 m.y. ago, and now the relative convergence rate is calculated to be 41 ± 5 mm/yr [Minster and Jordan, 1978]. The India plate is bounded on the north by the Himalaya, where thrust faulting predominates. The plate boundary is not sharp on the west, and deformation seems to occur primarily by strike-slip faulting along several subparallel faults. Accordingly, the junction between these two portions of the boundary in northeastern Afghanistan and northern Pakistan is not well defined, and the seismicity is scattered over a broad area [Armbruster et al., 1978; Seeber and Jacob, 1977; Seeber and Armbruster, 1979].

From aerial photos, Wellman [1966], and later Heuckroth and Karim [1970, 1973], inferred a complex pattern of faults in eastern Afghanistan. The major fault is the left-lateral Chaman fault (Figures 1 and 2), with a length of about 800 km and north-northeast strike. Wellman inferred a rate of slip along the fault of about 15 mm/yr, and several authors have inferred displacements of 300–500 km [Auden, 1974; de Laparent, 1972; Wellman, 1966]. Although the Chaman fault separates two very different geologic units and it clearly is active, the quantitative estimate of rates or total displacements is not well constrained. Its clear topographic expression and displacements during historic earthquakes [Griesbach, 1893; Heuckroth and Karim, 1970, 1973; McMahon, 1897; Richter, 1958] attest to recent activity. The Chaman fault seems to intersect the Herat fault near the town of Charikar (Figures 1 and 2), and it cannot be traced north beyond the Herat fault into the Hindu Kush.

Although a substantial fraction of the motion of India with respect to Eurasia may occur at the Chaman fault, the mere

fact that the direction of relative motion is not parallel to the fault requires that it alone is not the boundary. Surely some displacement occurs further east and southeast, in Pakistan, but there seem to be several other active faults in northeastern Afghanistan along which the relative motion of India and Eurasia can also be absorbed. Wellman [1966] infers that the Gardez fault, which is roughly parallel to the Chaman fault, is an active left-lateral strike-slip fault. Between it and the Chaman fault, the Sarubi fault shows clear topographic expression on aerial photos [Wellman, 1966] and the Landsat imagery (Figure 2), as well as from the ground. From first motions of *P* waves of earthquakes near the Sarubi fault, we infer a large component of right-lateral slip. The Kunar fault (Figures 1 and 2) seems to occupy the position of an important suture, possibly between an island arc and the Asian continent [Tahirikheli et al., 1977]. It too is very clear on the Landsat imagery (Figure 2) and seems to be associated with seismicity. These faults appear to divide the region into wedge-shaped blocks that move with respect to one another but also undergo some internal deformation [Carbonnel, 1977]. Although the seismicity located with teleseismic phases for the last 15 years has been low, numerous historical earthquakes attest to continuing activity (Figure 1) [Heuckroth and Karim, 1970, 1973; Quittmeyer and Jacob, 1979].

To examine the active deformation of the region, we installed temporary networks of portable seismographs in four parts of eastern Afghanistan for periods of 1–2 two weeks in 1976, 1977, and 1978. These studies were intended to supplement data obtained from a study of intermediate-depth seismicity in the Hindu-Kush region [Chatelain et al., 1980].

DATA

Instruments and Procedure

For each of the four networks we used portable Sprengnether MEQ-800 seismographs with Mark Product L-4C vertical seismometers. The amplifier was usually set at 84 db, corresponding to a total magnification of 5×10^3 at 10 Hz. The drum rotation rate was 60 mm/min. By checking the clocks every 2 days with radio signals from the ATA station in New

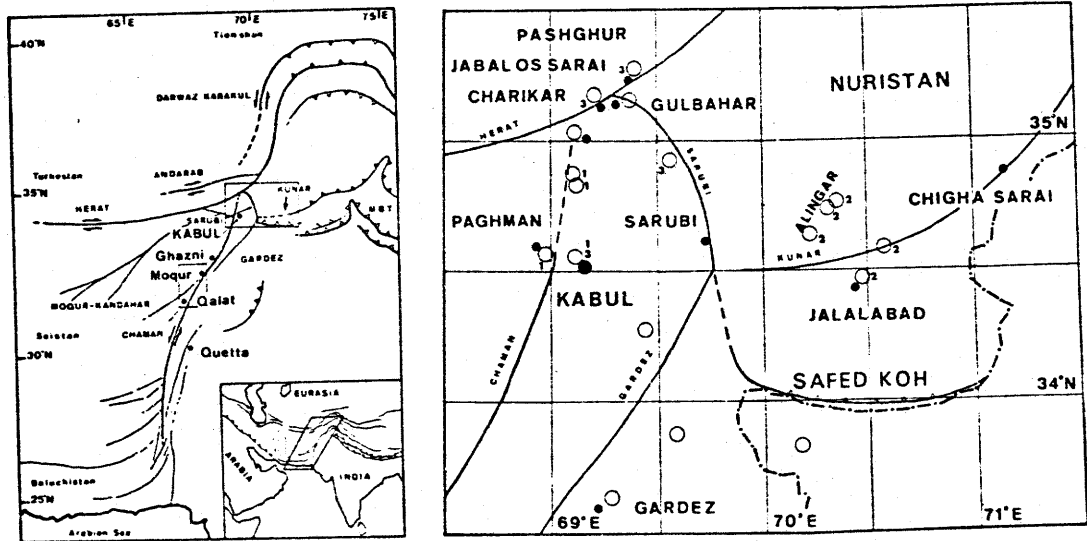


Fig. 1. Maps of the region studied showing the main faults. (Left) After Cassaigneau [1979] shows the regions investigated. (Right) Modified from Wellman [1966] shows faults, major towns (closed symbols), and epicenters of historical earthquakes from Quittmeyer and Jacob [1979] (open symbols). Dot-dashed line is border between Pakistan and Afghanistan.

Delhi, clock drifts were found to be less than 0.1 s for 2-day periods.

We measured arrival times with a hand lens, with a scale 12 cm long and graduated at 0.1-mm intervals. We estimate that, in general, *P* wave arrival times could be measured with un-

certainities of a tenth of a second and, in general, *S* wave arrival times are uncertain by less than 1 s. We used the computer program, Hypo 71 [Lee and Lahr, 1975], to determine the locations. The magnitudes of the earthquakes were estimated from the duration of the signal, *T* (in seconds) using

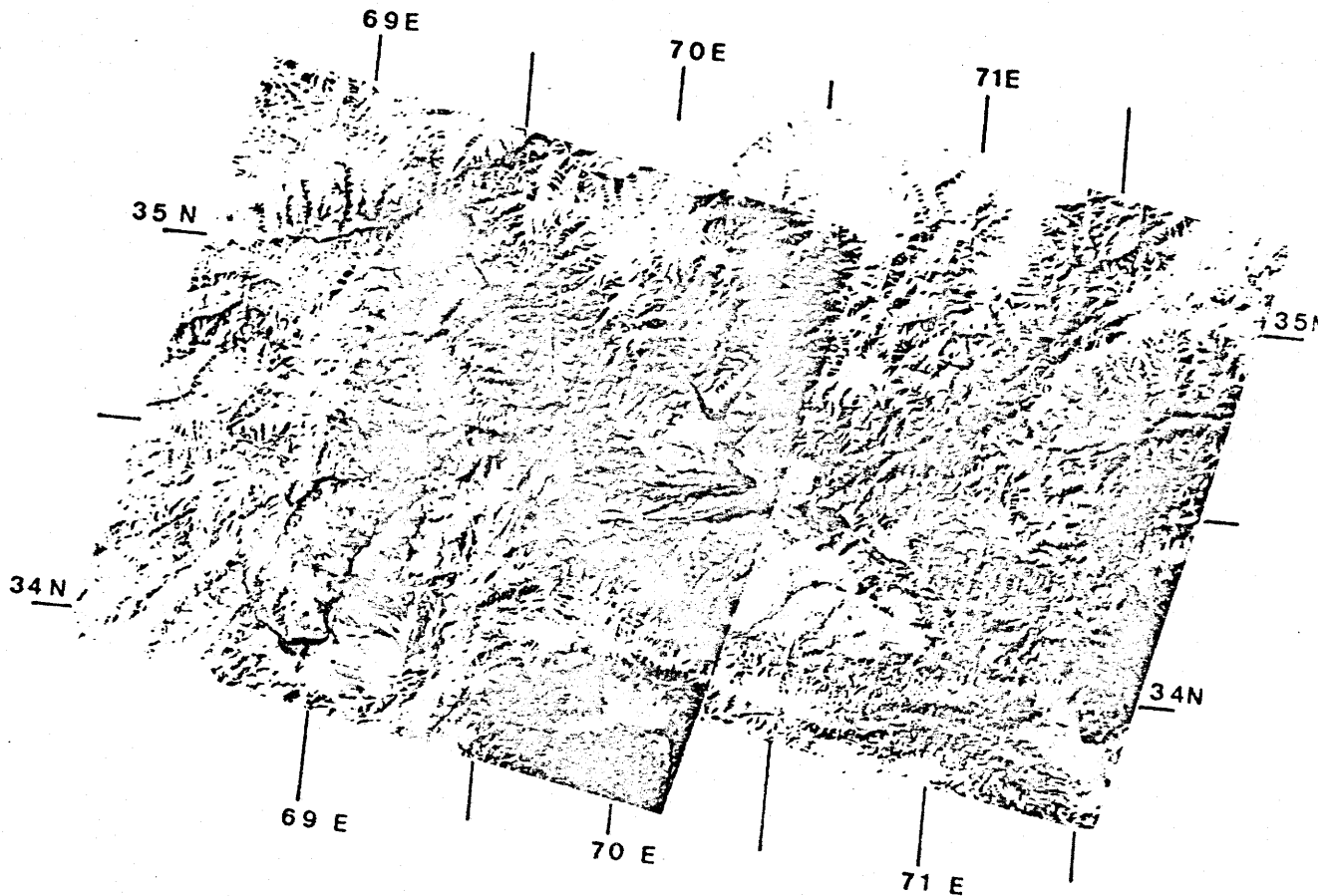


Fig. 2. Landsat imagery of the area studied. Landsat images E1517-05270-5 and E1517-05264-5.

the formula

$$M = 0.87 + 2 \log T + 0.0035\Delta$$

where Δ is hypocentral distance in kilometers [Lee and Lahr, 1975]. Because the instruments in Afghanistan were different from those used in determining this empirical formula, our estimates of signal duration are probably systematically too long. However, the magnitude depends on the logarithm of the duration, so the effect of this difference is probably not great. A complete list of the locations is available on microfiche.¹

Velocity Structure and Uncertainties in Locations

Since there are no studies of the velocity structure of any of the region considered here, we defined our own velocity structure (Table 1) as follows. First, we estimated a value for the ratio of the *P* wave and *S* wave velocities, v_p/v_s . Hypo 71 uses a constant ratio for all depths. We chose the 10 most well recorded events with *S* waves, and for each we constructed Wadati diagrams, plots of differences in *S* wave and *P* wave arrival times versus *P* arrival time. We obtained a range of values of $v_p/v_s = 1.70$ – 1.76 with a well-defined mean at 1.73, which we used for all locations. We used three criteria to define good locations: the root mean square (rms) residual of the arrival times used to determine the location (typically rms is 0.1 s), the uncertainty in the depth obtained from Hypo 71 (ERZ), and the *P* wave residual at the nearest station (PRZ). We explored different layered structures in order to find the structures that minimized these parameters for 46 well-recorded events.

For calculated depths less than 7 km, we examined locations calculated using a homogenous half space with v_p of 5.8, 6.0, 6.2, and 6.4 km/s. We found that the smallest residuals were obtained for $v_p = 5.8$ km/s and assumed that value for the upper 7 km. We then considered events with calculated depths between 7 and 25 km and found that a value of $v_p = 6.2$ km/s in this depth interval yielded the smallest computed uncertainties. There were not enough earthquakes below 25 km to carry out the same procedure, so we simply assumed that $v_p = 6.8$ km/s between 25- and 40-km depth and that $v_p = 8.0$ km/s below the Moho. Because very few rays penetrate below 25 km, ignorance of this portion of the structure is less important than that of shallower depths.

To estimate the uncertainties in the locations, we made several tests. First, we examined the influence of random noise in the arrival times on the calculated location. This should allow an estimate of the importance of random errors in arrival times. We calculated travel times from hypothetical events in different regions and then added random noise, with zero mean, of 0.1 s for *P* waves and 0.5 s for *S* waves to the arrival times. The differences between the computed and actual locations are generally less than 1 km (Table 2).

We then examined the influence of the station distribution by calculating locations of these hypothetical events with subsets of the arrival times. The results again show that for networks of five to six stations near the epicenter (those stations most likely to record the events), the differences in computed and actual locations are generally about 1 km (Table 2). For

TABLE 1. Velocities of Layered Model Used to Locate Events

Velocity, km/s	Depth, km
5.8	0.0
6.2	7.0
6.8	25.0
8.2	40.0

some cases the depths differ by more, but in no case by more than 6 km.

We then calculated locations using a different value of $v_p/v_s = 1.70$. For this case we used all of the stations. The computed locations differed by less than 1.5 km from the actual locations (Table 2).

Finally, we examined the effect of different velocity structures on the locations. In particular, we considered homogenous half spaces with different values of v_p of 5.8, 6.0, 6.2, and 6.4 km/s, and relocated the events with these structures. In general, the epicenters differ by less than 1 km and the depths by less than a few kilometers (Table 2).

From these tests we conclude that when five or more stations near the epicenter record clear arrivals, the precision of the calculated epicenter is probably about 4 km or less and that of the depths is about 6 km.

Fault Plane Solutions

Although we recorded first motions of *P* waves from only 12 stations in the optimum case, we attempted to determine fault plane solutions for individual events whenever possible. In a few cases, unique solutions could be obtained in this way, but in general, it was necessary to combine data and to construct composite fault plane solutions. For example, solution 5B in Figure 3 for a single event is poorly constrained, but by including data from another event in the same region (5D), two well-constrained planes can be drawn. Because it is difficult to evaluate the basic assumption used for composite solutions, that the radiation patterns for all of the events are the same, uncertainties for composite solutions are greater than those of single events. Indeed, when first motions from many events are combined, there are often many inconsistencies. In constructing the solutions therefore we did not, in general, combine data that were simply consistent with one another but instead chose all first motions from earthquakes in well-defined clusters. Thus from the scatter in the data we can evaluate the extent to which the nodal planes fit the data well (Figure 3). For some regions the lack of consistent data made it impossible to obtain composite solutions.

A principal source of uncertainty in the solutions arises from ignorance of the velocity structure. For a layered structure and for different depths of foci and different epicentral distances, the ray path can initially go up directly to the station or go down and refract along a deeper interface. An erroneous structure can strongly affect the calculated radiation pattern. To explore the influence of the velocity structure, we examined the calculated radiation patterns for all well-recorded earthquakes using three structures: A, which contains 20 layers and approximates a continuous gradient from 6.0 to 6.7 km/s in the crust; B, the three-layered model used for locations (Table 1); and C, a homogenous half space. In a few cases, solutions were discarded because they depended strongly on the assumed velocity structure. As examples of so-

¹ The appendix is available with entire article on microfiche. Order from American Geophysical Union, 2000 Florida Avenue, N. W., Washington, D. C. 20009. Document J80-001; \$1.00. Payment must accompany order.

TABLE 2. Relocations of Hypothetical Events

Real Position	With a Random Noise	Subarray	$v_p/v_s =$					
			1.70 km/s	$v_p = 5.8$ km/s	$v_p = 6.2$ km/s	$v_p = 6.2$ km/s	$v_p = 6.4$ km/s	
12h27 19.48	19.45	A	19.52	19.50	19.33	19.66	19.98	20.25
34°38.45	38.69		38.63	38.66	38.90	38.94	38.93	39.01
70°38.91	39.14		38.69	39.26	39.04	39.15	39.33	39.46
5.26	4.78		5.71	4.33	7.06	5.34	2.60	0.25
12h41 13.84	13.87	B	13.69	13.90	13.53	13.92	14.28	14.58
34°21.99	22.05		21.60	21.96	22.26	22.06	21.86	21.55
70°34.01	33.64		33.20	33.67	33.33	33.46	33.66	33.69
6.18	6.82		11.67	6.53	10.81	8.45	5.25	0.35
18h35 56.20	56.15	B	56.11	56.18	55.79	56.22	56.64	56.88
34°26.98	26.70		27.49	26.54	26.86	26.45	26.23	26.01
70°31.75	31.77		30.37	31.86	31.43	31.63	31.84	31.91
4.12	4.31		8.58	3.40	12.27	8.30	0.36	0.21
17h15 20.24	20.16	C	20.20	20.20	20.13	20.42	20.69	20.92
34°44.01	44.24		45.54	44.50	44.47	44.58	44.60	44.66
70°52.90	52.84		52.12	52.66	52.32	52.69	53.18	53.76
4.95	4.02		0.83	2.49	2.53	1.04	0.58	0.68
0h16 43.87	43.83	D	43.82	43.86	43.68	43.99	44.21	44.41
34°42.86	42.42		42.55	42.69	42.10	42.43	42.70	42.94
69°47.42	47.32		47.19	46.65	47.43	47.12	46.58	46.00
4.49								
13h08 45.87	45.89	D	45.90	45.58	46.07	46.17	46.13	45.99
34°52.87	53.16		53.06	54.28	52.21	53.03	54.15	55.25
69°39.71	40.26		40.36	38.99	41.44	40.53	39.10	37.29
5.34	4.48		4.56	5.43	1.98	2.35	1.77	0.86
14h22 50.69	50.55	C	50.65	50.54	49.95	50.35	50.80	51.29
34°55.97	56.23		57.03	56.37	55.82	56.16	56.34	56.49
70°20.59	20.24		20.78	20.38	20.52	20.46	20.41	20.38
17.21	18.76		16.34	19.48	20.76	19.78	18.10	14.99
3h21 23.12	23.10	B	23.27	23.04	22.55	22.96	23.34	23.64
34°24.70	24.57		24.77	24.34	24.59	24.65	24.39	24.01
70°00.30	00.44		01.50	0.20	0.40	0.64	0.29	59.81
13.70	13.44		15.94	14.91	16.33	15.57	13.35	11.84
16h31 38.76	38.76	A	38.61	38.80	38.75	39.01	39.28	39.52
34°39.49	39.12		39.13	39.21	39.17	39.20	39.17	39.18
70°28.50	28.86		29.26	28.68	28.74	28.64	28.59	28.51
1.13	2.12		3.55	0.90	0.73	1.09	0.89	0.70
21h40 2.15	2.23	A	2.07	2.27	1.80	2.23	2.65	2.97
34°34.86	35.15		35.28	35.20	35.12	35.18	35.16	35.14
70°20.36	20.72		19.95	20.76	20.63	20.62	20.59	20.54
8.64	7.43		9.49	6.71	10.82	8.46	5.01	0.04
15h56 56.88	56.98	A	57.04	57.02	56.43	56.86	57.25	57.62
34°34.93	34.94		35.19	34.91	35.06	34.98	34.91	34.84
70°33.18	33.04		32.87	33.16	32.79	32.96	33.13	33.28
16.46	15.14		15.33	15.46	17.36	15.99	14.54	13.00
0h21 45.89	45.77	D	45.82	45.73	45.33	45.63	46.02	46.31
34°42.82	43.29		43.45	43.57	43.07	43.39	43.62	43.80
69°57.21	56.79		56.91	56.56	57.46	56.96	56.59	56.28
8.96	10.81		9.94	12.41	14.06	13.59	10.94	10.32
19h19 54.07	54.08	C	53.82	54.01	53.30	53.60	53.88	54.15
34°59.55	58.69		58.50	59.37	57.60	57.89	58.31	58.79
70°31.92	31.69		31.25	31.78	31.86	31.76	31.68	31.69
40.64	42.46		45.57	43.34	42.13	42.27	42.66	42.65
21h25 10.32	10.32	A	10.18	10.37	10.33	10.61	10.87	11.14
34°39.09	39.21		38.24	39.32	39.13	39.37	39.57	39.52
70°38.44	38.38		38.97	38.43	38.38	38.30	38.37	38.51
4.18	3.60		2.17	3.14	2.32	0.46	0.81	0.78

Travel times calculated with three layer crustal model and $v_p/v_s = 1.73$. In each of the columns we change only one parameter. Random noise is 0.1 s for P and 0.5 s for S times. Subarrays are A (SLW, AMV, SLK, KKN, PJP), B (CHK, GBW, CRZ, KKN, AMV), C (CHK, CHS, SLW, KYN, AMV), and D (SLK, KKN, KYN, CRZ, GGM, TGB). Numbers giving locations are (from top to bottom) time, latitude, longitude, depth.

lutions not strongly altered, compare the various solutions for events 7, 8, 10, and 12 in Figure 3. The refracted waves are shown with crosses. In general, structure B was used for composite solutions, but they are labeled D in Figure 3 and Table 3 to distinguish them from solutions for single events.

RESULTS

Chaman Fault Region

Between September 2 and 9, 1976, we recorded earthquakes with six stations between Moqur and Qalat along the Chaman

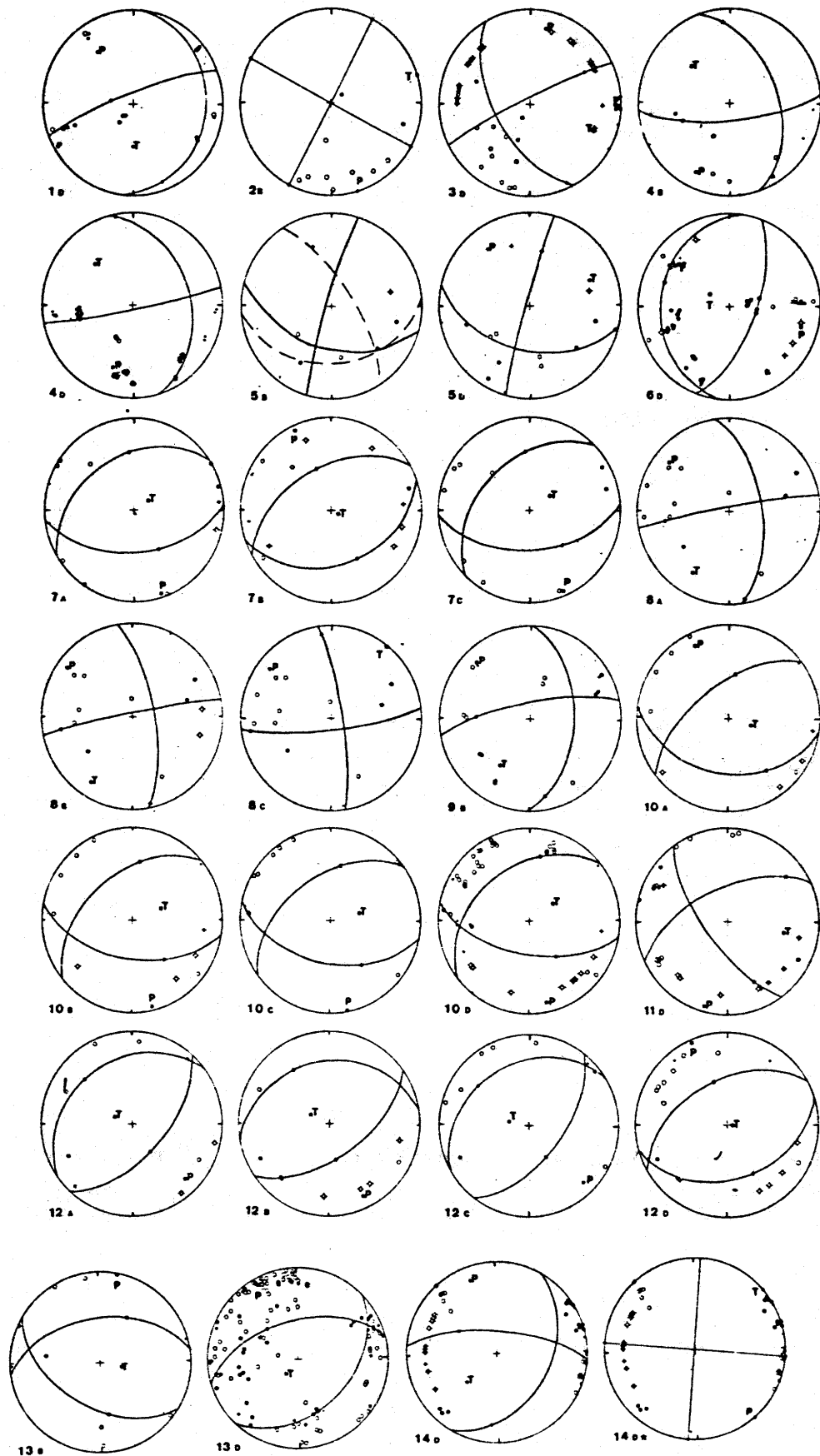


Fig. 3. Fault plane solutions in equal area projection of the upper hemisphere of the focal spheres. Solid circles are compressions, open circles are dilatations, and crosses indicate refracted waves. Solutions are determined with different velocity structures: A is a 20-layered model, B is a three-layered model (Table 2), and C is a homogenous half space. For composite fault plane solutions (D) the three-layered model was used. Numbers correspond to Table 3 and Figure 8.

TABLE 3. (continued)

Date	Origin Time	Lat., °N	Long., °E	Depth, km	P Axis		T Axis		B Axis		Pole of First Nodal Plane		Pole of Second Nodal Plane		
					Trend	Plunge	Trend	Plunge	Trend	Plunge	Trend	Plunge	Trend	Plunge	
10A	June 5	18:35	34.45	70.53	5	334	14	107	69	247	24	9	50	142	30
10B	June 5	18:35	34.45	70.53	4	166	4	70	62	259	27	10	35	141	44
10C	June 5	18:35	34.45	70.53	3	168	1	78	63	259	26	13	38	144	40
	June 2	02:07	34.47	70.51	6										
		13:42	34.47	70.53	14										
	June 5	07:19	34.47	70.53	13										
10D	June 5	18:35	34.45	70.53	4	168	10	55	64	266	24	9	30	143	50
	June 6	01:13	34.47	70.51	12										
		08:39	34.46	70.53	14										
		20:08	34.47	70.50	14										
	June 9	04:37	34.48	70.51	12										
		05:59	34.46	70.53	12										
11D	June 4	10:22	34.38	70.55	8										
		10:25	34.37	70.56	7	196	6	101	37	295	53	53	20	156	30
		18:47	34.37	70.56	6										
		20:57	34.37	70.57	5										
12A	June 4	12:41	34.37	70.57	9	136	16	292	72	44	5	312	30	147	60
12B	June 4	12:41	34.37	70.57	6	154	14	294	72	61	12	326	30	169	58
12C	June 4	12:41	34.37	70.57	7	135	16	280	70	42	10	306	28	150	60
		09:42	34.36	70.57	8										
		12:41	34.37	70.57	6	336	3	100	85	246	5	332	50	152	40
12D	June 4	20:57	34.37	70.57	5										
13B	June 2	21:40	34.58	70.34	9	13	1	104	70	282	20	32	42	172	40
	May 31	16:43	34.62	70.40	6										
	June 2	03:22	34.60	70.32	9										
		04:49	34.59	70.28	12										
		10:49	34.56	70.42	3										
		21:40	34.58	70.34	9										
	June 3	09:33	34.63	70.49	8										
	June 5	11:40	34.57	70.30	4										
	June 6	07:26	34.63	70.41	13										
		10:50	34.60	70.32	5										
		11:25	34.56	70.29	11										
		16:58	34.63	70.49	9										
13D	June 6	23:25	34.63	70.35	10	335	8	218	72	65	15	315	50	166	36
		23:41	34.61	70.32	1										
	June 7	16:31	34.66	70.48	1										
		22:27	34.58	70.35	9										
	June 8	02:58	34.67	70.38	10										
		03:35	34.56	70.48	3										
		14:32	34.55	70.32	12										
		15:36	34.56	70.31	3										
	June 9	17:27	34.52	70.27	8										
		11:06	34.56	70.30	8										
		15:49	34.59	70.41	2										
		17:17	34.66	70.34	5										
		20:36	34.61	70.34	6										
		20:36	34.61	70.34	6										
	June 10	06:19	34.62	70.37	5										
	June 2	21:39	34.71	69.78	3										
	June 4	04:44	34.74	69.78	6										
14D	June 7	05:25	34.75	69.78	7	141	0	41	0		90	6	0	96	0
		06:08	34.72	69.78	5										
	June 8	00:16	34.71	69.79	4										
14D	June 8	00:19	34.72	69.77	8	349	15	227	51	82	33	302	50	186	20
		00:25	34.72	69.77	7										
		01:27	34.75	69.77	12										
	Sept. 4, 1976	12:08	32.48	67.45	19										
		12:15	31.92	67.16	2										
	Sept. 7	06:23	31.97	67.17	2	356	40	86	4	180	50	305	27	50	30
	Sept. 8	04:56	31.71	67.06	7										
		22:51	32.17	67.28	3										

A, the crust contains 20 layers; B, the crust contains 3 layers; C, the crust is homogenous; D, composite solution.

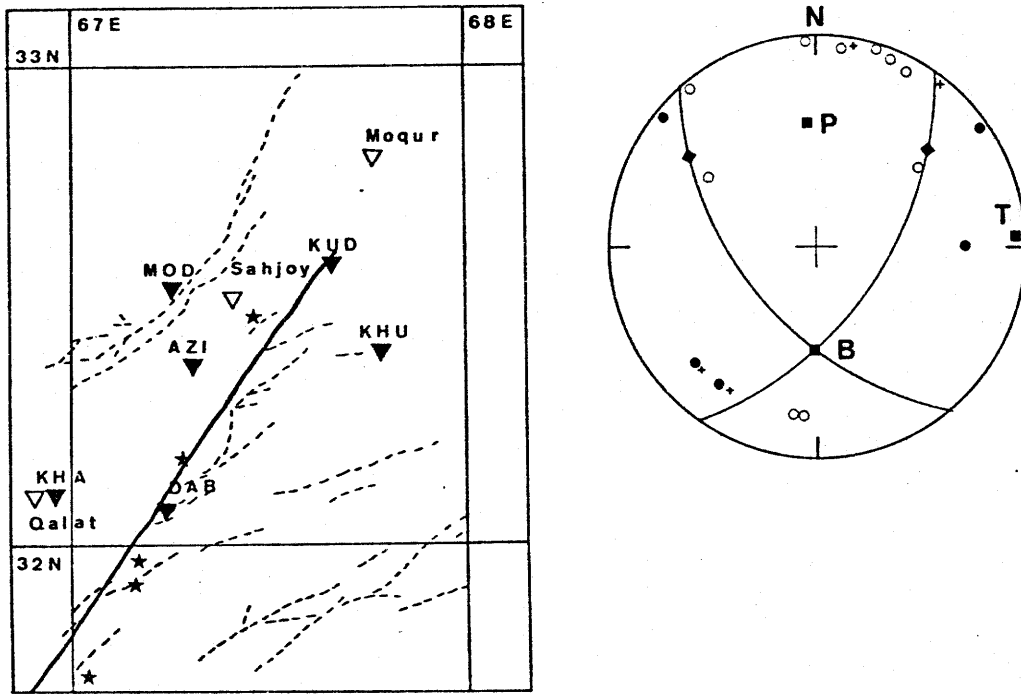


Fig. 4. Map of Chaman fault region and fault plane solution. Full triangles are seismological stations, empty triangles are towns, stars are earthquakes. Dashed lines show minor faults. The composite fault plane solution for the five events near the Chaman fault is shown on the right in an upper hemisphere projection.

fault (Figure 4). We chose this part because there has been historical seismic activity, the fault is geologically well defined, and it was possible to find accessible outcrops of bedrock on which to place the geophones. We located five small events with magnitudes less than 2 close to the fault itself at depths less than 20 km (Figure 4). Given the uncertainties in

the locations, all five events could have occurred on the fault. A composite fault plane solution for these five events is consistent with left-lateral strike motion along the Chaman fault. Also at station MOD (Figure 4) we recorded many very local events, which could have occurred on the Moqur-Kandahar fault. (Figure 1).

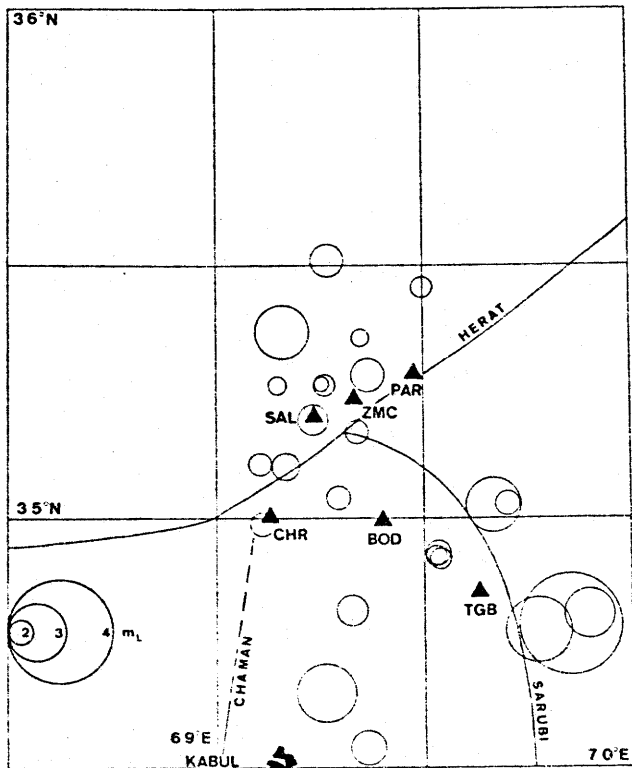


Fig. 5. Map of Kabul region. Circles show epicenters of earthquakes. The size of circles is function of M . Stations are full triangles.

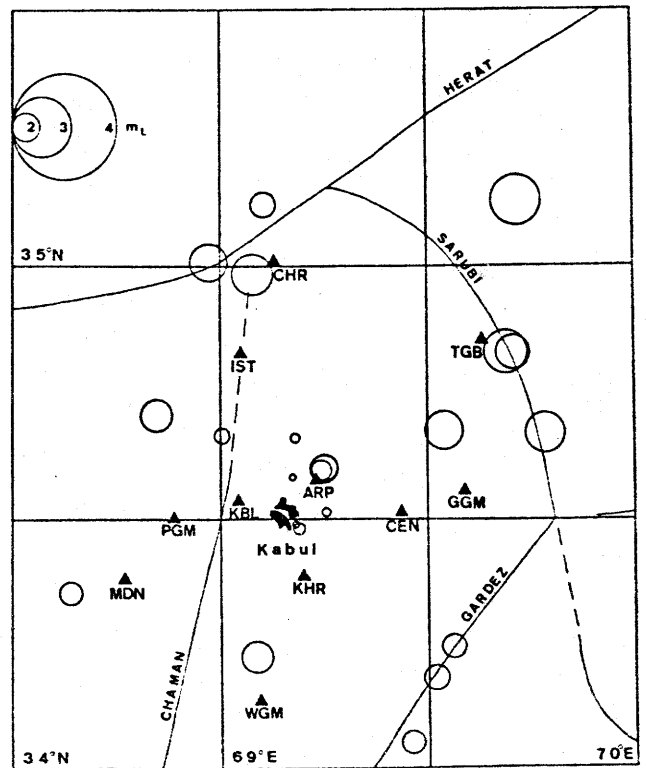


Fig. 6. Map of Charikar region. Symbols same as in Figure 5.

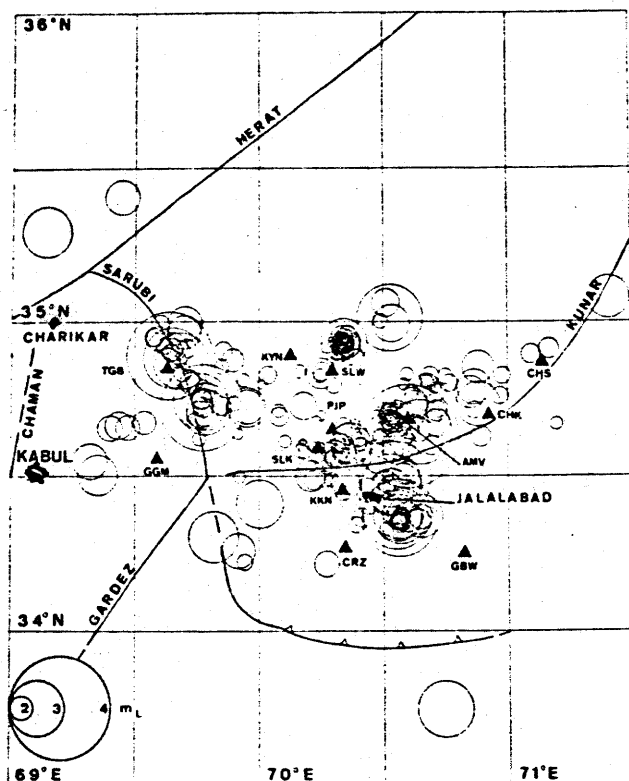


Fig. 7. Map of southern Nuristan-Jalalabad region. Symbols same as in Figure 5.

Kabul Region

Between May 19 and 26, 1977, we recorded with up to 10 stations in the Kabul region (Figure 5). This network was installed to determine the seismicity in the vicinity of Kabul and to study the junction of the Chaman, Sarubi, and Herat faults.

We were able to locate 27 earthquakes with magnitudes up to about 3. The calculated depths are between 5 and 25 km. There was inadequate activity to define a simple pattern, but it is clear that Kabul and its surroundings are active. Seven earthquakes occurred in the immediate vicinity of the city in this 1-week period.

A composite fault plane solution of mediocre quality for these events near Kabul (1D in Figure 3 and Table 3) indicates thrust faulting with an approximately northwest-southeast P axis. First motions from a single event (2B in Figure 3) on or near the Chaman fault are consistent with left-lateral strike-slip motion.

Charikar Region

We recorded with a network of six instruments between May 25 and June 6, 1978, near the junction of the Herat, Chaman, and Sarubi faults. (Political turmoil prevented a more thorough investigation.) We located 30 earthquakes with magnitudes between 1 and 3 (Figure 6). Poorer quality locations than for the other studies and the small number of events do not allow us to associate the activity with known features except perhaps the Sarubi fault near TGB. Nevertheless it is clear that the region is quite active.

Southern Nuristan-Jalalabad Region

Because of the high activity in the Alingar valley during a study of the Hindu Kush region in 1976 [Chatelain *et al.*, 1977], we installed a network of 11 stations in southern Nuristan to study the seismicity associated with the Sarubi and Kunar faults and the region between them (Figure 7). Between May 31 and June 10, 1977, we recorded 284 events that could be located (about 25/day), with a range of magnitude between 1 and 4.

Shallow activity ($h < 10$ km) seems to be associated with the Sarubi fault (Figure 7). A composite fault plane solution

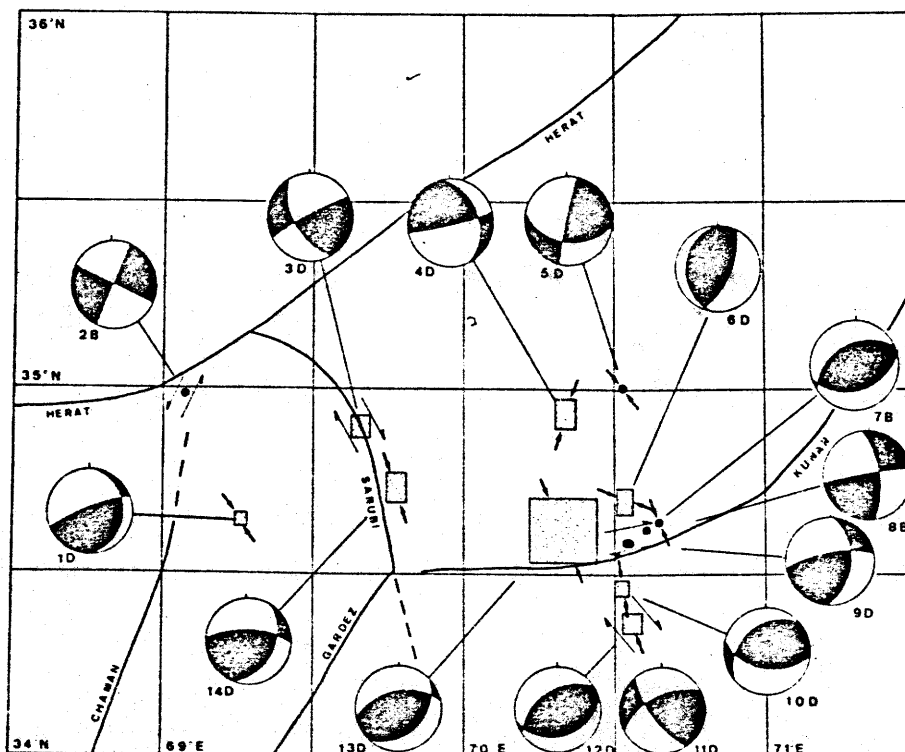


Fig. 8. Fault plane solutions in upper hemisphere abbreviated balloon format. Darkened areas are quadrants with compressional first motions. Boxes indicate region in which earthquakes in composite fault plane solutions occurred.

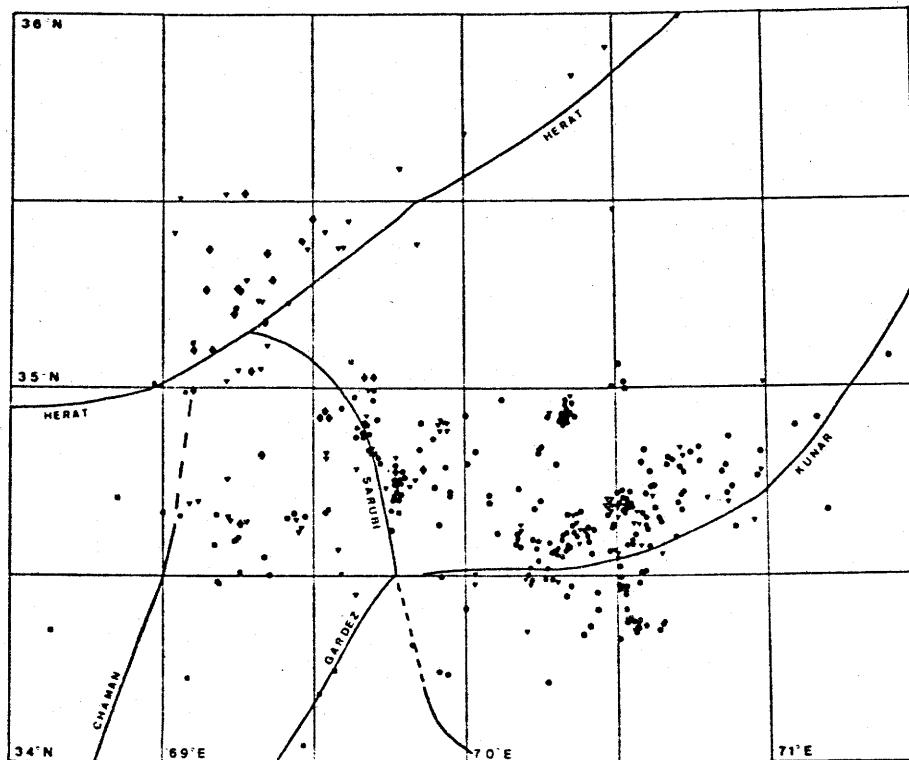


Fig. 9. Summary of seismicity of Kabul, Charikar, Southern Nuristan, and Jalalabad regions. Squares are from Kabul study, circles from southern Nuristan-Jalalabad study, diamonds from Charikar study, and triangles from Hindu-Kush study [Chatelain et al., 1980].

(3D in Figure 3) indicates a large component of right-lateral strike-slip motion on the fault (Figure 8).

The first motions from a cluster of events south of those used for solution 3D and east of the Sarubi fault show a very different pattern (solutions 14D and 14D* in Figure 3). The composite fault plane solution is not well constrained, and the data are consistent with both strike-slip faulting or nearly pure thrust faulting. The strike-slip solution (14D*) is consistent with left-lateral motion parallel to the Gardez fault (see Figure 1), whereas the thrust solution (14D) would represent

deformation of the region between the Sarubi fault and a possible continuation of the Gardez fault. In either case the P axis is oriented northwest-southeast to north-northwest-south-southeast.

Further east, seismicity is distributed over a broad area with clusters in various places but no clear zones or belts of activity that might indicate major active faults. There are some earthquakes that might be associated with the Kunar fault, and two fault plane solutions (8B and 9D) near the fault are consistent with right-lateral motion along it (Figure 8). First motions from events in different clusters indicate a variety of fault plane solutions that differ from one another, but with P axes generally aligned in a north-south to northwest-southeast direction (Figure 8).

CONCLUSIONS

The most obvious results of this study are that the seismicity is not confined to narrow zones but is scattered throughout the region of study (Figure 9) and that the fault plane solutions likewise show considerable variability (Figure 8). Most of the activity neither can be clearly associated with any known active faults nor clearly defines a major unrecognized fault. This activity seems to represent more diffuse deformation of a broad area. The most consistent pattern, however, is that the P axis is oriented approximately north-northwest-south-southeast, parallel to the present direction of convergence between India and Eurasia. An upper hemisphere projection of the P axes for all of the solutions (Figure 10) shows a mean azimuth of $337^\circ \pm 16^\circ$ with a plunge of $4^\circ \pm 17^\circ$ (down to the southeast). This direction is very close to the calculated direction of relative motion between India and Eurasia of 350° [Minster and Jordan, 1978]. It follows that the tectonic activity is probably a consequence of that convergence.

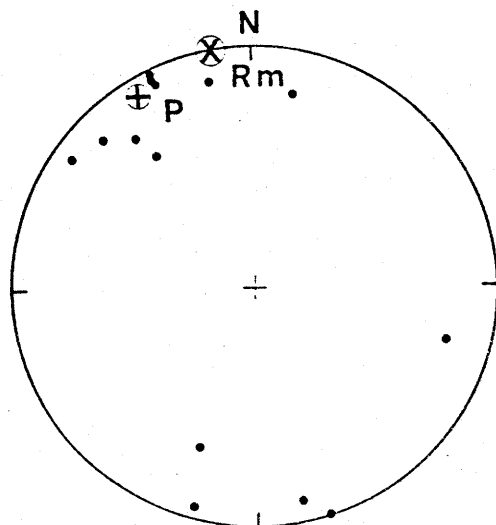


Fig. 10. Upper hemisphere stereographic projection of P axes of fault plane solutions. P is the mean direction of the P axes. Rm is the direction of relative motion between India and Eurasia [Minster and Jordan, 1978].

In addition, a modest amount of activity was recorded near the Chaman fault, and first motions of *P* waves are consistent with left-lateral motion. The Sarubi fault is well defined topographically (Figure 2) and seismically (Figures 7 and 9) and a composite fault plane solution indicates a large component of right-lateral strike-slip motion. The Gardez fault is less clearly active than the other faults recognized in this region.

There is scattered activity beneath Kabul and its immediate vicinity. A composite fault plane solution indicates thrust faulting with a northwest-southeast *P* axis. The occurrences of several earthquakes with magnitudes up to 3 in a 1-week period calls attention to the need for a more thorough investigation of the seismic risk of Kabul and its environs.

Acknowledgments. We thank J. P. Carbonnel for continuous assistance with both logistical and scientific questions, and in particular, for helping us in the field; M. Mattauer, G. Perrier, and P. Tapponnier for interesting discussions; J. L. Chatelain, M. Frogneux, X. Goula, M. Grosenbaugh, R. Guiget, L. Jones, J. King, J. Maurer, G. Suarez, and B. Tucker; Afghan engineers Amin, Kandari, Osman, Rabi, and Sharif for assistance in the field; J. Summers of the Afghan American Education Commission; and R. E. Gibson, H. Hafiz, and A. S. Saleem of Kabul University for assistance with logistics, laboratory facilities, and copies of seismograms from the station in Kabul; Woodward-Clyde consultants; and in particular, W. Savage and D. Tocher for loaning us two Sprengnether instruments; W. S. F. Kidd and L. Seeber for constructive criticism of the manuscript, and J. L. Chatelain for allowing us to use some of his data. This research was supported primarily by contracts ATP 35-06, 35-25, and 35-58 of INAG (Grenoble) and by grants EAR76-13367 and EAR78-13673 (MIT). The MIT portion of the work was made possible by an H. O. Wood award from the Carnegie Institute in Washington and by an Alfred P. Sloan Fellowship.

REFERENCES

- Armbruster, J., L. Seeber, and K. H. Jacob. The northwestern termination of the Himalayan front: Active tectonics from microearthquakes. *J. Geophys. Res.*, **83**, 269-282, 1978.
- Auden, J. B., Afghanistan-West Pakistan, Mesozoic-Cenozoic Orogenic Belts. Data for Orogenic Studies. *Spec. Publ.* **4**, pp. 365-378. Geol. Soc., London, 1974.
- Carbonnel, J. P., La limite de la plaque Indienne en Afghanistan, nouvelles données géologiques et sismologiques. *Mem. Ser. Soc. Geol. Fr.*, **8**, 145-152, 1977.
- Cassaigneau, C., Contribution à l'étude des sutures Inde-Eurasie, Thèse de 3ème cycle, Univ. des Sci. et Tech. du Languedoc, Montpellier, 1979.
- Chatelain, J. L., S. Roecker, D. Hatzfeld, P. Molnar, and G. Perrier. Etude sismologique en Afghanistan. Premiers résultats. *C. R. Somm. Soc. Geol. Fr.*, **5**, 260-262, 1977.
- Chatelain, J. L., S. W. Roecker, D. Hatzfeld, and P. Molnar. Microearthquake seismicity and fault plane solutions in the Hindu Kush region and their tectonic implications. *J. Geophys. Res.*, **85**, this issue, 1980.
- de Lapparent, A. F., L'Afghanistan et la dérive du Continent Indien. *Rev. Geogr. Phys. Geol. Dyn.*, **14**, 449-456, 1972.
- Dewey, J. F., and J. M. Bird. Mountain belts and the global tectonics. *J. Geophys. Res.*, **75**, 2625-2647, 1970.
- Griesbach, C. L., Note on the Quetta earthquake in Baluchistan on the 20th December 1892. *Rec. Geol. Surv. India*, **26**, part 2, 57-64, 1893.
- Heuckroth, L. E., and R. A. Karim. *Earthquake History. Seismicity and Tectonics of the Region of Afghanistan*. 200 pp., Seismological Center, Faculty of Engineering, Kabul University, Kabul, 1970.
- Heuckroth, L. E., and R. A. Karim. Afghan seismotectonics. *Phil. Trans. Roy. Soc. London. Ser. A*, **274**, 389-395, 1973.
- Lee, W. H. K., and J. C. Lahr. HYPO 71 (revised). A computer program for determining hypocenter, magnitude and first motion pattern of local earthquakes. *Open File Rep. 75-311*. U.S. Geol. Surv., Washington, D. C., 1975.
- McMahon, A. H., The southern borderlands of Afghanistan. *Geogr. J.*, **9**, 393-415, 1897.
- Minster, J. B., and T. H. Jordan. Present day plate motions. *J. Geophys. Res.*, **83**, 5331-5354, 1978.
- Molnar, P., and P. Tapponnier. Cenozoic tectonics of Asia: Effects of a continental collision. *Science*, **189**, 419-426, 1975.
- Quittmeyer, R. X., and K. H. Jacob. Historical and modern seismicity of Pakistan. Afghanistan, northwestern India and southeastern Iran. *Bull. Seismol. Soc. Amer.*, **69**, 773-824, 1979.
- Richter, C. F., *Elementary Seismology*. W. H. Freeman, San Francisco, Calif., 1958.
- Seeber, I., and J. Armbruster. Seismicity of the Hazara arc in Northern Pakistan: Decollement vs. basement faulting. in *Geodynamics of Pakistan*, edited by A. Farah and K. DeJong, Geological Survey of Pakistan, Quetta, 1979.
- Seeber, L., and K. H. Jacob. Microearthquakes survey of northern Pakistan. Preliminary results and tectonic implications. *Coll. Intern. CNRS 268*, pp. 347-360. Centre Nat. Res. Sci., Paris, 1977.
- Tahirkheli, R. A. K., M. Mattauer, F. Proust, and P. Tapponnier. Données nouvelles sur la suture Inde-Eurasie au Pakistan. *Coll. Intern. CNRS 268*, pp. 347-360. Centre Nat. Res. Sci., Paris, 1977.
- Wellman, H. N., Active wrench faults of Iran, Afghanistan and Pakistan. *Geol. Rundsch.*, **55**, 716-735, 1966.

(Received June 18, 1979;
accepted August 1, 1979.)

CHAPTER IV

*Jack : ... That, my dear Algy, is the whole truth
pure and simple.*

*Algernon : The truth is rarely pure and never simple.
Modern life would be very tedious if it were,
and modern literature a complete impossibility!*

- Oscar Wilde

The Importance of being Earnest

Sensitivity of the Earthquake Location Problem to
Network Geometry

W.L. Ellsworth and S.W. Roecker

U.S.G.S. and MIT

Summary

The influence of network geometry on the linearized hypocenter determination problem is studied through direct examination of the pseudoinverse operator. Analysis of simple array configurations for which the analytic form of the operator can be constructed reveals that the critical geometric factor controlling the location is the spread of ray take-off angles at the source. However, the slowness vector components, which are used to form the conditional equations, do not reliably predict the influence of a given observation on the hypocentral adjustment. In particular, focal depth adjustments commonly depend upon data for which $\partial T/\partial z = 0$. The suitability of a particular network to the earthquake location problem can be quantified by studying the correlation between rows of the pseudoinverse operator. High correlation between rows implies that the perturbations to the corresponding parameters are not independent. The analysis also demonstrates that problems with both P and S wave data are better posed problems than those which have only one type of data.

I. Introduction

Determination of earthquake hypocenters from observations of body wave arrival times is, perhaps, the most commonly solved geophysical inverse problem. Virtually all computational schemes in use today for the location problem stem from Geiger's solution [Geiger, 1912] which seeks linear perturbations to the four hypocentral parameters by minimizing a norm of the travel time residuals. Linearization is achieved by expanding the observed travel time about a trial hypocenter in a Taylor series of the hypocenter perturbations (δ_0 , δz , δx , δy) and retaining only first order terms.

Geiger's linearization may be written as

$$(1.1) \quad r_i = \delta_0 + \frac{\partial T_i}{\partial z} \delta z + \frac{\partial T_i}{\partial x} \delta x + \frac{\partial T_i}{\partial y} \delta y$$

where r_i is the travel time residual for the i^{th} station and T_i is the travel time. The system of linear equations defined by (1.1) has been solved by many different methods including least squares [Flynn, 1960, Bolt, 1960; Nordquist, 1962; Eaton, 1969], stepwise multiple regression [Lee and Lahr, 1975], singular value decomposition [Bolt, 1970; Buland, 1976; Klien, 1978], and hybrid methods [Anderson, 1979]. As simple as this method is to derive, and despite its widespread and successful application, comparatively little is known about the influence of network geometry upon the success or failure of the iterative procedure.

In this paper, we focus on analysis of the linear inverse operator for the least squares solution of (1.1), using both analytical and numerical approaches. This analysis of the linear inverse operator quantifies the relationship between each observation and the four hypocentral parameters. Direct examination of this operator, which is the pseudoinverse for the minimum length solution of (1.1), reveals information about the linear estimation procedure that is not readily obtained from more traditional methods of viewing the linear inverse problem. In particular, the partial derivatives in (1.1) often provide misleading information when inferences about the inverse problem are drawn from them alone.

In the discussion that follows we will make the following simplifying assumptions for the purpose of reducing algebraic complexity. The variance of the travel time observations are assumed to be uniform and Gaussian. We also assume that errors in the theoretical travel times caused by incomplete knowledge of the earth structure are also uniform and Gaussian. The application of variance equalization weights when these conditions are not met is straightforward, so these assumptions make the analysis no less general.

II. Evaluating The Minimum Length Solution

The minimum length solution for (1.1) can be constructed by forming the generalized inverse discussed by Lanczos [1961]. For convenience, we write (1.1) in matrix notation as $A\underline{\delta} = \underline{r}$, where $\underline{\delta} = (\delta_0, \delta_z, \delta_x, \delta_y)$ and A_{ij} contains the corresponding partial derivatives for T_i with respect to δ_j . The generalized inverse, A^+ , is a pseudoinverse [Lawson and Hanson, 1974] for the overdetermined systems considered in this paper. The singular value decomposition of the $n \times m$ matrix A ($n > m$) expresses the original matrix as the product of three matrices:

$$A = UV^T$$

where U and V are orthogonal matrices of dimension $n \times n$ and $m \times m$, respectively. Λ is an $n \times m$ matrix, the first n rows of which form a diagonal matrix of the singular values. The pseudoinverse of A is $A^+ = V \underset{p}{\Lambda}^{-1} \underset{p}{U}^T$ where only p non-zero singular values and their corresponding singular vectors are used to form A . When $p = m$, the space spanned by V is complete and the solution to (1.1) given by

$$(2.1) \quad \underline{\delta} = A^+ \underline{r}$$

is the least squares solution to the normal equations

$$(2.2) \quad A^T A \underline{\delta} = A^T \underline{r}$$

In this case, A^+ can be constructed from (2.2) by

$$(2.3) \quad A^+ = (A^T A)^{-1} A^T$$

We will be studying special cases of the analytic form of A^+ below and will use (2.3) to construct them.

The concept of parameter resolution, introduced by Backus and Gilbert [1967], which is invaluable in the analysis of many geophysical inverse problems, is rarely useful in the hypocenter problem because $p = m = 4$ in most cases. When V is complete, the resolution matrix $R = V_p V_p^T$ is the identity matrix.

The information density matrix, or data resolution matrix, S , does contain useful information in the problem when $p = m$:

$$(2.4) \quad S = U_p U_p^T = A(A^T A)^{-1} A^T$$

The parameter covariance matrix, C , formed under the assumption of uncorrelated data errors, also provides useful information:

$$(2.5) \quad C = \sigma_d^2 A^+ (A^+)^T = \sigma_d^2 V \Lambda^{-2} V^T$$

Additional and often unique information about the linear solution can be extracted directly from A^+ . Viewing A^+ as a linear operator which transforms the data vector into the solution (2.1), we recognize that each element of A^+ is the weight or "sensitivity" that a particular

observation has on a given parameter.

Each column of A^+ contains a complete description of how the corresponding observation contributes to the solution. The euclidian length of the column is a measure of the net contribution the datum makes to the solution. Its square occupies the diagonal element of the matrix $(A^+)^T A^+$ which we will refer to as the data importance matrix T :

$$(2.6) \quad T = U \Lambda^{-2} U^T = (A^+)^T A^+$$

T is equivalent to the data covariance matrix divided by σ_d^2 .

Each row of A^+ describes how the observations combine to form the perturbation for the corresponding parameter. The euclidian length of the row, formed by taking the inner product of A^+ , is a diagonal element of the parameter covariance matrix C (2.5) divided by σ_d^2 . Under the assumption of a Gaussian error distribution, the off-diagonal elements of C quantify the interdependence of the elements of the solution, δ . The linear correlation coefficient

$$(2.7) \quad R_{ij}^2 = C_{ij}^2 / (C_{ii} C_{jj})$$

is a measure of this interdependence.

III. General Form of the Pseudoinverse for Geiger's Method

Partial derivatives of the travel time with respect to the three spatial coordinates of the hypocenter in equation (1.1) may be written as the components of the slowness vector for the unperturbed raypath evaluated at the trial hypocenter [Flynn, 1960; Lee and Stewart, 1980]. Referring to figure 1, these components are

$$\begin{aligned} \frac{\partial T_i}{\partial x} &= p_{x_i} = \sin\theta_i \cos\psi_i / V \\ (3.1) \quad \frac{\partial T_i}{\partial y} &= p_{y_i} = \sin\theta_i \sin\psi_i / V \\ \frac{\partial T_i}{\partial z} &= p_{z_i} = \cos\theta_i / V \end{aligned}$$

where θ is the take off angle, ψ is the azimuth for the ray to the i^{th} station, and V is the velocity at the source.

Because the partial derivatives are evaluated at the source, the results to be discussed below do not depend upon the nature of the earth model. For illustrative purposes, we will occasionally apply the results to one-dimensional earth models.

Using (3.1), equation (1.1) may be written as

$$r_i = \delta t + p_{z_i} \delta z + p_{x_i} \delta x + p_{y_i} \delta y$$

IV. Analytical Form of A^+ for Special Network Geometries

The complete analytic form of A^+ for the general problem is tedious to form and difficult to evaluate. A useful algebraic simplification occurs when the depth-origin time (0-z) and latitude-longitude (x-y) problems decouple. Decoupling occurs when

$$\sum p_{x_i} = 0$$

$$\sum p_{y_i} = 0$$

(4.1)

$$\sum p_{x_i} p_{z_i} = 0$$

$$\sum p_{y_i} p_{z_i} = 0$$

It is, in general, possible to find many network geometries where these requirements are approximately met. For example, decoupling occurs for geometries in which pairs of stations record rays that have the same take-off angle and complimentary azimuths. For a one-dimensional earth model, networks with an n -fold symmetry ($n \geq 2$) axis about the epicenter decouple the (0-z) and (x-y) problems. An example of this type of network is shown in figure 2.

Depth-Origin Time Problem

The normal equations for the decoupled (0-z) problem

are

$$(4.2) \quad \begin{bmatrix} n & \Sigma p_{z_i} \\ \Sigma p_{z_i} & \Sigma p_{z_i}^2 \end{bmatrix} \begin{bmatrix} \delta 0 \\ \delta z \end{bmatrix} = \begin{bmatrix} 1, 1, \dots, 1 \\ p_{z_1}, \dots, p_{z_n} \end{bmatrix} \begin{bmatrix} r_1 \\ r_2 \\ \cdot \\ r_n \end{bmatrix}$$

To form A_{0-z}^+ , we first construct $(A^T A)^{-1}$

$$(A^T A)_{0-z}^{-1} = \frac{1}{(n\sigma)^2} \begin{bmatrix} \Sigma p_{z_i}^2 & -\Sigma p_{z_i} \\ -\Sigma p_{z_i} & n \end{bmatrix}$$

where σ^2 is the variance of the vertical slowness. The k^{th} column of A^+ is

$$\frac{1}{(n\sigma)^2} \begin{bmatrix} \Sigma p_{z_i}^2 - p_{z_k} \Sigma p_{z_i} \\ np_{z_k} - \Sigma p_{z_i} \end{bmatrix}$$

and the explicit form of the solution is

$$(4.3) \quad \delta 0 = \frac{1}{(n\sigma)^2} \sum (\Sigma p_{z_i}^2 - p_{z_k} \Sigma p_{z_i})$$

$$\delta z = \frac{1}{(n\sigma)^2} \sum (np_{z_k} - \Sigma p_{z_i}) r_k$$

The first row of A_{0-z}^+ contains the weights or sensitivities that transform the travel time residuals into

the origin time perturbation $\delta 0$. They quantitatively express the sensitivity of $\delta 0$ to each observation. Figure 3a shows the sensitivity curve for the cross-shaped array of figure 2 which overlies a halfspace. The ratio $\hat{p} = \frac{\sum p_{z_i}^2}{\sum p_{z_i}}$ has a special meaning for origin time sensitivities. Rays with $p_{z_i} = \hat{p}$ have no influence on the origin time as the corresponding elements of A_{0-z}^+ are zero. When $p_{z_i} < \hat{p}$, positive travel time residuals act to make the origin time earlier and when $p_{z_i} > \hat{p}$ positive residuals act to make the origin time later (figure 3a). None of these features is readily apparent in the conditional equations (1.1) since $\partial T_k / \partial 0 = 1$ for all observations.

The second row of A_{0-z}^+ contains the sensitivities for the depth perturbation δz . This row is nearly the mirror image of the $\delta 0$ sensitivities (figure 3b). The sensitivity is zero when $p_{z_k} = \frac{\sum p_{z_i}}{n}$ or at that station where the vertical slowness is equal to the mean vertical slowness. Again, the partial derivatives fail to predict the impact of a particular observation on the solution. Even when $\frac{\partial T}{\partial z} = 0$, equation (4.3) shows that the sensitivity which weights the residual in the solution is, in general, nonzero.

The functional similarity between the rows of A_{0-z}^+ illustrates the well known trade-off between origin time and depth which exists even when the model space resolution matrix is the identity matrix. This trade-off between $\delta 0$ and δz becomes complete when

$$(\sum p_{z_i})^2 = n \sum p_{z_i}^2$$

or when both sensitivity curves cross zero at the same p_{z_k} value. Geometrically, this occurs when all stations have a common vertical component of the slowness vector.

The linear correlation coefficient R^2 (2.7) expresses the degree of interdependence between δ_0 and δz . For geometries satisfying the decoupling criteria (4.1) :

$$(4.4) \quad R_{0-z}^2 = 1 - \frac{n\sigma^2}{\sum p_{z_i}^2} = \frac{(\sum p_{z_i})^2}{n \sum p_{z_i}^2}$$

Clearly, if we seek to reduce the interdependence of focal depth and origin times, R_{0-z}^2 needs to be minimized. The "optimal" geometry for a network of stations can also be defined as that geometry which minimizes the diagonals of the covariance matrix [e.g. Kijko, 1977a, 1977b]. The covariance matrix (2.5) for this problem is

$$(4.5) \quad C_{0-z} = \left(\frac{\sigma_d}{n\sigma} \right)^2 \begin{bmatrix} \sum p_{z_i}^2 & -\sum p_{z_i} \\ -\sum p_{z_i} & n \end{bmatrix}$$

We see that optimization entails the maximization of σ^2 .

This perspective makes clear the role of including both upgoing and downgoing rays in the determination of depth and origin time, since the maximization of σ^2 occurs when $\sum p_{z_i} = 0$. If only rays in the upper or lower focal sphere are

used, all vertical slowness values are of the same sign. By including both upgoing and downgoing rays, the contributions to $\sum p_{z_i}$ tend to cancel.

Finally, we note that when the depth-origin time problems decouple, the k^{th} column of the pseudoinverse takes the form

$$A^+ = \begin{bmatrix} 1/n \\ p_{z_k} / \sum p_{z_i}^2 \end{bmatrix}$$

Because of the removal of coupling effects, the sensitivities are equal to the partial derivatives, within a scale factor.

Latitude-Longitude Problem

When the depth-origin time problem decouples from the latitude-longitude problem, the normal equations for the

(x-y) problem become

$$\begin{bmatrix} \sum p_{x_i}^2 & \sum p_{x_i} p_{y_i} \\ \sum p_{x_i} p_{y_i} & \sum p_{y_i}^2 \end{bmatrix} \begin{bmatrix} \delta x \\ \delta y \end{bmatrix} = \begin{bmatrix} p_{x_1}, \dots, p_{x_n} \\ p_{y_1}, \dots, p_{y_n} \end{bmatrix} \begin{bmatrix} r_1 \\ r_2 \\ \vdots \\ r_n \end{bmatrix}$$

Constructing A_{x-y}^+ as above, the general form for the k^{th} column of A_{x-y}^+ is

$$(4.6) \quad \frac{1}{D} \begin{bmatrix} p_{x_k} \sum p_{y_i}^2 - p_{y_k} \sum p_{x_i} p_{y_i} \\ p_{y_k} \sum p_{x_i}^2 - p_{x_k} \sum p_{y_i} p_{x_i} \end{bmatrix}$$

where $D = \text{Det } (A^T A)_{x-y} = \sum p_{x_i}^2 \sum p_{y_i}^2 - (\sum p_{x_i} p_{y_i})^2$.

Because the elements of A_{x-y}^+ depend upon both azimuth and take-off angle, it is more difficult to generalize about the behavior of the sensitivities than it was for the origin time-depth problem. Still, we can make some observations. The total impact of a single observation on the epicentral adjustment can be studied by examining the diagonal elements of the data importance matrix T . For simplicity, we examine stations lying along the $+x$ axis (the results are no less general because of this). After some algebra, we find the length of the k^{th} column of A_{x-y}^+ is

$$(4.7) \quad T_{kk}^{1/2} = w p_{x_k}$$

where $w^2 = ((\sum p_{y_i}^2)^2 + (\sum p_{x_i} p_{y_i})^2) / D^2$. Figure 3c illustrates the behavior of $T_{kk}^{1/2}$ for the array shown in figure 2.

While the behavior of the total sensitivity for the epicentral perturbation agrees with the behavior we would predict from knowledge of the horizontal component of \underline{p} , the individual horizontal components of \underline{p} do not necessarily reflect the sensitivity contained in A_{x-y}^+ . For example, when the raypath to a particular station leaves the source in a direction parallel to the x -axis, $\partial T / \partial y = 0$, and one might expect that the sensitivity of δy to this observation would be zero as well, when actually the sensitivity is $-p_{x_k} \sum p_{x_i} p_{y_i}$. As in the depth-origin time problem, it is only when the latitude problem decouples from the longitude

problem that the sensitivities of A_{x-y}^+ mirror the partial derivatives of A.

The covariance matrix for the (x-y) problem is

$$(4.8) \quad C_{x-y} = \frac{\sigma_d^2}{D} \begin{bmatrix} \Sigma p_{y_i}^2 & -\Sigma p_{x_i} p_{y_i} \\ -\Sigma p_{x_i} p_{y_i} & \Sigma p_{x_i}^2 \end{bmatrix}$$

and the linear correlation coefficient is

$$(4.9) \quad R_{x-y}^2 = 1 - \frac{D}{\Sigma p_{x_i}^2 \Sigma p_{y_i}^2} = \frac{(\Sigma p_{x_i} \Sigma p_{y_i})^2}{\Sigma p_{x_i}^2 \Sigma p_{y_i}^2}$$

V. Influence of Network Geometry

In this section, expressions for sensitivities associated with symmetric arrays developed above are used to illustrate the effects of different network geometries and velocity models on the location problem. Specifically, we examine the effects on sensitivity of the array apertures for a half space and for a layer over a half space structures. These examples are intended to be a suggestion of how sensitivities can be used to evaluate some geometric effects, rather than an exhaustive review of the phenomena associated with earthquake location.

Half Space Model

Sensitivity values of A^+ for hypocenters between 1 and 20 kilometers depth recorded by a cross-shaped array appear in figure 4. At all focal depths, the depth and origin time sensitivities (figure 4a and 4b) are essentially mirror images of each other. The magnitude of the sensitivities increases with increasing focal depth, or, equivalently, as the solid angle subtended by the array becomes smaller. Following our previous expressions, this change in magnitude can be viewed as a decrease in σ^2 . Because the covariance matrix is inversely related to σ^2 , the standard errors of depth and origin time increase as the effective array aperture decreases. One significant difference between the behavior of A^+ for depth and origin time is that the magnitude of the origin time sensitivities increases

monotonically with depth, while the depth sensitivities have a minimum value. The increase in depth sensitivity at shallower focal depths is caused by the low density of stations within one focal depth of the epicenter.

The behavior of A^+ for the epicentral adjustment shows an increase in sensitivity magnitude with decreasing array aperture (figure 4c). The epicentral sensitivity approaches a constant value for observations at epicentral distances greater than about four focal depths.

Layer Over a Half Space Model

Sensitivities for a layer over a half space model illustrate the effects of a mixture of upgoing and downgoing rays (figure 5). Sensitivities for sources in the half space exhibit the same behavior described above. However, when the source is located within the layer, the addition of downgoing rays dramatically alters the form of A^+ . In particular, the magnitude of the sensitivities are smaller than in the case where only upgoing rays are present, and therefore the covariance of the parameter corrections are smaller. While the differences between the magnitudes of the sensitivity for events in the layer are all small, events closer to the interface have smaller magnitudes overall.

In figure 6 we show the partial derivatives used to form the pseudoinverse for this model. Comparison of the elements of A^+ (figure 5) for any parameter with the

derivatives used to generate them (figure 6) again leads to the conclusion that coupling prohibits a reliable prediction of the influence of a given observation on the solution.

VI. Importance of S Wave Arrivals to the Hypocenter Problem

Anyone who has experience in locating earthquakes with a sparse network appreciates the value of a few S wave readings in improving the quality of the hypocenter solution. Buland [1976] states that "the marginal utility of adding an S arrival is large compared with the marginal utility of adding one more P arrival". He also notes that the use of P and S arrival time data typically leads to superlinear convergence whereas use of one type of data results in linear or slower convergence.

To see how S waves add such important information to the location problem, we examine the partial derivatives for S. If we express each partial derivative, or component of the slowness vector, as an equivalent P wave at a different take-off angle θ_k , we have, from (3.1):

$$(5.1) \quad \frac{\partial T_k}{\partial z} = \frac{\cos \theta_k}{V_s} = \frac{\cos \theta_k}{V_p}$$

Clearly θ_k does not exist if $|\cos \theta_k| > V_s/V_p$. For take-off angles in this range, S waves add unique information that cannot be replicated by any P observations. When $|\cos \theta_k| \leq V_s/V_p$, the S observation behaves as an equivalent P observation along a more vertical raypath. For an upgoing ray in a half space in the decoupled (0-z) problem discussed above, the S observation has the same effect as if the

station were nearer the epicenter improving the depth control by increasing σ^2 .

The partial derivatives $\partial T/\partial x$ and $\partial T/\partial y$ for the S wave can also be viewed as equivalent P wave derivatives with take-off angles given by

$$(5.2) \quad \sin\theta_k = \frac{V_p}{V_s} \sin\theta_k$$

where $|\sin\theta_k| \leq V_s/V_p$. When (5.2) is satisfied, an S observation has the same effect as a P observation from a more distant station in the decoupled epicenter problem, again giving more control to the epicenter determination. Remarkably, the S observation is equivalent to both a closer and more distant station for the whole problem.

In general, S waves cannot be viewed as equivalent P observation. When $V_p/V_s > 1.414$, there is no θ which can simultaneously be converted into an equivalent θ for all three spatial partial derivatives. Consequently, S waves add unique information whenever one component of its slowness vector exceeds the compressional wave slowness of the medium.

VII. Application to Arbitrary Array Geometries

In order to simplify the form of $A^T A$, much of the analysis in sections IV-VI assumed certain symmetries of the stations with respect to the hypocenter. In the general case, these conditions are rarely met and the specter of coupling between unknowns in the normal equations haunts our intuition to an even greater extent. Many of the observations made in this paper concerning the relative sensitivities of decoupled problems and the effects of S waves are for the most part congruous with what someone who has experience with earthquake location problem knows intuitively. We therefore suspect that in cases where an earthquake is adequately recorded by a large array, simple forms for A^+ (4.3 and 4.6) are approximately correct. While a detailed analysis of A^+ for a given array is beyond the scope of this paper, some numerical tests have shown that the decoupling conditions (4.1) do not need to be satisfied exactly for the decoupled solutions to be useful. An example of an array which violates the symmetry conditions but has sensitivities similar to those predicted when (O-z) and (x-y) problems decouple is shown in figure 7. At the same time, the use of intuition in predicting the influence of an observation when the (O-z) and (x-y) problems are coupled can be misleading. This is typically the case for small, irregular arrays (e.g., see Chatelain et al., 1980). We suggest, therefore, that direct inspection of A^+ as part of the routine hypocenter program output is one practical

approach to the evaluation of the effects of network geometry. The covariance matrix and correlation coefficients are also useful indicators of the geometric suitability of the observation set. The correlation coefficient R^2 provides a natural way to examine the independence of the hypocentral adjustments. Since the analytic form of $(A^T A)^+$ for the complete 4 x 4 problem is complicated, this is best handled numerically. Jackson [1980] shows the utility of this approach for studying the coupling of focal depths and origin times from teleseismic observations.

Some generalizations about the influence of network geometry can also be made by noting that instability in A^+ arises when two or more columns of A become parallel to each other. As the epicenter moves outside the network, the horizontal components of the slowness vector, p_x and p_y , tend toward constant values for all stations. As the epicentral angle subtended by the network closes, the corresponding columns of A (3.2) become more parallel to each other and to the column corresponding to δ_0 , which is a constant. Consequently, the condition number of A increases and the least squares solution becomes unstable. Similarly, the column of A corresponding to δ_z becomes parallel to the column corresponding to δ_0 when p_z is equal for all raypaths and the inversion becomes unstable.

VIII. Discussion and Conclusions

Accurate location of earthquake hypocenters depends critically upon the geometric distribution of ray take-off angles at the source. The influence that a particular observation exerts upon the hypocenter adjustment cannot, in general, be reliably predicted from the partial derivatives in (1.1) unless the correlation coefficients (2.7) are small. The influence of a particular datum upon the minimum length solution can be determined directly through examination of the columns of the pseudoinverse A^+ .

If we view A^+ as the linear operator which transforms the data vector \underline{r} into the solution vector $\underline{\delta}$, the rows of A^+ are the weights which express the sensitivity of the components of $\underline{\delta}$ to each datum in \underline{r} . Errors in the observational data set arising from inaccuracies in arrival time measurements or errors in the earth model are also projected into $\underline{\delta}$ by A^+ . Therefore, the elements of A^+ also express the sensitivity of the components in $\underline{\delta}$ to errors in the data. A large sensitivity value in A^+ for a particular datum may not be a virtue if errors in travel-time measurement or their prediction through an earth model are large.

Analytic forms of A^+ that can be constructed for special network configurations illustrate some of the non-intuitive facets of the least-squares solution. In general, sensitivities for δ_0 are not constant and are nearly a mirror image of sensitivities for δ_z . Observations for

which $\partial T/\partial z = 0$ may have significant influence on δz when $\sum \partial T_i/\partial z \neq 0$. This condition will always occur when only either upgoing or downgoing rays are present in the observational set. A mixture of upgoing and downgoing rays improves the quality of the solution by reducing its covariance. Sensitivities for δx and δy appear to be more faithfully predicted by their corresponding partial derivatives, at least when the epicenter is within the network.

Control over the hypocentral parameters can also be greatly enhanced by mixing P and S wave data. Hypocenter location problems so formulated are better posed than those that contain only one type of data because S waves add information which cannot be replicated by P waves.

Finally, we note that $\delta 0$ is the only unknown that depends upon the mean travel time residual. Solving the first normal equation (2.2) for $\delta 0$ gives

$$(8.1) \quad \delta 0 = \frac{1}{n} (\sum r_i - \delta z \sum p_{z_i} - \delta x \sum p_{x_i} - \delta y \sum p_{y_i})$$

The origin time correction is thus the difference between the mean travel time residual and the mean of the components of the slowness vector weighted by their respective perturbations. Algebraic substitution of (8.1) into (2.2) removes the means of both the residuals and the partial derivatives from the system of equations.

The conclusion that the mean residual exclusively

affects the origin time also applies to any linear problem containing a column vector. Consequently, the mean residual does not affect velocity perturbations in joint hypocenter-velocity inversions. Velocity perturbations, as well as hypocentral coordinates, are controlled exclusively by the shape of the travel time residual curve.

References

- Anderson, K.R., 1978, Automatic processing of local earthquake data, Ph.D. thesis, MIT, Cambridge, Ma.
- Backus, G., and Gilbert, J.F., 1967, Numerical applications of a formation for geophysical inverse problems, Geophys J. R. astr. Soc., 13, 247-276.
- Bolt, B.A., 1960, The revision of earthquake epicenters, focal depths, and origin time using a high-speed computer, Geophys J. R. astr. Soc., 3, 433-440.
- Buland, R., 1976, The mechanics of locating earthquakes, Bull. Seism. Soc. Am., 66, 173-187.
- Businger, P.A., and Golub, G.H., 1969, Singular value decomposition of a complex matrix, Comm. ACM, 12, 564-565.
- Chatelain, J.L., Roecker, S.W., Hatzfeld, D., and Molnar, P., 1980, Microearthquake seismicity and fault plane solutions in the Hindu Kush region and their tectonic implications, Jour. Geophys. Res., 85, 1365-1387.
- Eaton, J.P., 1969, Hypolayer, a computer program for determination of local earthquakes in an earth consisting of uniform flat layers over a half space, U.S. Geol. Surv. Open-File Report, 155 pp.

- Flynn, E.A., 1960, Local earthquake location with an electronic computer, Bull. Seism. Soc. Am., 50, 467-470.
- Gieger, L., 1910, Herdbestimmung bie erdbeben aus den ankunftszeiten, K. Gessel. Wiss. Goett., 4, 331-349.
- Jackson, J.A., 1980, The focal depth of earthquakes in Iran and Turkey, Geophys. J. R. astr. Soc., 66, 285-301.
- Kijko, A., 1977a, An algorithm for the optimum distribution of a regional seismic network-I, Pure Appl. Geophys., 115, 999-1009.
- Kijko, A., 1977b, An algorithm for the optimum distribution of a regional seismic network-II. An analysis of the accuracy of location of local earthquakes depending on the number of seismic stations, Pure Appl. Geophys., 115, 1010-1021.
- Klein, F., 1978, Hypocenter location program hypoinverse, U.S. Geol. Surv. Open-File Report, 78-694, 113 pp.
- Lanczos, C., 1961, Linear Differential Operators, Van-
Nostrand Co. Ltd., London, 564 pp.
- Lawson, C.L., and Hanson, R.J., 1974, Solving least square problems, Prentice-Hall, New Jersey, 340 pp.

Lee, W.H.K., and Lahr, J.C., 1974. HYPO71 (revised): a computer program for determining hypocenter, magnitude and first motion patterns of local earthquakes, U.S. Geol. Surv. Open-File Report, 75-311, 114 pp.

Lee, W.H.K., and Stewart, S.W., 1980, Principles and Applications of Microearthquake Networks, Advances in Geophysics, 23, Academic Press, New York.

Nordquist, J.M., 1962, A special-purpose program for earthquake location with an electronic computer, Bull. Seism. Soc. Am., 52, 431-437.

Wilkenson, J.H., and Reinsch, C., 1971, Handbook for automatic computation, II, Linear Algebra, Springer-Verlag, New York, 439 pp.

Captions

- Figure 1. Coordinate geometry for the hypocenter problem showing components of the slowness vector at the trial hypocenter.
- Figure 2. Cross-shaped array with a 2-fold symmetry axis about the epicenter.
- Figure 3. Elements of the pseudoinverse of A for a cross-shaped array with 20 stations in each leg and one above the epicenter. The medium is a half space with $V = 6.0$ km/sec. Elements are organized by row and sorted by epicentral distance for a) origin time perturbation, b) depth perturbation, and c) magnitude of the epicentral perturbation. Hypocentral perturbations are formed by summing the product of the travel time residual and the appropriate sensitivity function.
- Figure 4. Elements of the pseudoinverse of A for hypocenters at various focal depths in a half space velocity model. The station array is the same as that used to construct figure 3. Elements of A are shown for a) origin time perturbation, b) depth perturbation, and c) total epicentral perturbation.

Figure 5. Elements of the pseudoinverse of A for hypocenters at various focal depths in a layer-over-a-half-space velocity model. Velocity increases from 4 km/sec to 6 km/sec at 8 km depth. Elements of A are shown in the same format as figure 4.

Figure 6. Travel time surface (a) and its partial derivatives (b,c) corresponding to the elements of A^+ shown in figure 5.

Figure 7. Example of sensitivities from an irregular network for which the decoupling conditions (4.1) are not satisfied. Elements of the pseudoinverse of A for origin time, depth, and total epicentral perturbations are shown in a, b, and c, respectively.

Figure 1.

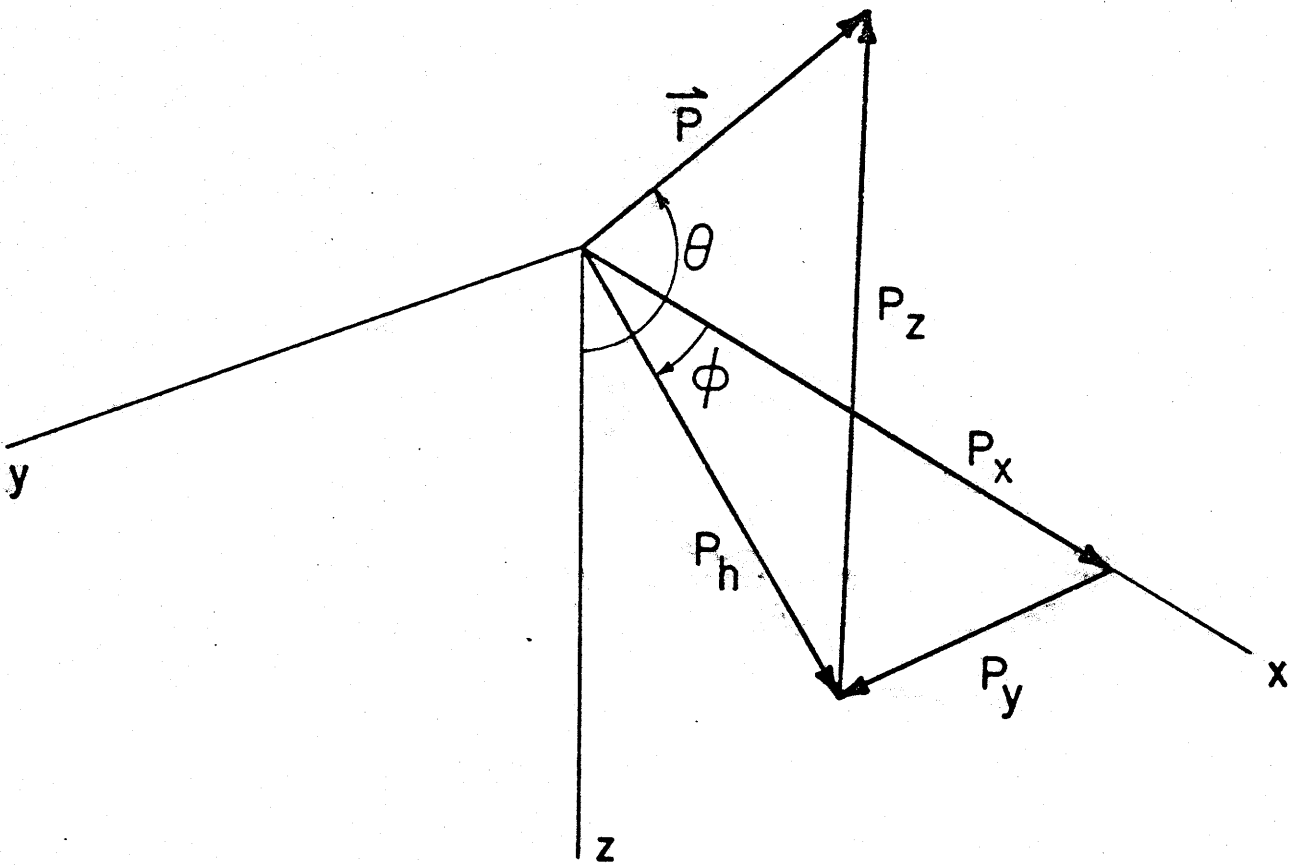
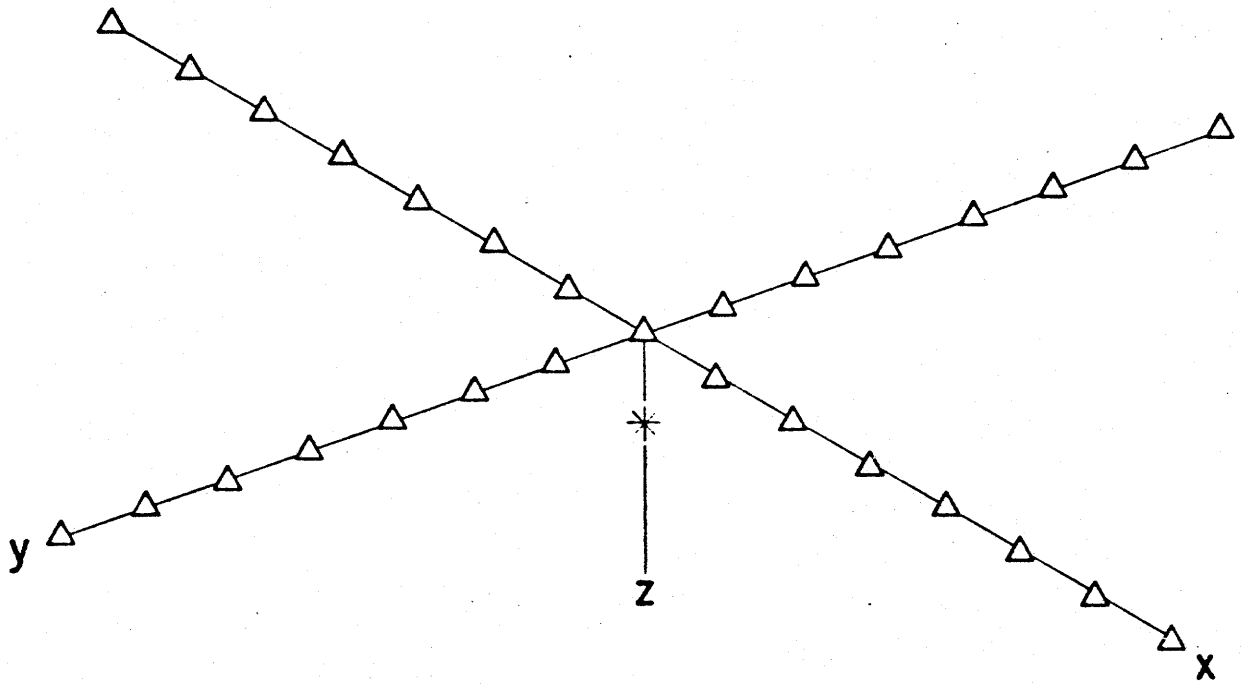


Figure 2.



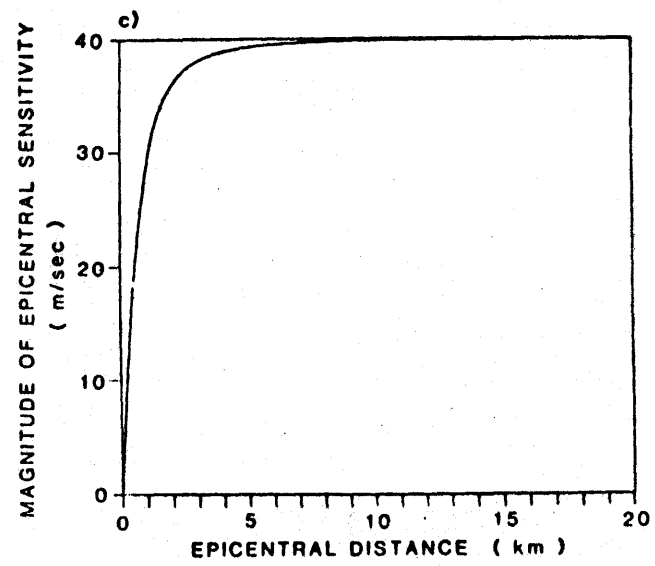
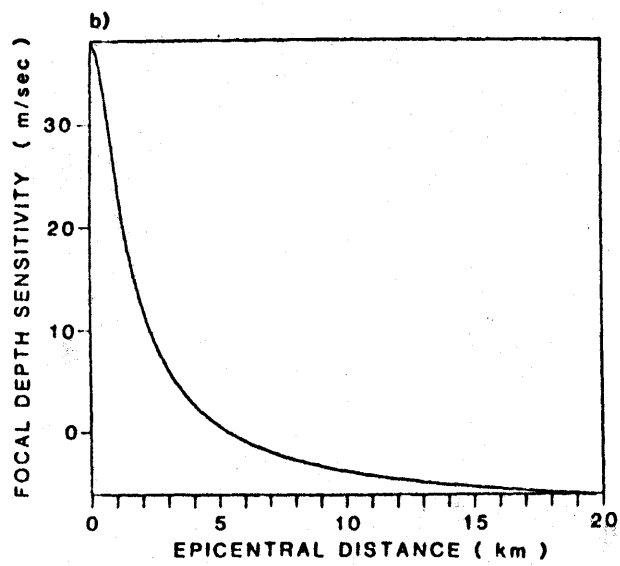
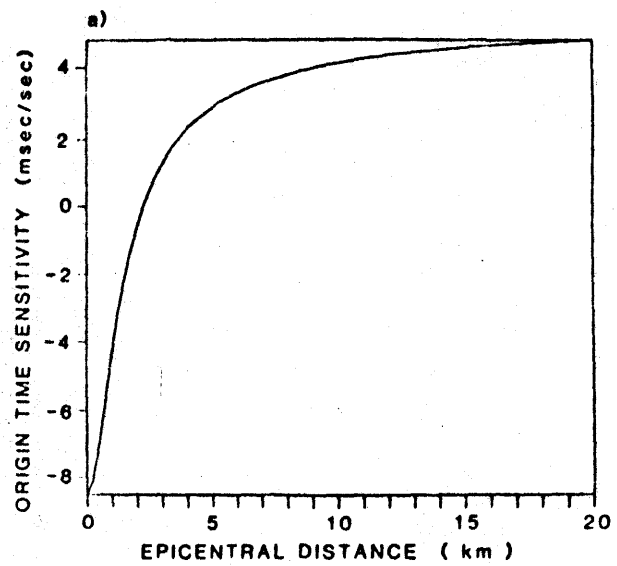


Figure 3.

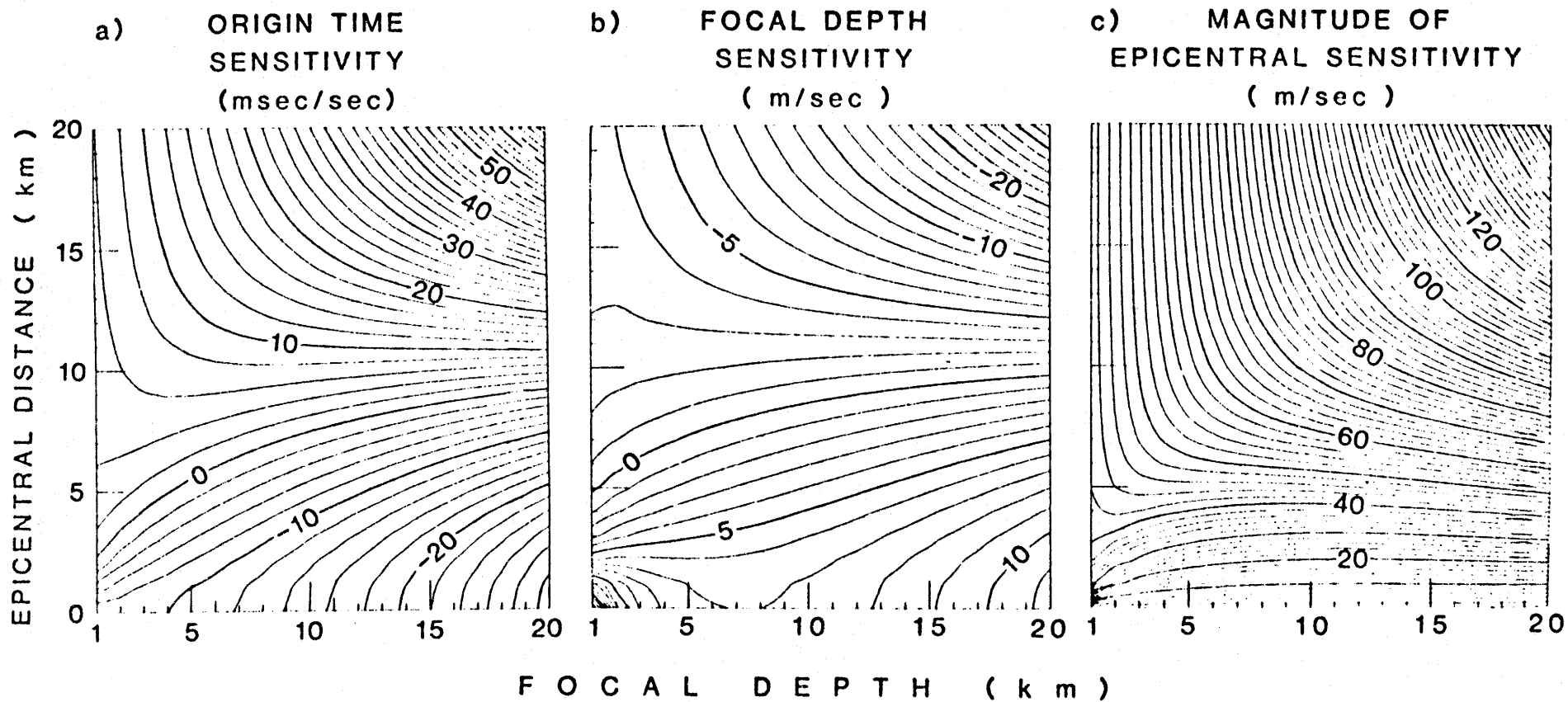


Figure 4.

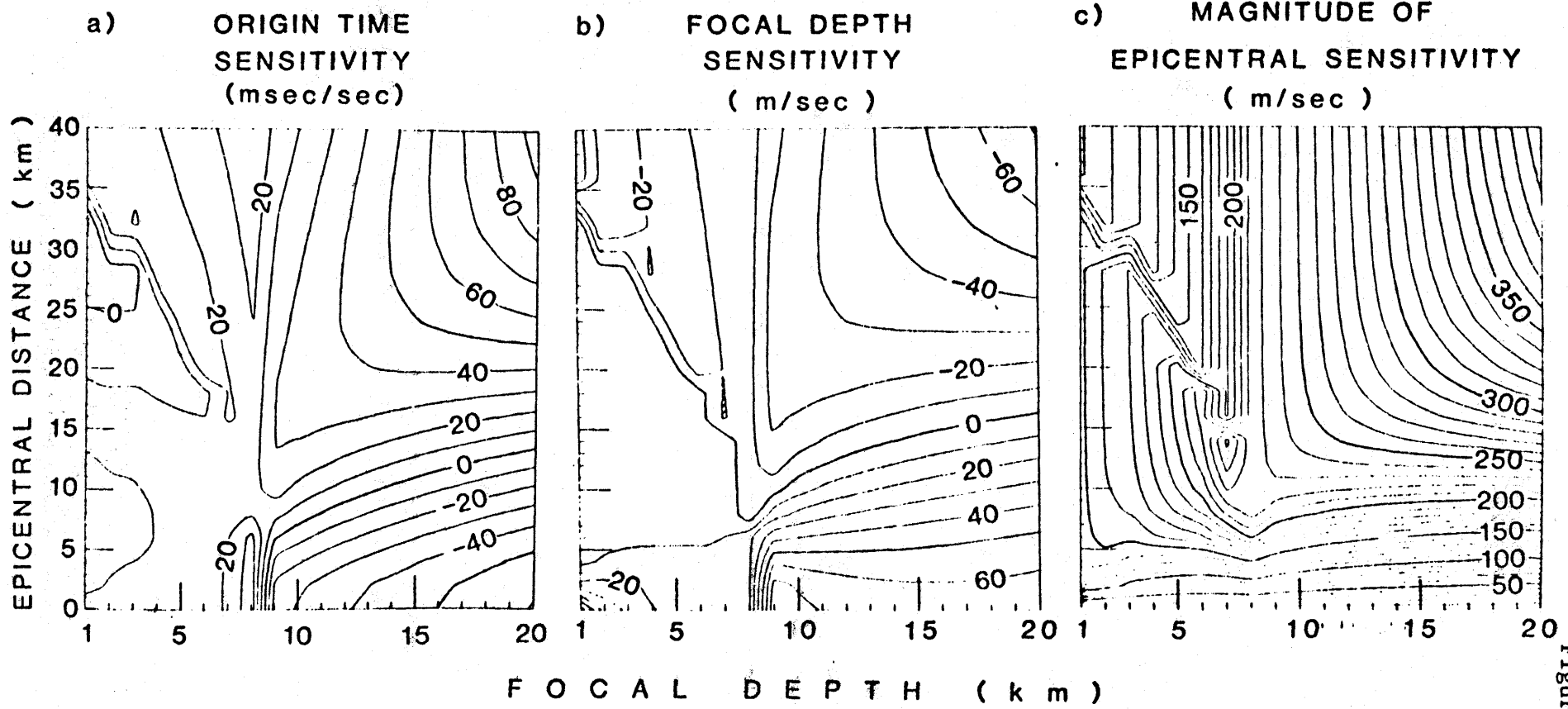


Figure 5.

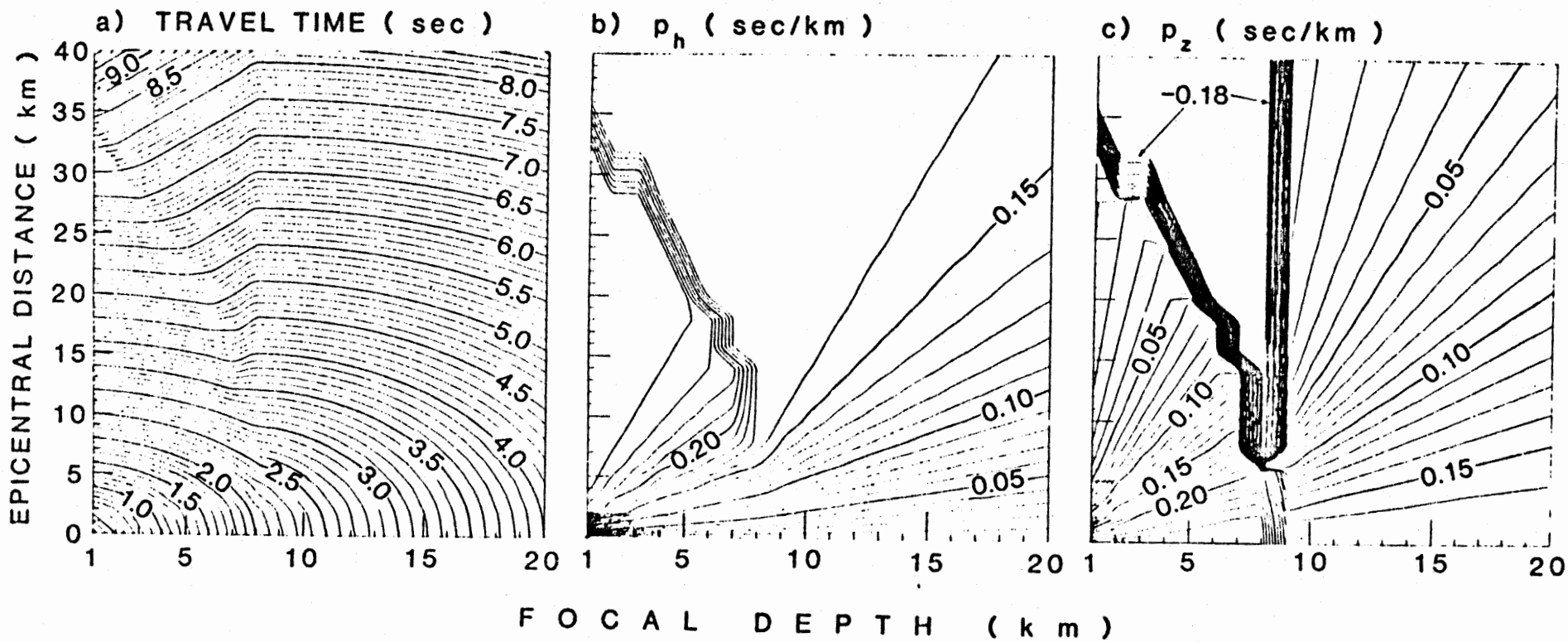


Figure 6.

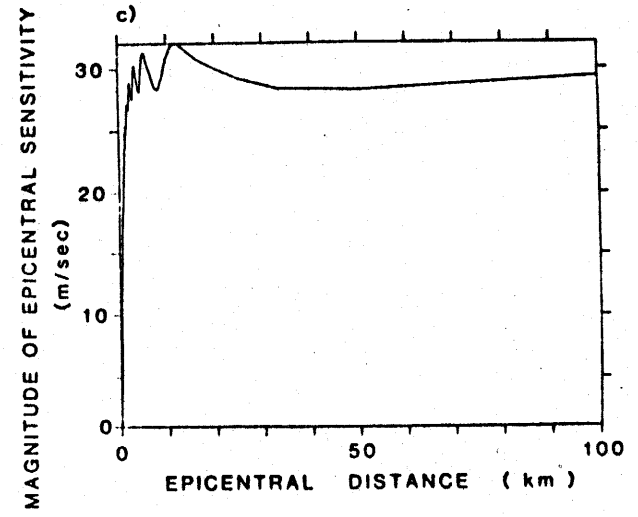
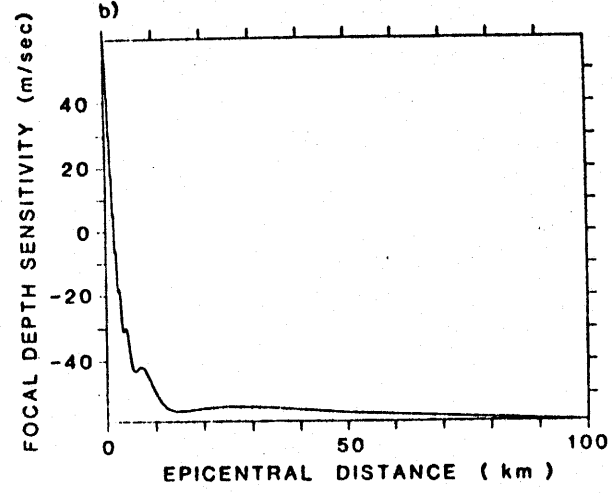
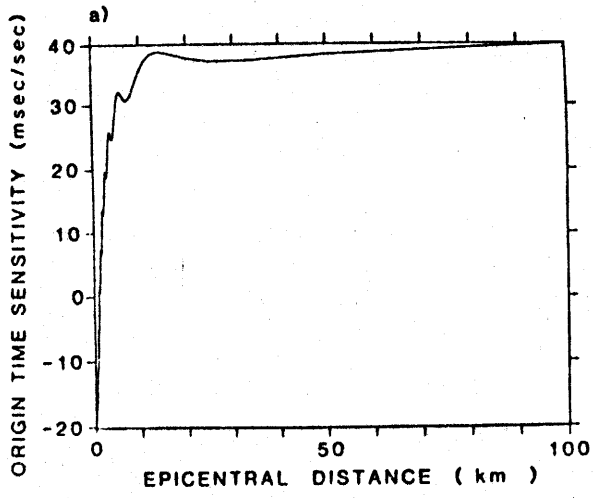


Figure 7.

CHAPTER V

"You don't have to buy, just have a look"

- Chicken Street shopkeeper

Estimates of Q in central Asia as a function of
frequency and depth using the coda of locally
recorded earthquakes

S.W. Roecker, B. Tucker, J. King, and D. Hatzfeld

MIT, UCSD, and Grenoble

ABSTRACT

Digital recordings of microearthquake codas from shallow and intermediate depth earthquakes in the Hindu Kush region of Afghanistan were used to determine the attenuation factors of the S wave coda (Q_c) and of primary S waves (Q_β). An anomalously rapid decay of the coda shortly after the S wave arrival, observed also in a study of coda in central Asia by Rautian and Khalturin [1978], seems to be due primarily to depth dependent variations in Q_c . In particular, we deduce that the the average Q_c in the crust and uppermost mantle (< 100 km depth) is approximately four times lower than in the deeper mantle (< 400 km depth) over a wide frequency range (0.4-24 Hz). Further, while Q_c generally increases with frequency at any depth, the degree of frequency dependence of Q_c depends on depth. Except at the highest frequency studied here (~48 Hz), the magnitude of Q_c at a particular frequency increases with depth while its frequency dependence decreases. For similar depths, determinations of Q_β and Q_c agree, suggesting a common wave composition and attenuation mechanism for S waves and codas.

Comparison of these determinations of Q_c in Afghanistan with those in other parts of the world shows that the degree of frequency dependence of Q_c correlates with the expected regional heterogeneity. Such a correlation supports the prejudice that Q_c is primarily influenced by scattering and suggests that tectonic processes such as folding and faulting are instrumental in creating scattering environments.

INTRODUCTION

The successful interpretation of the high frequency seismograms of microearthquakes can provide a wealth of information about the earth, if only because the quantity of data that can be gathered in a given space and time far exceeds that provided by large events. However, there is a major difficulty in using high frequency data, namely their sensitivity to details in the earth's structure. Accordingly, any model which explains a high frequency seismogram exactly requires too many parameters to be useful. One can reduce the number of parameters by assuming stochastic processes and considering the average behavior of the seismogram over certain intervals of time. As a result of this averaging, deterministic considerations must be simple, since we do not yet understand how to decouple deterministic and stochastic processes of a medium. For the analysis of the data to remain practicable with stochastic modeling, the earth model is homogeneous, in the sense that the medium is assumed to be filled with randomly distributed inhomogeneities.

In general, the behavior of the seismic coda is described by the average decay of the envelope of a seismogram, rather than by the amplitude of a particular arrival. The results of several investigators [Aki(1969,1980a,1980b), Aki and Chouet(1975), Chouet(1976,1979), Dainty and Toksoz(1977,1980), Herrmann(1980), Kopnichev(1975), Nakamura(1976), Rautian and

Khalturin(1978), Sato(1977a, 1977b,1978), Tsujiura(1978)]* confirm that the envelope of the coda can be adequately explained by the scattering of primary elastic waves in a random medium. In this paper similar explanations of the coda envelopes are used to determine the attenuation properties of the crust and upper mantle of the Hindu Kush region of central Asia, using digital recordings of microearthquakes in that area.

* Because of repeated referencing, Aki and Chouet[1975] will hereafter be referred to as AC75, Rautian and Khal-turin[1978] as RK78, and Sato [1977a] as S77.

DATA

Between June 11 and July 13 of 1977, 11 smoked paper recorders and 4 digital event detector recorders were deployed around the Hindu Kush mountains of northeastern Afghanistan (figure 1). The earthquake locations and fault plane solutions derived from the analogue data in this and in similar investigations were discussed in detail by Chatelain et al. [1977,1980], Prevot et al.[1980], and Roecker et al.[1980].

Each digital station was equipped with four Soviet S5S seismometers (one high gain for each component and one vertical low gain). The seismometers had a natural period of four seconds, and, for an intermediate period seismometer, proved to be exceptionally stable in field conditions. During the investigation, the integrity of each seismometer was checked by recording an automatic calibration pulse every 16 hours and maintained by regular manual adjustments. The recorders were of the event detector type described by Prothero[1976]. Before being recorded, the signal from each seismometer was passed through a preamplifier (20 or 40 db) and an amplifier (52 or 58 db), digitized at 128 samples per second, and multiplexed. The response of the amplifier was modified by a 3 pole, low-pass, antialiasing filter with a corner frequency of 32 Hertz. The response of the entire system is shown in figure 2. When the signal exceeded the pre-set trigger level, one second of data preceding the triggering

signal were recorded.

Our choices of trigger level and run time (32 seconds), dictated by the frequency that stations were serviced (once every two days) and by the length of recording tape, create a bias in the data collected. First, the magnitude of the recorded events, with the exception of a few local earthquakes, is usually greater than 3 (Table 1). Therefore, any interpretation of the data is biased towards larger events. Second, and more important, the limitations on the length of the data sample, determined indirectly by the trigger level and the run time, often meant that distant events were recorded for less than twice the S travel time. As discussed later, this places restrictions on models for the generation of the coda.

All of the seventy five earthquakes recorded digitally were located using the arrival times on smoked paper records (figure 3, Table 1). For the purpose of analyzing the coda, either the east-west or north-south component was selected depending on the quality and regularity of their automatic calibration pulse responses before and after the event of interest. cursory inspection of records indicated that the coda of a given earthquake had approximately the same appearance on all components, but no quantitative assessment of similarity was attempted. The recordings selected were band pass filtered (high passed and then low passed) in the time domain in 8 bands (figure 4, Table 2), using a 6 pole, phase free, Butterworth filter. RMS

amplitude values for points in time windows were determined from the data in each band (Table 2). The length of the time windows were chosen to smooth out irregularities in the amplitudes of the arrivals. The starting point was chosen at some point after the S arrival where the amplitude appeared to decay monotonically. The resulting values were corrected for instrument response using the response at the center frequency of the bandpass, although this step was not necessary for the analysis presented in this paper.

ANALYSIS

Models of Coda Generation

At present, models for the generation of the coda generally fall into one of two extreme categories: the diffusion or strong scattering models and the single or weak scattering models. Recently, Dainty and Toksoz[1980] have argued that diffusion models may not be appropriate for earthquakes, since the observed diffusion rise times (i.e. time from the onset of the P wave to the seismogram's maximum amplitude) are much shorter than the theory predicts. AC75 derived a usable single scattering model which predicts a time dependence for coda amplitudes as

$$A(\omega;t) = c(\omega)t^{-1} \exp(-\omega t/2Q_c) \quad (1)$$

where $\omega = 2\pi f$ is the angular frequency and the -1 power of time is for body wave scattering. The term $c(\omega)$ is usually called the "coda source factor" and is related to the earthquake source spectrum. This derivation assumes that the source and receiver are at the same point, which is a good approximation for signals recorded long after the primary arrival. However, when one is restricted, because of short recording times, to signals near the S arrival, the separation of source and receiver must be taken into account. Such a separation is included in the single scattering model developed by S77. Below we briefly review the derivation of this model and then test its applicability

to our data.

Imagine a source and a receiver imbedded in an infinite medium populated by a random distribution of scatters of number density (per unit volume) N and crosssectional area σ . The product $N\sigma$ is called the turbidity and is equivalent to $g(\theta)$ derived by Chernov[1960], where θ is the angle between the incident and scattered waves. In the analysis of S77, the θ dependence is ignored by assuming isotropic scattering. Energy observed at the receiver at a given time after the S wave is the sum of energy scattered by inhomogeneities on the surface of an expanding ellipsoid whose foci are the source and receiver (figure 5). From this sum, S77 obtained the following expression for the mean energy density of the scattered body waves:

$$E_s(r,t|\omega) = \frac{N\sigma W_o(\omega)}{4\pi r^2} K(\alpha) \quad (2)$$

where

$$\alpha = t/t_s$$

$$t_s = S \text{ travel time}$$

$$r = \text{source-receiver distance}$$

$$K(\alpha) = \frac{1}{\alpha} \frac{|\alpha+1|}{|\alpha-1|}$$

$$W_o(\omega) = \text{total energy radiated by the source within a unit angular frequency band}$$

The earthquake source in this derivation is a point which radiates isotropically and instantaneously. The analysis of

S77 is for body waves and therefore for 3 dimensional geometric spreading. Although the derivation of E_s for surface waves is straightforward, most of the events recorded in the Hindu Kush are deep and local and therefore the application in this paper assumes only body wave type scattering.

One observation concerning this analysis may be made here for clarity. As a wave travels a distance x through a random medium, the energy in the wave decreases as $e^{-x/L}$, where L is the mean free path and is the reciprocal of the turbidity (see Chernov [1960] for details). In his analysis of singly scattered waves, S77 assumed that $x \ll L$, and therefore could neglect this decay term. (This is the Born approximation, since the primary wave is not dissipated). However, his estimate of 100 km for L in Japan [Sato, 1978] suggests that x and L are of similar magnitude, so that ignoring the decay term is probably not justified. It is simple to show that leaving the $e^{-x/L}$ term in the analysis results in the multiplication of (2) by $e^{-vt/L}$. Usually, [e.g. AC75; Sato, 1978] factors like e^{-bt} ($b = u/Q_i$) are included only subsequent to the analysis of scattering effects to allow for intrinsic attenuation. Note that since we now determine $b = u/Q_i + v/L$ instead of u/Q_i alone, it is not obvious how to separate "intrinsic $Q (Q_i)$ " from "scattered $Q (Q_s = uL/v)$ " by using only the decay of the coda. This should be kept in mind when one is trying to interpret Q_c values in cases where Q_i and uL/v are of similar

magnitude or in cases where an accounting of the energy radiated cannot be made.

To relate (2) to the data, we use the relations suggested by AC75 for band-passed signals:

$$A(r, \omega | t) = [2P(r, \omega | t) \Delta f]^{1/2} \quad (3)$$

$$E_s(r, \omega | t) = \rho \omega^2 P(r, \omega | t) \quad (4)$$

where $P(r, \omega | t)$ is the coda power spectral density, Δf is the bandwidth, ρ is the density, and $A(r, \omega | t)$ is the RMS amplitude. Combining these relations with (2) gives

$$A(r, t | \omega) = \left[\frac{2W_o(\omega) \Delta f}{4\pi \rho \omega^2 L} \right]^{1/2} \left[\frac{K(\alpha)}{r^2} \right]^{1/2} e^{(-\omega t / 2Q_c)} \quad (5)$$

$$= C(\omega) k(r, \alpha) e^{-bt}$$

where $b = (\omega / Q_i + v/L) = \omega / Q_c$. Taking the logarithm of (5) gives

$$\log_{10} A_c(r, t | \omega) = \log_{10} C(\omega) - b(\log_{10} e) t \quad (6)$$

where $A_c(r, t | \omega) = A(r, t | \omega) \left[\frac{r^2}{K(\alpha)} \right]^{1/2}$ is the corrected amplitude. The factor 'b' is then determined by a least squares fit of $\log_{10} A_c(r, t | \omega)$ versus t from (6).

Regional Considerations

The coda is comprised of waves scattered in an expanding, ellipsoidal volume and therefore represents an average over a large region. (This averaging quality is the

usual explanation for the similarity of the codas of different events at a given station.) Since we are using relatively short recording intervals and widely distributed earthquakes (400 km in breadth and 300 km in depth), the regions sampled by codas often do not overlap significantly. For this reason, different zones of activity were defined (figure 1, Table 3) and the extent of sampling by the coda of earthquakes in these various zones was examined.

For small α , the shape of the expanding ellipsoid is difficult to describe, but it can be characterized approximately by two parameters (figure 5) : $H = D(\alpha^2 - 1)^{1/2}/2$, and $Z = D\alpha/2$, where D is the distance from source to receiver. For an event directly beneath a station, H is the extent of horizontal sampling and Z is the extent of vertical sampling (Note that as α increases, the sampled region approximates a sphere of radius $D\alpha/2$). This description becomes more complicated when the event is not directly beneath the station. Representative plots of the sampled regions are shown in both horizontal and vertical cross-section in figures 6 and 7. Combining the information on these plots with a knowledge of the variation of α for the different zones (Table 3) will describe the regions actually sampled. To a good approximation, codas from earthquakes in the same zone sample the same region at a given α .

DETERMINATION OF Q_c

In a previous study of the behavior of coda in central Asia, RK78 overlaid the peaks of arrivals following the S wave from many events recorded at Garm, Tadjikistan (39°N , 70.8°E). For travel times longer than twice the S travel time, they observed that the decay of the peaks of the coda was very regular from one event to another within each frequency band. RK78 were able to fit all of these data with simple curves of a form similar to that described by (1). For data arriving before twice the S travel time, however, there was a more rapid decay. In the data discussed here an initial rapid decay is also often observed. Such behavior is qualitatively consistent with the corrections represented by the $K(\omega)$ function, which contains a singularity at the S wave travel time and becomes asymptotic to the smoother t^{-1} behavior proposed by AC75 for the coda after $2*t_s$ (see figure 2 of S77). In fact, data taken from the curves in figure 7 of RK78 agree fairly well with Sato's theoretical decay.

Even after taking the $K(\omega)$ decay into consideration, however, the coda decays more rapidly at the beginning than at the end (figure 8). Values of Q_c generated by fitting (6) to windows of data 40 seconds long (figure 9) quantify this observation. The increase of Q_c with travel time is indicated by the decreasing rate of decay of the coda with time. In the following, we examine the possibility that

this residual rapid initial decay is due to the inadequacies of some explicit or implicit assumptions of the model.

Sato's model neglects the effects of the free surface, directional scattering, multiple scattering, and regionally varying properties. While all these effects are difficult to evaluate quantitatively, but useful bounds can be estimated for the first two. The question is whether the neglect of any of these effects can cause the observed variations of Q_c of about a factor of ten at low frequencies (see "E" in figure 11) We shall see that the neglect of regionally varying properties plays the key role in causing the initial rapid decay.

Free Surface

S77 neglects the free surface by assuming an infinite medium when a half-space is more realistic. For simplicity, let us assume that, after reaching the surface, energy is either completely attenuated, due to some anelastic behavior at near-surface, or totally reflected without change of phase. In the case of total energy attenuation the problem can be solved exactly. Since $K(\alpha) = \int \frac{\sin \eta}{\alpha^2 - \cos^2 \eta} d\eta$ (S77), we can derive $K(\alpha)$ for those values of η (figure 5) corresponding to rays confined to the subsurface. For a source directly beneath the station the integration limits are from $\cos^{-1}(1/\alpha)$ to π , and the half space correction is

$$K_H(\alpha) = \frac{1}{2\alpha} \ln \left| \frac{\alpha^2 + 1}{(\alpha - 1)^2} \right| \quad (7)$$

As shown in figure 10, the decay predicted by (7) is faster than for an infinite medium (by $K_I(\alpha)$). To compare the values of Q_c predicted for the half space (Q_H) with those for the infinite medium (Q_I), we examine (from (6))

$$\frac{Q_H}{Q_I} = \frac{\Delta \log_{10} A - \Delta \log_{10} K_I(\alpha)^{1/2}}{\Delta \log_{10} A - \Delta \log_{10} K_H(\alpha)^{1/2}} \quad (8)$$

Typically, $\Delta \log_{10} A \sim 1.0$ between t_s and $2*t_s$. This gives

$$\frac{Q_H}{Q_I} \sim 1.03$$

which is much smaller than the observed change in Q_c with time. Therefore, although our assumption of an infinite medium may overestimate the later arriving energy (by a factor of 2 when $t \gg t_s$), the rate of decay is underestimated only slightly.

In the case of perfect reflection with no phase change, the problem is does not depend on the relative position of source and receiver, so the $K(\alpha)$ corrections for the half space and the infinite space are the same. It should be noted for later discussion that in this case the sampling is initially biased towards the near surface, since it is essentially being sampled twice. In the case where converted phases result on reflection, energy will be concentrated in the initial part of the coda, because the resulting scattered P to P energy will arrive earlier than the S to S energy. The effect of phase conversion is difficult to estimate, but, since SV to P conversion is significant only

over a small range of incidence angles (approximately 15 to 30 degrees), we will assume it is small.

Directional Scattering

Most of the energy of the early part of the coda has been scattered in the forward direction, while that of the later parts has been backscattered; the proportion of backscattered to forward scattered energy increases with time. In order to estimate the effect of ignoring directionally dependent scattering on the decay of coda, let us examine an extreme case where the energy changes from being completely forward scattered to completely back scattered within t_s and $2*t_s$.

Our stochastic model of the earth contains inhomogeneities that can be described by a slowness fluctuation function $\langle \mu(\xi) \rangle$, where ξ is a point in space relative to the origin. We can describe the magnitude and smoothness of $\mu(\xi)$ by examining the spatial autocorrelation function $N(\xi - \xi_1) = \langle \mu(\xi) \mu(\xi_1) \rangle / \langle \mu^2 \rangle$. Assuming different forms for $N(r)$ ($r = \xi - \xi_1$), Chernov [1960] gives the following formulas for directionally dependent turbidity:

$$g(\theta) = \frac{8k^4 a^3 \langle \mu^2 \rangle}{(1 + 4k^2 a^2 \sin^2 \frac{\theta}{2})^2} \quad \text{for } N(r) = e^{-r/a} \quad (9)$$

and

$$g(\theta) = \pi^{1/2} k^4 a^3 \langle \mu^2 \rangle \exp(-k^2 a^2 \sin^2 \frac{\theta}{2}) \quad \text{for } N(r) = e^{-r^2/a^2} \quad (10)$$

where θ is the angle between the incident and scattered waves, $k = 2\pi/\lambda$ is the wavenumber, a is the correlation distance, and $\langle \mu^2 \rangle$ is the mean square slowness fluctuation. For $ka = O(1)$, these two estimates of turbidity imply differences in the ratio of forward to back scattered energy (from (2) where $g = N\sigma$) of 9 and 25. In the extreme case of $g(0)/g(\pi) = 25$, the ratio of directionally corrected Q (Q_d) to the isotropic Q (Q_p) is (since $\Delta \log_{10} g^{1/2} = 0$ for the isotropic case)

$$\frac{Q_d}{Q_p} = \frac{\Delta \log_{10} A_c}{\Delta \log_{10} A_c - \Delta \log_{10} g^{1/2}} \approx 3.3 \quad (11)$$

which is substantial but still somewhat less than the differences among the estimates of Q_c made at low frequencies. This analysis is not carried further (in the form of deriving an additional correction), however, because the spatial autocorrelation functions which Chernov assumed to derive $g(\theta)$ may not be appropriate here (see Flatte et. al., 1979, for a discussion on alternative correlation functions).

Multiple Scattering

The evaluation of multiple scattering effects is even more difficult than that of the above effects, as witnessed by the prevalence of single scattering models. To give a gross estimate of the adequacy of single scattering models, one needs estimates of σ , an indicator of the strength of an individual scatterer, and of N , an indicator of the amount

of scattered energy to be summed. Since only the product $N\sigma$ can be determined in this analysis, even these estimates are beyond our reach. It is encouraging that data can be fit by single scattering models for regions where $N\sigma$ is small ($\sim 0.01 \text{ km}^{-1}$ for Japan, Sato[1978]), but this by no means proves the adequacy of single scattering models.

Regional Variations

We note that equation (6) fits the individually windowed data quite well (less than 20% error for most events, see figure 9), suggesting that our stochastic model is sufficient on a geographically small scale. This, to some extent, makes the consideration of more complicated models superfluous. In examining the differences between Q_c determinations in the various windowed data, it is instructive to consider how this time dependent decay can be explained by regional sampling.

Comparing Q_c values determined by least squares fitting all the available data in a zone, one finds a strong correlation between the recording time (as parameterized by α_{max}) and Q_c . For instance, Q_c values at low frequencies at all stations for region 'b', at stations JOR and PEN for region 'c', and at CHS and JOR for region 'E', are determined with short samples of data and are notably smaller than those determined with longer samples (Table 3, figures 11b, 11c). Such behavior can be explained by an increase of Q_c with depth, but, since these shorter sampling

intervals are frequently less than $2*t_s$, the effects discussed above provide equally viable explanations.

The choice of explanations is narrowed by a determination of Q_c from a group of crustal events (31,42,51,64,67,69,70) which occurred near station PEN. Because of these events' proximity to the station, the recording time was several times the S travel time, and therefore the effects of all the model deficiencies (except perhaps multiple scattering, about which we know little) are reduced. The relatively low values of Q_c determined from these events, even for large values of Q_{max} ('cr' in figure 11 and figure 12), imply that Q_c at shallow depths is small. An increase in Q_c with depth would also account for the rapid initial decay of coda from deeper events. We infer, therefore, that the variation between the initial and later decays of the coda is due to a Q_c that varies with depth.

DETERMINATION OF Q_{β}

Recently, Aki[1980a] proposed a method to determine Q_{β} by comparing S and coda amplitudes of events at different distances from the observer. After being adjusted to allow for the separation of source and receiver, Aki's equation becomes :

$$\left\langle \ln \left| \frac{A_i(\omega, D)}{A_c(\omega|t_o, D)} \right| \right\rangle_{D+\Delta D} = \left\langle \ln \left| \frac{S_i(\omega, \theta)R(\omega, \theta)}{S_i^c(\omega)R^c(\omega)P_c(\omega|t_o, \alpha)} \right| \right\rangle - BD \quad (12)$$

where

$\langle x \rangle_{D+\Delta D}$ = average of x within a distance range of $2\Delta D$ centered at D

D = source-receiver distance

θ = source-receiver orientation

$S_i(\omega, \theta)$ = source spectrum of the event

$S_i^c(\omega)$ = coda source spectrum

$R(\omega, \theta)$, $R^c(\omega)$ = receiver site effects for S wave and coda

$A_i(\omega, D)$ = spectral amplitude of S wave

$A_c(\omega|t_o, D)$ = corrected (eqn 6) amplitude of coda at a fixed time t_o

$P_c(\omega|t_o, \alpha)$ = corrected coda power spectra = $P(\omega|t_o)/(K(\alpha))^{1/2}$

$$B = \frac{\omega}{2Q_{\beta}v}$$

Q_{β} is determined by a least squares fit of (12). One major assumption in the derivation of this equation is that averaging over a number of S waves from events at different azimuths in a particular distance range diminishes radiation pattern and directionally dependent station site effects.

This assumption, along with the choice of a value for t_0 , makes the second term in the equation a constant and leaves a linear relation between measured amplitudes and distance. To determine Q_β for the Hindu Kush, the t_0 chosen for the coda amplitude was 75 seconds, basically because data existed for most of the events out to this time and because the differences in Q_c for longer durations made extrapolation to later times unreliable.

Unfortunately, there were many fewer usable S waves than codas, primarily because large events were clipped and often the first two seconds of the record (which sometimes contains the S arrival) were lost. In addition, because stations CHS and PEN were far from most of the events, reasonable distributions of events with distance could be obtained with recordings at stations JOR and FAR. Even so, events were not distributed evenly with distance from these stations, but instead tended to be clustered. Therefore, in dividing the events by distance, there was some irregular spacing. Events were usually divided into intervals of ± 15 km about the center of a cluster.

The results of this analysis justify many of our assumptions. First, a linear relation consistent with (12) could be determined (figure 13) with an acceptable variance (<50%), even though a small dataset was used. Second, the values of Q_β determined from this method at the two stations for given frequencies agree quite well (figure 14), so that the assumption that receiver and source effects were

averaged out is probably reasonable. (Coda amplitudes corrected for $K(\alpha)$ and distance usually showed very little difference from one station to another, so site effects apparently did not modify the data significantly.) Third, Q_{β} is indistinguishable (at one standard deviation) from Q_c determined for $t < 2*t_s$ (figure 14), suggesting that the coda consists of S waves and that the mechanisms of attenuation for S waves and coda are similar (this is a fundamental assumption in the preceding analysis of the coda). Therefore, Q_c at shallow depths represents an average of Q_{β} over the same depths. This result is in accordance with the results of studies (Aki [1980a, 1980b]) that used this method to determine Q_{β} in Japan.

DISCUSSION

Depth Dependent Q_c

In this paper we assert that simple deterministic dependencies of Q_c (in our case, a depth dependence) can be made evident by considering the regions sampled by the coda. In their study of coda in central Asia, RK78 determined that $Q_c(f) = 360(f)^{1/2}$ for travel times between about 20 and 200 seconds and $Q_c(f) = 900(f)^{1/2}$ between 200 and 2000 seconds. The first relation indicates a similar, although somewhat weaker, frequency dependence for Q_c than determined in this paper for deeper regions over a wide frequency range ("ALL" row in figure 11). Given the distance (~400 km) and travel times (~200 seconds) of most Hindu Kush events from the Garm observatory, the depths sampled (~400 km) are similar to those in this study. Similarly, the second relation, determined with travel times an order of magnitude larger, represents sampling to depths to approximately 1000 km. Combining these results, we can estimate an average Q_c structure from the crust to well into the mantle for central Asia (figure 15). Note that while Q_c generally increases with depth, the frequency dependence decreases from $\sim f^{1.0}$ for depths to about 100 km to $\sim f^{0.75}$ for depths to about 400 km to $\sim f^{0.5}$ for depths to about 1000 km.

The relatively low Q_c at shallow depths, deduced here for Afghanistan, may be evident in other areas of the world as well. RK78 also observed a divergence in the decay of

the coda of local events (the 'b' leg in their paper) that would correspond to such an effect in the crust and uppermost mantle of Tadjikistan. The frequency dependence of the Q_c determined by their 'b' leg is strikingly different from that determined from later arrivals (see figure 11 of RK78), and again the Q_c values are much smaller than those deduced from more distant events.

One may infer from the published data of Sato [1978] that a depth dependent Q_c may also be appropriate for Japan. Averaging over the entire coda, Sato determined a relation which shows the mean free path (or, equivalently, Q_c) increasing with magnitude of the event. Since larger earthquakes enable longer recording times and therefore deeper sampling, and since the contribution at shallow depths becomes less significant with time, averaging over the whole coda would produce this result if Q_c increased with depth. Figure 3 of Sato [1978] shows that the decays of the codas at the beginning of the M4.7 and M3 events in Japan are similar. Since most of these events occur at similar depths, which implies that depths sampled by scattered waves from these events at a given time will be similar, the resemblance of the early parts of the codas from different magnitude events is probably a reflection of the similarity of the sampled regions. Differences between the early and late parts of the coda of larger events therefore suggests that a depth dependent Q_c exists in Japan.

Relation of Q_c to Tectonics.

Aki [1980] reviewed results from Japan, California, Hawaii, central and eastern U.S., and Kamchatka, and noted that Q_β^{-1} values tended to converge at high frequencies (~ 20 Hz) and diverge at low frequencies (~ 1 Hz). The degree of divergence correlated to what he called the tectonic "intensity" of the area. These results, along with those of RK78 and this study, are replotted in figures 16 and 17. (Note that "convergence at high frequencies" for Q^{-1} generally means that Q increases with frequency and that $Q > 400$ for frequencies greater than about 12 Hz.)

Two correlations are apparent in figure 17. One is between the magnitude of Q_c and depth. For example, the values of Q_c determined from stations using only crustal events (PEN in Afghanistan, PAC in California, OTL in Hawaii, and OIS in Japan) are consistently lower than those using events whose codas sample deeper mantle (TSK in Japan and at 400 kms (CA400) and 1000 kms (CA1000) depth in central Asia). The other correlation is between the degree of frequency dependence of Q_c and the heterogeneity of the region. For example, the crust beneath PEN, the station with the strongest frequency dependent Q_c determination, is very thick (~ 70 km, Krestnikov and Nersesov, 1964) and is the site of an ongoing continental collision. Stations PAC and OIS, whose Q_c determinations are less frequency dependent than those of PEN, are located on crusts of normal

thickness. In addition, these crusts are probably folded and faulted to a lesser degree than the crust of central Asia. Finally, OTL, whose Q_c determination is practically independent of frequency, is located on a thin (~12 km) oceanic crust which implies that the coda samples the more homogeneous mantle shortly after the S arrival.

The correlation between the frequency dependence of Q_c and heterogeneity extends into the mantle if we argue that the earth becomes more homogeneous with depth due to factors such as closure of cracks with increased pressure and assimilation of small scale heterogeneities with increased temperature. The correlation between frequency dependence and depth is evident when one compares the results at PEN, CA400, and CA1000, since, as mentioned above, the degree of frequency dependence for Q_c in central Asia decreases as depth increases (figure 15).

In attempting to further relate the Q_c structure of central Asia to its tectonics, we are hampered by the fact that Q_c is a combination of two the intrinsic Q , Q_i , and the scattering Q , $Q_s = \omega L/v$. Because of the conceivably great differences in attenuation mechanisms associated with these two parameters, physical interpretations of Q_c are tenuous. Still, one at least can deduce some bounds on these quantities. Note that since $Q_c = Q_i Q_s / (Q_s + Q_i)$, Q_c is a minimum value for Q_i and Q_s . Also, as Q_i approaches infinity, vQ_c/ω becomes the minimum mean free path (L_{\min}). Note that L_{\min} is practically constant over a wide frequency

range (1.5 - 48 Hz) at shallow depths (figure 18).

Because of the association of "heterogeneity" with "scatterers", the correlation between characteristics of Q_c and the expected degree of heterogeneity lends support to the prejudice of other studies [Aki 1980a, 1980b] that Q_s is the dominant attenuation parameter in the frequency range of 0.3 to 48 Hz. This is an important consideration for the interpretation of Q . For example, since Q traditionally has been viewed as Q_i , i.e., as a measure of the conversion of seismic energy to other forms of energy, Q was usually associated with easily conceived physical entities (molten blobs, sunken slabs, etc.). If one is to make similar observations with Q_s , it is necessary first to create models for the generation of scattering media.

The correlation between heterogeneity and Q_c suggests that the processes forming the various tectonic environments discussed here are instrumental in forming different scattering environments as well. For instance, the creation of oceanic lithosphere at ridges can be expected to introduce few scatterers. Similarly, processes such as strike slip faulting can create scattering environments in active areas such as Japan and California by juxtaposing cracked rocks of different seismic velocities. Finally, folding and thrust faulting can introduce large scale heterogeneities in convergent regions such as Afghanistan. We infer, therefore, that, like Q_i , the characteristics of Q_s in a region are closely tied to the tectonics of that region.

ACKNOWLEDGEMENTS

We thank J.P. Carbonnel of the Mission Geologique Francaise, J. Summers of the Afghan American Educational Commission, and R.E. Gibson, H. Hafiz, and A.S. Saleem of Kabul University for their hospitality and help in logistical and technical matters. We were ably assisted in the field by M. Frogneux, X. Goula, M. Grosenbaugh, J. Maurer, P. Molnar, R. Prevot, G. Suarez, and Afghan engineers Kandari, Osman, Rabi, and Sharif. We thank the Applied Seismology Group of the Lincoln Laboratory for allowing us to use their computing facilities for much of the analysis. We also benefitted from discussion and encouragement from Keiliti Aki, Bernard Chouet, and Anton Dainty. This research was supported primarily by NSF grants EAR76-13367A01 and EAR78-13673 (MIT), but also by contract ATP No. 35-06 of INAG (Grenoble). The MIT group's part, however, was made possible by an H.O. Wood award from the Carnegie Institution in Washington and by an Alfred P. Sloan Fellowship.

References

- Aki, K., Analysis of the seismic coda of local earthquakes as scattered waves, J. Geophys. Res. ,74, 615-631, 1969.
- Aki, K., Attenuation of shear waves in the lithosphere for frequencies from 0.05 to 25 Hz., J. Phys. Earth ,21, 50-60, 1980a.
- Aki, K., Scattering and attenuation of shear waves in the lithosphere, submitted to J. Geophys. Res., 1980b.
- Aki, K., and B. Chouet, Origin of coda waves: Source, attenuation, and scattering effects, J. Geophys. Res., 80, 3322-3342, 1975.
- Chatelain, J. L., S.W. Roecker, D. Hatzfeld, P. Molnar, and G. Perrier, Etude seismologique en Afghanistan, Premiers resultats, C. R. Somm. Soc. Geol. Fr., 5, 260-262, 1977.
- Chatelain, J. L., S.W. Roecker, D. Hatzfeld, and P. Molnar, Microearthquake seismicity and fault plane solutions in the Hindu Kush region and their tectonic implications, J. Geophys. Res., 85, 1365-1387, 1980.
- Chernov, L.A., Wave Propagation in a Random Medium, pp. 35-57, McGraw-Hill, New York, 1960.

Chouet, B., Source, scattering, and attenuation effects on high frequency seismic waves, Ph.D. thesis, Massachusetts Institute of Technology, Cambridge, MA., 1976.

Chouet, B., Temporal variation in the attenuation of earthquake coda near Stone Canyon, California, Geophys. Res. Lett., 6, 143-146, 1979.

Dainty, A., and M.N. Toksoz, Elastic wave propagation in a highly scattering medium - a diffusion approach, Jour. Geophysics, 43, 375-388, 1977.

Dainty, A., and M.N. Toksoz, Seismic codas on the Earth and the Moon: a comparison, submitted to the proceedings of the seventh general assembly of the international union of geodesy and geophysics, 1980.

Flatté, S.M., R. Dashen, W.H. Monk, K.M. Watson, and F. Zachariason, Sound Transmission through a Fluctuating Ocean, Cambridge University Press, 299 pp., 1979.

Herrmann, R., Q estimates using the coda of local earthquakes, Bull. Seism. Soc. Am., 70, 447-468, 1980.

Kopnichev, Y.F., Models for the formation of the coda part of seismograms, Acad. Nauk USSR, 222, 333-335, 1975 (in Russian).

Krestnikov, V.V., and I.L. Nersesov, Relations of the deep structure of the Pamirs and Tien Shan to their tectonics, Tectonophysics, 1, 183-191, 1964.

Lee, W.H.K., R.G. Bennett, and K.L. Meagher, A method of estimating magnitude of local earthquakes from signal durations, USGS Open-File Report, 1972.

Nakamura, Y., Seismic energy transmission in the lunar surface zone determined from signals generated by movements of lunar rovers, Bull. Seis. Soc. Amer., 66, 593-608, 1976.

Prevot, R., D. Hatzfeld, S.W. Roecker, and P. Molnar, Shallow earthquakes and active tectonics in eastern Afghanistan, J. Geophys. Res., 85, 1347-1357, 1980.

Prothero, W.A., A portable digital seismic recorder with event recording capability, Bull. Seism. Soc. Am., 66, 3, 979-985, 1976.

Rautian, T.G. and V.I. Khalturin, The use of the coda for determination of the earthquake source spectrum, Bull. Seism. Soc. Am., 68, 923-948, 1978.

Roecker, S.W., O.V. Soboleva, I.L. Nersesov, A.A. Lukk, D. Hatzfeld, J.L. Chatelain, and P. Molnar, Seismicity and fault plane solutions of intermediate depth earthquakes in the Pamir-Hindu Kush region, J. Geophys. Res., 85, 1358-1364, 1980.

- Sato, H., Energy propagation including scattering effects; single isotropic scattering approximation, J. Phys. Earth, 25, 27-41, 1977a.
- Sato, H., Single isotropic scattering model including wave conversions; simple theoretical model of the short period body wave propagation, J. Phys. Earth, 25, 163-176, 1977b.
- Sato, H., Mean free path of S waves under the Kantō district of Japan, J. Phys. Earth, 26, 185-198, 1978.
- Tsujiura, M., Spectral analysis of the coda waves from local earthquakes, Bull. Earthq. Res. Inst., Tokyo Univ., 53, 1-48, 1978.

Table Captions

Table 1. Events recorded by digital stations and located with the smoked paper records. Magnitude was determined from the formula $M = -1.47 + 2.0 \log t - 0.0035D$, where t is the signal duration and D is the source receiver separation (Lee et. al., 1972). Coefficients in the formula were calibrated by comparing some events' local signal duration magnitude with their teleseismic body wave magnitude (M_b) as determined by the United States Geological Survey (USGS).

Table 2. Frequency bands of filtered data with time window length used for averaging.

Table 3. Events located in the various zones of figure 1. T_{max}/T_s (α_{max}) is the ratio of the travel time of the last signal recorded to the S travel time. The border between "Deep" and "Shallow" zones is 150 km.

Table 1

DATE	ORIGIN TIME		LAT		LON		DEPTH (KM)	EVENT NO.	MAG
			N	MIN	E	MIN			
77 616	1616	55.26	36	31.76	70	16.13	102.26	16	3.9
77 617	8 6	32.45	35	23.30	69	28.05	1.49	18	2.4
77 617	1714	20.46	36	32.89	70	57.20	197.00	19	3.8
77 617	1930	38.16	35	43.12	69	40.23	77.98	20	3.7
77 617	22 1	47.14	36	30.00	71	14.24	112.19	21	3.6
77 618	528	43.58	34	54.80	69	55.45	1.87	23	2.5
77 618	753	35.31	34	39.56	70	34.71	1.42	24	2.4
77 618	9 3	40.71	34	34.30	72	48.84	340.70	25	5.3
77 618	1150	22.64	36	6.23	69	23.71	131.94	26	3.3
77 618	2320	3.27	35	59.24	70	38.49	112.21	27	3.5
77 620	148	49.52	36	5.63	70	26.43	98.55	28	4.3
77 620	4 5	56.23	36	7.01	70	26.17	105.32	29	4.0
77 620	1156	30.60	36	30.35	70	18.96	215.02	30	3.8
77 620	2335	16.51	35	30.68	69	3.71	2.50	31	3.1
77 621	316	2.84	36	38.92	71	18.30	98.13	32	3.7
77 621	2133	46.80	36	33.34	71	22.42	159.81	33	4.3
77 622	832	21.95	36	35.21	70	53.23	232.49	02	4.1
77 622	1430	58.92	36	10.33	69	19.52	4.57	34	3.9
77 623	934	59.59	36	27.15	71	14.84	136.57	03	3.5
77 623	2054	13.26	36	2.75	70	32.94	106.25	04	3.5
77 624	2358	0.19	36	31.68	70	22.24	218.87	05	4.6
77 624	2243	57.24	36	11.90	69	17.27	9.65	35	3.3
77 626	824	11.00	36	18.48	70	55.67	119.35	36	3.4
77 626	1833	58.79	36	47.06	71	23.74	155.28	37	3.5
77 627	759	14.12	36	27.88	70	50.11	127.76	38	3.3
77 628	1034	26.75	36	7.26	70	32.94	100.00	39	3.6
77 628	1520	4.70	36	10.48	71	8.95	86.02	40	2.9
77 628	1623	51.79	37	11.64	71	25.61	108.66	41	3.4
77 628	17 3	36.25	35	17.53	69	16.85	8.68	42	2.1
77 629	636	27.30	36	21.49	71	10.14	105.56	43	3.5
77 629	1031	4.37	36	28.76	71	18.43	138.44	44	3.4
77 629	1521	33.18	37	27.39	72	21.65	221.95	45	4.3
77 629	1540	1.48	34	46.64	70	58.65	2.04	46	2.5
77 629	16 6	30.59	36	24.00	71	9.33	103.31	06	4.7
77 630	220	47.74	36	29.06	70	26.98	219.25	07	4.1
77 630	338	34.03	36	37.07	71	17.14	86.83	47	3.5
77 630	1353	29.92	36	17.64	71	11.71	98.83	48	3.4
77 7 1	348	32.15	34	38.56	70	28.55	16.27	08	4.5
77 7 1	1444	10.80	36	28.05	71	6.59	264.91	09	4.9
77 7 1	1627	3.09	36	14.58	70	19.05	108.83	49	3.0
77 7 2	330	48.81	36	34.45	70	39.80	174.84	50	4.1
77 7 2	2028	19.63	35	13.97	69	25.26	8.32	51	2.2
77 7 2	2111	49.19	35	59.39	70	43.29	93.93	52	3.2
77 7 3	17 0	4.91	36	56.43	71	2.82	76.67	53	3.0
77 7 4	614	15.39	36	32.71	71	21.16	122.09	54	3.5
77 7 4	824	3.03	36	19.90	69	33.71	134.72	55	3.6
77 7 4	1128	47.08	36	26.39	70	12.86	221.59	10	4.6

77 7 4 2041	5.58	36	11.73	69	26.72	128.00	56	3.3
77 7 4 21 1	56.74	37	31.97	72	0.62	157.19	11	4.7
77 7 5 14 7	12.46	36	29.72	69	47.10	271.19	57	2.9
77 7 6 055	22.50	36	39.45	71	5.04	229.10	58	3.9
77 7 6 1328	56.27	37	4.49	71	34.93	96.33	59	3.4
77 7 6 1659	8.76	36	17.72	69	50.94	9.46	60	3.0
77 7 7 620	43.34	36	25.26	70	37.26	228.86	61	4.1
77 7 8 130	36.15	36	38.20	71	8.46	214.61	12	4.0
77 7 8 525	26.60	36	41.86	71	12.24	230.79	13	4.7
77 7 8 7 2	10.28	36	31.90	71	20.23	94.37	62	3.3
77 7 8 950	6.99	36	41.21	71	12.71	233.80	63	3.8
77 7 9 1141	13.94	35	30.46	68	52.81	38.00	64	2.7
77 7 9 1211	40.56	37	36.71	71	45.78	129.68	65	3.7
77 7 9 1616	39.67	36	28.06	71	12.71	143.71	66	3.3
77 710 028	19.08	35	41.93	68	38.41	3.74	67	3.6
77 710 1347	18.52	35	6.83	69	21.09	17.57	69	2.3
77 710 1612	22.07	35	31.28	69	13.05	17.04	70	3.6
77 711 11 2	56.61	36	26.37	71	20.63	104.40	14	3.9
77 711 1224	5.07	36	45.50	71	28.64	188.43	72	3.6
77 711 1651	7.33	36	28.89	71	9.82	118.48	15	4.2
77 712 11 7	59.16	36	32.53	70	58.27	192.49	73	4.3
77 712 1518	28.82	36	12.21	69	15.96	5.57	74	3.8
77 712 1718	2.32	36	16.59	70	40.23	103.88	75	3.7

Table 2

BAND	WIDTH (Hz)	CENTER FREQUENCY (Hz)	SAMPLING WINDOW (Secs)
1	0.25	0.38	8.0 - 16.0 *
2	0.50	0.75	8.0 - 16.0 *
3	1.00	1.50	8.0
4	2.00	3.00	8.0
5	4.00	6.00	8.0
6	8.00	12.00	4.0
7	16.00	24.00	4.0
8	28.00 #	46.00	4.0

* Depending on amount of data available

High corner is 60 Hz (Nyquist frequency is 64 Hz)

Table 3

Event No.	T _{max} /T _s (α_{max})			
	JOR	FAR	CHS	PEN
Crustal (CR)				
67	1.44		1.51	3.00
64				3.12
31				3.57
74	2.30		1.84	2.42
34	2.17	5.17	1.87	3.23
35		4.00	1.56	2.62
60		5.12		
70	1.64		1.88	
42				6.56
51				10.69
69				7.87
23			1.56	2.32
24			2.10	
18				2.64
8	2.81		12.18	5.13
Pamir (P)				
65	1.75	1.70	1.45	1.40
11	5.80	5.96	3.36	
45	1.68	1.66	1.36	1.45
Transform (T)				
59	2.62	1.73		
41		1.83		
Shallow B (b)				
20		2.03	1.53	2.43
26		1.43		
55	1.69	2.16		
56	1.66	2.45		
68				
Shallow C (c)				
04	2.44	2.55	1.96	2.11
27		1.97	1.52	
28		9.20	5.55	
29		5.27	3.36	
16			1.66	1.95
49		2.23		
52	2.56	3.92	1.74	1.69
75	2.87		1.95	1.73

Event No.	Tmax/Ts (α_{max})			
	JOR	FAR	CHS	PEN
Shallow D (d)				
40	2.16	1.83		
6	6.09	5.16	3.34	2.85
15	6.64		4.37	2.89
36	2.54	2.28		1.66
38	2.16	2.04		1.64
43	2.70	2.82		1.24
47	3.35	2.44	1.50	1.53
48	2.56	2.17	1.73	1.63
50	2.73	3.18	1.91	1.96
Shallow E (e)				
53	3.32	2.15		
32		2.46		1.81
62	2.24	1.84		
3	2.31	1.68		1.69
44	2.45	2.11	1.62	1.44
54	2.21	2.12		
66	2.30		1.62	
37	2.20	1.94		
33	5.28		3.67	3.20
72	1.82	1.63	1.54	
14	4.41	3.40	2.80	
Deep C (C)				
5	6.18	7.45	3.98	4.29
7	2.23	2.27	1.69	1.73
10		5.97	3.13	3.32
30		1.72		
Deep D (D)				
2		1.95	1.70	1.61
9	6.40	6.52	4.69	4.55
12	2.02	1.91	1.86	1.48
19		1.79	1.53	1.43
73	2.89		2.73	1.60
61	2.54		2.04	
Deep E (E)				
13		6.93		3.95
58		1.83	1.46	
63	1.69	1.82	1.63	

Captions

Figure 1. Map view of seismicity in the Hindu Kush, as determined by Chatelain et. al. (1980). Sections delimit zones into which events are grouped for regional sampling considerations. Locations of smoked paper stations are indicated by solid diamonds, and digital stations by open stars. Epicenters are plotted with symbols corresponding to depth as follows: open circles, $0 < z < 50$ km; squares, $50 < z < 100$ km; triangles, $100 < z < 150$ km; inverted triangles $150 < z < 200$ km; pluses, $200 < z < 250$ km; and y's, $z > 250$ km.

Figure 2. Combined frequency response of S5S seismometer and recorder in digital counts recorded per micron of ground displacement for 0 db gain (typical gain was 92 db).

Figure 3. Map view of all the Hindu Kush seismicity recorded on smoked paper stations, divided into 50 km depth intervals. Locations of events recorded on the digital recorders and used in this analysis are denoted by the numbers used in Table 1.

Figure 4. (top) Uncorrected seismograms of events 44 and 3 from different stations (locations are shown in figure 1). (bottom) Corresponding band-passed

signals, numbered 1 through 8 (see Table 2 for a description of the bands). Scales to the left of each plot are in units of digital counts.

Figure 5. Coordinate frame for an ellipsoidal region of scatterers in an infinite space.

Figure 6. Horizontal crosssections of regions sampled by coda of events in regions shallow B-E. Small letters indicate a typical earthquake epicenter in the region and capital letters to the limits of the sampling of coda from this earthquake. All plots drawn for a depth of 70 km and for $\alpha = 2.0$.

Figure 7. Vertical crosssections of regions sampled by coda from events in regions Shallow B-E and Deep C-E. Triangles are the stations (all rotated into the same plane) and the bold x is a representative event location. All plots drawn are for $\alpha = 2.0$. Approximate depth of Moho is denoted by dotted line. Vertical scale is in kilometers.

Figure 8. Comparison of coda envelope shapes before and after correcting for the $K(\alpha)$ decay and source-receiver distance for shallow and deep E events. Top two plots pertain to all of the data in frequency band 3 recorded in the deep E region (all events at all stations). Bottom two pictures are shallow E events recorded at JOR. In both

pairs of plots, the upper one is uncorrected data, the lower is corrected data. Note how, in both corrected and uncorrected data, the decay at beginning of coda is rapid relative to that in the later parts (as approximated by the solid straight lines). T_0 is the origin time.

Figure 9. Q_c determinations from events of the shallow D region recorded by JOR, made by partitioning data into windows of forty seconds. Numbers indicate the frequency band used. Note the general increase in the Q_c estimate for later arrivals, especially at low frequency, which is evidenced by the decrease in the decay of the coda with time. All values plotted here were determined with errors less than 15%. T_0 is the origin time.

Figure 10. Comparison of energy decay predicted by the infinite medium K (K_I) with that by the total loss, half space K (K_h) as a function of α .

Figure 11. Values of $\log_{10} Q_c$ versus frequency band obtained from all available data from each station and each region by a simultaneous least squares fit (except crustal PEN, which used selected events; see text). Letters refer to the regions described in Table 3. Values for band 8 (center frequency = 46 Hz) were occasionally excluded if low energy levels made the record indistinguishable from

noise. Row "ALL" is a superposition of values determined at each station. Dotted line is the $Q(f) = 360 f^{1/2}$ relation determined by RK78. For comparison, the trends of different frequency powers are drawn to the right.

Figure 12. Coda envelopes for crustal events recorded at PEN for bands 4-7. Original data is on the left, the same data corrected by $(r^2/K(\alpha))^{1/2}$ is on the right. Note, event on corrected data, the rapid decay of the codas on the extreme left of the plots. These events occurred very close to PEN and sample only the crust.

Figure 13. Plot of $\langle \ln(A_s/A_c) \rangle$ vs. Distance for events recorded at FAR and JOR for all frequency bands. A_s is the S wave amplitude and A_c is the amplitude of the coda envelope at t_0 (=75 seconds) for the same event and the same frequency band (indicated by numbers to the right of each plot). Dotted lines denote the least squares fit to the data.

Figure 14. Determination of $\log_{10} Q_\beta$ vs. frequency for stations FAR and JOR, and comparison with $\log_{10} Q_c$ determined from PEN crustal events. Q_β values could not be determined at JOR for bands 1 and 2 with acceptable variance (<100%) and were not plotted.

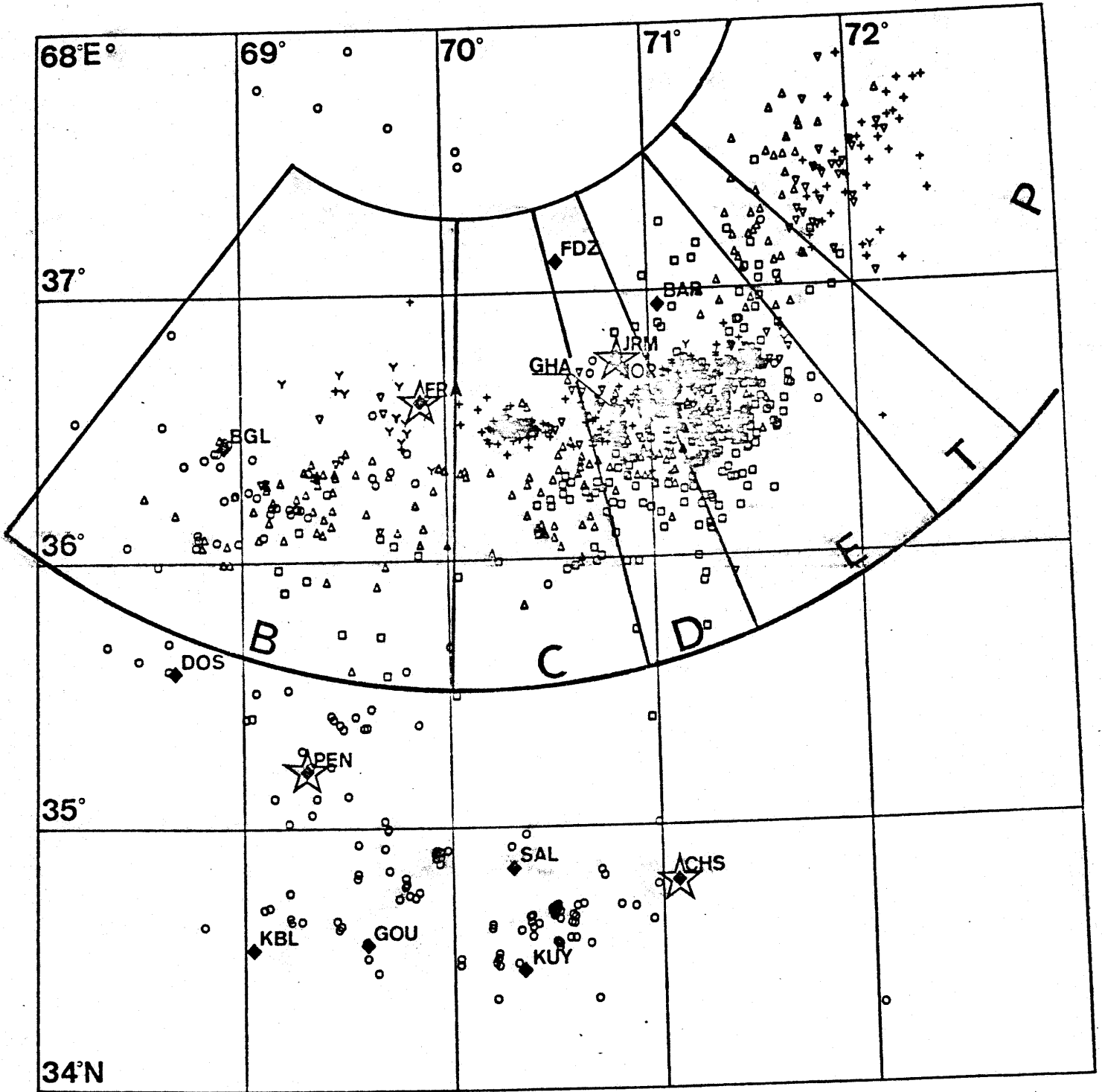
Figure 15. Average $Q_c(f)$ to different depths as a function of frequency. Depths refer to approximate maximum sampling depths.

Figure 16. Comparison of Q_c^{-1} determined for central Asia in RK78 (CA1000 = central Asia at 1000 kms depth) and in this study (PEN, CA400 = central Asia at 400 kms depth) with Q_c^{-1} of other regions deduced by Chouet (1976). TSK is in central Japan, PAC is in central California, OIS is in western Japan, and OTL is in Hawaii. Note apparent convergence of Q_c^{-1} values at high frequency. Errors of the values are comparable to those in figure 15.

Figure 17. Same data as in figure 16, replotted as $\log_{10} Q_c$.

Figure 18. Same data as in figure 15 replotted as the minimum mean free path ($L_{\min} = vQ_i/\omega$). Note near frequency independence of L_{\min} at shallow depths.

Figure 1.



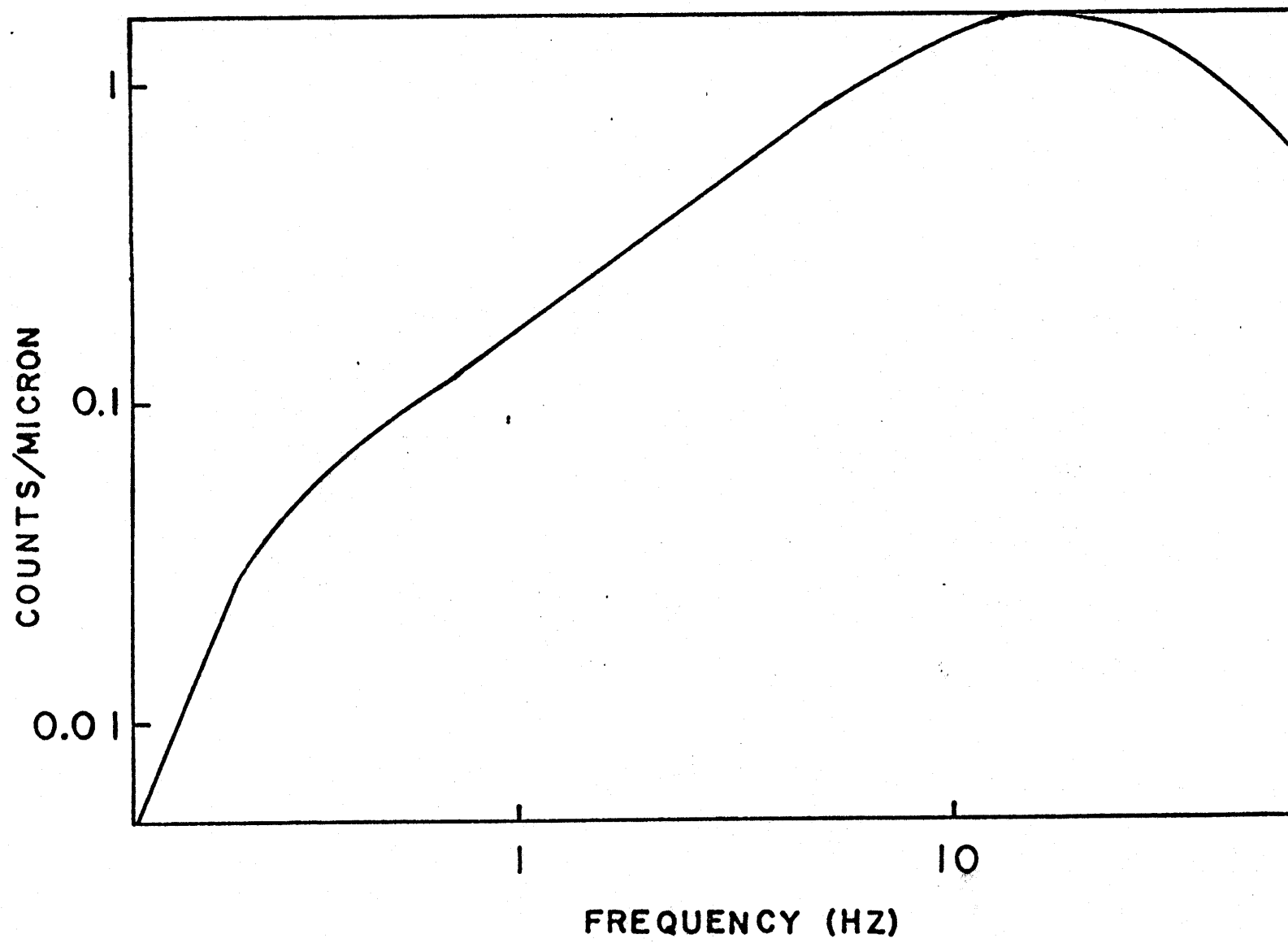


Figure 2.

Figure 3.

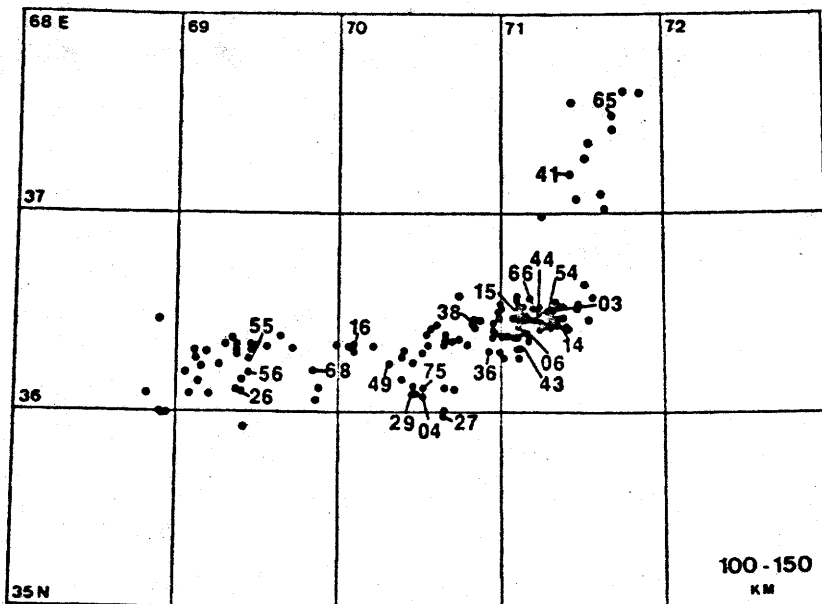
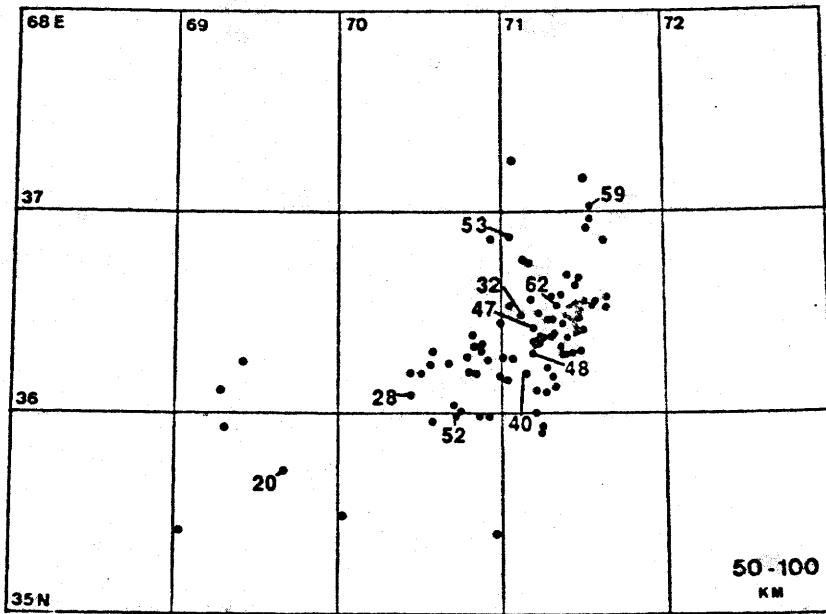
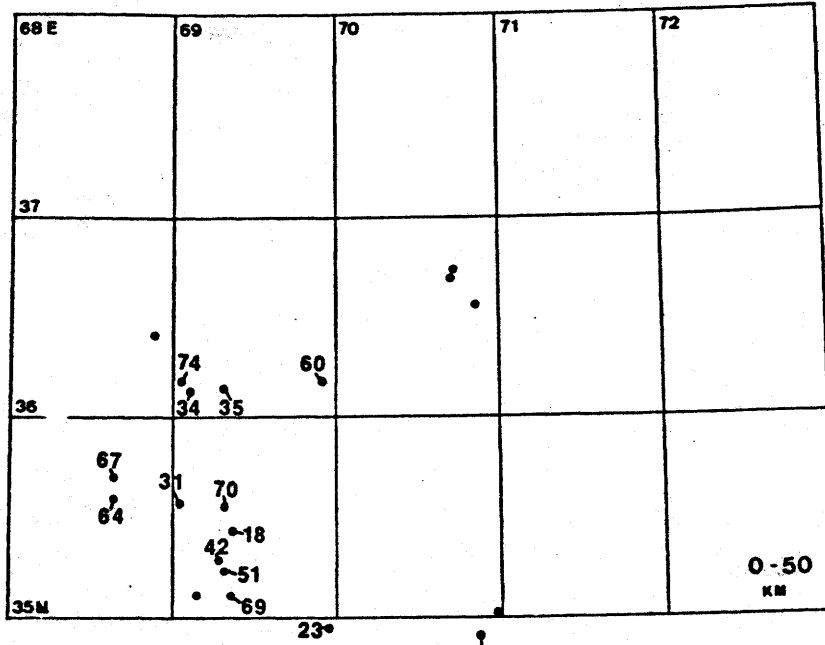


Figure 3 (cont.)

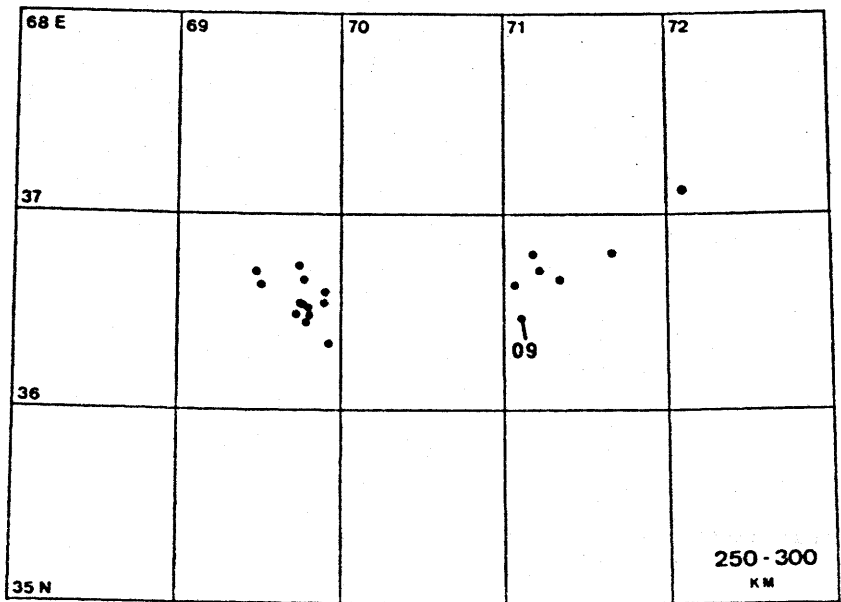
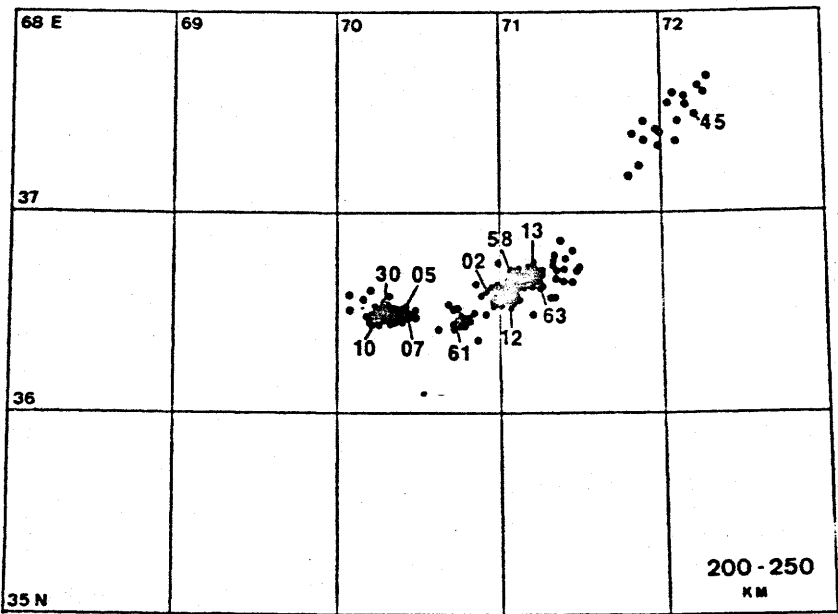
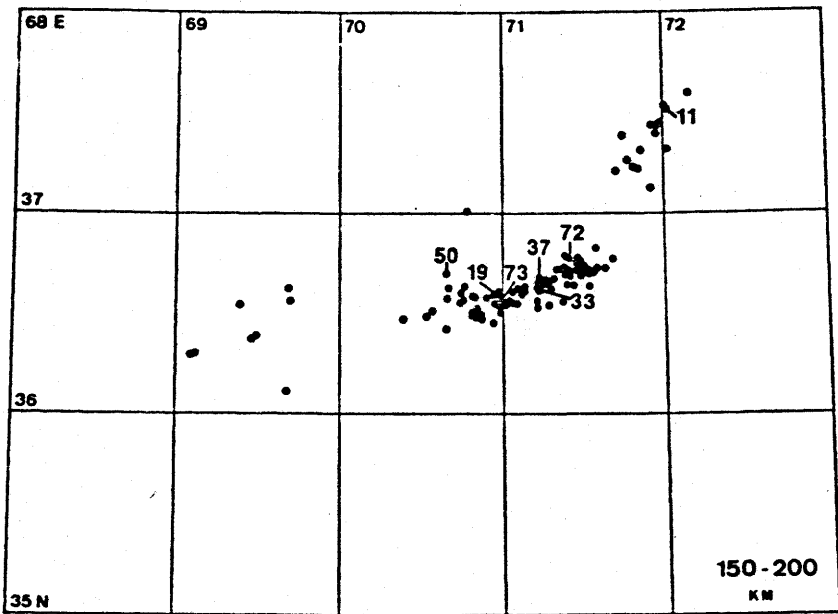
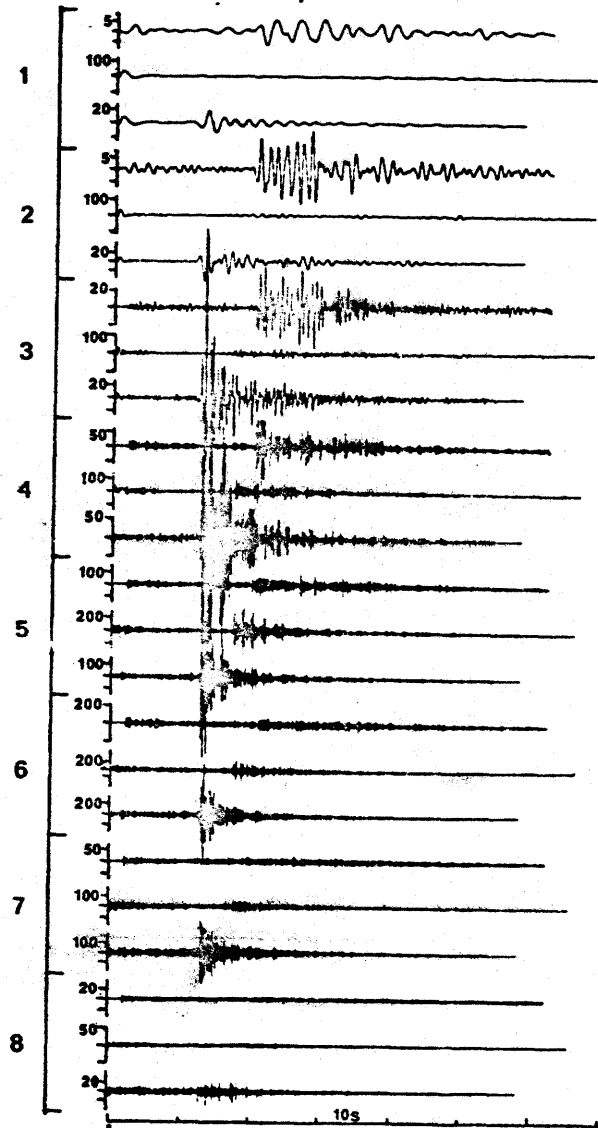
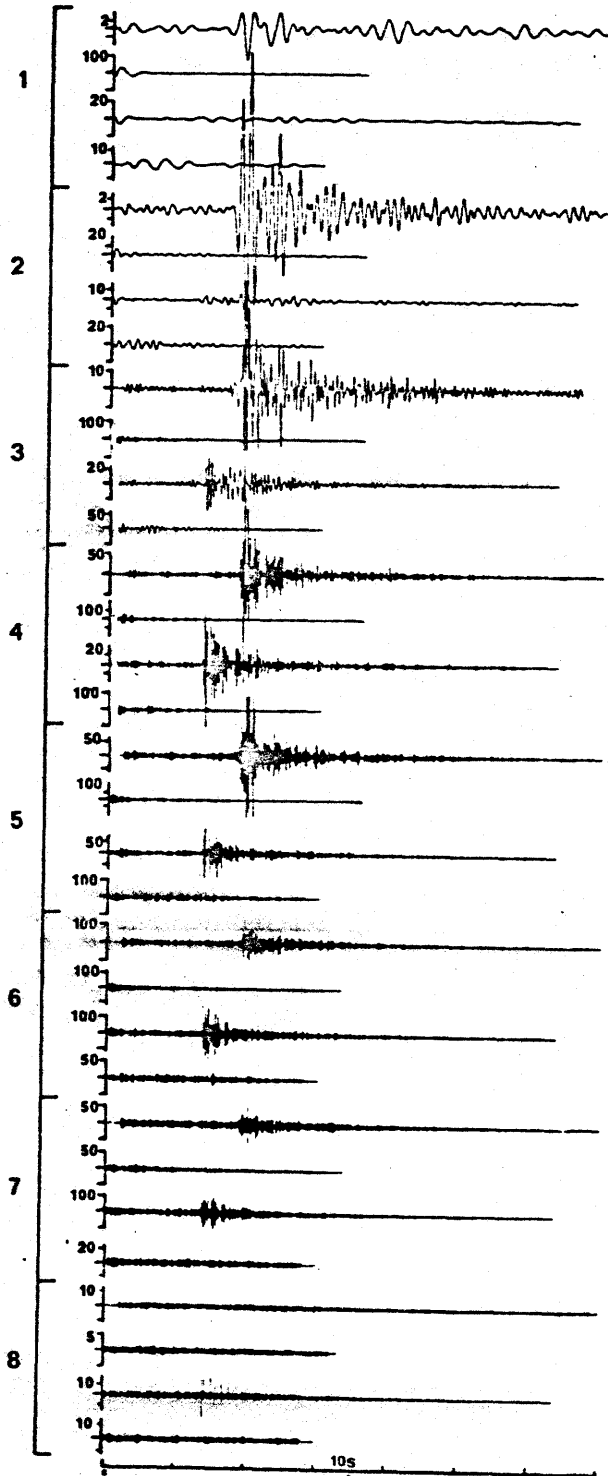
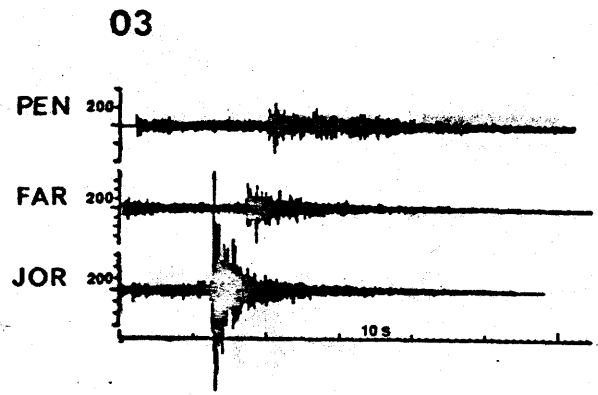
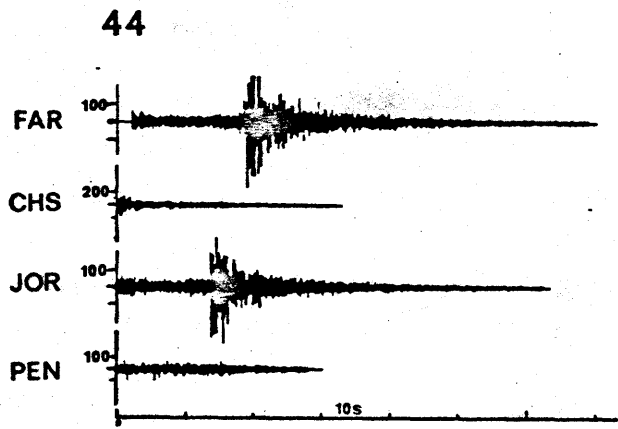


Figure 4.



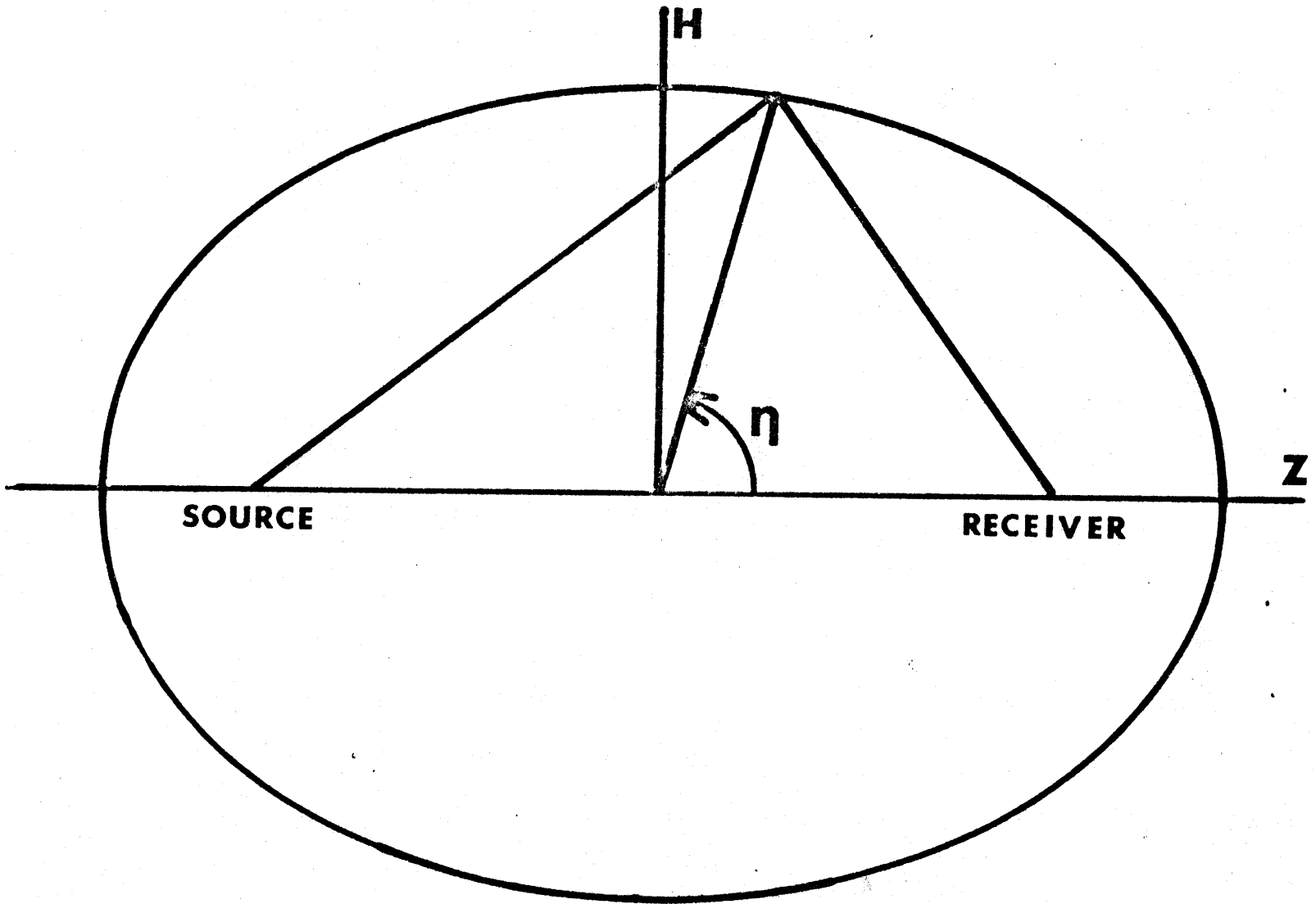


Figure 5.

Figure 6.

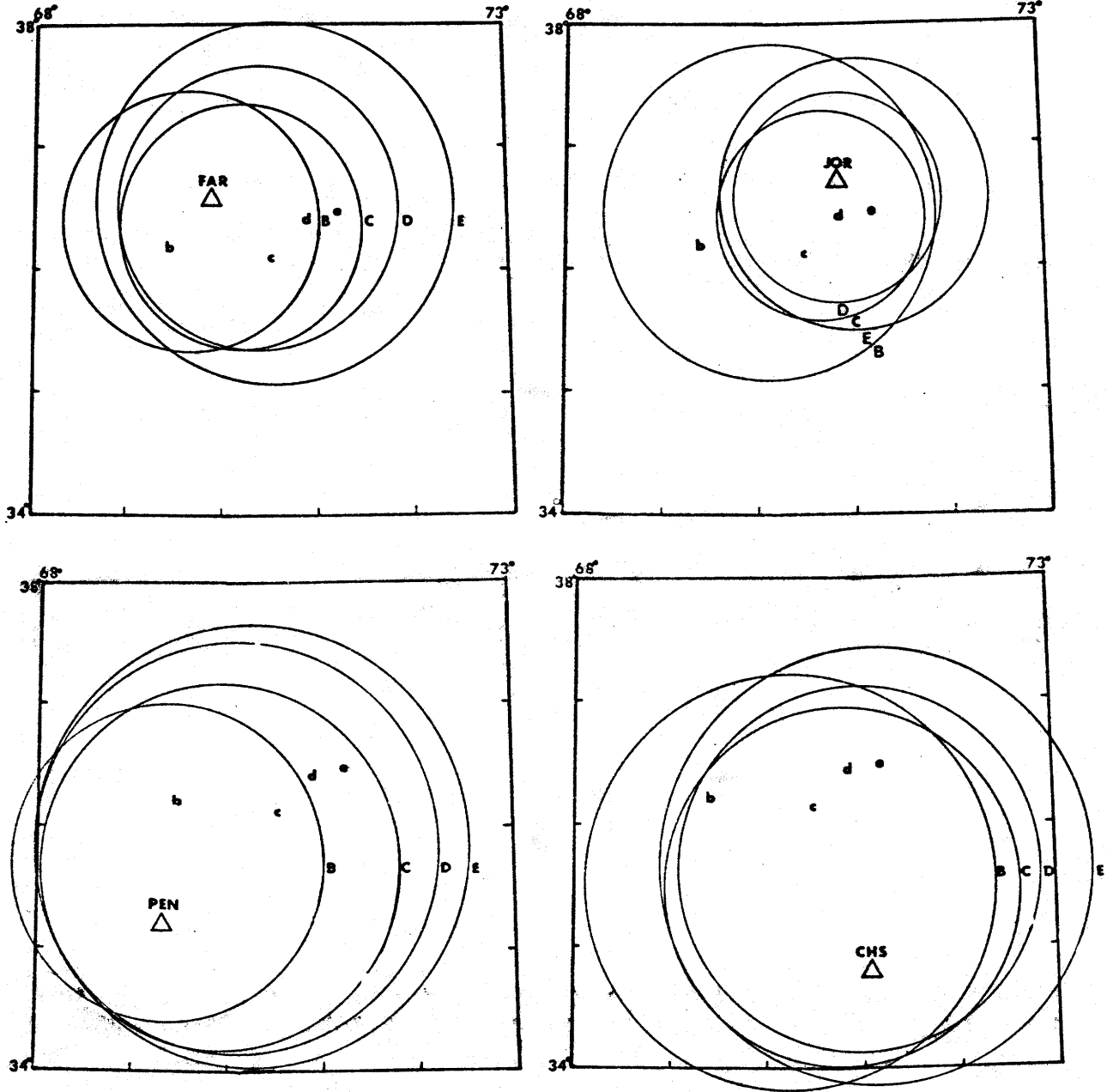


Figure 7.

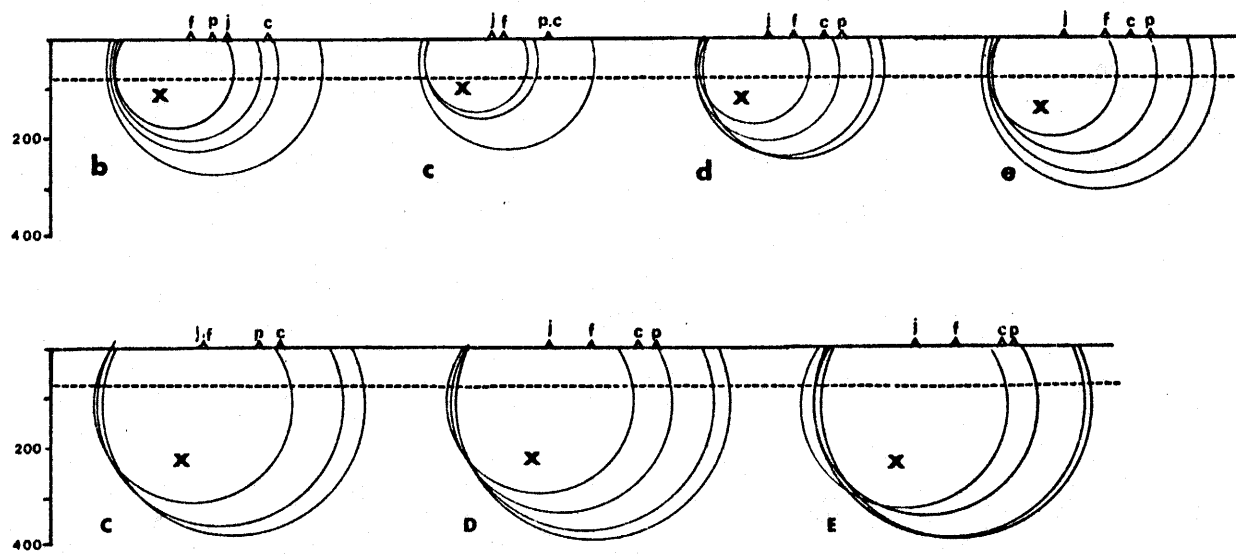
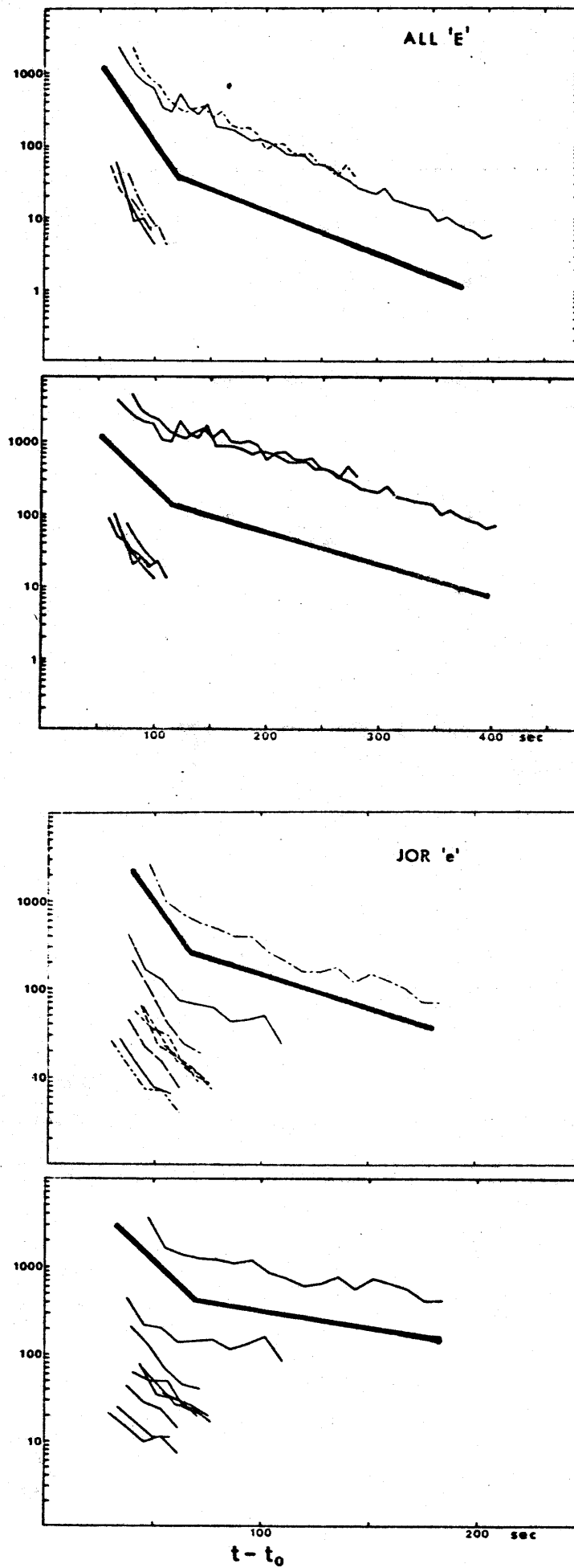


Figure 8.



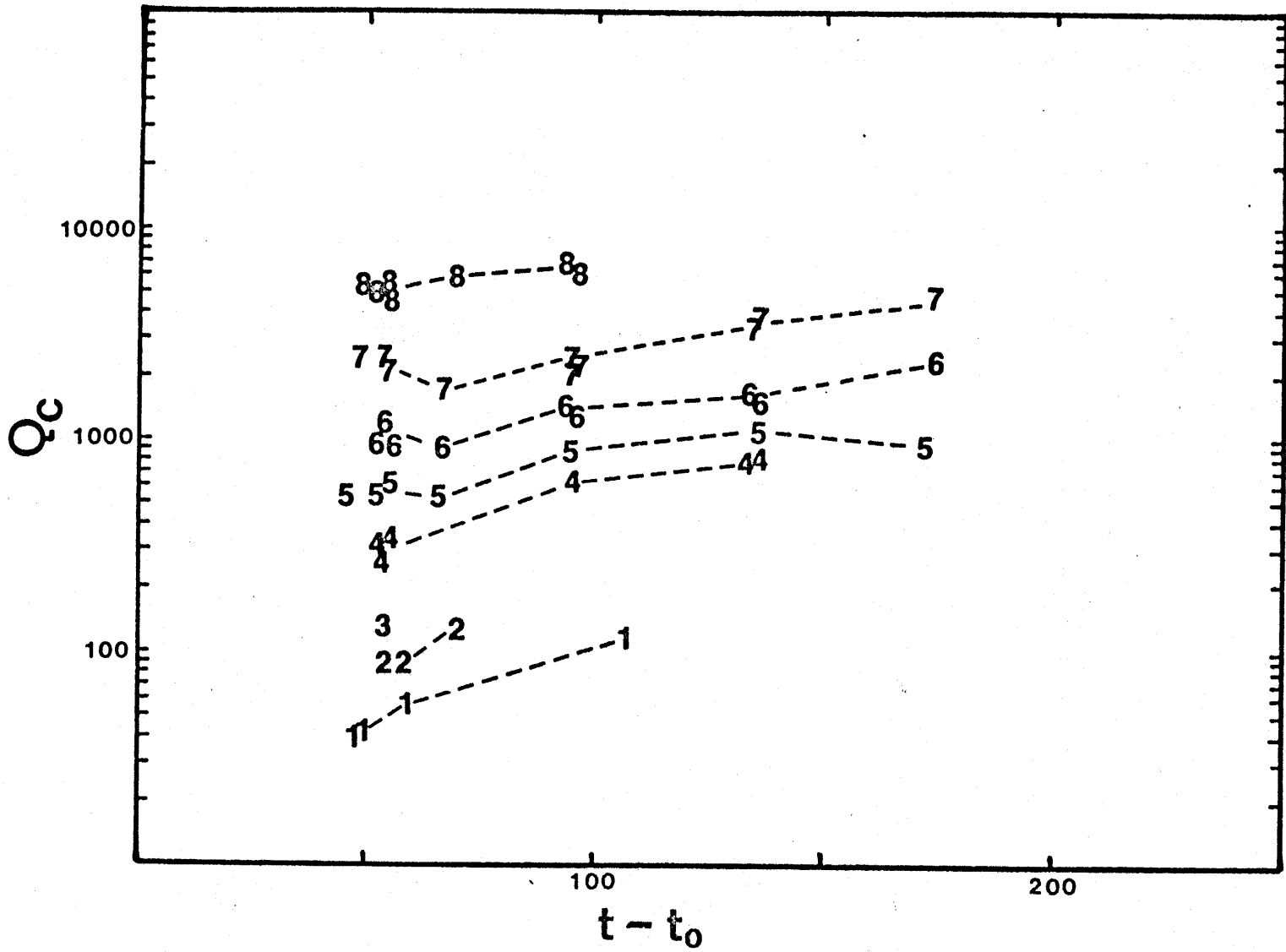


Figure 9.

Figure 10.

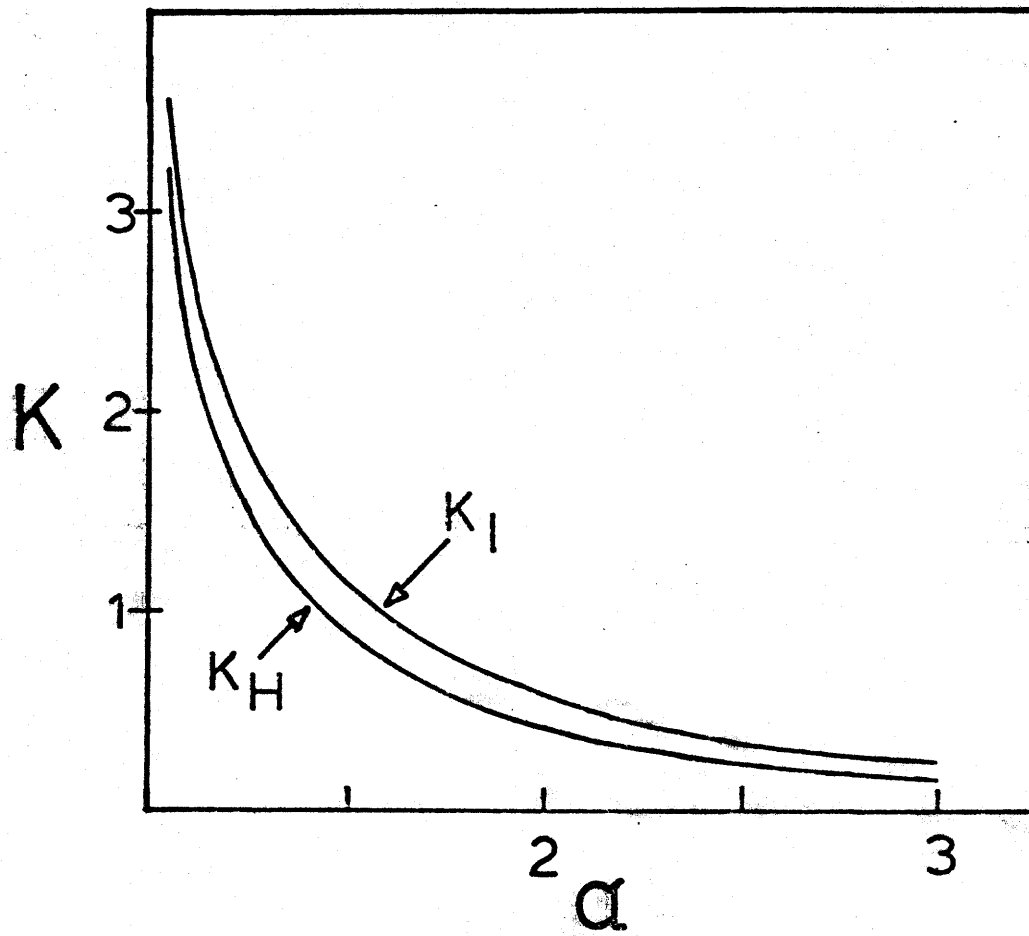


Figure 11.

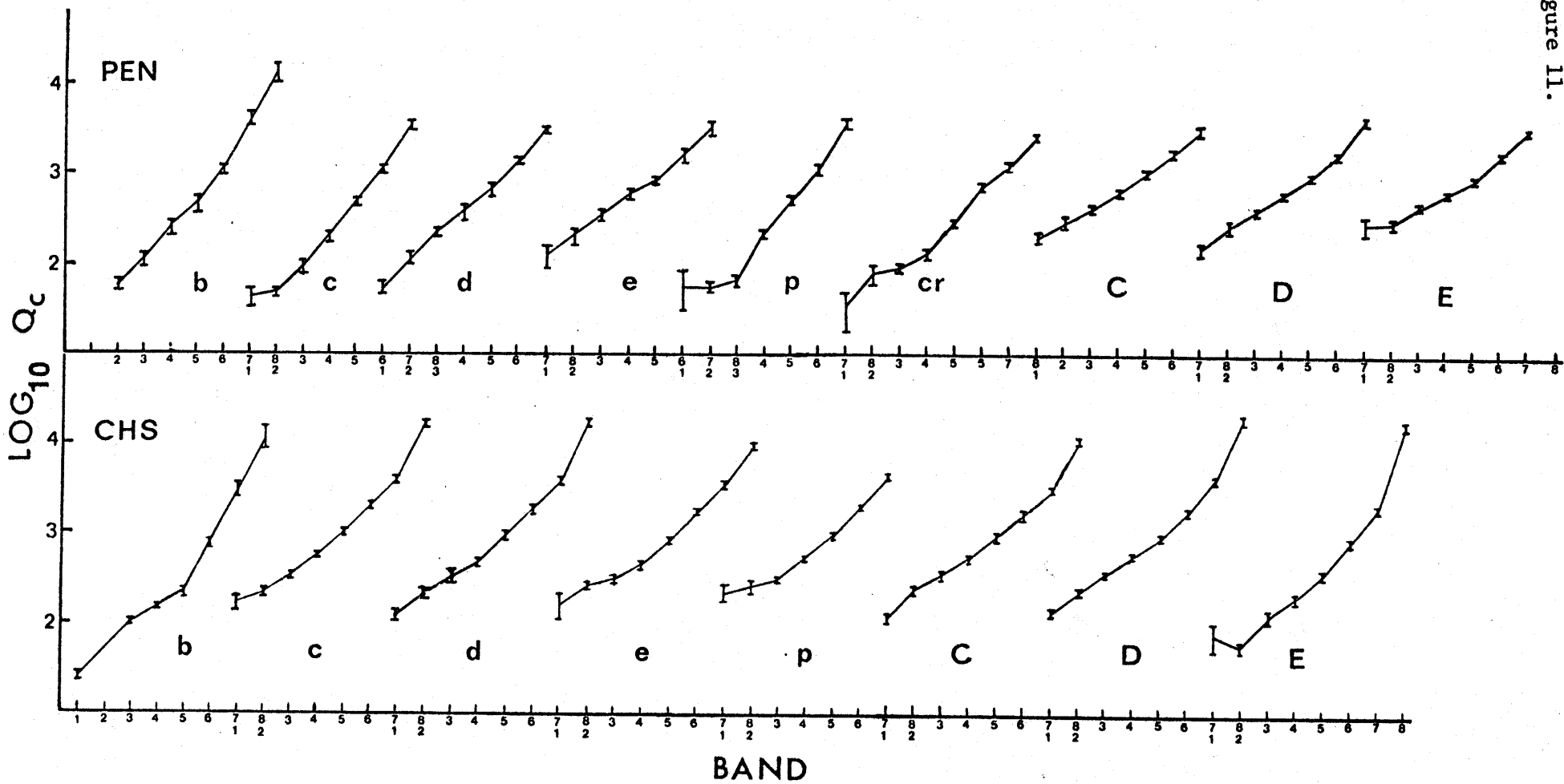


Figure 11. (cont.)

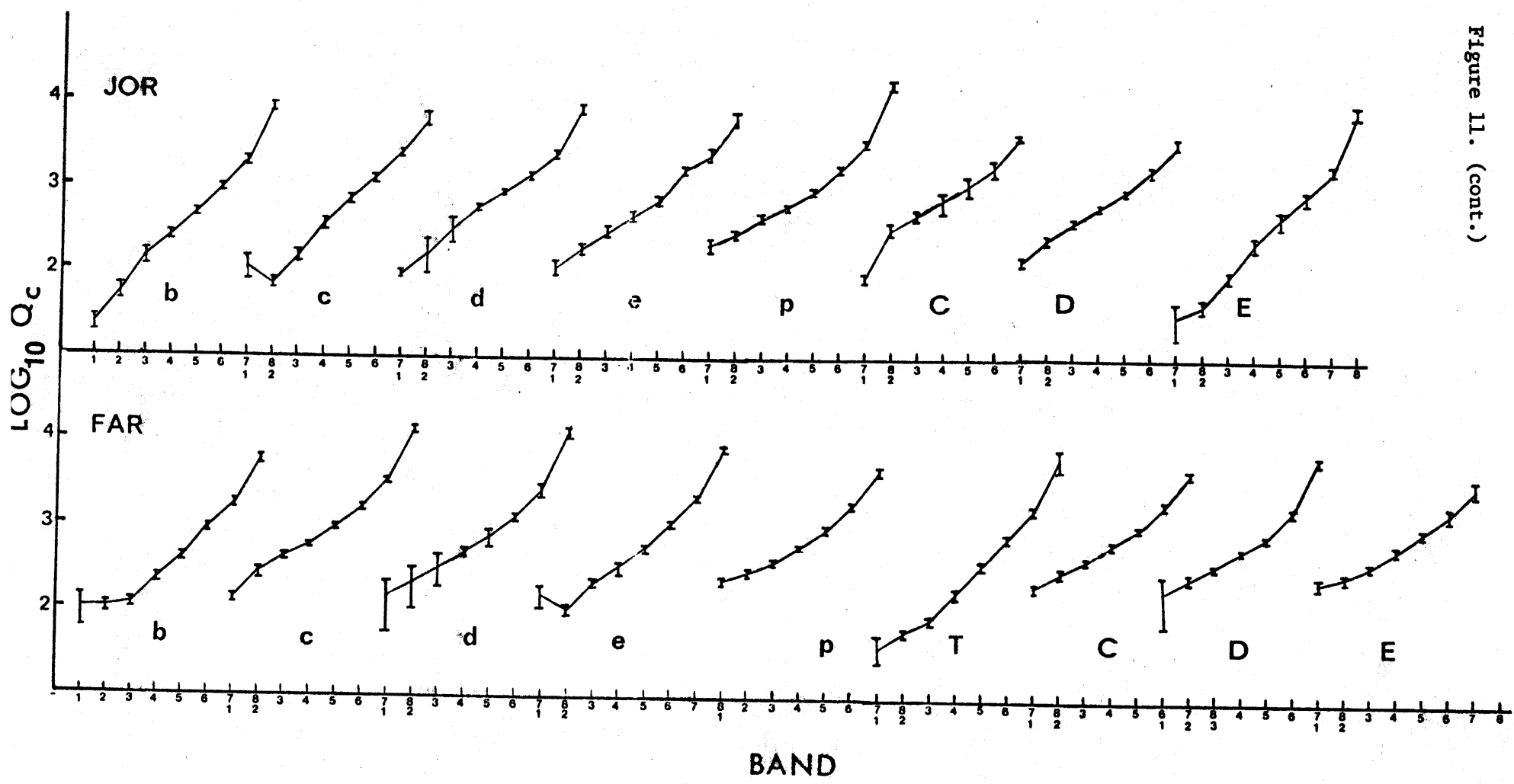


Figure 11. (cont.)

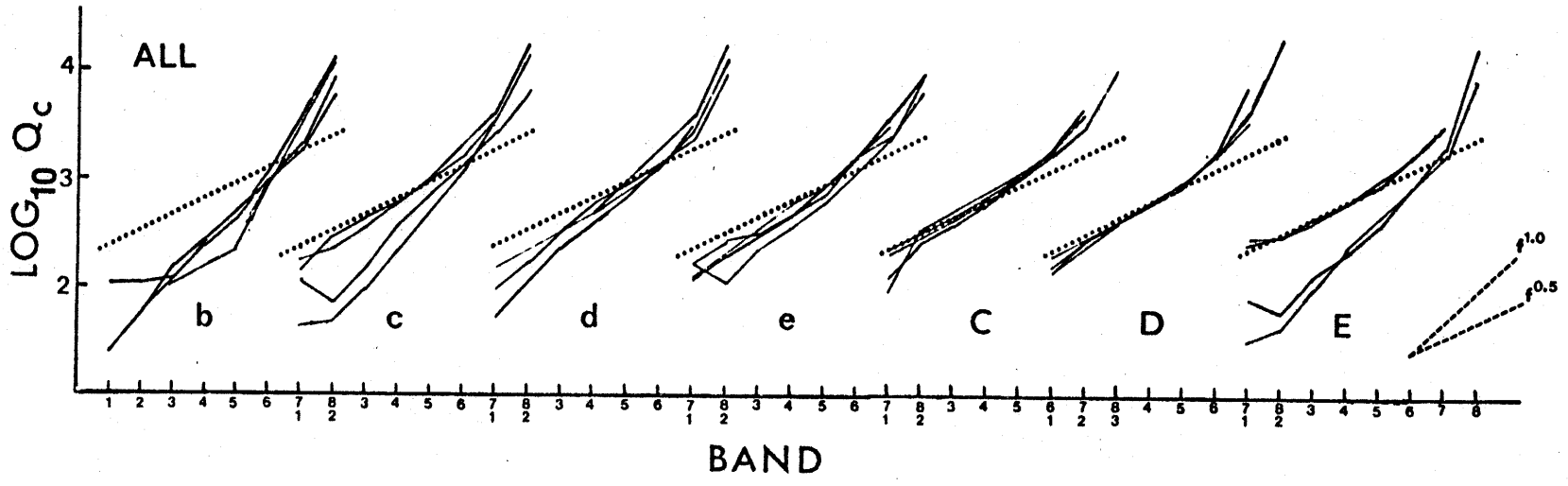


Figure 12.

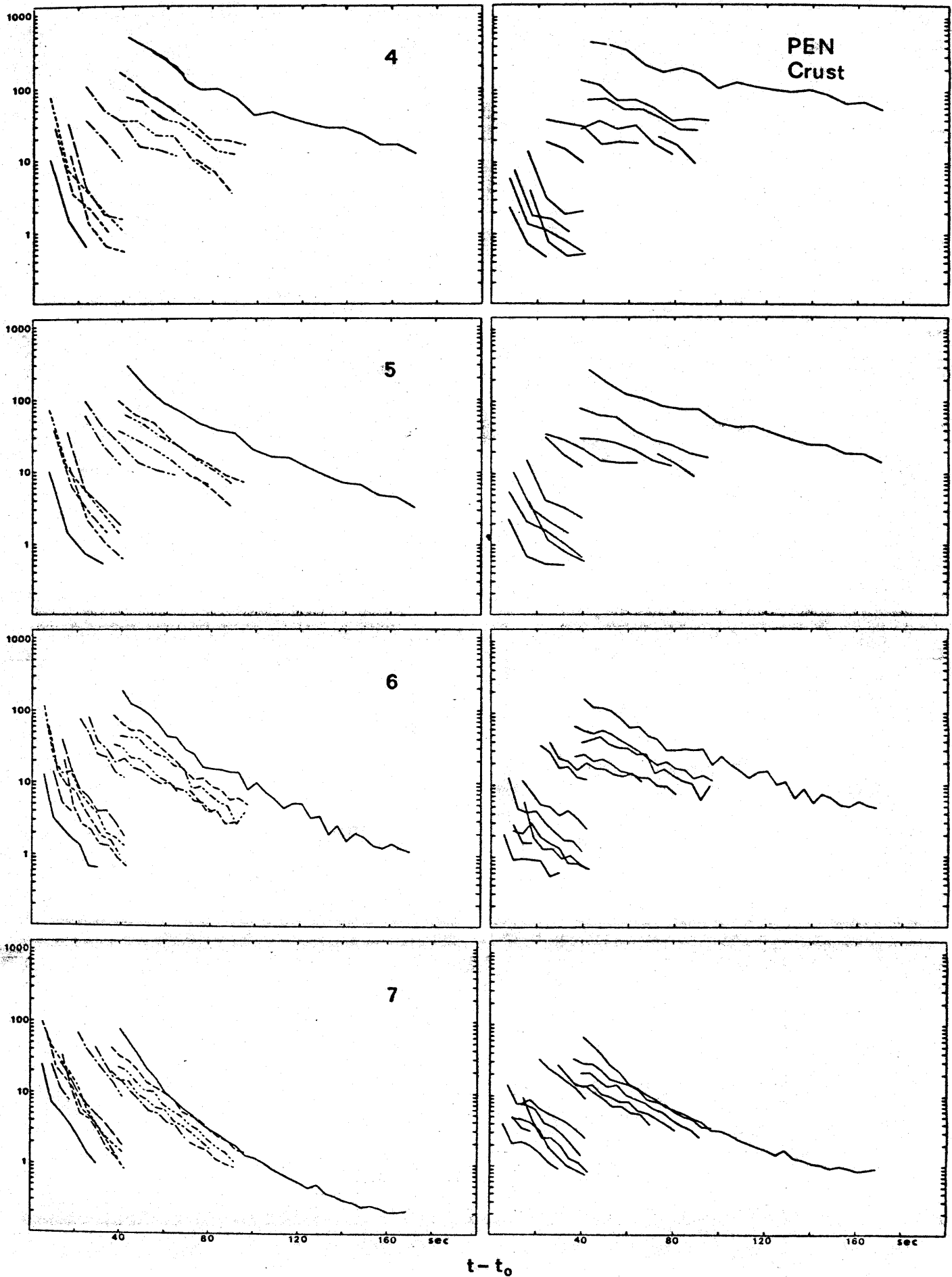
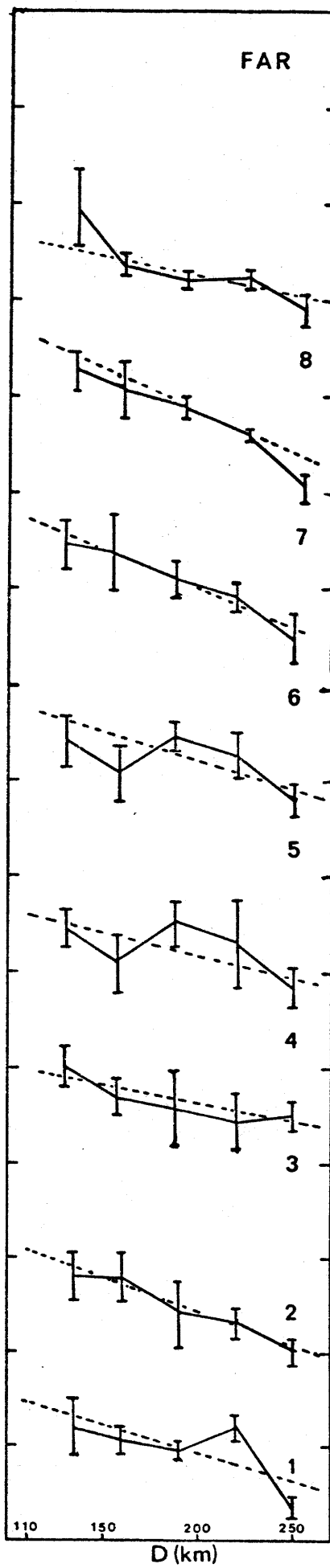
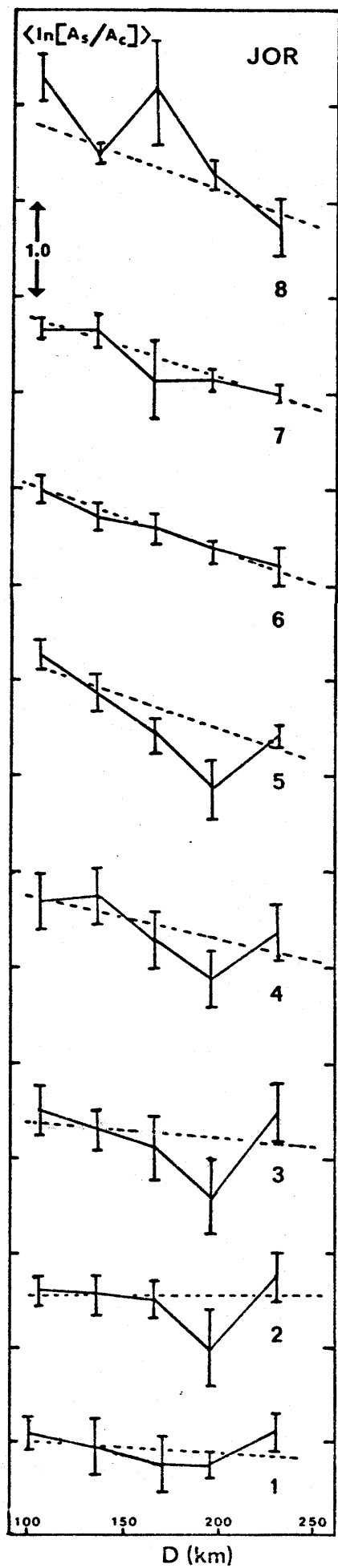


Figure 13.



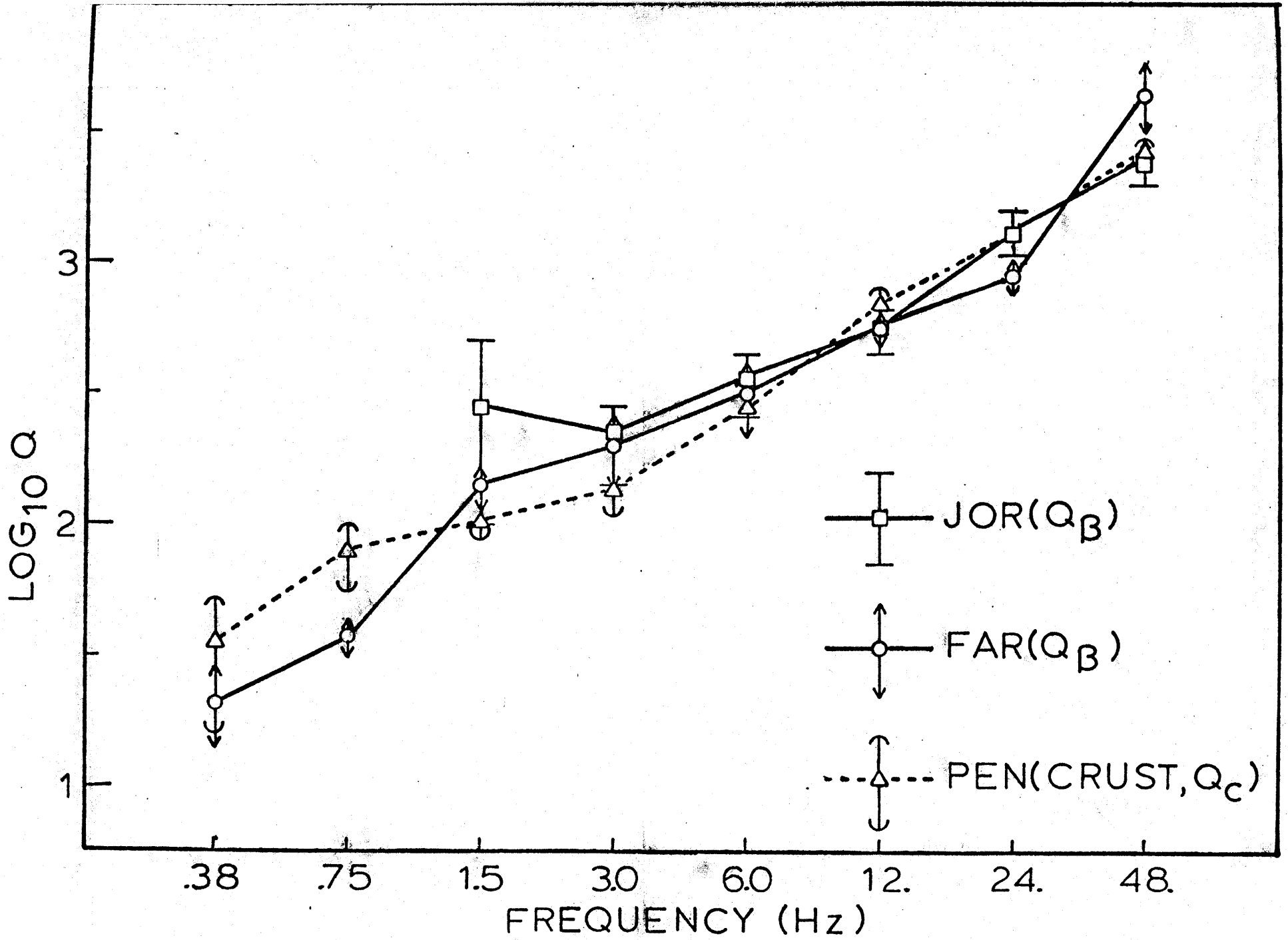


Figure 14.

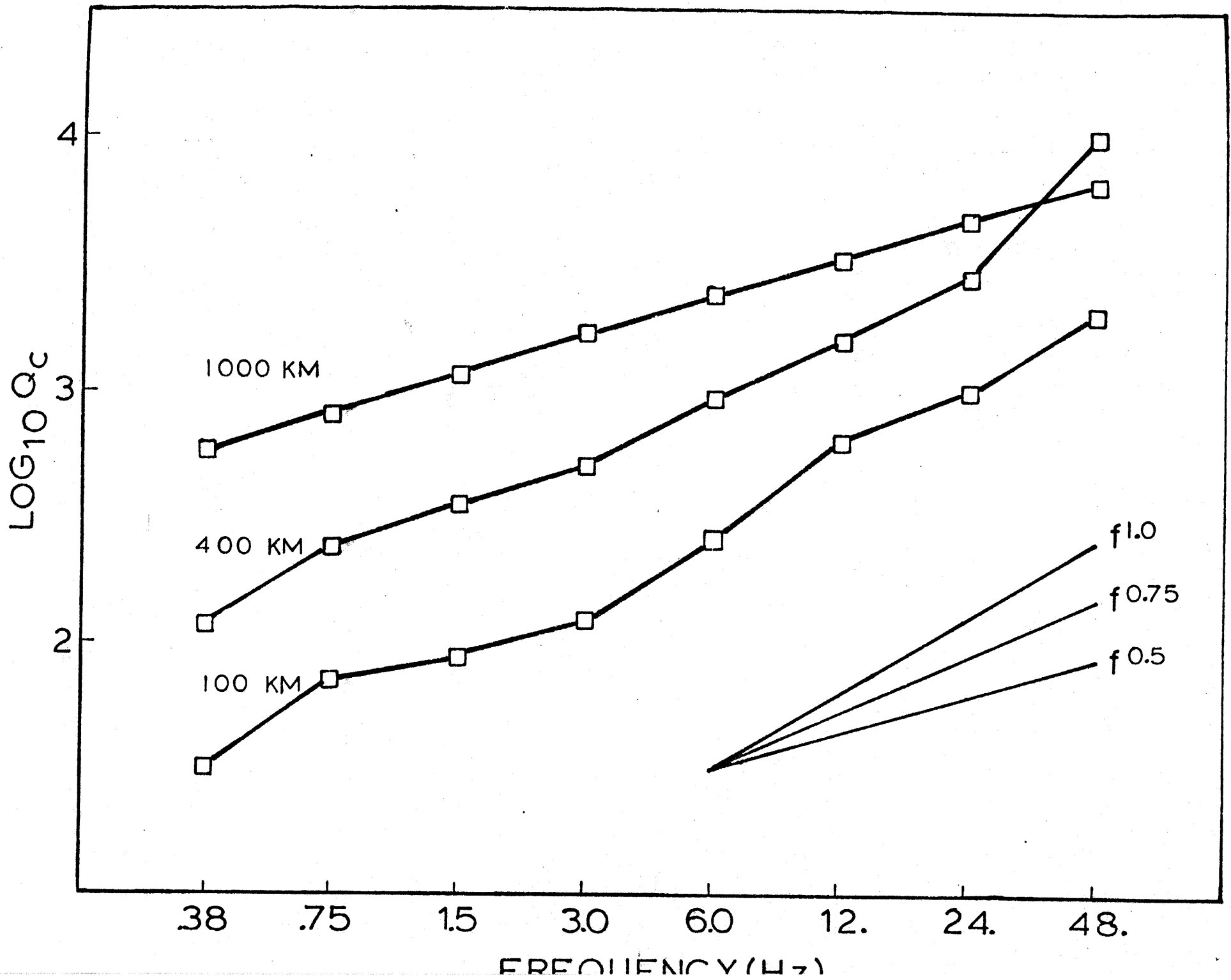


Figure 15.

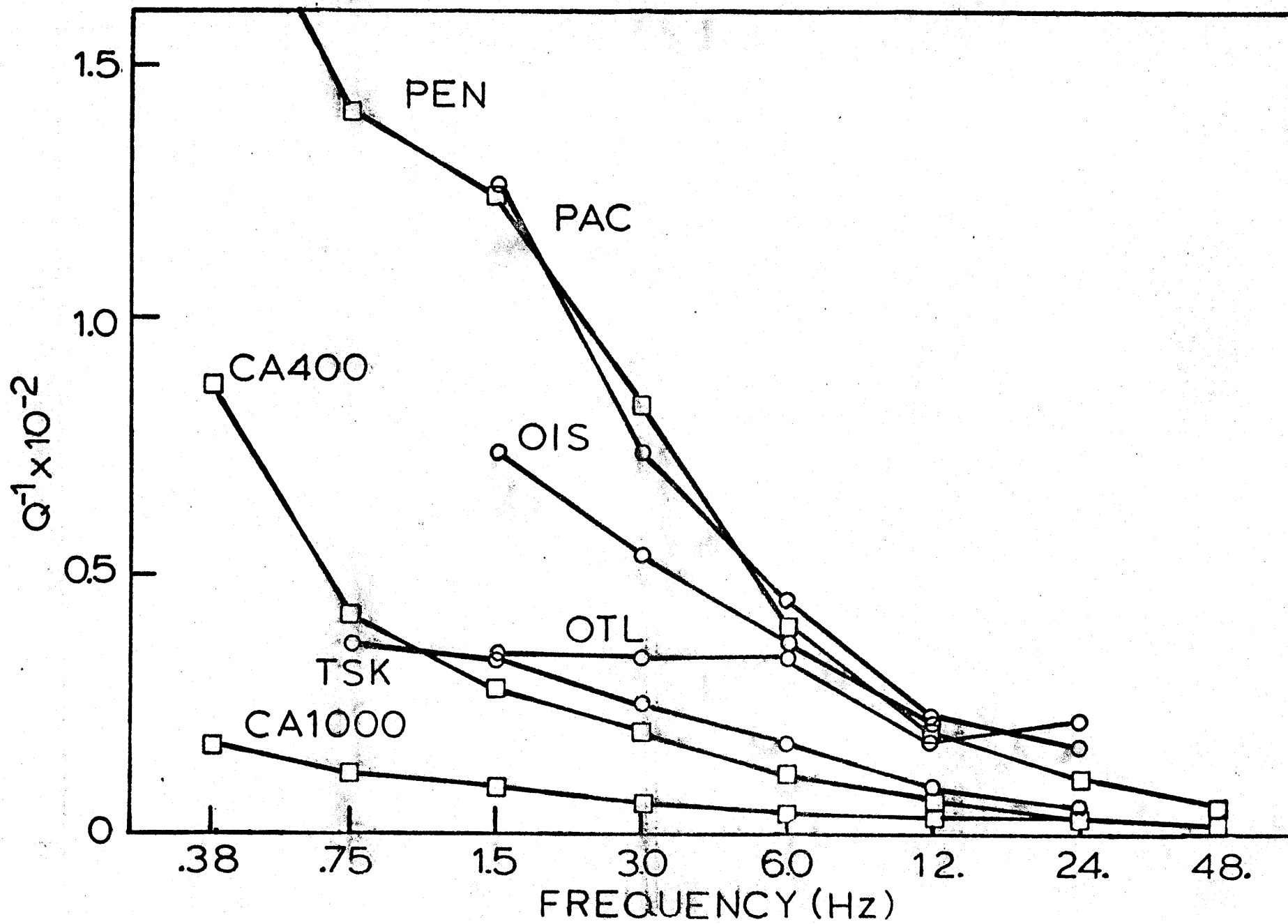


Figure 16.

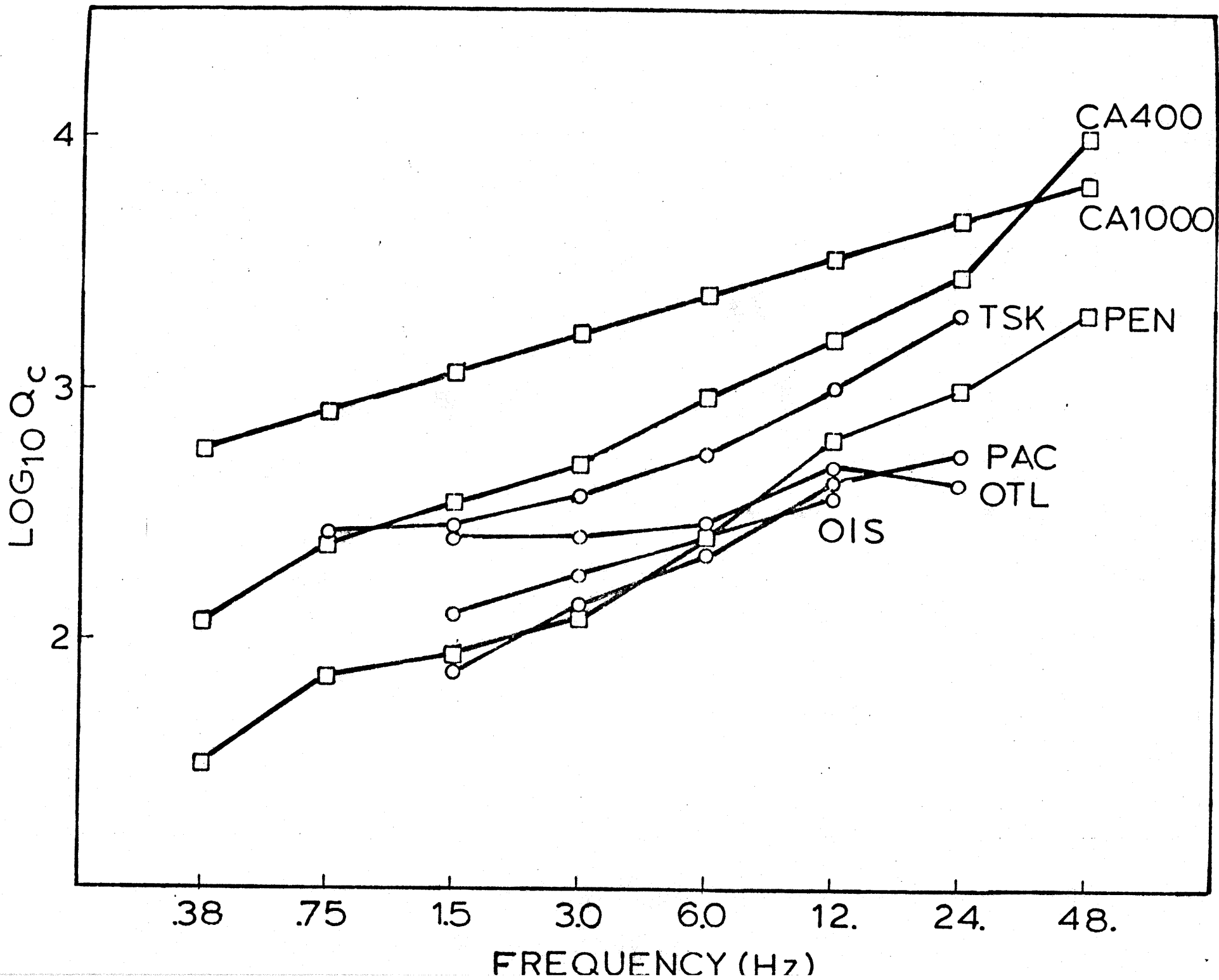


Figure 17.

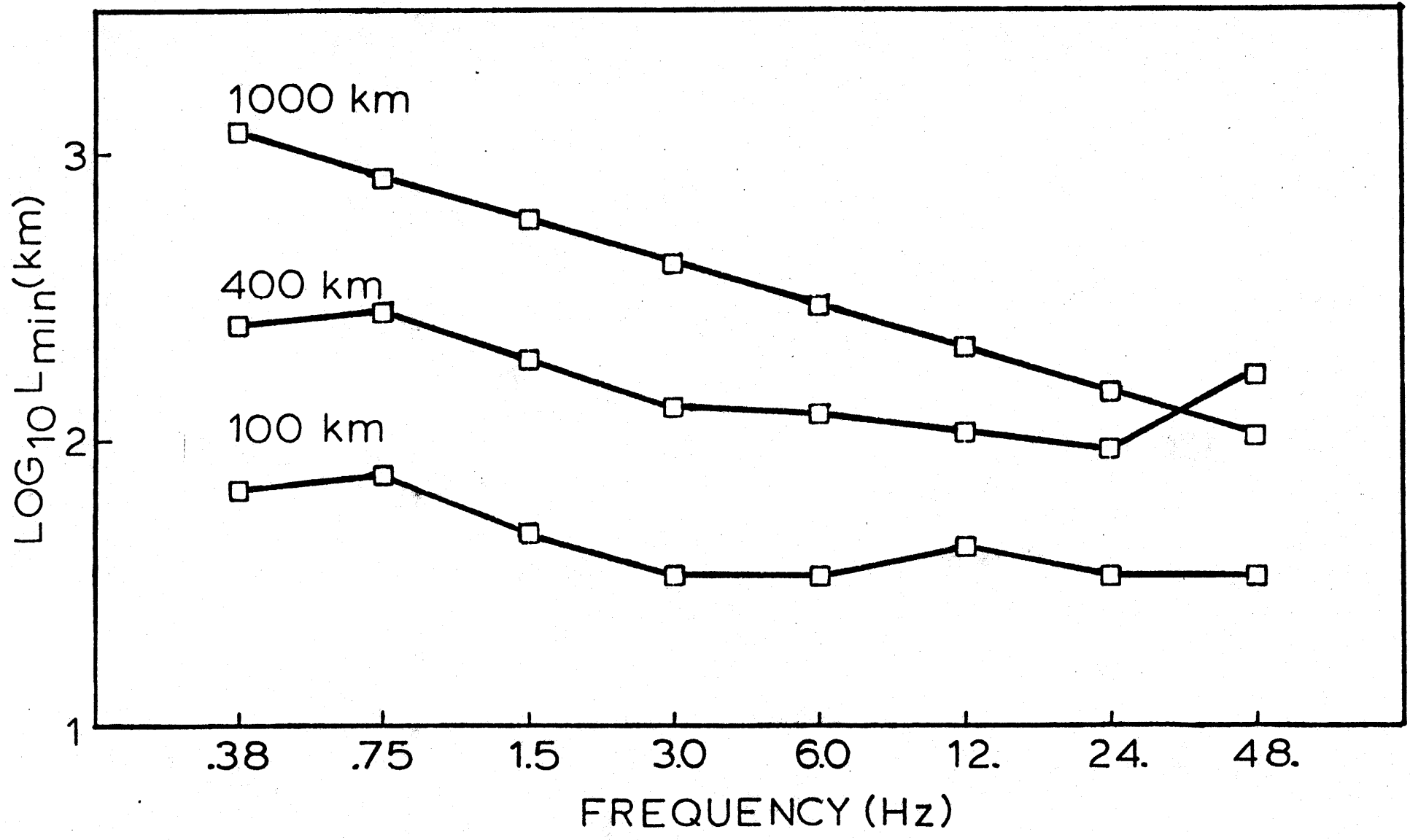


Figure 18.

CHAPTER VI

As far as could be learnt it appeared that the poor young dog, still under the impression that since he was kept for running the sheep, the more he ran after them the better, had at the end of his meal off the dead lamb, which may have given him additional energy and spirits, collected all the ewes into a corner, driven the timid creatures through the hedge, across the upper field, and by main force of worrying had given them momentum enough to break down a portion of the rotten railing, and so hurled them over the edge.

George's son had done his work so thoroughly that he was considered too good a workman to live, and was, in fact, taken and tragically shot at twelve o'clock that same day - another instance of the untoward fate which so often attends dogs and other philosophers who follow out a train of reasoning to its logical conclusion

- Thomas Hardy

Far from the Madding Crowd

The Velocity Structure of the Pamir-Hindu Kush
Region: Possible Evidence of Subducted Crust

S.W. Roecker

MIT

ABSTRACT

The arrival times of compressional (P) and shear (S) waves from approximately 580 microearthquakes recorded by a temporary array in the Pamir-Hindu Kush region in central Asia are used in deducing one- and three-dimensional velocity structures of this region. The results for one-dimensional structures imply that the Moho is at 70 ± 5 kilometers depth. Also, there is a velocity reversal near 160 kilometers depth, which is inferred to be the beginning of the low velocity zone. This reversal continues to depths of approximately 230 kilometers. Below 230 kilometers, velocities are somewhat higher than those of normal mantle at similar depths (9.3 km/sec vs. 8.4 km/sec for P waves). The outstanding feature of the results for three-dimensional velocity structures is a broad (>40 kilometers), centrally located region with 8% to 10% lower velocities than those in the surrounding regions. This low velocity region envelopes the seismic zone at depths between 70 and 150 kilometers. The region may actually extend beyond these depths, but the results for shallower and deeper structure lack sufficient

resolution to decide. Several tests, using both hypothetical and real data, were performed to estimate the reliability of the three-dimensional solutions. The results of these tests suggest that the inferred velocities are reasonably accurate representations of the average velocities in the blocks, although one must be cautious of the effects of averaging in interpreting the solution. The low velocity region is inferred to be a manifestation of substantial quantities of subducted continental crust. Therefore, while subduction has occurred in the Pamir-Hindu Kush, the results of the three-dimensional inversions suggest that continental, rather than only oceanic, lithosphere has been subducted to depths of at least 150 kilometers.

INTRODUCTION

Throughout their histories, continents have been modified extensively by collisions with island arcs and other continents. Discerning collision processes is therefore fundamental to understanding continental development. However, since there are presently no incipient continental collisions, we must deduce these properties solely from their aftereffects - a difficult task if only because it is never clear how much or what kind of material originally existed between the collided members. Such uncertainty naturally gives rise to controversies, one of which concerns the subduction of continental crust.

In several collision regions, including the Himalaya [Gansser, 1966; Peive, 1964], the Calidonides [Gee, 1975], the Alps [Laubscher, 1971; Oxburgh, 1972], and the Carpathians [Burchfiel, 1980], there is geologic evidence of thin (15 km) allochthonous nappes or thrust sheets that have traversed hundreds of kilometers over an autochthon. These sheets are believed to represent a portion of the subducted lithosphere that was stripped off and left behind. If the subducted lithosphere had a crust of normal thickness (35 km), the thinness of the sheets implies that much of the crust was subducted along with the rest of the continental lithosphere.

Assuming average values for the density, temperature, thermal expansion coefficient, and thickness of the

continental crust and lithosphere, it can be shown [Molnar and Gray, 1979] that the continental lithosphere can sink under its own weight if only 10 kilometers or less of its crust remains attached to it. Molnar and Gray also showed that if a heavy oceanic slab can transmit stress to the surface, then a substantial amount of crust may be subducted before the negative buoyancy of the slab is compensated. In either of these situations, however, the uncertainties are such that the limits on the length of subducted crust range from a few kilometers to a few hundred kilometers. In extreme cases, even the steady state subduction of crust may be possible.

Geophysicists tend to argue against the wholesale subduction of continental crust, however, principally because of the lack of evidence for it. Observations that would imply either the presence of, or the conditions necessary for, subducted crust have yet to be made.

One may gain insight into controversies such as subducted crust by examining the deep structure of a collision zone in some detail. A geophysical method that suits this purpose is the inversion of compressional (P) and shear (S) wave arrival times for a three-dimensional velocity structure. Since its original inception by Aki et. al. [1976] and Aki and Lee [1976], several authors [e.g. Cockerham and Ellsworth, 1979; Ellsworth, 1977; Horie, 1980; Hirahawa and Mikumo, 1980; Raikes, 1980; Romanowicz, 1980; Zandt, 1978] have used this technique, or modifications of

it, to study the deep structure of various tectonic regions.

The only data that this technique requires are the arrival times of several earthquakes at an array of stations situated over the area in question. If the area is relatively inactive, one must maintain the array for a period of time long enough (perhaps years) to record a reasonable distribution of large, distant events. If, on the other hand, the area is seismically active, a sufficient amount of data may be acquired in a relatively short period of time (weeks). Unfortunately, there are at present few long term arrays situated over known collision regions. There is, however, at least one collision region that is seismically active below depths of a few tens of kilometers - the Pamir-Hindu Kush region of central Asia.

Located at the far western end of the suture between Eurasia and India, the Pamir-Hindu Kush seismic zone represents the last phase of the collision between these two continents. Because of its high (40 recordable events/day) and dispersed (70-300 km depth) activity, this seismic zone provides an excellent opportunity to study the deep structure of a convergent region with a short term array.

The results of an investigation with such an array is the subject of this paper. Using the arrival times of P and S waves from microearthquakes in the Pamir-Hindu Kush, one- and three-dimensional velocity structures of the region are determined, and then are used to comment on the general nature of subduction in collision zones.

DATA

From June 11 to July 13, 1977, 11 smoked paper recorders were operated around the Hindu Kush region of Afghanistan (figure 1). The arrival times of P and S waves recorded during the investigation by either this array or the World-Wide Standardized Seismic Network (WWSSN) station in Kabul (KBL) were used by Chatelain et al. [1980] to locate the microearthquakes of the seismic zone. The techniques employed in reading the records were also discussed in detail by Chatelain et al.

These arrival times constitute the principal database of this study. In addition, some 230 arrival times (also read by the author) from the Soviet station at Khorog (KHO), Tadjikistan (figure 1), are included. KHO is a useful addition since it improves the control over the locations of the many events in the eastern part of the array.

Approximately 1200 events were located using the data discussed in Chatelain et al. On the basis of extensive tests with real and hypothetical data, Chatelain et al. developed criteria for discriminating high quality locations from less reliable ones. These criteria are :

- 1) A minimum of 8 phases are recorded, one of which is an S wave.
- 2) If the azimuthal gap in recording stations is greater than 60 degrees, a minimum of 10 phases are used.
- 3) The root mean square (rms) residual is less than

0.55 seconds.

4) The distance to nearest station is less than one focal depth.

In selecting events to use in the velocity inversion, we modify these criteria slightly. The crude requirement that the rms be less than 0.55 seconds is replaced by one where the standard deviation of all hypocentral parameters is less than 10 km. This rule excludes unstable locations even if the fit to the data appears good, and includes stable locations even if the fit seems relatively poor. Also, the rule excluding events with no stations within one focal depth is relaxed in order to include some of the well-recorded crustal events. Finally, a criterion is added where the condition number of the hypocenter matrix (the ratio of largest to smallest singular values) is required to be less than 100. The reason for this criterion is discussed in the next section.

In all, approximately 580 events comprising some 5000 P and 3800 S arrivals were selected for the velocity inversions (events were reviewed for satisfying criteria as one-dimensional velocity models were changed). The locations of these events are plotted in map view in figure 1.

THEORY

The inverse problems discussed in this paper generally involve fitting arrival time data with a simultaneous solution for the four hypocentral parameters (latitude, longitude, depth, and origin time), S and P wave velocities in one or three dimensional structures, and, occasionally, station corrections. The purpose of this section is to review the mathematical background of the inverse methods used, with particular emphasis on establishing definitions and concepts that will be useful in discussing the results.

General Formulation.

We require a method which fits a set of m observed arrival times, \underline{T}_0 , with a mapping function (or forward problem), \underline{T} , by adjusting a finite number n of discrete parameters, \underline{x} . The standard first step is to express \underline{T} as a Taylor series:

$$(1) \quad \underline{T}_0 - \underline{T}(\underline{x}_0) = \underline{\nabla} \cdot \underline{T}(\underline{x})(\underline{x} - \underline{x}_0) + \underline{e}$$

where \underline{x}_0 is a set of trial values for the n parameters. Equation (1) is linearized by assuming that higher order terms are zero and that \underline{e} represents Gaussian error. In matrix form, (1) is written as

$$(2) \quad \underline{d} = \underline{A}\underline{m} + \underline{e}$$

where \underline{d} is a vector of travel time residuals, and A is an $m \times n$ matrix of partial derivatives. The correction vector $\underline{m} [= (\underline{x} - \underline{x}_0)]$ is determined in the least squares sense by minimizing $\underline{e}^T \underline{e}$. The generalized inverse solution to the least squares problem is [Aki and Richards, 1980]

$$(3) \quad \hat{m} = (A^T A)^{-1} A^T \underline{d}$$

where \hat{m} is an approximation to the true least square solution \underline{m} . All solutions discussed here are of the damped least squares variety, which is a special case of the stochastic inverse [Franklin, 1960; Levenburg, 1944; Aki and Richards, 1980]. In the damped case

$$(4) \quad \hat{m} = (A^T A + \theta^2 I)^{-1} A^T \underline{Am}$$

where θ^2 is the ratio of model variance (σ_m^2) to data variance (σ_n^2), and I is the identity matrix.

The conventional estimators of the reliability of the least squares solution are the resolution matrix, R , and the covariance matrix, C . The resolution matrix expresses the relation between the true least squares solution and our estimate of it as

$$(5) \quad \hat{m} = R \underline{m} = (A^T A + \theta^2 I)^{-1} A^T \underline{Am}$$

If $R = I$ (identity), then $\hat{m} = \underline{m}$ and the solution is perfectly resolved. If any diagonal of R is zero, the corresponding parameter is completely unresolved.

Interpretation of R diagonals falling in between these extremes is somewhat qualitative, but can be useful in discriminating reliable from spurious solutions.

The covariance matrix estimates the standard error of the linear solution as

$$(6) \quad C = \langle \underline{\Delta}_m \underline{\Delta}_m^T \rangle = \sigma^2 (A^T A + \theta^2 I)^{-1} R$$

where σ^2 is an estimate of the variance of the data. The standard deviation of any parameter is the square root of the corresponding diagonal of C. The expression for covariance in equation (6) assumes that the variance for all the data is the same. Note also that the error estimates provided by C are intrinsically related to the assumption of linearity and are therefore only as valid as the linearity assumption is valid.

Joint Hypocenter-Velocity Inversion.

The inversions performed in this study simultaneously solve for perturbations to hypocenter parameters as well as to any additional parameters (velocities or station corrections). Inversions which constrain hypocenters make a usually unjustifiable assumption that there is no coupling between the hypocenter and velocity solutions. The principal drawback to including hypocenter parameters, however, is that each event adds four rows and columns to the matrix of normal equations, thus creating a severe computational storage problem.

Fortunately, methods of parameter separation proposed by Palvis and Booker [1980] and Spencer and Gubbins [1980] allow us to formulate an equivalent problem, which retains only a subset of the parameters. In this study we apply the approach of Palvis and Booker, although the near equivalence of the Palvis and Booker and Spencer and Gubbins formulations can be demonstrated (Appendix A). A brief review of the Palvis and Booker approach is given in the following.

The joint hypocenter-velocity inversion problem can be expressed (from (1)) as

$$(7) \quad \underline{d} = A\underline{h} + B\underline{v} + \underline{e}$$

where \underline{h} contains the hypocenter perturbations and \underline{v} the velocity perturbations. Let us examine the A matrix in some detail. It is well known [Lanczos, 1961], that any $m \times n$ matrix can be decomposed into three matrices

$$(8) \quad A = UV^T$$

where U is an $m \times m$ matrix whose columns are the eigenvectors of AA^T , V^T is an $n \times n$ matrix whose rows are the eigenvectors of $A^T A$, and Λ is an $m \times n$ matrix containing the singular values of A. The column vectors of U are usually described as spanning the data space of A, while the columns of V span the model space of A. Equation (8) can be written schematically as

$$(9) \quad A = \begin{bmatrix} p & n-p & \\ U_1 & U_0 & U_2 \end{bmatrix} \begin{bmatrix} \lambda_1 & & & \\ & \ddots & & \\ & & \lambda_p & \\ \hline & & & 0 \end{bmatrix} \begin{bmatrix} n \\ V_P^T \\ \hline V_0^T \end{bmatrix} \begin{matrix} m \\ n \end{matrix}$$

where p is the number of nonzero singular values.

In any overdetermined system of m equations and p independent parameters ($m > p$) there are p bits of relevant data and $m-p$ bits of extra data. As can be seen in (9), the U_1 portion of the U matrix completely describes the relevant data space, while U_0 and U_2 span the extra data space. All components of the residuals that project onto the U_1 space of A determine the hypocenter solution. All data components orthogonal to U_1 are either relevant to the velocity solution or classified as noise.

The existence of U_2 is guaranteed in any overdetermined system of equations. Further, since the columns of U_2 are orthonormal to U_1 , U_2^T can be used as an annihilator to separate the hypocenter solution from the velocity solution, since

$$(10) \quad U_2^T d = U_2^T B \underline{v} + U_2^T e$$

By employing this method, we can make use of as much data as we like while storing only as many columns and rows as the number of parameters we wish to determine.

Equation (9) shows that when U_0 space (those components corresponding to zero singular values) exists, it can be combined with the U_2 annihilator and thereby increase the amount of extra information that goes into the velocity

solution. One may then conclude that events with large U_0 spaces are preferable sources of velocity data since less data is used in determining the hypocenter. However, the existence of U_0 space implies that there is no control over some part of the hypocenter location. Since velocity derivatives are always dependent in some way on the path of a ray between source and receiver, gross errors in hypocentral coordinates can contribute to gross errors in the estimates of velocity derivatives. Therefore, including events with zero singular values is ill-advised, unless the location of the event is constrained by some other means.

For our purposes, a zero singular value is defined as one whose ratio to the largest singular value is less than 0.01. Events with singular value ratios smaller than 0.01 are excluded from the inversion.

The method used in initially setting up the one-dimensional velocity inversion is essentially the same as that described by Crosson [1976]. Station corrections are included to lessen the effects of any strong, near-station lateral heterogeneities that would not be accommodated by the one-dimensional velocity model. The final solution for hypocenters and velocities is obtained by a two-part iterative procedure. The first part is the separated solution of velocities and station corrections. The second part is the relocation of the hypocenters after these adjustments have been made.

Results from the layered inversions were used as a

starting point for the three-dimensional block inversion. The approach is essentially the same as that presented by Aki and Lee [1976], with some modification of the procedure in which portions of a ray are assigned to the various blocks (see Ellsworth, 1977, for details). The forward problem employs a one-dimensional ray tracing routine which makes the procedure non-iterative.

Use of S waves.

One may wonder about the motivation behind including S wave velocities in the solution, since the number of parameters practically doubles by doing so. Some advantages are that S waves may be more sensitive to changes in tectonic conditions than P waves, and, by correlation, the S wave solution corroborates the P wave solution. But the real advantage of adding S waves lies in the added accuracy they lend to the hypocenter location. Not only do S waves stabilize a location in a given velocity structure, as is often advertised, but tests performed by Chatelain et al. suggest that locations with S waves are much less sensitive to variations in the velocity structure than when only P waves are used. In the vocabulary used above, S waves appear to rotate the U_1 space of the hypocenter matrix out of the U_1 space of the velocity matrix, thereby uncoupling the solutions.

Note that one cannot take the short-cut of using a location deduced with P and S waves and then use only P

waves in solving for a velocity structure. The hypocenter matrix using P waves alone has a different U space than that for P and S, and therefore different components of residuals project onto the hypocenter solution. Similarly, one cannot include S arrival data in the solution and keep S wave velocities fixed, since, as in the joint hypocenter-velocity case, some coupling may exist between the parameters. It is theoretically possible to separate the solutions for P and S velocities in the same fashion as hypocenters and velocities, but it is computationally much more difficult to do so. The only viable way to take advantage of the accuracy provided by S waves is to allow S wave velocities to vary.

Progressive Solutions

In approximating a linear relationship between residuals and corrections, we assume either that the partial derivatives are constants or that the corrections are small. Violations of this assumption introduce instabilities due to nonlinearity.

To minimize the effects of nonlinearity, a solution is obtained by progressively varying parameters, rather than by allowing all of the parameters to vary at once. That is, only the least sensitive parameters (i.e., those with the smallest partial derivatives) are allowed to vary first, then the next least sensitive, and so on until all the parameters vary. With each step the residuals, and

therefore the potential sizes of the corrections, are reduced, and nonlinear effects are lessened.

It is important that the least sensitive parameters continue to vary while solving for the most sensitive ones so that any biasing introduced by the progressive solution can be detected. For example, it could happen that certain components of the residual vector project in the same way onto the data (U_1) spaces of fixed and free parameters. These residuals will be satisfied by the free parameters since they are corrected first. Then later a minimal correction to the fixed parameters will result when they are allowed to vary. If we solve for the second set of parameters without allowing the first to vary, we may wrongly conclude that the solutions for all the parameters are well resolved. A more honest estimate will be had if resolution is calculated with all the parameters allowed to vary.

For the inversions performed here, the order in which parameters are allowed to vary is: hypocentral latitude and longitude, hypocentral depth and origin time, layered velocities and station corrections, and, finally, fractional slowness change in the block structure. This hierarchy is dictated by the typical size of the partial derivatives associated with each of these parameters.

APPLICATION - PART I: TOWARDS A STARTING MODEL

In this section we describe how the theories discussed above are applied in determining one-dimensional velocity structures in the Pamir-Hindu Kush. These structures will be used as starting models for the three-dimensional inversions.

Hypocenter Locations

A first estimate of hypocenter locations was provided by the HYPO71 location routine [Lee and Lahr, 1971]. The results of the HYPO71 runs are discussed at great length by Chatelain et al. All the hypocenters were relocated in the various one-dimensional models before and after inverting for the best-fitting layered structures. These relocations were performed with a routine that computes a singular value decomposition of the hypocentral matrix so that the quality criteria discussed in the DATA section could be applied. The result of the relocations pertinent to this study is that, as the one-dimensional models varied, the hypocentral coordinates rarely changed substantially (never more than 10 km in any direction and usually much less).

One-Dimensional Solutions

The one-dimensional, or layered, inversions provide an estimate of how velocity varies with depth. The inversions solve for P and S wave velocities within a fixed set of

horizontal boundaries, along with travel time corrections at each station (hypocentral parameters are obtained separately, as discussed previously). Since we assume that the velocity in each layer is constant, the solutions, at best, represent the average velocities between the layer boundaries. If the velocities change smoothly with depth, similar solutions will be obtained no matter where the boundaries are placed. However, if the boundaries are deep enough, they will cross at least one abrupt change in velocity at the Mohorovičić discontinuity (or Moho), and possibly another at the beginning of the low velocity zone (LVZ). To estimate the depth of these transitions, it is necessary to compare inversions that employ different configurations of boundaries.

In all, four one-dimensional inversions were attempted: three with two-layered crusts and with Mohos at 70, 80, and 90 kilometers depth, and one with a five-layered crust with (initially) gradually increasing velocities with depth. The results of all the one-dimensional inversions are shown in figures 2-5, and an overlay of the results of the inversions with two-layer crusts is shown in figure 6. Two features dominate these solutions: one, a rapid increase in the velocity between approximately 40 and 90 kilometers, and two, a velocity reversal somewhere between 150 and 220 kilometers. To first order, one may infer that the boundaries of the crust and LVZ lay within these limits.

Position of the Moho.

The five-layer crustal model is an attempt to detect a preferred discontinuity by relaxing the requirement that the Moho occur at a particular depth. The results (figure 2) show a substantial increase in both P and S wave velocities at the 60 kilometer boundary, with standard mantle velocities beginning at 80 kilometers. Taken at face value, this result suggests that the Moho lies between 60 and 80 kilometers depth.

One must be cautious in interpreting this solution, however, because there are almost no events between 30 and 70 kilometers depth. Layers with few sources are notoriously unstable and poorly resolved, and, indeed, the layers between 20 and 100 kilometers vary substantially from the first to the second iteration. Most noticeable is the tradeoff between velocities in the layers beginning at 60 and at 80 kilometer depth, which makes the lower estimate of the Moho suspect. Therefore, while the depth of the Moho is certainly greater than 60 kilometers, it might perhaps be greater than 80 kilometers.

In contrast to the five-layer crust, the two-layer crusts have stable solutions. Of the three, the solution with the Moho at 70 kilometers shows the largest contrast between lower crust and upper mantle, and is also closest to what is considered to be normal velocities for these two regions (6.4 km/sec and 8.1 km/sec for P, 3.7 km/sec and 4.7 km/sec for S, figure 6). Comparing this result with the

five-layer crust solution suggests that the Moho is at approximately 70 ± 5 kilometers depth. This figure is in agreement with that given by Krestnikov and Nersesov [1964] and McGinnis [1971] for crustal thickness in this area.

Low Velocity Zone (LVZ)

In each of the layered inversions a velocity reversal occurs at depths of 150 to 210 kilometers. Comparison of inversions suggests that this boundary is most likely at about 160 kilometers. The lower boundary of the reversal appears to be at less than 230 kilometers depth, but, because of lack of resolution, it is not clear how much less.

The uncertainties in interpreting this reversal as the LVZ are first that, as in the lower crust, the fewer events in the reversal region make for an unstable solution, and second that the velocity below the reversal is higher than the normal mantle velocity for similar depths.

The arguments supporting the LVZ interpretation are that the inferred depths of the boundaries of the reversal at 160 and 230 kilometers are close to typical depths for the LVZ, and that both P and S wave velocities in the 160-200 kilometer layer (figures 4 and 6) are close to standard values for the LVZ. The low activity in the region is also consistent with an LVZ interpretation. In fact, there is a recognizable gap in the activity at about 160 kilometers depth (see figure 9 of Chatelain et al. and figure 7). Even

if the solution is somewhat unstable because of the low activity, the reversal seems too substantial to deny its existence. In regard to the unusually high velocities below the reversal, note that the events below the gap in activity presumably occur in dense (and therefore high velocity), subducted oceanic lithosphere. Based on the relative locations of events above and below the 160 kilometer depth gap, Chatelain et al. suggested that the subducted lithosphere is discontinuous in this region. Under such circumstances, a thin wedge of asthenosphere might have penetrated between the two pieces of subducted lithosphere and thus create a narrow region of low velocity.

Station Corrections.

As mentioned before, station corrections are included in the solution to allow for any near-receiver, lateral heterogeneities that would create instabilities in the layered solution. One must have some appreciation for whether the scale of these anomalies is closer to one kilometer or one hundred kilometers, since the three-dimensional inversions without station corrections implicitly assume that the scale is on the order of the block size (usually about 40 kilometers in this case).

The major source of small scale heterogeneities is relatively thick sediments underlying any of the station sites. Fortunately, there is some evidence suggesting that such thick sediments do not exist. First, most of the

stations are located on either Paleozoic crystalline basement or on competent metamorphic schists and gneisses [Desio, 1975; Boulin, 1972; De Lapparent, 1972; Mennessier, 1972]. Sediments under the remaining stations appear to be thin (< 200 meters). Second, in a study of the coda of Hindu Kush earthquakes, Roecker et al. [1981] found that the excitation of the coda is nearly the same at four of the stations (JOR, FAR, PEN, and CHS) surrounding the zone. Since coda amplitudes are notoriously sensitive to near receiver anomalies (e.g. Tsujiura, 1979), similar coda excitations imply that near-receiver conditions are similar. From this evidence, we presume that station corrections result from some large scale (i.e. tens of kilometers), rather than local, lateral heterogeneities.

The station corrections deduced in the layered inversions are listed in Table 1. The results can be summarized by noting that most of the stations to the northwest and southeast of the seismic zone (FDZ, FRA, KUY, SAL, and CHS) have negative corrections while stations to the southwest and northeast (PEN, GOU, and KHO) have positive corrections.

APPLICATION PART II: THREE-DIMENSIONAL VELOCITY STRUCTURES

The inversion for three-dimensional velocity structures involves dividing the layered structures of the previous section into blocks, and then determining the changes in the blocks' fractional slownesses that best fit

the residuals. In this section we discuss the results obtained by applying this method to deduce lateral variations in the Pamir-Hindu Kush region.

Overview

In all, eight three-dimensional inversions were performed, using various starting models and subsets of data. The starting models for these inversions are the best-fitting layered structures discussed in the previous section. Except in one case, station corrections are not applied. The details of the starting models are listed in Table 2.

The blocks are usually cubes of 40 kilometers dimension. While the choice of block size is primarily dictated by storage limitations, solutions with blocks of much smaller dimensions (20 kilometer cubes) proved to be poorly resolved. The orientation of the blocks is governed by the concentration of ray paths in each layer. A representative plot of the number of times the blocks are sampled by rays is shown in figure 8. Only those blocks that are sampled by at least 20 rays are included in the inversion.

The results of the three-dimensional inversions are presented in two formats. First, the percent change of the initial velocities in each block, along with corresponding resolution and covariance diagonals, are superimposed on a simplified tectonic map (figure 9). Second, contours of

percent changes in velocities are shown on a similar map. Results of inversions AF2, AF4, AF9, and AF10 are shown in figures 10-17 in this text, and all other solutions appear in Appendix C. In addition, a vertical crosssection of the lateral changes in velocity inferred from the AF2 inversion is shown in figure 18.

To first order, the results of all the inversions are similar. First, resolution deteriorates with depth. The two main reasons for the deterioration are that the seismic zone thins with depth, restricting the region through which the rays pass, and that the velocity derivatives from approximately vertical rays couple with changes in the hypocentral origin time. Velocity variations below about 150 kilometers depth are thus difficult to discern. Second, in nearly every layer of each inversion, the P and S solutions correlate well. Third, in nearly every case there is a significant reduction in the data variance (>50%), and the resulting variance is near the assumed noise level in the data (0.1 seconds). Finally, there is a broad, centrally located, low velocity region that extends from the near-surface to some unresolved depth. This last result is unusual, since the earthquakes occur in the blocks with low velocities. In most subduction zones, active regions are normally associated with cold, subducted lithosphere, which implies the presence of high velocities.

Estimations of Reliability

The first question that comes to mind when an inverse solution is presented is How much can one believe? The answer to this question is nontrivial when one considers how solutions may be affected by problems such as nonlinearity and improper parameterizations, which were implicitly assumed not to exist. While necessary, a lengthy discussion of the possible effects of situations for which one or more assumptions is violated is somewhat tedious and is relegated to Appendices B and C. Only the salient results of these appendices are summarized here.

The following results were obtained through the hypothetical tests discussed in Appendix B. If, in a laterally heterogeneous medium, the regions of differing velocities are not confined to short wavelength features (i.e. features smaller than the block dimension), the block parameterization provides a reasonable lens through which we may view the velocity structure. If, on the other hand, such features do exist, the lens may distort the image: exaggerating variations in some regions and underestimating them in others. Often it is difficult to distinguish such distortions from reality without any a priori information. However, there are a few traits associated with distortions that, although often not diagnostic, should be kept in mind when interpreting the solutions. (1) A basic rule is that the inferred velocities should be contourable. Trends should persist in several adjoining blocks instead of being

defined by the fluctuations in a single block. This rule applies to variations from one layer to the next as well as to variations within a layer. (2) Large variations in velocity that occur at the edges of layers with few events are unreliable, and extreme variations in regions of low activity can be exaggerated. (3) High amplitude, short wavelength variations that occur outside of the seismic zone can cause a misrepresentation of the velocity in the surrounding regions, and thus may be inferred to be much wider than they are.

Some estimates of the applicability of the conventional estimators also result from the hypothetical solutions. First, a reasonable cutoff value for resolution (equation 5) is about 0.6 for P velocities and 0.5 for S velocities (lower for S because the S wave data are weighted less). Second, for the array used and for the types of anomalies modeled, variations less than two percent are probably insignificant, even if the linear error estimate is less than two percent. These two rules are applied to the solutions before the contours of figures 11, 13, 15, and 17 are drawn.

The results from runs using various subsets of real data (Appendix C) allow us to conclude that coupling between layers does not significantly change our interpretation of the velocity structure of the medium, except perhaps in the relatively event-free regions shallower than 70 kilometers depth. Further, it appears that the estimates of velocity

variations in a layer are principally controlled by the data from events in the layer.

The discussions in Appendices B and C apply these interpretation rules to the inverse solutions, and also consider the existence of assumption-violating situations that may cause a misrepresentation of velocity by the solution. The general conclusion from these discussions is that, while one must be mindful of the approximations of the method, the systematic variations in inferred velocity of several percent provide a reasonably accurate description of the real velocity structure.

Extent of the Low Velocity Zone.

Having girded our loins against the shortcomings of the method, a general description of the three-dimensional velocity structure of the Pamir-Hindu Kush can be given. Most of the following description is synthesized from inverse solutions AF2, AF9, and AF10 (Table 3, figures 10-15 and figure 18). These runs use the two-layered crust results discussed in the section on one-dimensional inversions as a starting model.

Crust (0 - 70 km)

Determination of the velocity structure in the crust is hampered by both the large, unsampled region in the center of the upper crust, and the apparent coupling that exists between the upper and lower crustal solutions (see

Appendix C). Still, some general comments may be made. Low velocities in the upper crust are associated with the stations PEN, GOU, and KHO. In the northeast, the boundary between high and low velocity regions coincides with the Darvas-Karakul fault, although this may be a fortuitous compensation for the large low velocity anomaly associated with KHO. The low velocities near the station GOU appears to begin at shallow depths (<35 kilometers) and migrate northwards to join the low velocity region near PEN, which begins at a depth of approximately 30 kilometers. Again, because of coupling, the low velocities near GOU may occur at greater depths, and the low velocities near PEN at lesser depths, than the solution indicates.

Upper Mantle (70 - 120 km)

From approximately 70 to 120 kilometers depth, the low velocities near PEN develop into a prominent east-west feature, the eastern and western boundaries of which are beyond the extent of the array. The northern boundary closely follows the trend of the seismicity, changing from an east-west orientation in the west to a northeast-southwest orientation in the east. The southern boundary also appears to be oriented east-west, but its position is less well known. Run AF4 (Table 3, figures 16 and 17) is an attempt to trace this boundary by employing narrower blocks, but little of the solution can be resolved in the south. In any event, the low velocity region probably has a maximum

thickness of 60 kilometers at its narrowest point, near 68° E, and becomes broader to the east and west. The maximum velocity contrast given by the inversion is 14%, but may be closer to 8% since the region of highest contrast is also a region containing relatively few sources.

Deeper Mantle (120 - 300 km)

The low velocity region is continuous to depths exceeding 120 kilometers. In fact, strong correlations between low velocities and seismicity can be found to the limits of resolution with depth, which is about 200 kilometers. Below depths of about 150 kilometers, however, the number of resolvable blocks is small and it is not clear to which, if any, tectonic features the lows and highs should be related. In any event, it appears that the low velocity zone extends to at least some 150 kilometers depth.

DISCUSSION

Because the patterns of seismicity in the Pamir-Hindu Kush resemble those of normal subduction zones, it seems reasonable to infer that subduction has taken place in this region. Instead of the typically high velocities associated with the seismicity in subducted oceanic lithosphere, however, the seismic zone of the Pamir-Hindu Kush is a region of abnormally low velocity. As a general conclusion, we infer from this result that the nature of the subduction in the Pamir-Hindu Kush is significantly different from that in typical subduction zones.

Because the low velocity region appears to extend continuously into the mantle from depths shallower than the Moho, we infer that the lower velocities are a manifestation of subducted crust. In this section, we discuss some of the corroborating evidence for and tectonic implications of this inference, and speculate on some of the physical processes which may facilitate the subduction of crust.

Gravity

The spatial relation of the measured gravity anomalies [Marussi, 1963; McGinnis, 1971] and average elevations in the Pamir-Hindu Kush to the low velocity region in the mantle is shown in figures 19 and 20. The dominant feature of the gravity profiles is a broad (~400 kilometers), negative (~-80 mgals) isostatic anomaly. Negative isostatic

anomalies imply a deficiency of mass, and, therefore, the gravity data do not conflict with the inference of subducted crust. The patterns in the anomalies are rather complicated, however, probably because mass deficiencies created by other types of tectonic activity are contributing to the overall anomaly. For example, the maximum negative anomaly is not centered over the low velocity region but occurs over the Tadjik depression to the north. Therefore, attempts to draw any additional inference from the gravity data in support of subducted crust are tenuous.

On the other hand, if the crust is subducted in the quantities suggested by the velocity inversions, then the crust probably does not retain its original density. As shown in Appendix D, the anomaly created by a 40 kilometer thick slab of crust between 70 and 150 kilometers depth and with a density 0.5 gm/cm^3 less than the surrounding mantle would produce a maximum anomaly of ~ -200 mgals that decays to -100 mgals at about 100 kilometers from the peak. The maximum anomaly is more than twice the magnitude of the observed anomaly, which suggests that more appropriate density contrasts between mantle and subducted crust are closer to 0.25 gm/cm^3 .

Effects of Phase Transformations

Richardson and England (1978) argued that if a crust of normal thickness were overthrust by a 30 kilometer thick nappe, the substantial pressure and minor temperature

increases would cause the low density amphibolite or granulite facies (2.85 gm/cm^3) of the lower crust to turn into higher density eclogite facies (3.15 gm/cm^3). A similar argument can be made for eclogite phase transformations in subducted crust, as long as the subduction occurs rapidly enough that the crust maintains its relatively cold temperatures. In addition, it is possible that at depths exceeding approximately 120 kilometers, quartz (2.65 gm/cm^3) will transform into coesite (3.01 gm/cm^3).

The increased density resulting from phase transformations (~15% from granulite to eclogite) would decrease the buoyancy of the unadulterated crust by a factor of about 2, thereby making it easier to subduct in great quantities. One may further imagine that if the subducted crust undergoes relatively rapid transformation, the negative buoyancy of the rest of the continental lithosphere may be enough to maintain steady state subduction after a collision. Moreover, the increased density would reduce the effect of subducted crust on the gravity anomaly.

Phase transformations may also increase the magnitude of the velocities in the subducted crust. An application of Birch's law (Birch, 1961) suggests that the P wave velocity in the higher density eclogite facies would be about 1.0 km/sec higher than that in the original granulite facies. This increase in velocity is in accordance with the inferred velocities in the low velocity region, which are closer to

7.5 km/sec than the average lower crustal velocity of 6.5 km/sec.

Except under near-surface conditions, crustal materials are generally considered to be too weak to undergo catastrophic deformation. It is curious, therefore, that the earthquakes in the Pamir-Hindu Kush seismic zone should occur in subducted crust. One explanation may be that crustal materials become stronger after certain phase transformations. Alternatively, McGarr [1977] suggested that large stress concentrations would result from either the vacuum left by a rising crustal melt or the volume change associated with a phase transformation. The rapid application of a large amount of stress resulting from these processes may facilitate the occurrence of earthquakes in a normally ductile medium. Finally, the volume change associated with the transformation may itself be a cause of the earthquakes [e.g. Randall, 1966].

The locations of events in the Pamir-Hindu Kush from 70 to 160 kilometers depth are scattered in a 30 kilometer thick region (figure 6 in Chatelain et al.) rather than being confined to a thin (less than 10 km), planar region as in most subduction zones. This scatter in locations occurs even though the configuration of the array is best suited for locating events in this depth range (see Appendix A of Chatelain et al.), and persists in master event relocations [T.J. Fitch, unpublished results, 1979]. Furthermore, the fault plane solutions in this region show no consistent

pattern. While the relation between these observations and phase transitions may not be obvious, it seems likely that, at least in this depth range, different physical processes are associated with subduction in the Pamir-Hindu Kush than in normal subduction zones.

Tectonic Implications

The major implication of the results of this study is that it is possible to subduct substantial amounts of continental crust. This implication is especially relevant to regions where continental collisions have taken place, since at least one of the collided members was at one time connected to a slab of downgoing oceanic lithosphere. A cartoon illustrating the configuration of the subducted crust in the western Hindu Kush along with related tectonic features is shown in figure 21.

Combining the results of this paper with those of Chatelain et al., one can draw some inferences about the tectonics of the Pamir-Hindu Kush. For instance, Chatelain et al. argued that subduction rates in the Pamir-Hindu Kush have been between 20 mm/year and 43 mm/year. If, as this study suggests, crust has been subducted to 150 kilometers depth, these rates imply that the crust has been heating up in the mantle for a length of time on the order of a few million years. Such a time span is probably too short for the crust to completely assimilate into the mantle, but is perhaps long enough for relatively sluggish reactions (e.g.

alkali feldspars to kyanite or hollandite) to run.

Chatelain et al. also pointed out that while the patterns in the seismicity and fault plane solutions in the upper 160 kilometers of the Pamir-Hindu Kush are unusual for a subduction zone, the seismicity beneath about 170 kilometers is confined to a narrow region and the corresponding fault plane solutions consistently reveal reverse faulting with nearly vertically oriented T axes. The results of the one-dimensional inversions suggest that velocities below about 200 kilometers are higher (~ 9.3 km/sec vs. 8.4 km/sec for P waves) than those of normal mantle at similar depths. It could be, therefore, that the subducted oceanic lithosphere begins at these depths.

Finally, we note that the low velocity region in the mantle is broad (>40 kilometers), and extends upwards into the lower crust. Moreover, the velocities of the low velocity region in the lower crust are similar to those of the upper crust (~ 6.0 km/sec). These results suggest that a significant amount of upper crustal material is residing in the lower crust, and possibly in the mantle as well. Therefore, it is possible that the entire, rather than just the lower, crust has been subducted beneath the Pamir-Hindu Kush.

SUMMARY

Because relatively few stations were operated during the 1977 investigation of seismicity in the Pamir-Hindu Kush, it was necessary to use data from many events in determining the velocity structure of the region. By employing the methods of parameter separation introduced by Palvis and Booker [1980] and Spencer and Gubbins [1980], we were able to use a sufficiently large number of events in the inversions for velocity structures without challenging computational storage limitations. The inversion procedure allowed hypocentral parameters, one- or three-dimensional velocity structures for both P and S waves, and, on occasion, station corrections for P and S arrival times, to vary simultaneously.

The results of inversions for one-dimensional velocity structures suggest that the Moho is at 70 ± 5 kilometers depth, and that the low velocity zone (LVZ) begins at approximately 160 kilometers depth. The LVZ continues to about 230 kilometers depth. The mantle beneath this depth has a higher velocities (9.3 km/sec vs. 8.4 km/sec for P waves) than those of normal mantle at similar depths.

The velocities inferred from the three-dimensional inversions outline a broad (>40 kilometers), centrally located region of low velocities extending from somewhere in the lower crust (35-70 kilometers) to depths possibly greater than 150 kilometers. The low velocity region

envelopes the seismic zone, and its velocities are about 8% to 10% lower than those of surrounding regions.

Several three-dimensional inversions were performed with both hypothetical and real data in an effort to estimate the reliability of the inferred velocities. The results of these tests can be summarized as various rules of interpretation, some of which may apply to three-dimensional velocity inversions in general. We find that reliable solutions are usually contourable. The resolution diagonals associated with reliable results are greater than about 0.6. Variations in velocity less than 2% seem to be insignificant, even if the linearly estimated standard deviation is less than 2%. Large changes in inferred velocity occurring on the edges of layers with few sources are generally unreliable. Finally, while the inferred velocity in a block usually represents an average of the actual velocities, some velocities may be completely misrepresented by the broadening of small scale, isolated anomalies. Application of these rules of interpretation to the three-dimensional inversions suggests that the results are generally reliable, although one must be mindful of the effects of the averaging of adjacent regions with abrupt changes in velocity.

Because the Pamir-Hindu Kush seismic zone is probably related to the subduction of oceanic lithosphere prior to the collision of India and Eurasia, the inferred low velocity region around the seismic zone is an unexpected

result; high velocities normally accompany subduction zones because oceanic lithosphere is colder than the surrounding asthenosphere. We infer from this result that while the seismic zone of the Pamir-Hindu Kush is related to subduction in the region, the low velocities enveloping the zone are due to the subduction of a substantial amount of continental crust, and therefore the upper 150 km of subducted lithosphere is not oceanic but continental.

While the patterns in the gravity anomalies in the Pamir-Hindu Kush are too complicated to permit any definite conclusions, the large, negative isostatic anomalies over the low velocity region imply a substantial mass deficiency which is in accordance with the inference of subducted, low density crust.

For various reasons, one may suspect that the subducted crust does not completely retain its original density. First, the gravity anomaly associated with unadulterated subducted crust would be more than twice that observed. Second, the velocities in the low velocity region are about 1.0 km/sec higher than those in normal crust. Third, although the lower crust is presumably too weak to sustain catastrophic deformation, most of the earthquakes occur in the low velocity region. One possible explanation for these observations is that much of the subducted crust has undergone a phase transformation, resulting in a mixture of crustal and mantle material in the low velocity region.

The subduction of continental crust in collision

regions has long been suggested by geologic evidence. Geophysicists, however, have generally held a prejudice against any suggestion that more than a minor amount of crust can be subducted, because the density of the crust is lower than that of the mantle. We infer from the results of this study that substantial amounts of continental crust may be subducted. Further, in the event of phase transformations or other favorable processes, the steady state subduction of crust may be feasible.

ACKNOWLEDGEMENTS

Carl Spencer generated the hypothetical data used in the thin, high velocity test of Appendix B, and loaned his advice and encouragement. I appreciate his contributions.

I thank J.P. Carbonnel of the Mission Geologique Francaise, J. Summers of the Afghan American Educational Commission, and R.E. Geibson, H. Hafiz, and A.S. Saleem of Kabul University for their hospitality and help in logistical and technical matters. I was ably assisted in the field by J.L. Chatelain, M. Frogneux, X. Goula, D. Hatzfeld, M. Grosenbaugh, J. King, J. Maurer, P. Molnar, R. Prevot, G. Suarez, Brian Tucker, and Afghan engineers Kandari, Osman, Rabi, and Sharif. I thank the Applied Seismology Group of the Lincoln Laboratory for allowing me to use their computing facilities for much of the analysis. This research was supported primarily by NSF grants EAR76-13367A01 and EAR78-13673 and by NASA grants NAG5-19 and NAG5-41, but also by contract ATP No. 35-06 of INAG (Grenoble). The MIT group's part, however was made possible by an H.O. Wood award from the Carnegie Institution in Washington and by an Alfred P. Sloan Fellowship.

References

- Aki, K., and Lee, W.H.K., Determination of the three-dimensional velocity anomalies under a seismic array using first P arrival times from local earthquakes. 1. A homogeneous initial model, J. Geophys. Res., 81, 4381-4399, 1976.
- Aki, K., A. Christoffersson, and E.S. Husebye, Three-dimensional seismic structure of the lithosphere under Montana, LASA, Bull. Seismol. Soc. Am., 66, 501-524, 1976.
- Aki, K., and P. Richards, Quantitative Seismology: Theory and Methods, chapter 12, 932 pp., W.H. Freeman and Company, San Francisco, 1980.
- Birch, F., The velocity of compressional waves in rocks to 10 kbar, part 2, J. Geophys. Res., 66, 2199-2224, 1961.
- Burchfiel, B.C., Eastern European Alpine system and the Carpathian orocline as an example of collision tectonics, Tectonophysics, 63, 31-61, 1980.
- Boulin, J., L'Evolution stratigraphique et structurale de L'Hindou Kouch central, en Afghanistan, d'apres la transversale du Salang, Revue de Geographie Physique et de Geologie Dynamic, (2), 14, 371-382, 1972.
- Chatelain, J.L., S.W. Roecker, D. Hatzfeld, and P. Molnar, Microearthquake seismicity and fault plane solutions in

the Hindu Kush region and their tectonic implications,
J. Geophys. Res., 85, 1365-1387, 1980.

Cockerham R.S., and W.L. Ellsworth, Three-dimensional large
scale mantle structure in central California, E.O.S.
Trans. A.G.U., 60, 875, 1979.

Crosson, R.S., Crustal structure modelling of earthquake
data, 1. Simultaneous least squares estimation of
hypocentre and velocity parameters, J. Geophys. Res.,
81, 3036-3046, 1976.

De Lapparent, A.F., Esquisse Geologique de L'Afghanistan,
Revue de Geographie Physique et de Geologie Dynamic,
(2), 14, 345-356, 1972.

Desio, A., (ed.), Italian Expeditions to the Karakorum and
Hindu Kush, vol. 3, Geology of central Badakhshan
(North-EastAfghanistan) and surrounding countries, 628
pp., E.J. Brill, Leiden, Netherlands, 1975.

Ellsworth, W.L., Three-dimensional structure of the crust
and mantle beneath the island of Hawaii, Ph.D thesis,
Mass. Inst. of Tech., Cambridge, 327 pp., 1977.

Franklin, J.N., Well-posed stochastic extensions of ill-
posed linear problems, Journal of Mathematical Analysis
and Applications, 31, 3682-3716, 1970.

Gansser, A., The Indian Ocean and the Himalayas: A geologic
interpretation, Eclogae Geologicae Helvetiae, 59, 831-

848, 1966.

Gee, D.G., A tectonic model for the central part of the Scandinavian Caledonides, American Journal of Science, 275-A, 468-515, 1975.

Hirahara, K., and T. Mikumo, Three-dimensional seismic structure of subducting lithospheric plates under the Japan islands, Phys. Earth Planet. Inter., 21, 109-119, 1980.

Horie, A., Three-dimensional seismic velocity structure beneath the Kanto district by inversion of P wave arrival times, Ph.D. thesis, Geophys. Inst. Fac. Sci. Univ. of Tokyo, Tokyo, 59 pp., 1980.

Julian, B.R., and D. Gubbins, Three-dimensional seismic ray tracing, J. Geophys. Res., 43, 95-113, 1977.

Krestnikov, V.V., and I.L. Nersesov, Relations of the deep structure of the Pamirs and Tien Shan to their tectonics, Tectonophysics, 1, 183-191, 1964.

Lanczos, C., Linear Differential Operators, Chapter 3, 564 pp., Van Nostrand, New York, 1961.

Laubscher, H.P., The large-scale kinematics of the western Alps and the northern Apennines and its palinspastic implications, American Journal of Science, 271, 193-226, 1971.

- Lee, W.H.K, and J.C. Lahr, HYPO71 (revised): A computer program for determining hypocenter, magnitude, and first motion pattern of local earthquakes, Open File Rep., 75-311, U.S. Geol. Survey, Reston, Va., 1975.
- Levenburg, K., A method for the solution of certain non-linear problems in least squares, Quart. Appl. Math., 2, 164-168, 1944.
- Marussi, A., Le anomalie della gravita lungo la catena del Karakorum-Hindu Kush, Pubblicazioni Dell'Istituto di Geodesia e Geofisica, 198-210, 1963.
- McGarr, A., Seismic moments of earthquakes beneath island arcs, phase changes, and subduction velocities, J. Geophys. Res., 82, 256-264, 1972.
- Menessier, G., Geologie de la chaine d'Altimour (Afghanistan Oriental), Revue de Geographie Physique et de Geologie Dynamic, (2), 14, 341-356, 1972.
- McGinnis, L.D., Gravity fields and tectonics in the Hindu Kush, J. Geophys. Res., 76, 1894-1904, 1971.
- Molnar, P., and D. Gray, Subduction of continental lithosphere: Some constraints and uncertainties, Geology, 7, 58-62, 1979.
- Oxburgh, E.R., Flake tectonics and continental collision, Nature, 239, 202-204, 1969.

Palvis, G.L., and J.R. Booker, The mixed discrete-continuous inverse problem, Application to the simultaneous determination of earthquake hypocenters and velocity structure, J. Geophys. Res., in press.

Peive, A.V., V.S. Burtman, S.V. Ruzhentsev, and A.I. Suvorov, Tectonics of the Pamir-Himalayan sector of Asia, paper presented at the 22nd Session of the International Geological Congress, Sponsor, New Delhi, India, 1964.

Raikes, S. A., Regional variations in upper mantle structure beneath Southern California, Geophys. J. R. ast. Soc., 63, 187-216, 1980.

Randall, M.J., Seismic radiation from a sudden phase transition, J. Geophys. Res., 71, 5297-5302, 1966.

Richardson, S.W., and P.C. England, Metamorphic consequences of crustal production in overthrust orogenic zones, Earth and Plan. Sci. Lett., 42, 183-190, 1979.

Roecker, S.W., B. Tucker, J. King, and D. Hatzfeld, Estimates of Q in central Asia as a function of frequency, depth, and position using the coda of locally recorded earthquakes, manuscript in preparation.

Romanowicz, B., A study of large scale lateral variations of P velocity in the upper mantle beneath western Europe,

Geophys. J. R. astr. Soc., 63, 217-231, 1980.

Spencer, C., and D. Gubbins, Travel time inversion for simultaneous earthquake location and velocity structure determination in laterally varying media, Geophys. J. R. astr. Soc., 63, 95-116, 1980.

Tsujiura, M., Spectral analysis of the coda waves from local earthquakes, Bull. Earthq. Res. Inst., Tokyo Univ., 53, 1-48, 1978.

Zandt, G., Study of three-dimensional heterogeneity beneath seismic arrays in central California and Yellowstone, Wyoming, Ph.D. thesis, Mass. Inst. of Tech., Cambridge, 490 pp., 1978.

Captions

Figure 1. Arrangement of seismographs and location of epicenters used in determining the velocity structure. Station locations are indicated by solid triangles. The epicenters are plotted with symbols corresponding to depth intervals as follows: open circles, $0 \leq z < 70$ km, stars, $70 \leq z < 150$ kms, and Y's, $z \geq 150$ kms.

Figure 2. Results of an inversion for one-dimensional P and S wave velocity structures using a starting model with a five-layer crust. The velocities of the starting model are shown by the thin-dashed lines, the results of the first iteration are shown by the thick-dashed lines, and the results of the second (and final) iteration are shown by the solid lines. The vertical bars on either side of the solid lines represent the standard deviations of the inferred velocities. The diagonals of the resolution matrix are printed alongside the corresponding layer velocity.

Figure 3. Results of an inversion for one-dimensional P and S wave velocity structures using a starting model with a two-layer, 70 km thick crust. Presentation of results is the same as in figure 2. The ratio of P wave velocity to S wave velocity is shown at

the far right of the figure.

Figure 4. Results of an inversion for one-dimensional P and S wave velocity structures using a starting model with a two-layer, 80 km thick crust. Presentation of results is the same as in figure 2.

Figure 5. Results of an inversion for one-dimensional P and S wave velocity structures using a starting model with a two-layer, 90 km thick crust. Presentation of results is the same as in figure 2.

Figure 6. Overlay of the one-dimensional P and S wave velocity structures deduced from starting models with different crustal thicknesses. The thin-dashed line corresponds to the model with a 90 km thick crust, the thick-dashed line to the model with an 80 km thick crust, and the solid line to the model with a 70 km thick crust. Note the significantly greater difference between inferred crustal and mantle velocities in the model with a 70 km thick crust compared to the models with thicker crusts.

Figure 7. A projection of hypocenters onto a cylindrical surface parallel to the seismic zone (H'H in figure 1). The shaded area indicates the gap in seismicity in the depth range of the velocity reversal inferred from the one-dimensional velocity inversions.

Figure 8. A map of the density of the rays at indicated depths. The numbers in the figure refer to the number of rays that pass through the 40 km cubes used in the three-dimensional velocity inversion.

Figure 9. Simplified tectonic map used as a template to display the inferred three-dimensional velocity structures. The numbers on the map refer to the following features: (1) Amu-Darya river, (2) Darvas-Karakul fault, (3) Kunar fault, (4) Panjer fault, (5) Sarubi fault, (6) Chaman fault, (7) Herat fault.

Figure 10. Results of run AF2, an inversion for P and S wave velocity structures using the one-dimensional results of figure 3 as a starting model (70 km thick crust). The four columns in the figure pertain to: (1) Percent changes from the initial P wave velocity, (2) Percent changes from the initial S wave velocity, (3) Standard deviations (upper number) and resolution (lower number) for the P wave solution, and (4) Standard deviations and resolution for the S wave solution. Each row contains all the results for one layer. The layer number and the depth range in kilometers are given at the far left of the figure. The percent changes occurring in boxes with a diagonal slash across them are considered unresolvable. The

small cross which appears near the center of the plots is the center of coordinates for the inversion, which is 36°N , $70^{\circ}30'\text{E}$. The tick marks along the edges of the figure delimit distances of 20 kilometers. All the squares in the figure are 40 kms by 40 kms. The results for layer 7 are not shown because none of the inferred changes in the layer were resolvable.

Figure 11. Contour maps of the percent changes in P and S wave velocity for the upper 5 layers of the AF2 inversion, with the epicenters of the earthquakes in the layers. Only the resolvable changes in velocity were used in drawing the contours. The configuration of the blocks used in the inversion is superimposed upon the seismicity map. The symbols in the upper left corner of the plots are abbreviated labels indicating the layer and phase represented. For example, "AF2 L4S" means "percent changes in S wave velocity for layer 4 of inversion AF2".

Figure 12. Resolvable results of run AF9, an inversion for a three-dimensional velocity structure using the one-dimensional results of figure 5 (90 km thick crust) as a starting model. Presentation of the results is the same as in figure 10.

Figure 13. Contour maps of the resolvable percent changes

in P and S wave velocities in the AF9 inversion, along with the epicenters of the earthquakes used. Presentation of the results is the same as in figure 11.

Figure 14. Resolvable results of run AF10, an inversion for a three-dimensional velocity structure using the one-dimensional results of figure 4 (80 km thick crust) as a starting model. Presentation of the results is the same as in figure 10.

Figure 15. Contour maps of the resolvable percent changes in P and S wave velocities in the AF10 inversion, along with the epicenters of the earthquakes used. Presentation of the results is the same as in figure 11.

Figure 16. Percent changes in P and S wave velocities in layer 3 of run AF4. The starting model in AF4 is the same as the upper 4 layers in AF2, with layer 3 divided into thinner blocks. Presentation of results is the same as in figure 10.

Figure 17. Contour plots of percent changes in velocity in layer 3 of AF4 along with the epicenters of earthquakes occurring in the layer. Presentation of results is the same as in figure 11.

Figure 18. Contour plot of the vertical variations in velocity inferred from inversion AF2, along with the

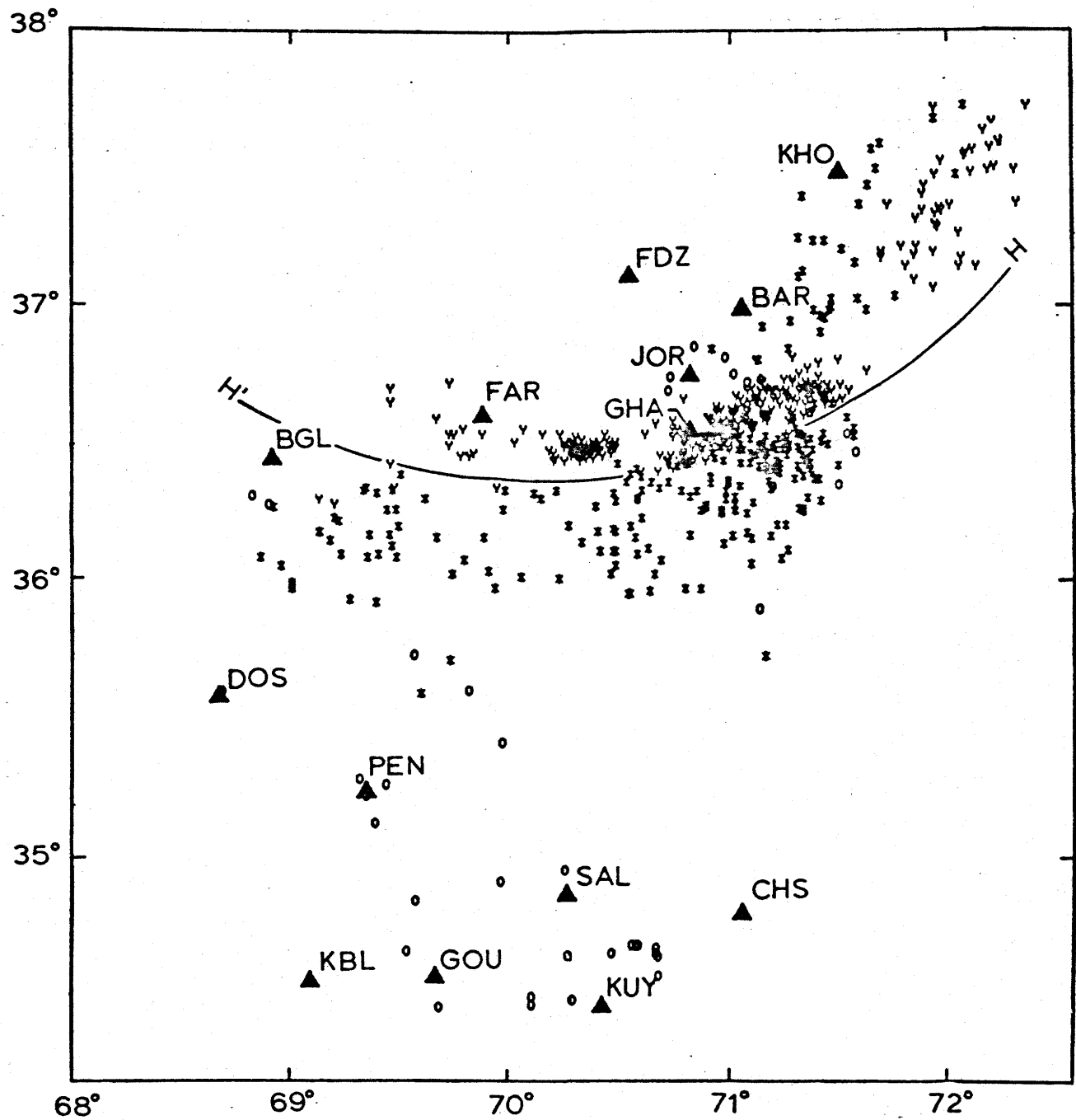
seismicity in the region. The north-south cross-section is made along 69°E . Locations of earthquakes occurring between 68°E and 70°E are indicated by closed circles. Percent changes in P and S wave velocities are shown in the upper and lower parts of the figure, respectively.

Figure 19. Spatial relation of the low velocity region (broad contours) in the upper mantle (70-110 kilometers depth) of the Pamir-Hindu Kush to the isostatic gravity anomalies (thin contours).

Figure 20. Spatial relation of the low velocity region (broad contours) of the upper mantle (70-110 kilometers depth) of the Pamir-Hindu Kush to the mean elevation (thin contours).

Figure 21. Cartoon illustrating the tectonics of the Pamir-Hindu Kush, as inferred from the results of the three-dimensional velocity inversions. The shaded region indicates the location of the seismic zone. The position of the Panjer and Kunar faults is shown at the top of the figure.

Figure 1.



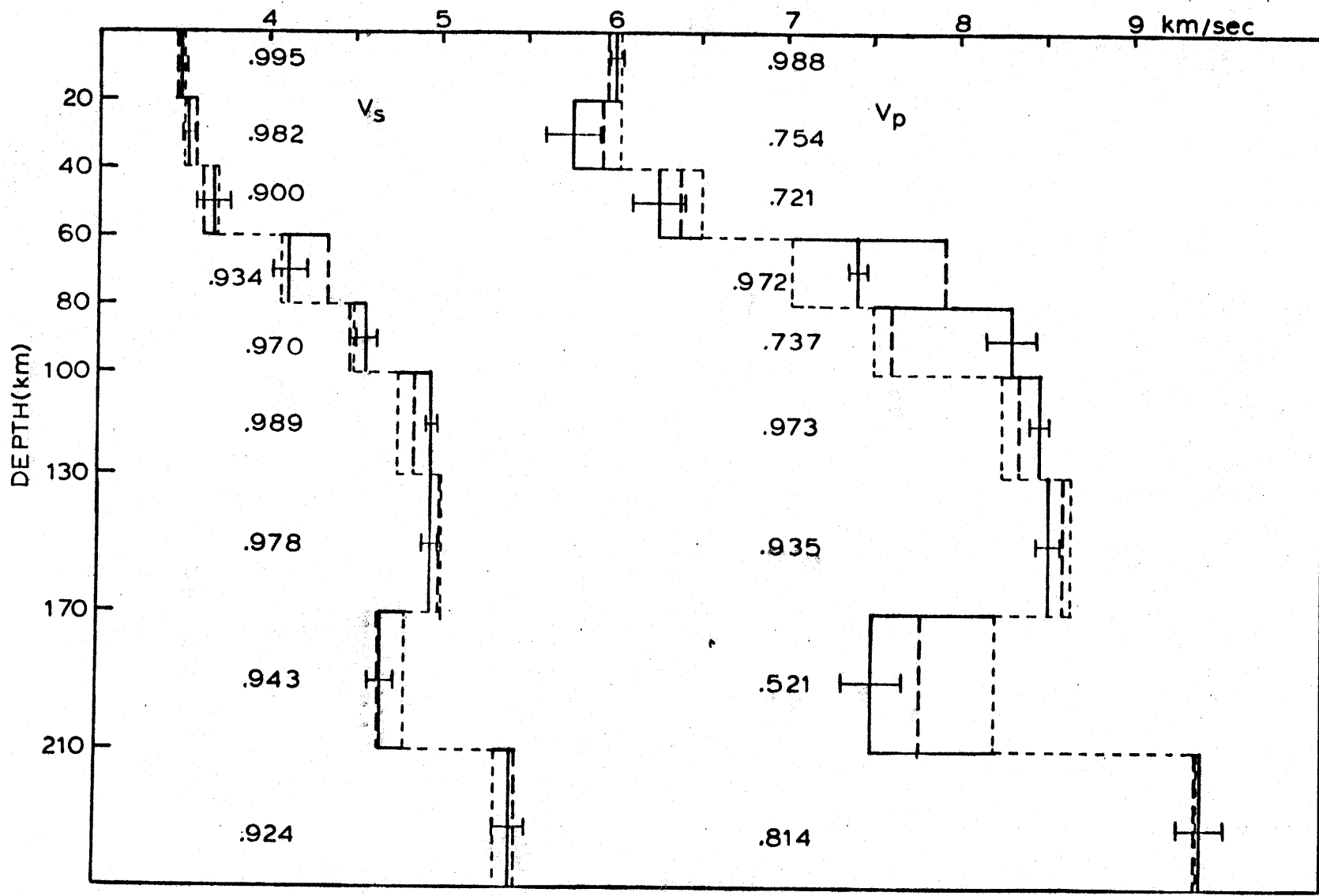


Figure 2.

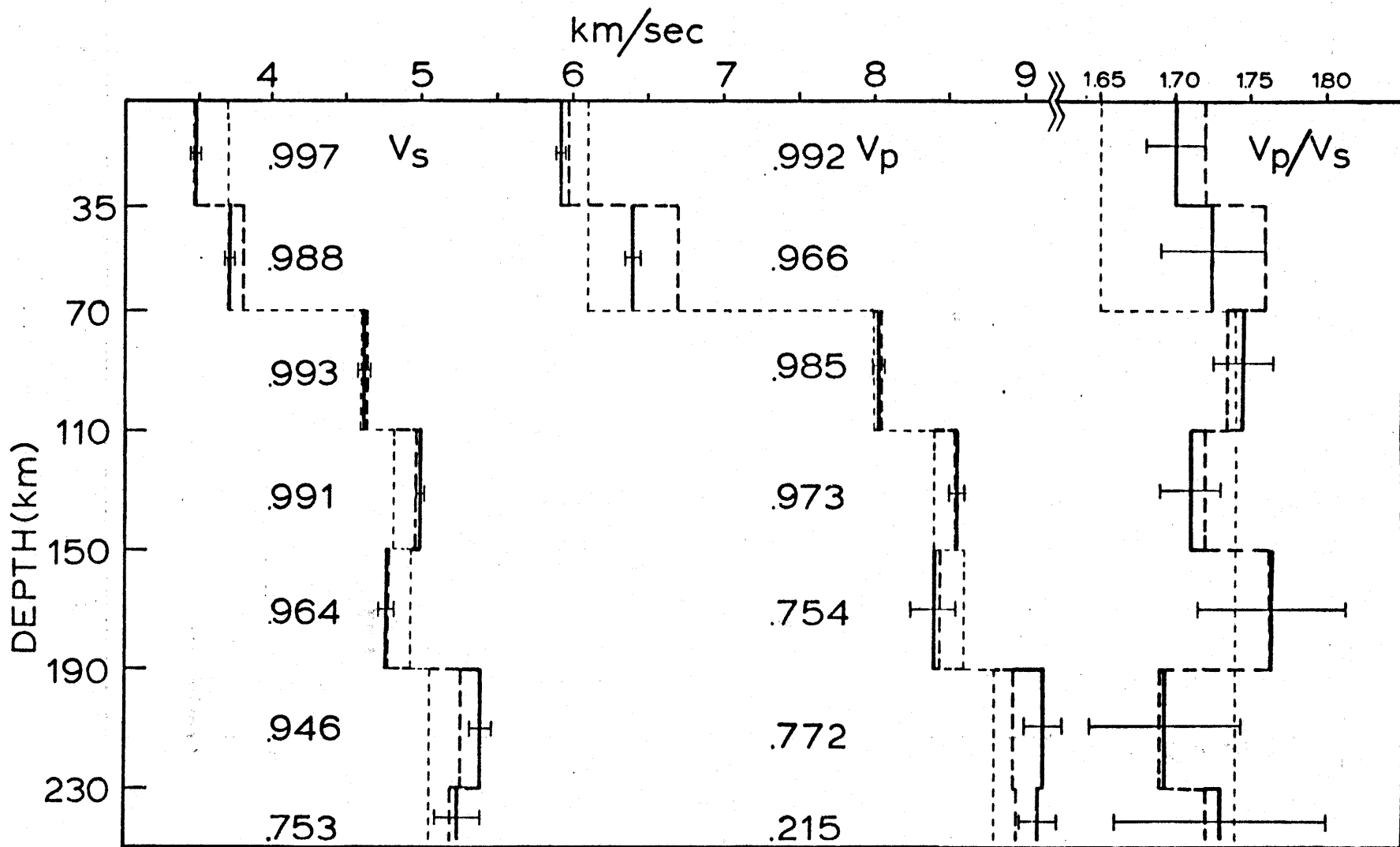


Figure 3.

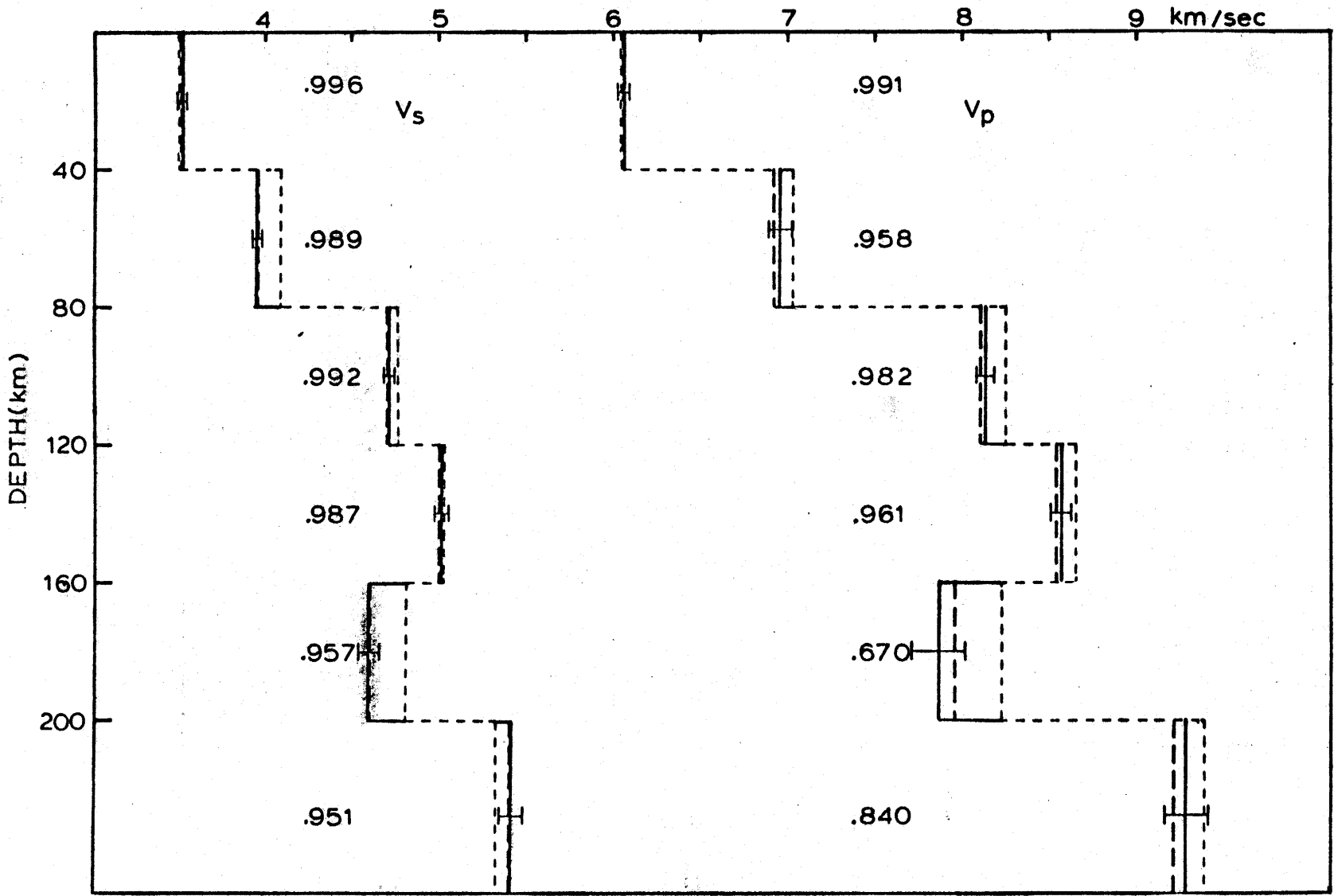


Figure 4.

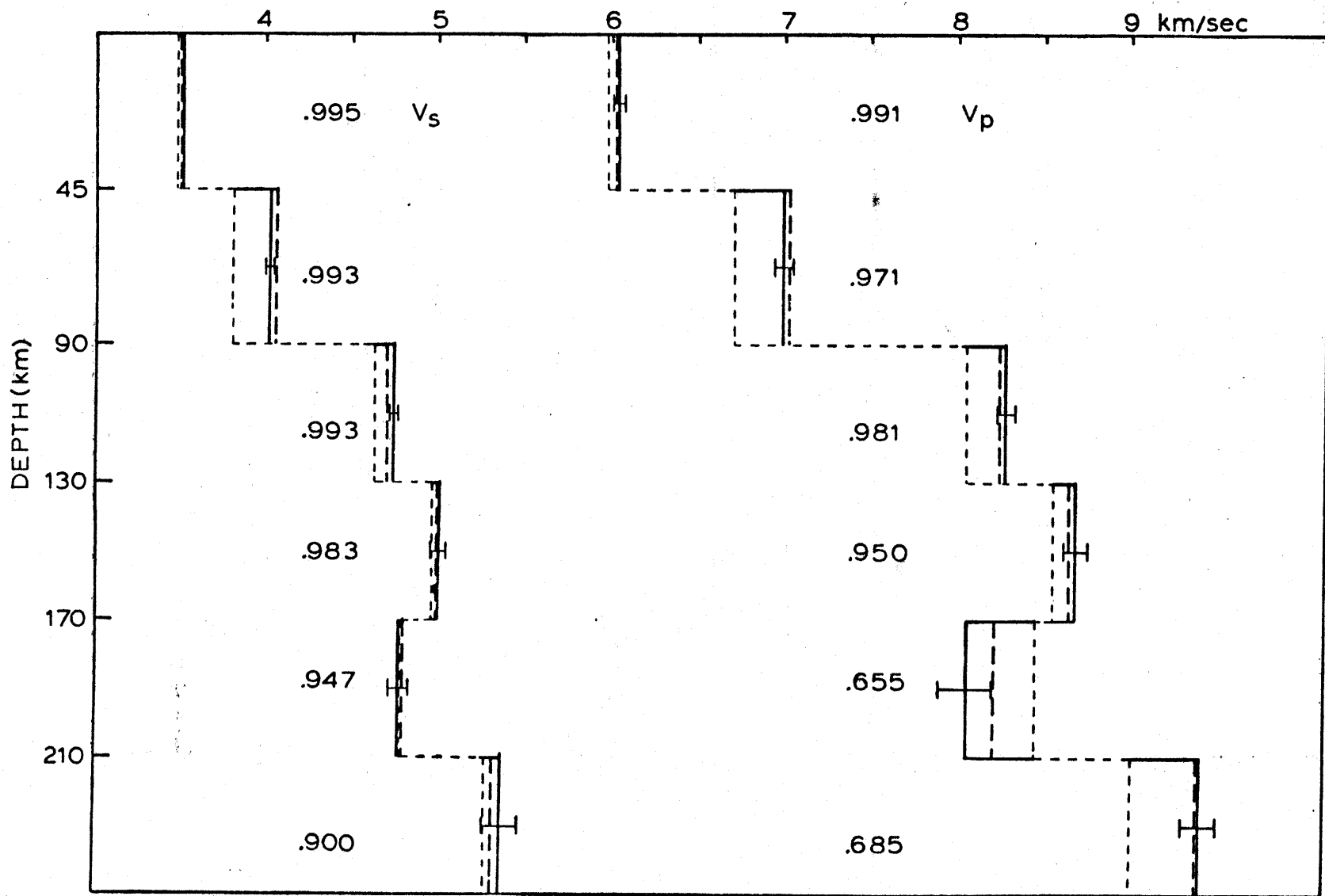


Figure 5.

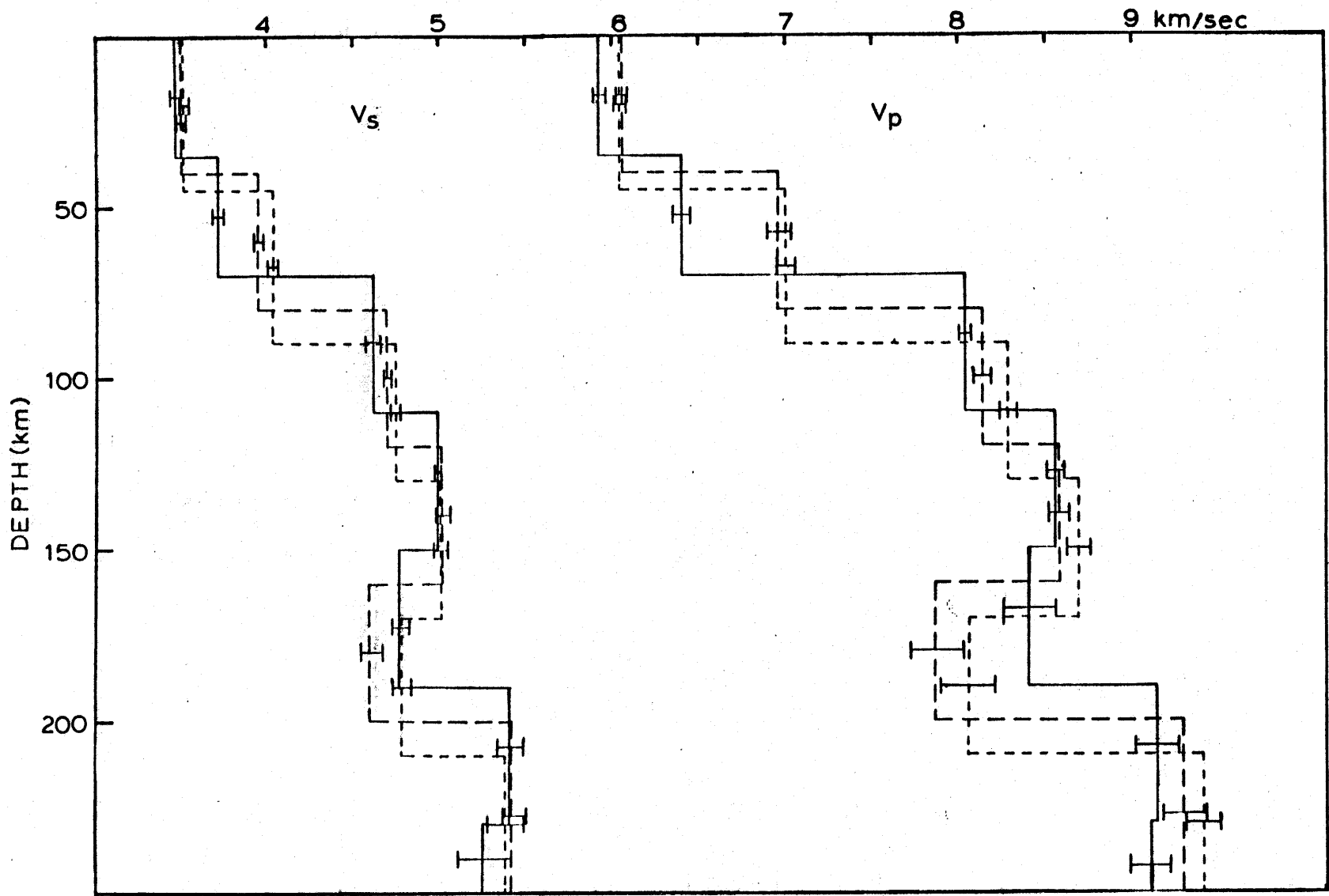


Figure 6.

Figure 7.

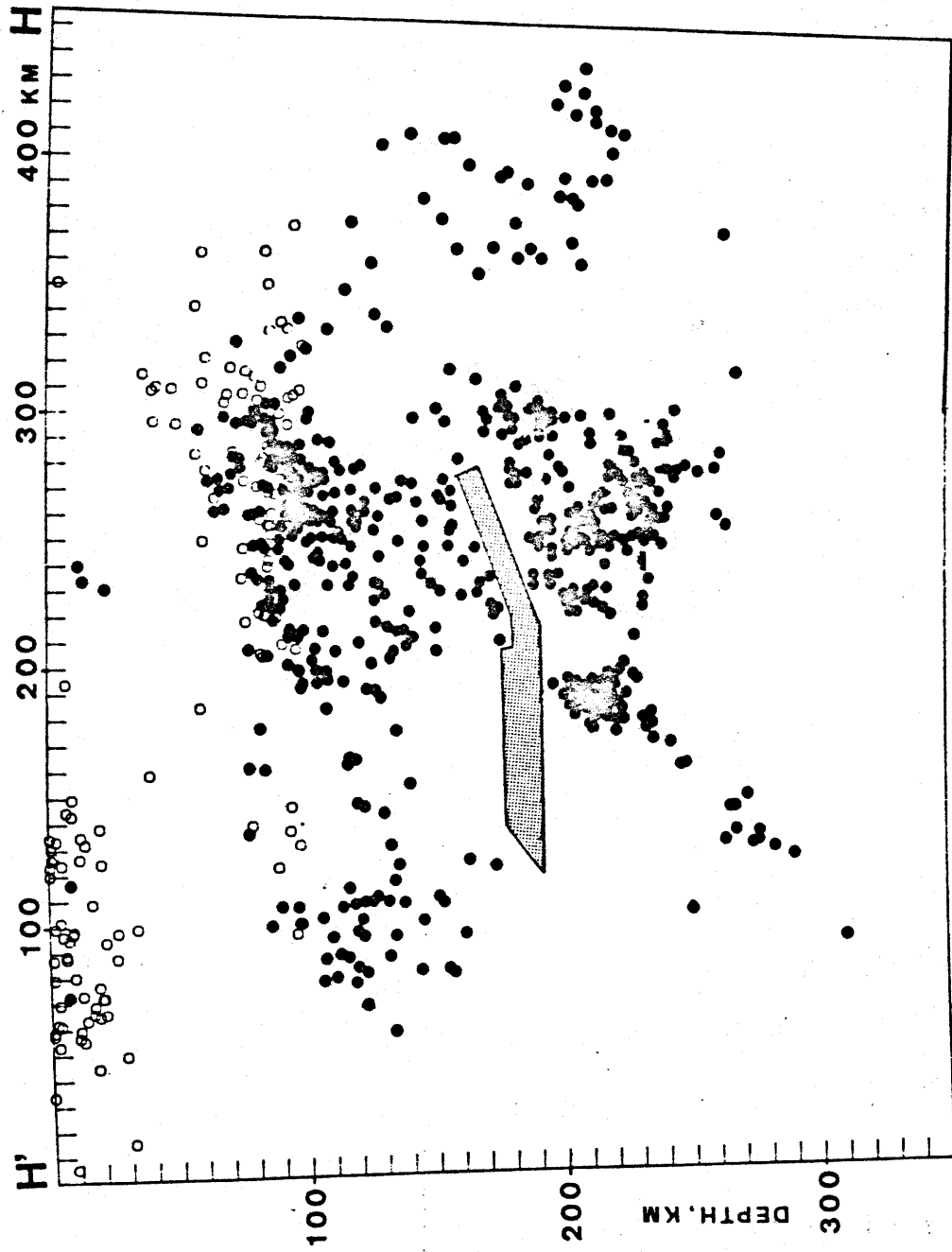
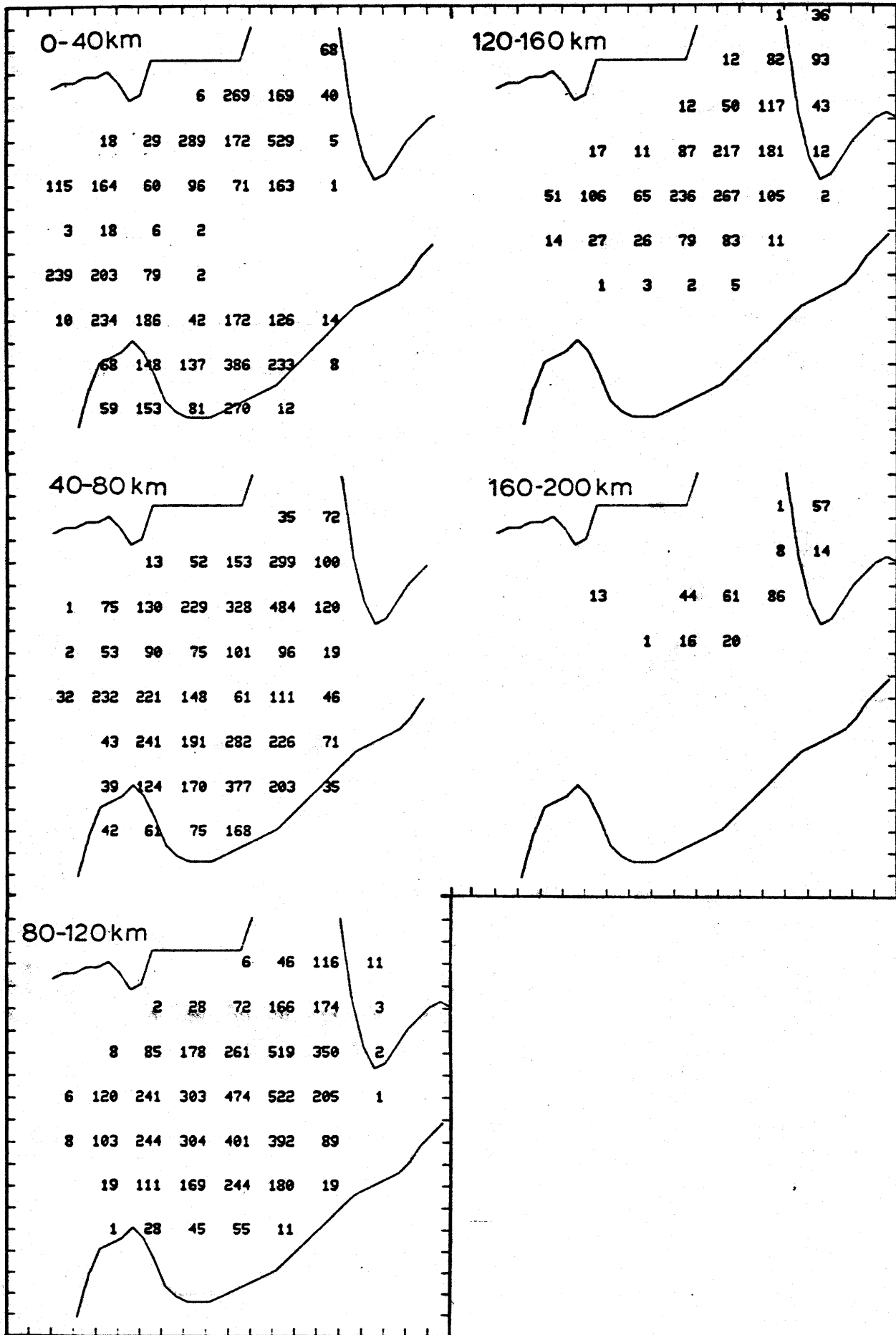


Figure 8.



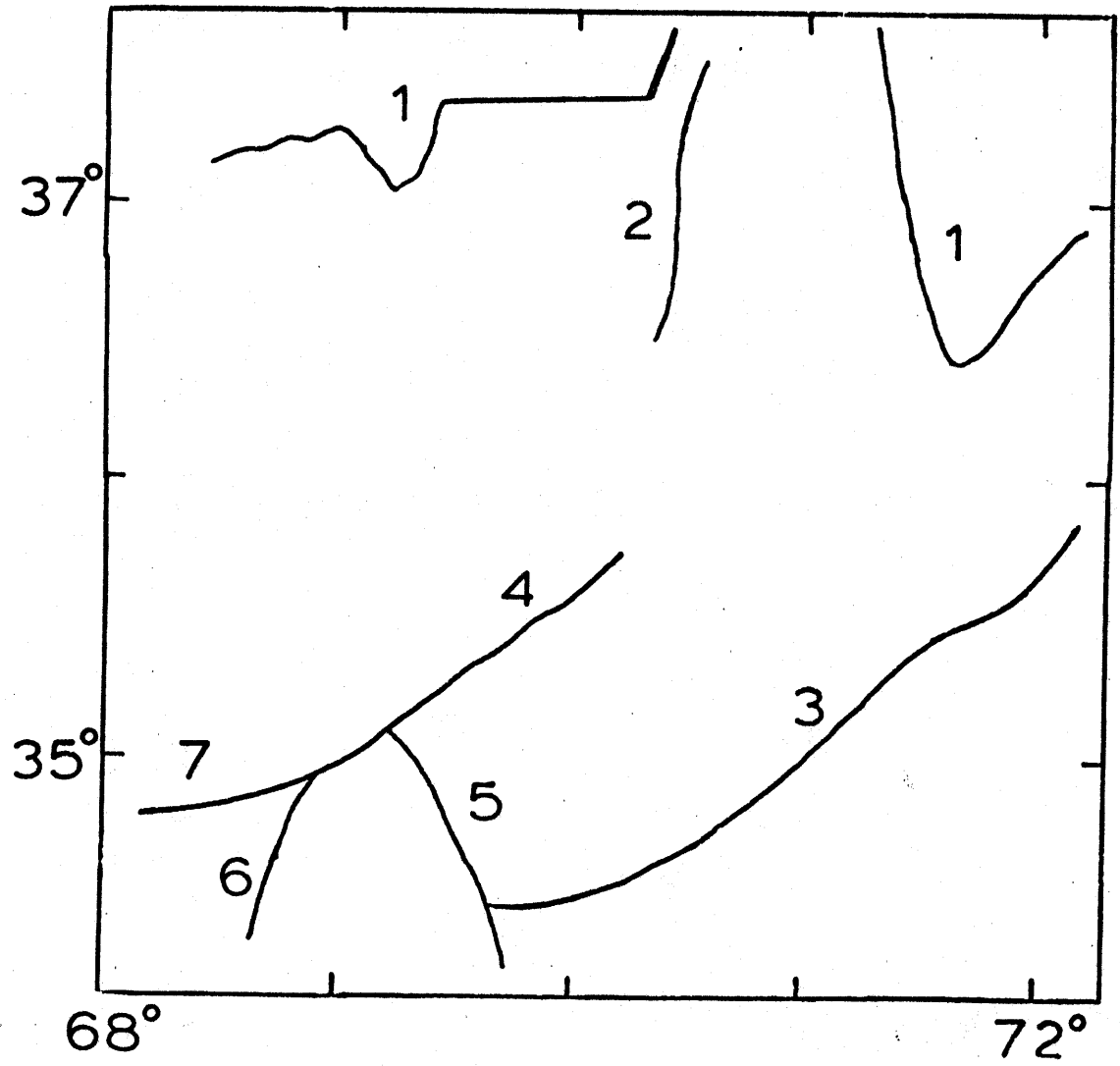


Figure 9.

AF2

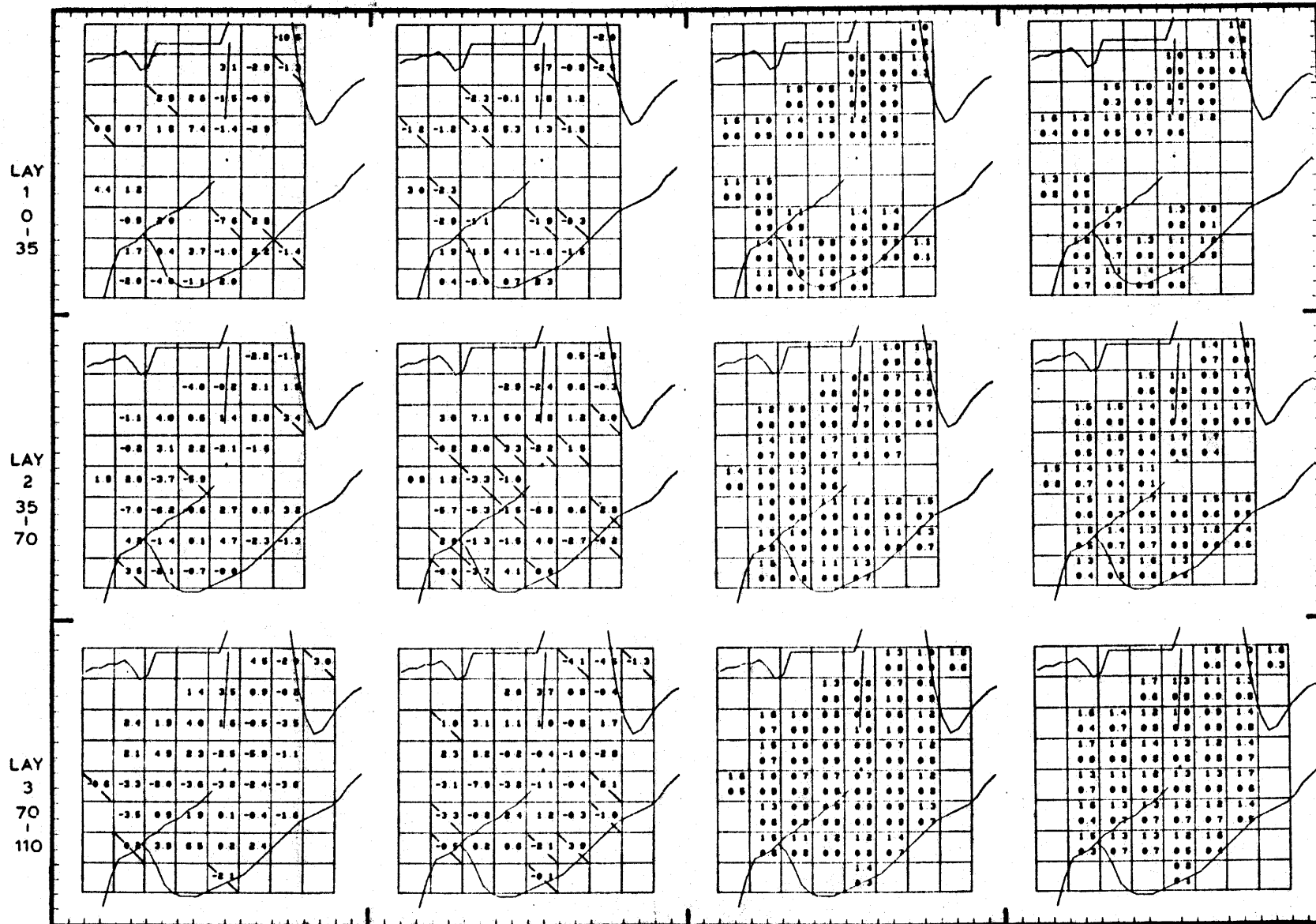


Figure 10.

AF2

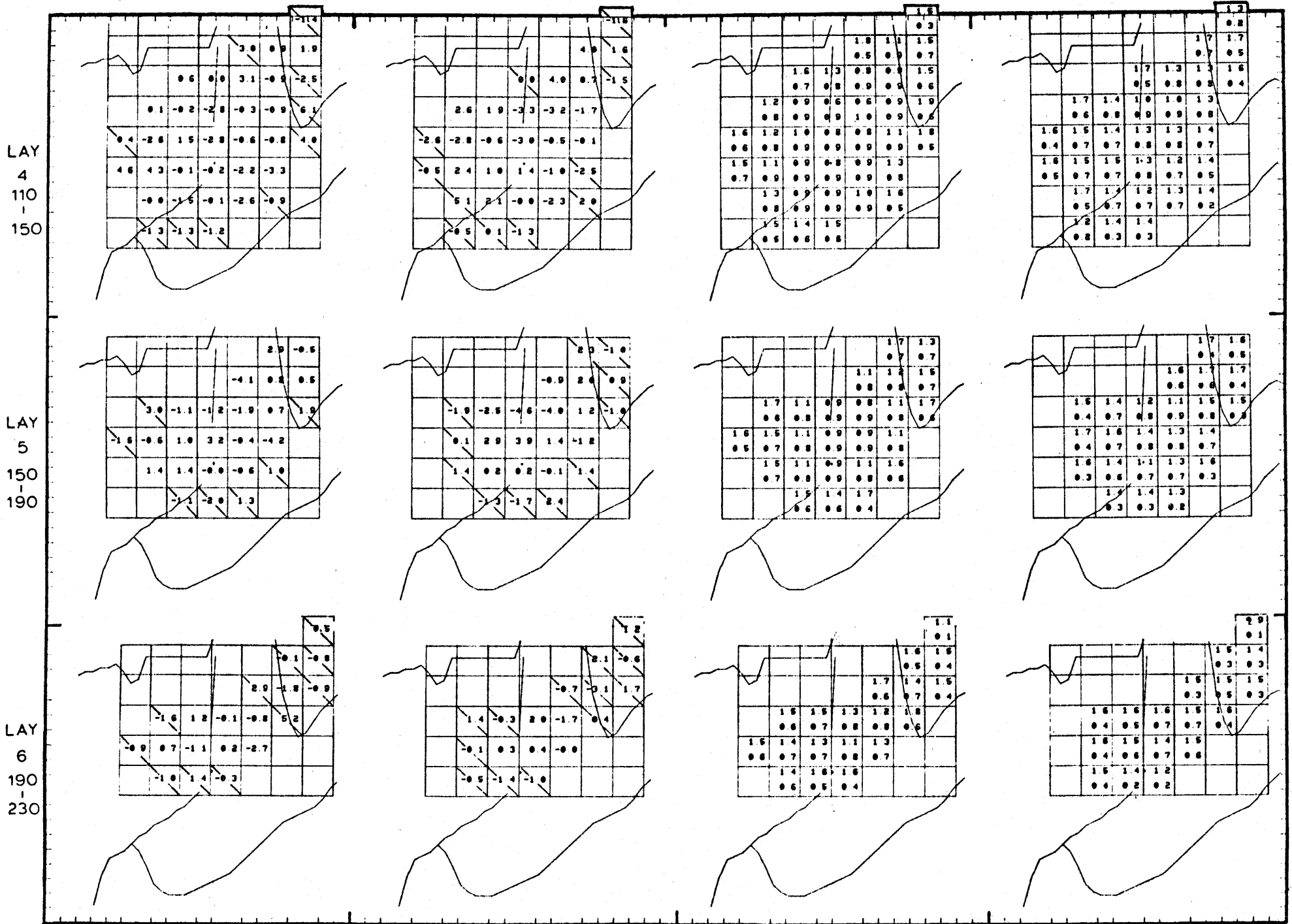


Figure 10 (cont).

Figure 11.

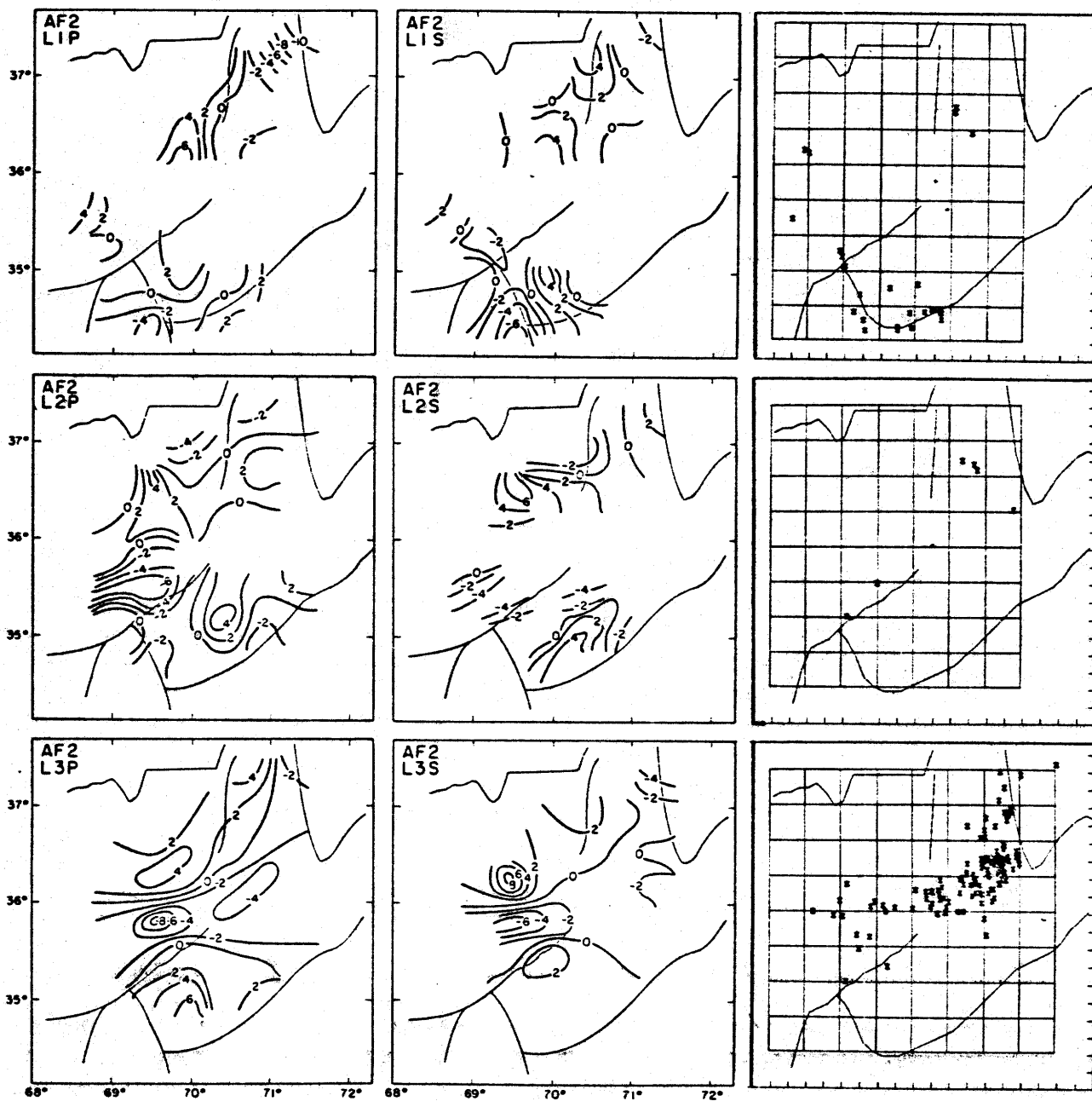
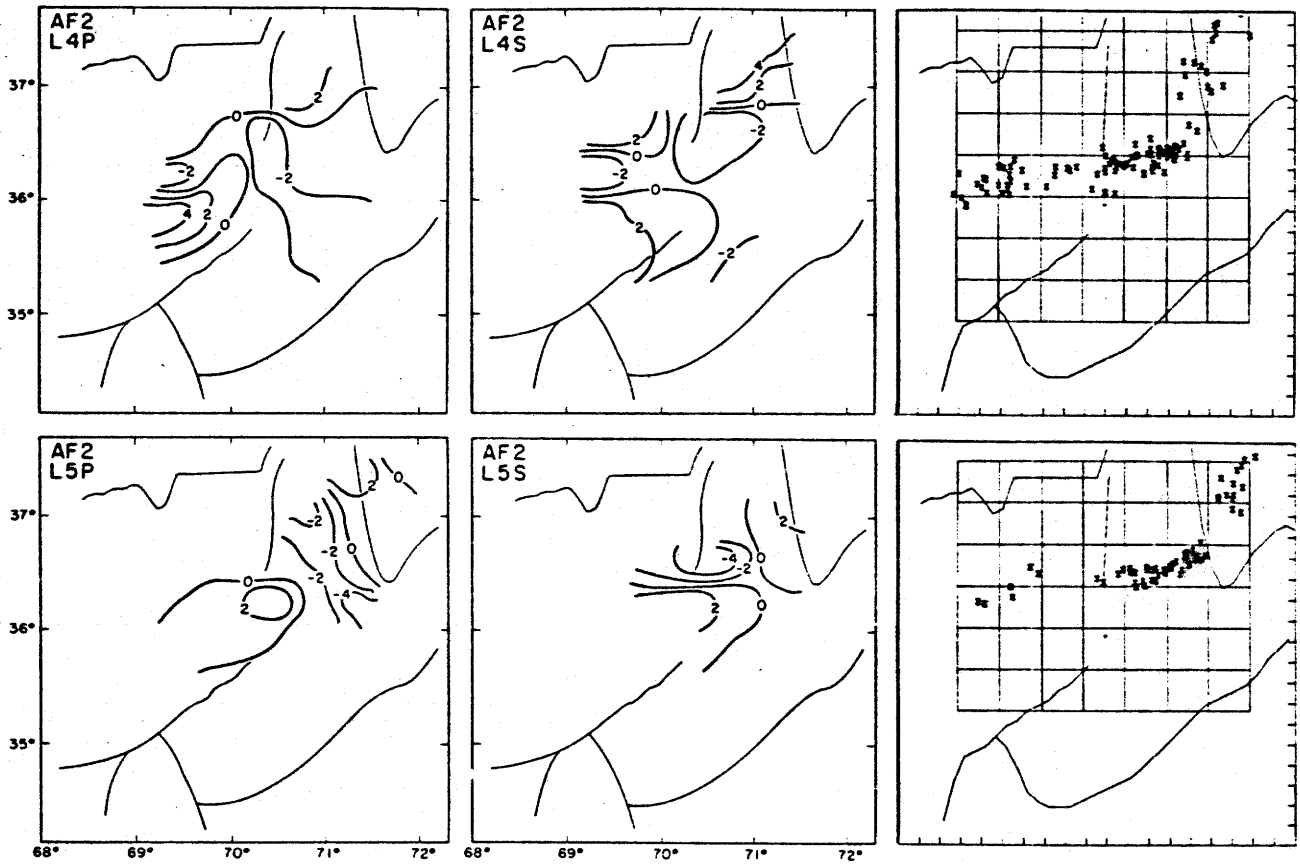


Figure 11. (cont.)



AF9

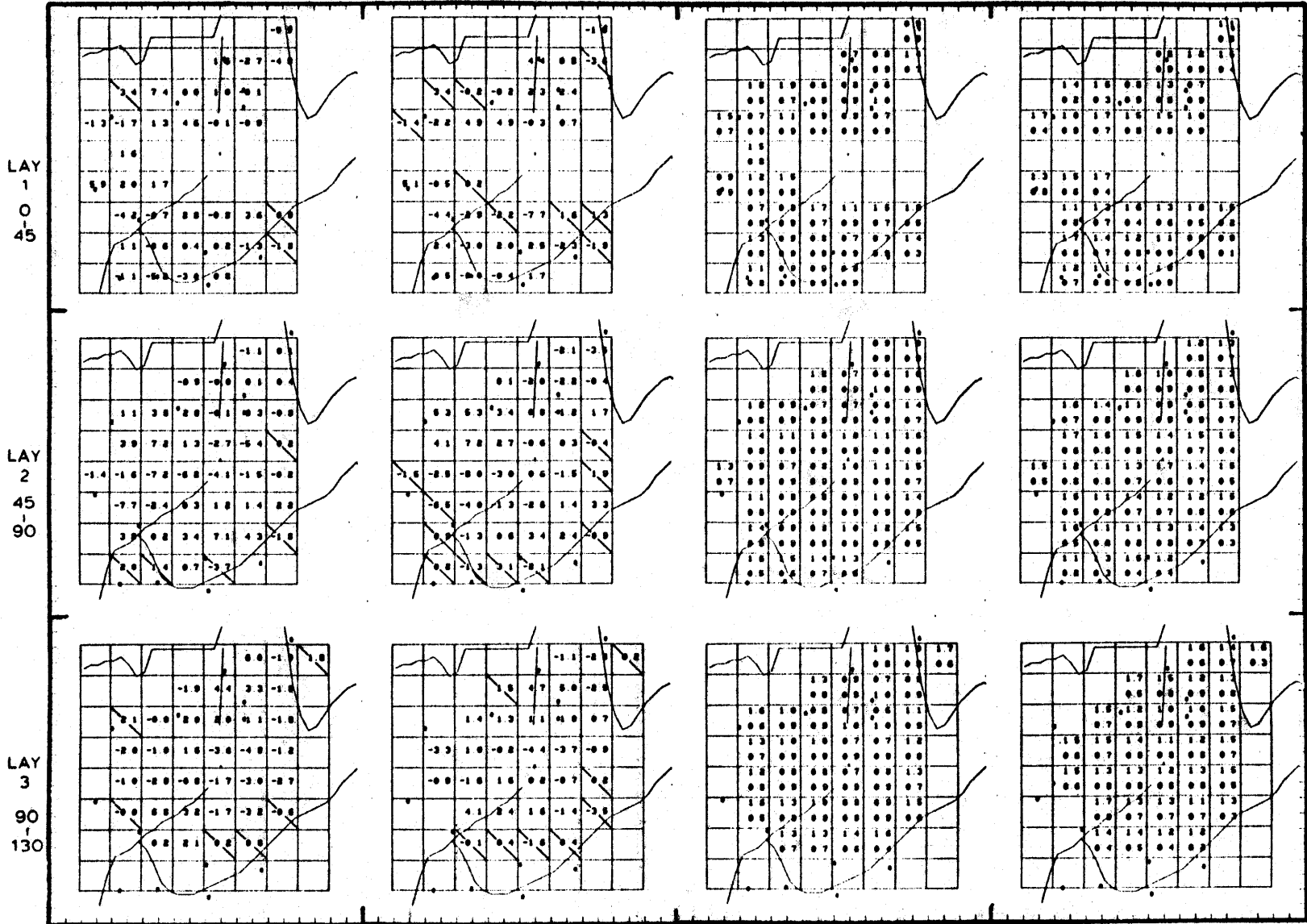


Figure 12.

AF9

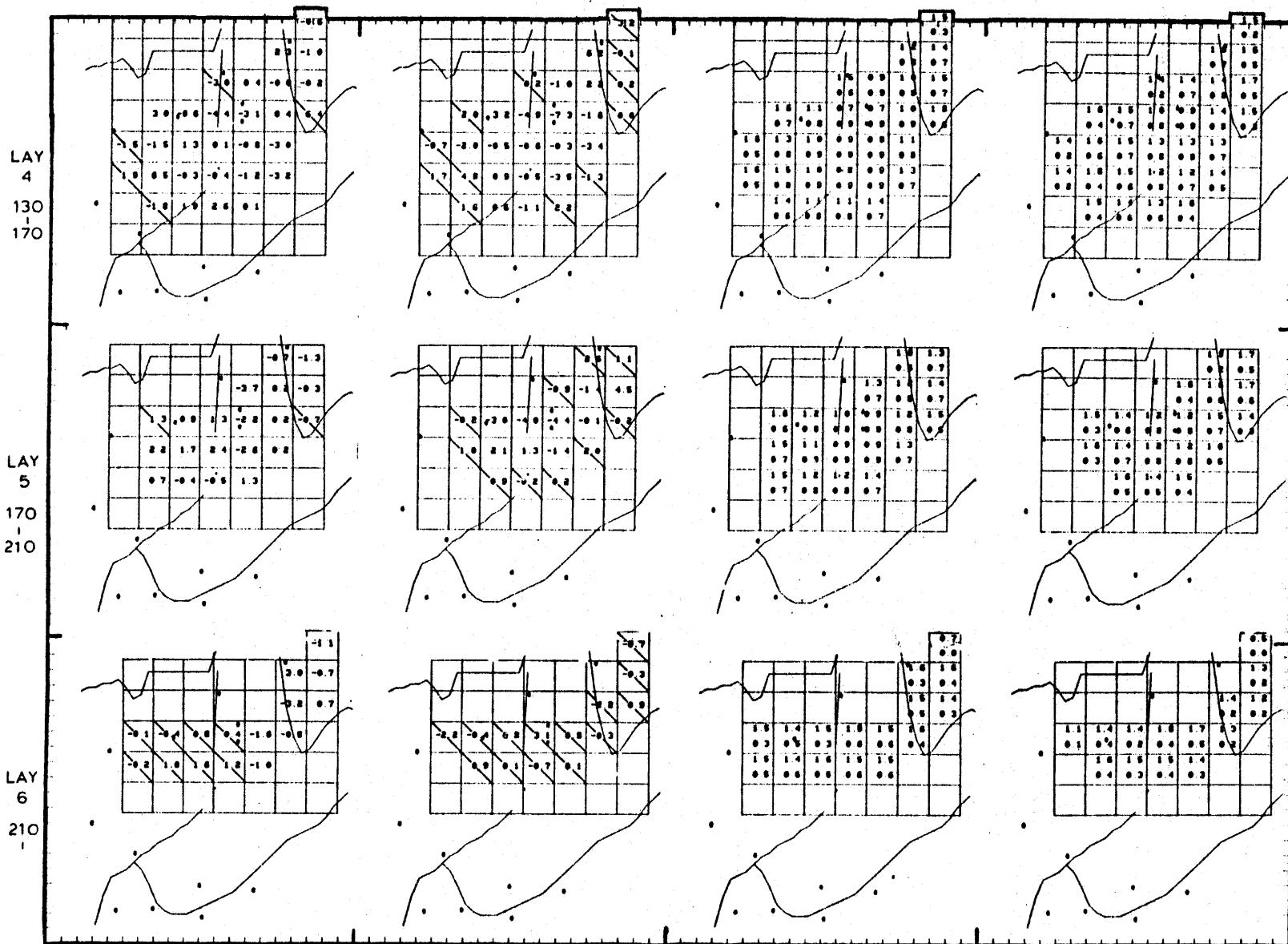


Figure 12. (cont.)

Figure 13.

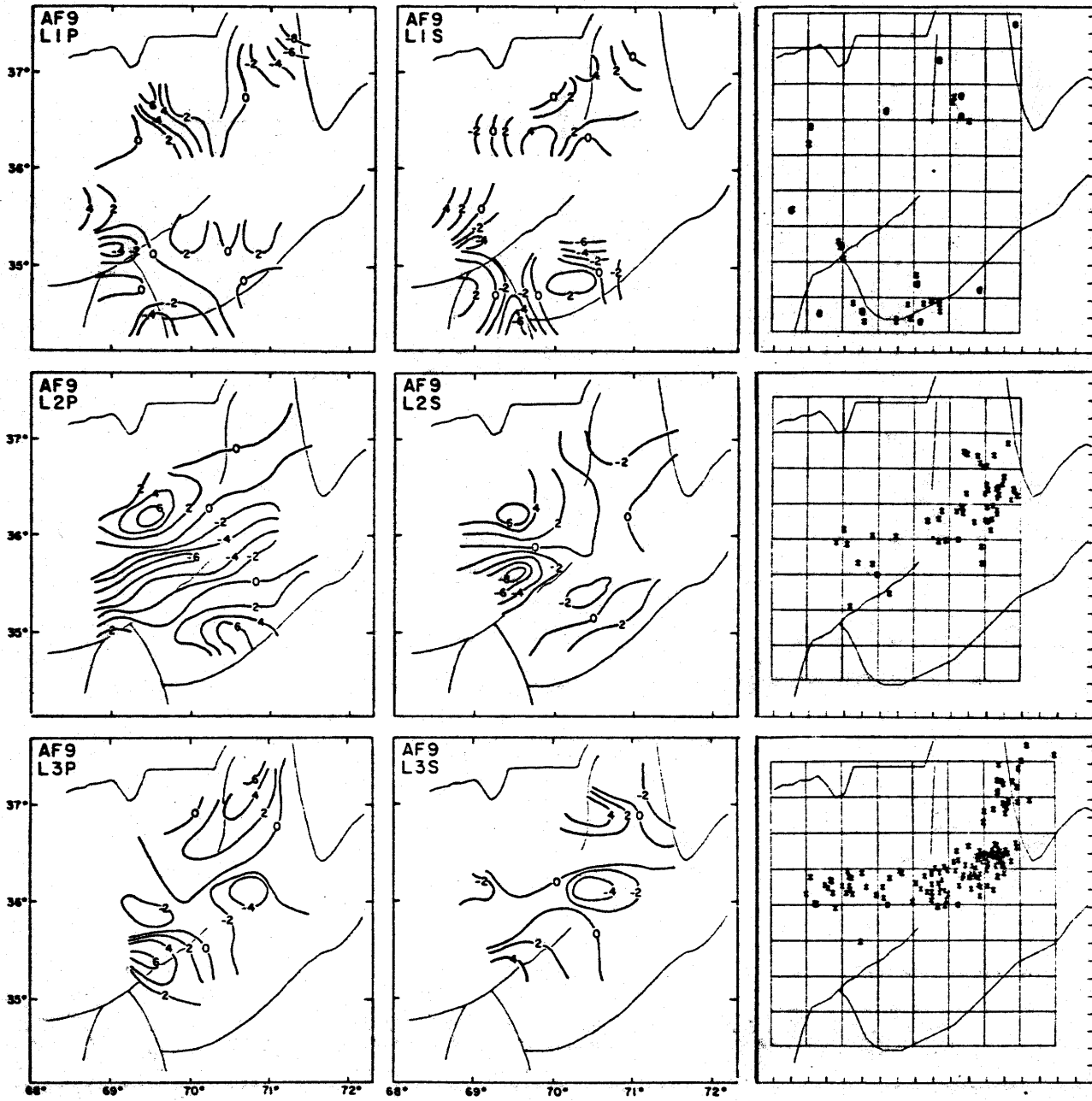
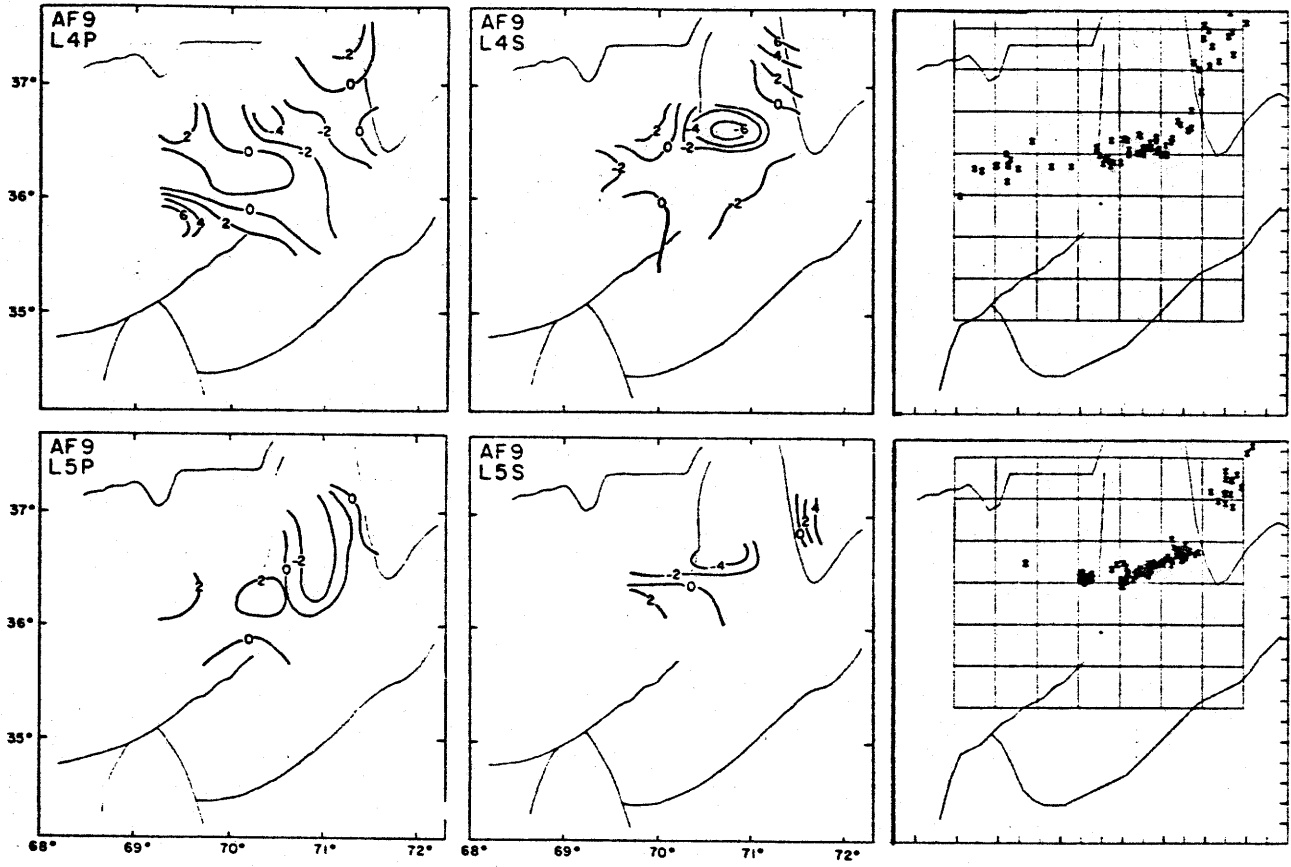


Figure 13. (cont.)



AF10

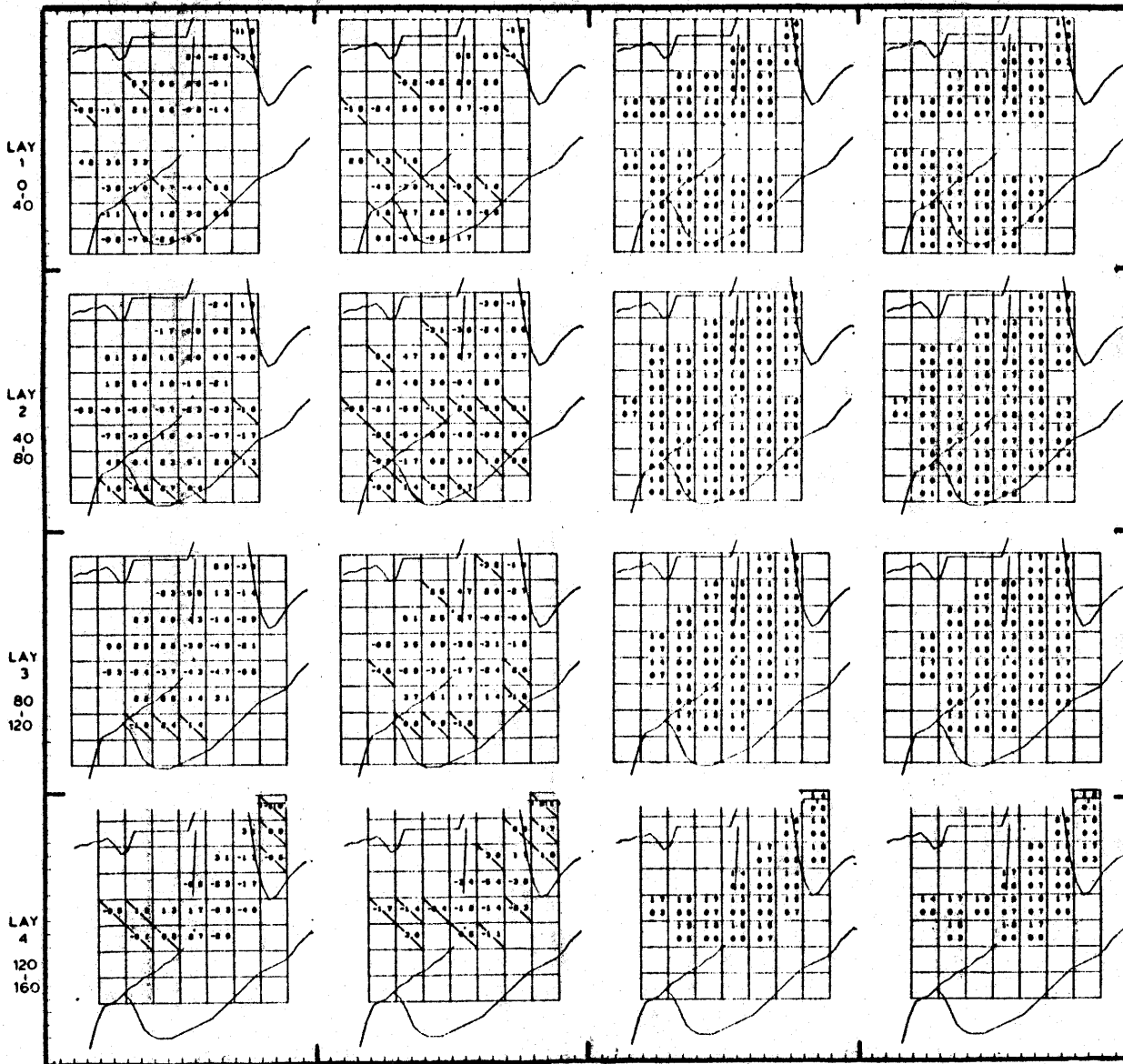


Figure 14.

Figure 15.

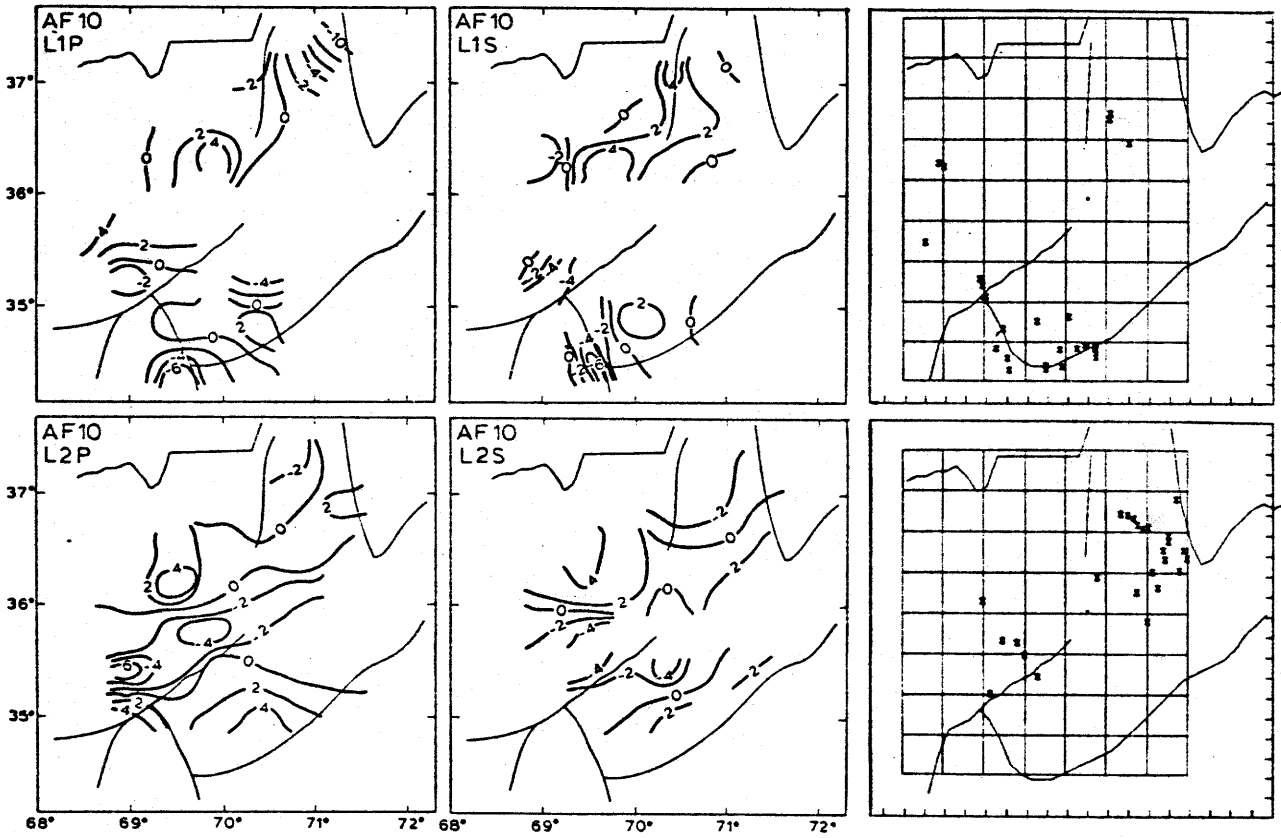
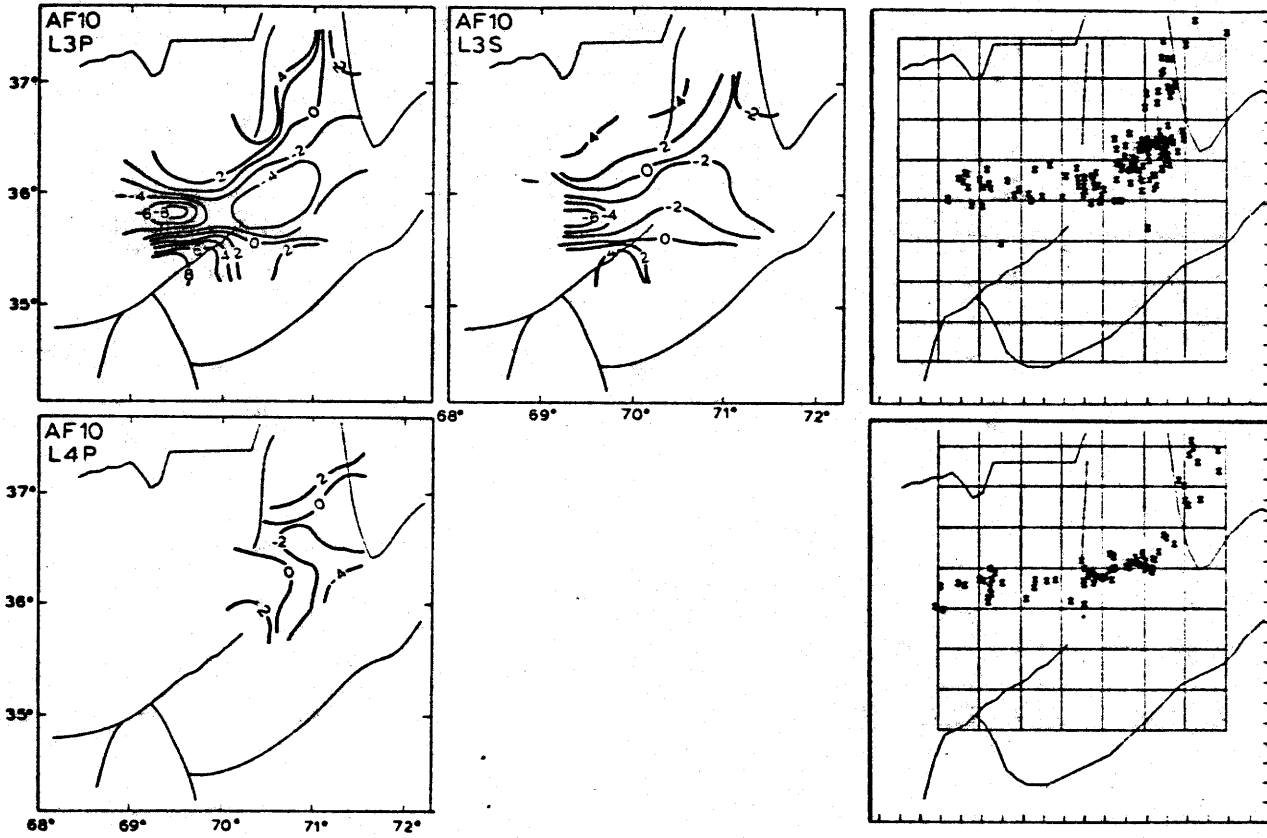


Figure 15. (cont.)



AF4

LAY
3
70
110

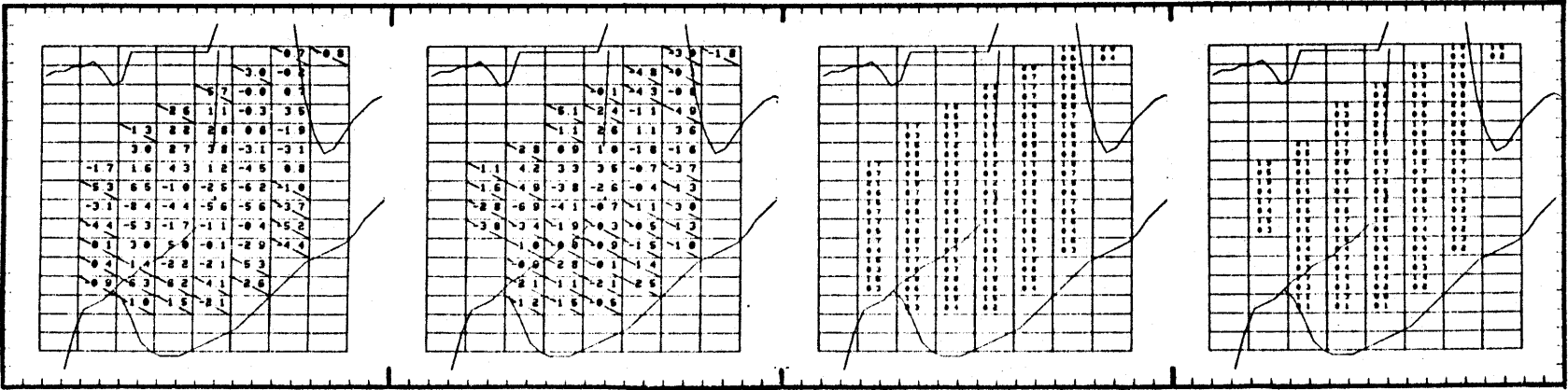


Figure 17.

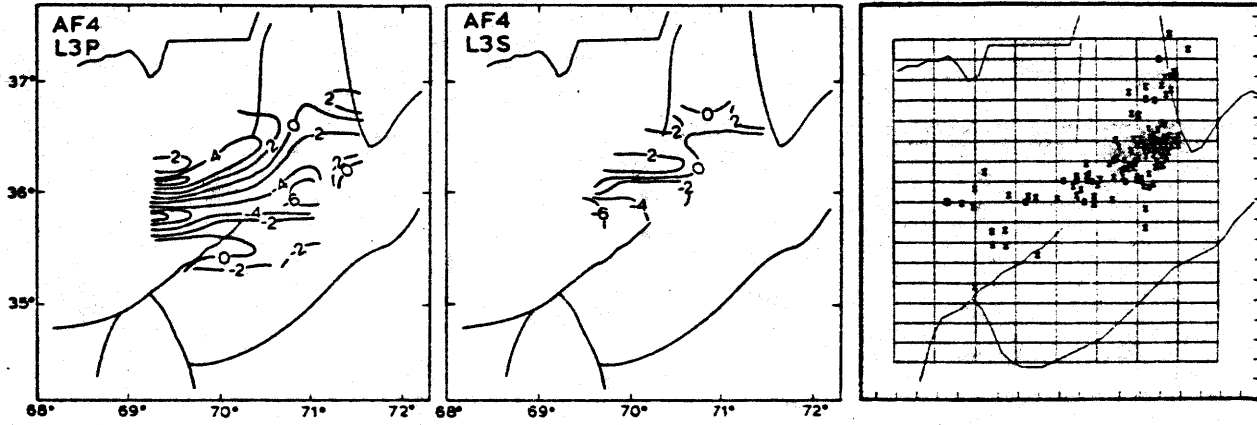


Figure 18.

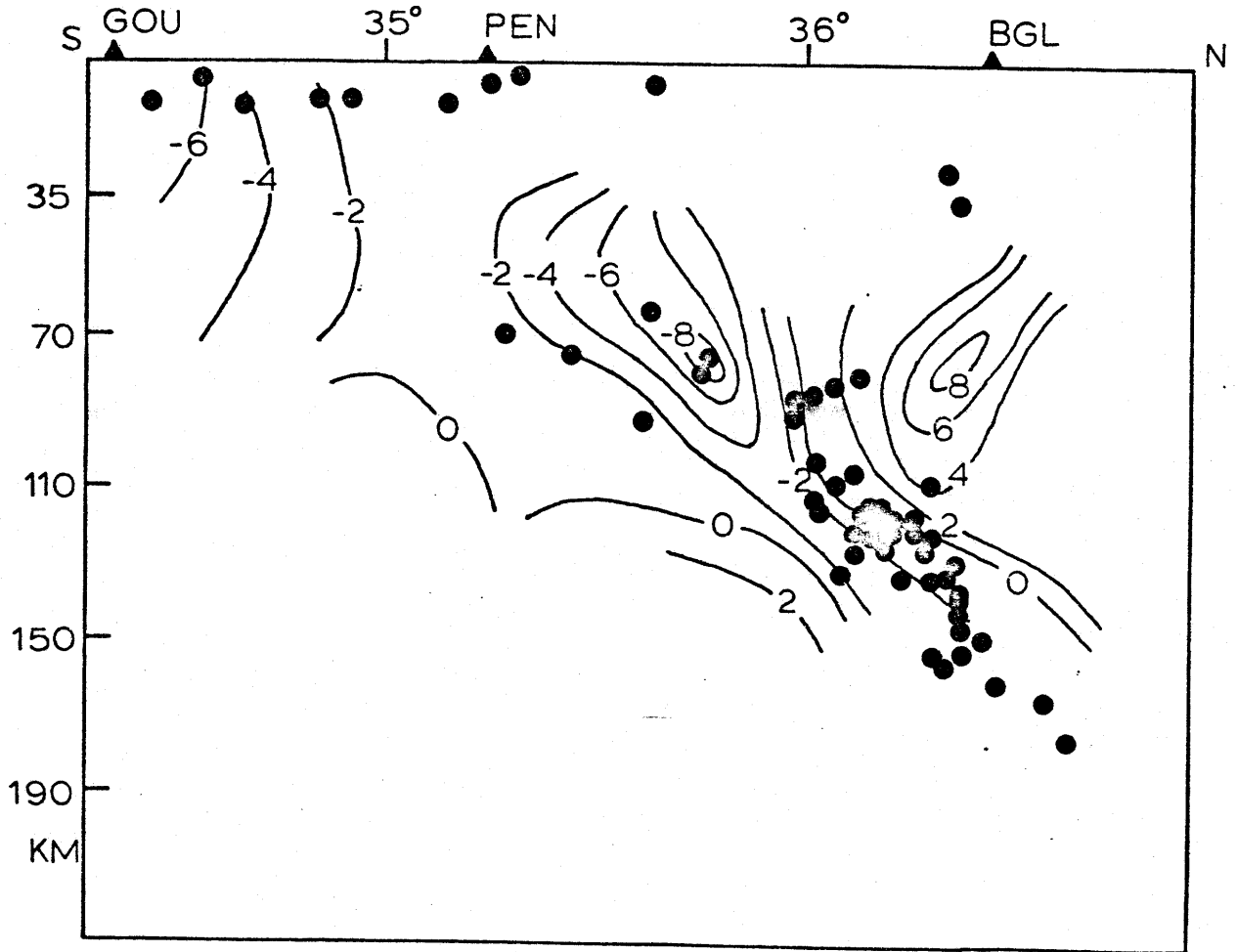
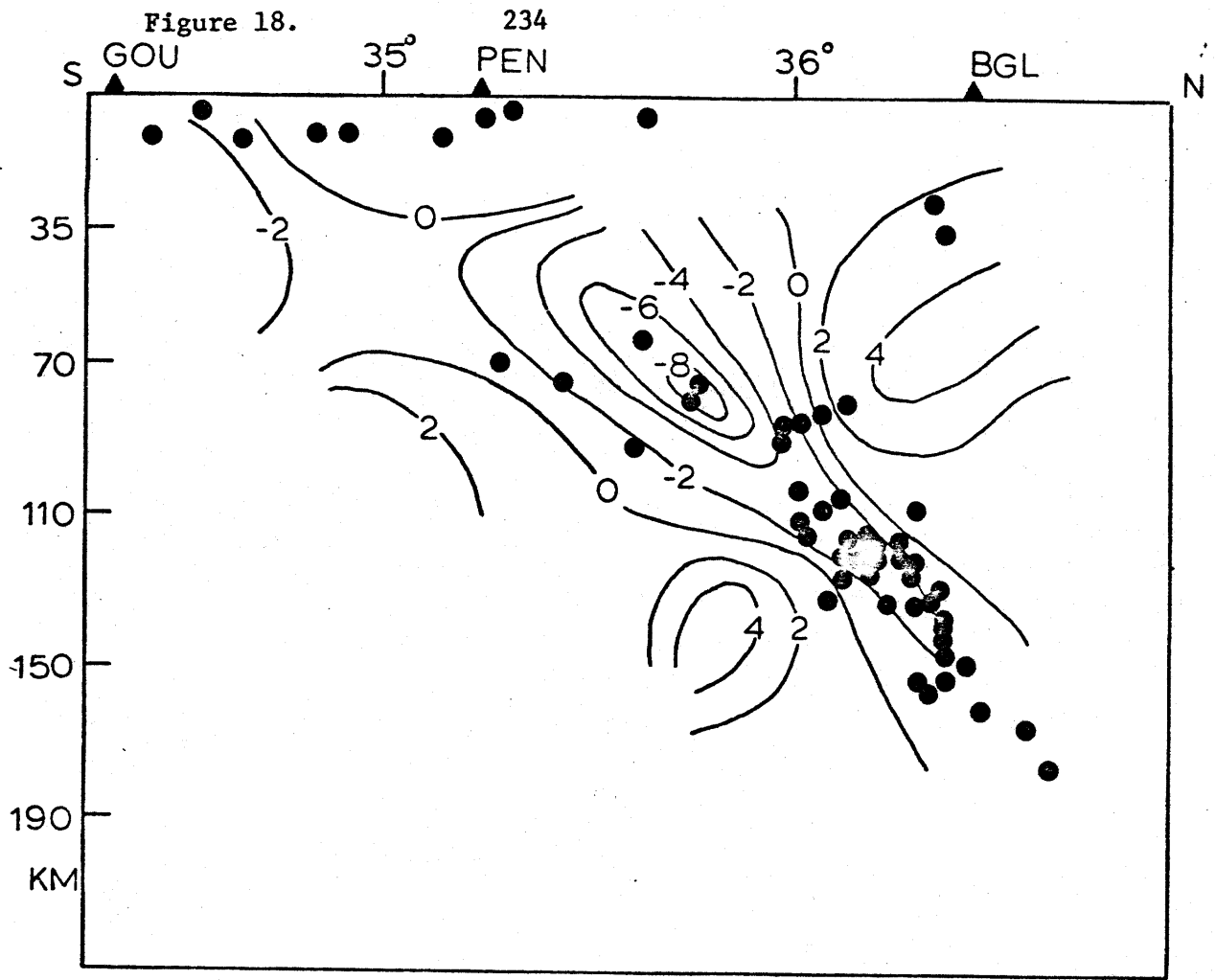


Figure 19.

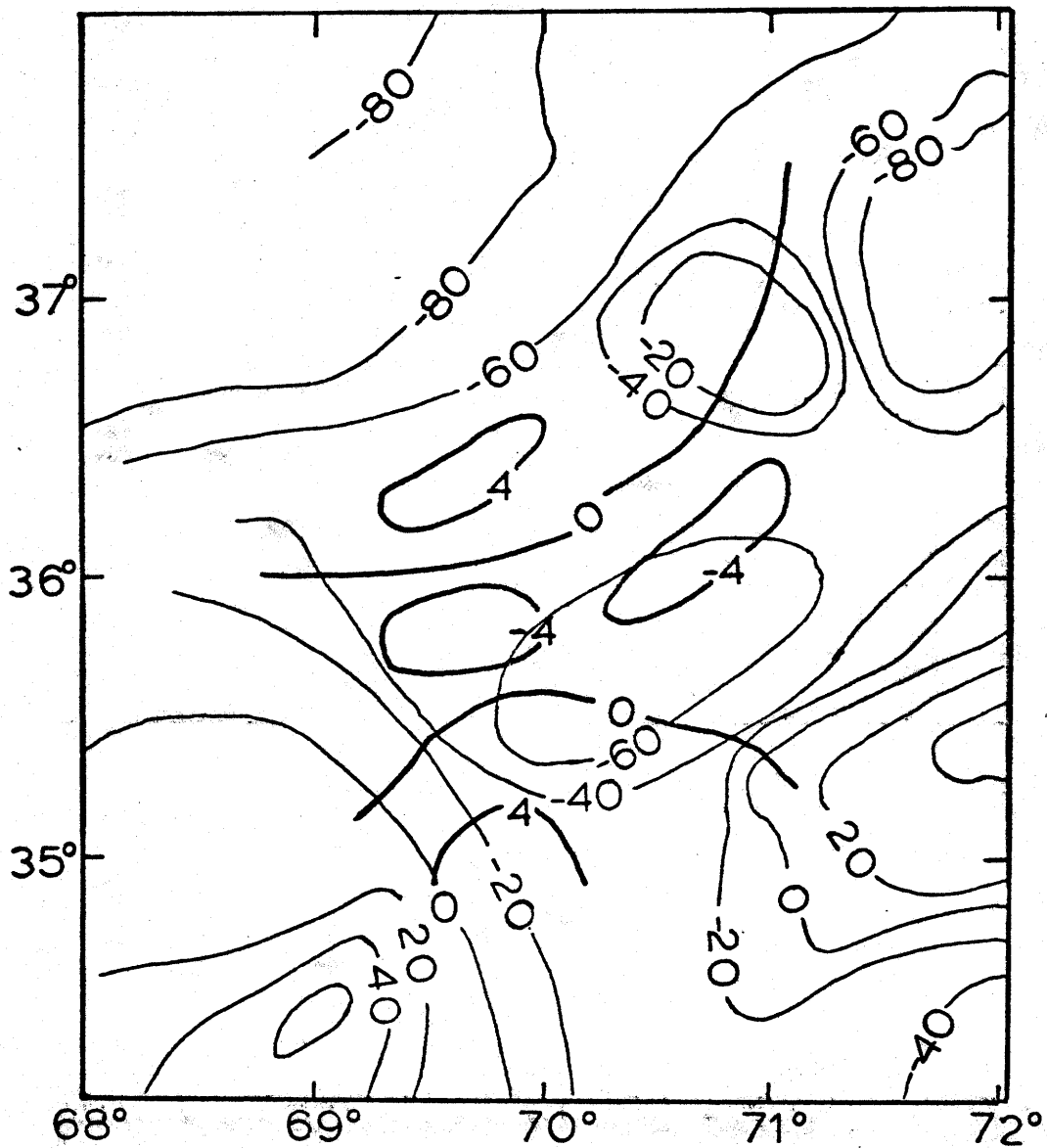
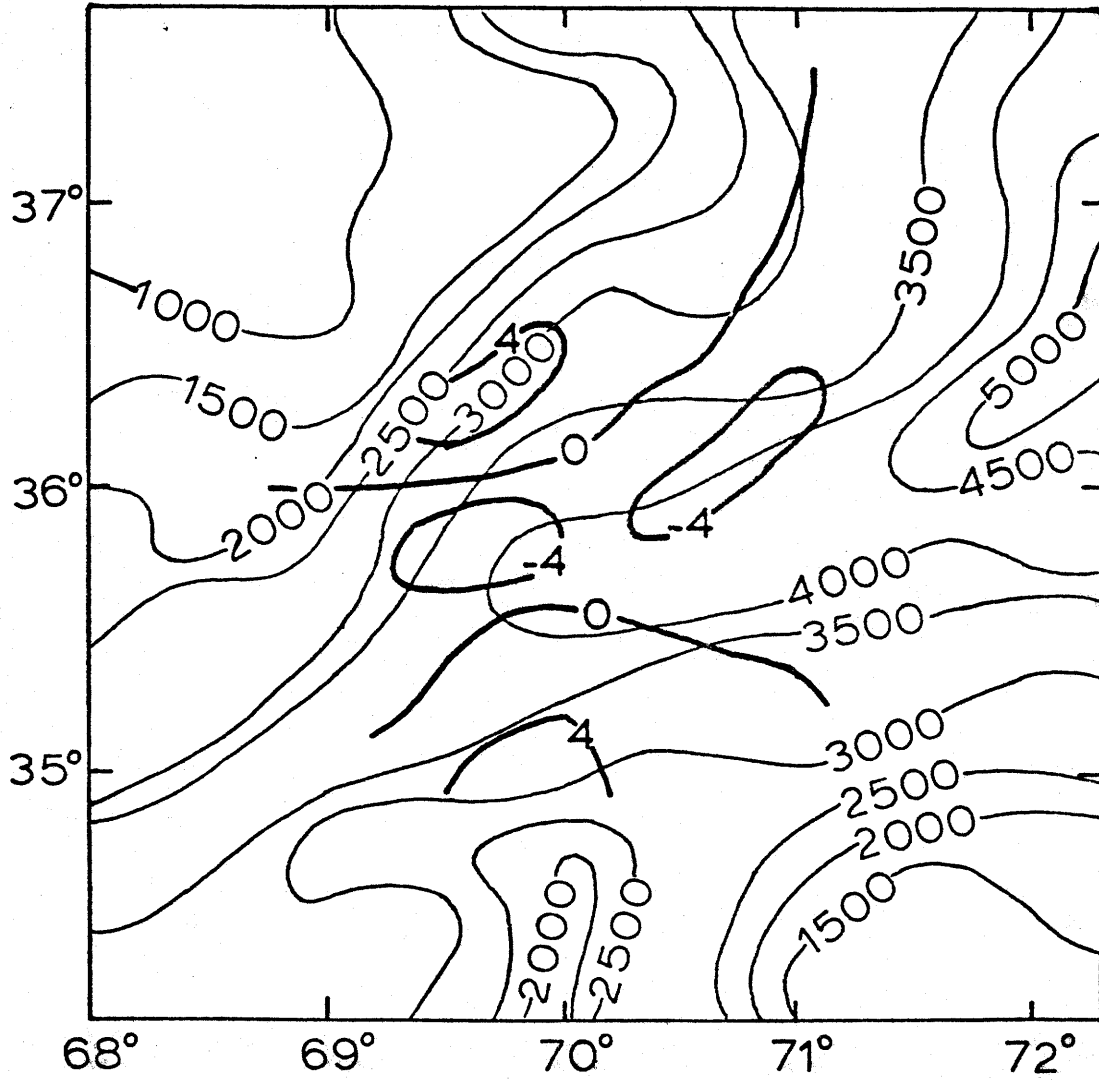


Figure 20.



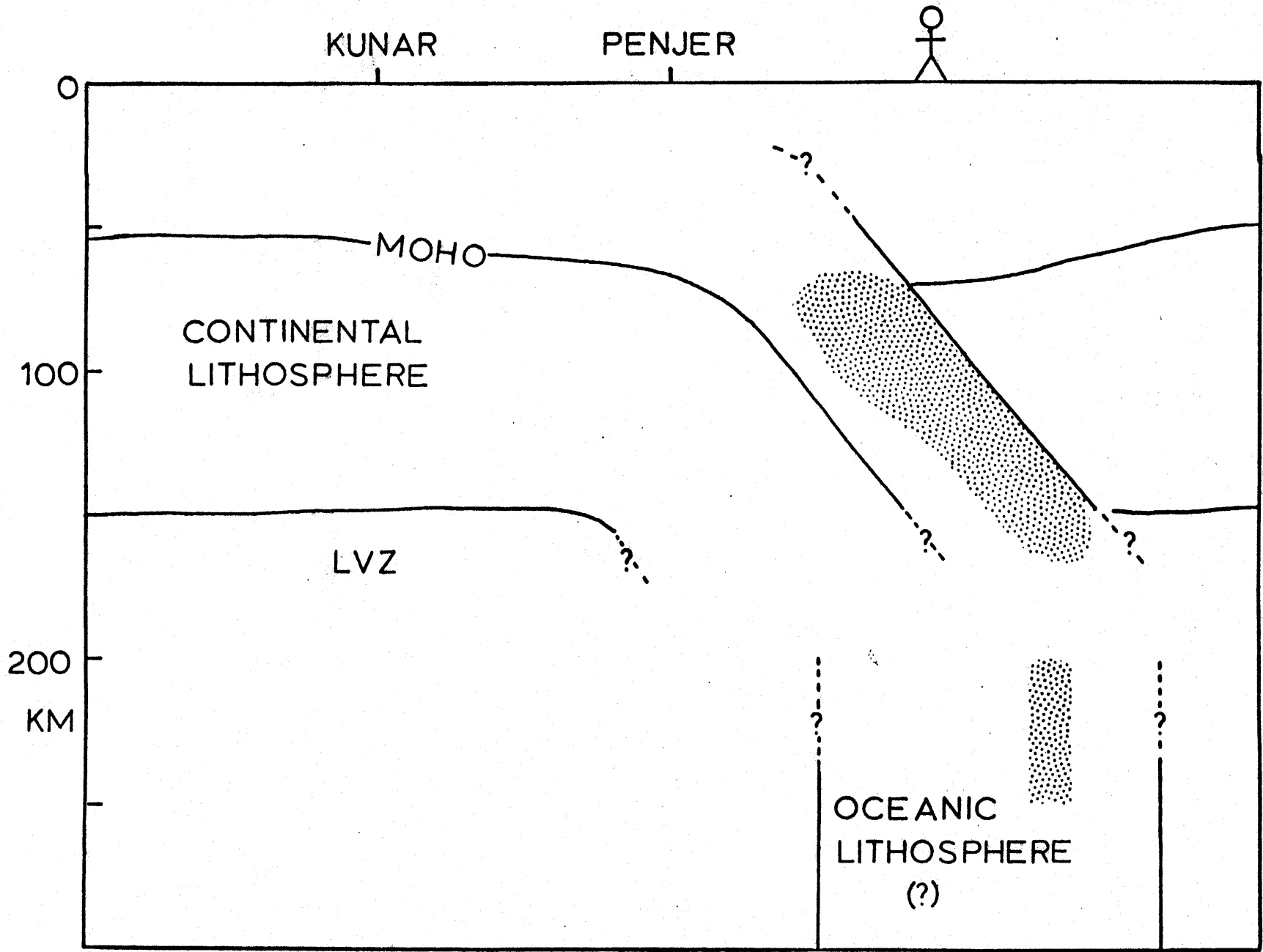


Figure 21.

Table Captions

Table 1. P and S wave station corrections determined jointly with the one-dimensional velocity structure. These values are from the inversion using a two-layer, 70 km thick crust as a starting model.

Table 2. Specifications of the starting models used in the three-dimensional inversions, along with the variance in the data before and after the inversions.

Table 1.

Station	Latitude	Longitude	P Correction	S Correction
GHA	36 32.87	70 50.67	-0.06	-0.22
JOR	36 45.14	70 50.42	0.01	-0.33
JRM	36 44.00	70 50.33	-0.04	-0.22
BAR	36 56.73	71 2.92	0.04	-0.09
FDZ	37 6.87	70 33.33	-0.09	-0.40
FRA	36 36.00	69 52.66	-0.10	-0.26
BGL	36 26.14	68 55.00	0.11	-0.08
DOS	35 35.14	68 40.33	-0.04	0.08
PEN	35 13.70	69 19.20	0.67	1.09
KBL	34 32.45	69 2.59	-0.10	-0.24
GOU	34 33.53	69 35.42	0.18	0.67
KUY	34 27.53	70 20.08	-0.16	-0.46
SAL	34 50.73	70 17.33	-0.09	-0.20
CHS	34 47.44	71 4.58	-0.02	-0.06
KHO	37 29.00	71 32.00	0.83	0.40

Inversion AF2

585 Events
5115 P Arrivals
3840 S Arrivals

Starting Model

Layer	Depth	P Velocity	S Velocity
1	-2.0	5.93	3.48
2	35.0	6.41	3.71
3	70.0	8.08	4.63
4	110.0	8.55	4.99
5	150.0	8.41	4.77
6	190.0	9.14	5.40
7	210.0	9.09	5.25

Original Variance	0.206
Final Variance	0.098
Percentage Improvement	52.354

Inversion AF9

576 Events
5042 P Arrivals
3792 S Arrivals

Starting Model

Layer	Depth	P Velocity	S Velocity
1	-2.0	6.03	3.49
2	45.0	7.03	4.08
3	90.0	8.24	4.76
4	130.0	8.64	5.02
5	170.0	8.22	4.81
6	210.0	9.38	5.33

Original Variance	0.201
Final Variance	0.096
Percentage Improvement	51.951

Inversion AF4

248 Events
2155 P Arrivals
1586 S Arrivals

Starting Model

Layer	Depth	P Velocity	S Velocity
1	-2.0	5.93	3.48
2	35.0	6.41	3.71
3	70.0	8.08	4.63
4	110.0	8.55	4.99

Original Variance	0.298
Final Variance	0.132
Percentage Improvement	55.456

Inversion AF10

314 Events
2648 P Arrivals
1951 S Arrivals

Starting Model

Layer	Depth	P Velocity	S Velocity
1	-2.0	6.09	3.50
2	40.0	6.92	3.96
3	80.0	8.10	4.69
4	120.0	8.53	4.99
5	160.0	7.95	4.60

Original Variance	0.265
Final Variance	0.123
Percentage Improvement	53.608

Table 2.

240.

APPENDIX A

COMMENT ON THE JOINT HYPOCENTER-VELOCITY FORMULATIONS

The formulations of both Palvis and Booker [1980] and Spencer and Gubbins [1980] desire a solution for \underline{y} in the equation

$$(A1) \quad \underline{d} = \underline{A}\underline{x} + \underline{B}\underline{v} + \underline{e}$$

Palvis and Booker suggest decomposing A as following

$$(A2) \quad A = \begin{bmatrix} | & | & | \\ U_1 & U_0 & U_2 \\ | & | & | \end{bmatrix} \begin{bmatrix} \lambda_1 \\ \lambda_p \\ 0 \end{bmatrix} \begin{bmatrix} v^T \\ p \\ v_0^T \end{bmatrix}$$

and then using U_2 (and possibly U_0) as an annihilator of A.

Equation A1 becomes

$$(A3) \quad \begin{bmatrix} U_0^T \underline{d} \\ U_2^T \underline{d} \end{bmatrix} = \begin{bmatrix} U_0^T B \\ U_2^T B \end{bmatrix} \underline{v}$$

which, in the least squares solution, becomes

$$(A4) \quad B^T [U_0 U_0^T + U_2 U_2^T] \underline{d} = B^T [U_0 U_0^T + U_2 U_2^T] B \underline{v}$$

or, letting $C = B^T [U_0 U_0^T + U_2 U_2^T]$,

$$(A5) \quad C \underline{d} = C B \underline{v}$$

Palvis and Booker referred to the inclusion of U_0 space in the annihilator as the "liberal approach", while strict exclusion of U_0 was referred to as the "conservative

approach". By analogy, the method employed in this paper might be called the "ultra-conservative approach" because, for reasons discussed in the text, hypocenter solutions with a U_0 space were excluded altogether.

The method of Spencer and Gubbins proposes inverting the equation

$$(A6) \quad O\bar{d} = O\bar{B}v$$

where the annihilator O has the form

$$(A7) \quad O = B^T [I - A(A^T A)^{-1} A^T]$$

Note that

$$(A8) \quad A(A^T A)^{-1} A^T = U_p \wedge V_p^T V_p \wedge^{-2} V_p^T V_p \wedge U_p^T$$

$$= U_p U_p^T = U_1 U_1^T$$

and that

$$(A9) \quad U U^T = U_1 U_1^T + U_0 U_0^T + U_2 U_2^T = I$$

Therefore

$$(A10) \quad O = B^T [I - U_1 U_1^T] = B^T [U_2 U_2^T + U_0 U_0^T] = C$$

Since $O = C$, equation (A10) shows that the method proposed by Spencer and Gubbins is equivalent to the "liberal approach" of Palvis and Booker.

APPENDIX B

RESULTS OF HYPOTHETICAL TESTS

As mentioned in the section on layered inversions, the imposition of boundaries on a medium can bias our interpretation of the results if the velocity is not smoothly varying. While the earth is approximately layered, there is no reason to believe that it is composed of blocks. Thus the boundaries imposed by the three-dimensional inversion are fairly arbitrary. Clearly, some understanding of how improper parameterizations affect a solution is required before an honest interpretation of a block inversion can be made.

Like nonlinearity, incorrect parameterizations are implicitly assumed not to exist and are therefore beyond the powers of detection of the conventional linear estimators. One must resort to other means, such as solving problems for which the solution is known, to acquire an appreciation for the effects of situations which violate basic assumptions. In this appendix we describe the results of such tests, and discuss their relevance to the solutions with real data.

Naturally, for any method as approximate as the one used here, one can envision a number of pathological schemes foiling our interpretations. Inverse solutions themselves are inherently nonunique. Further, given the complexity of the three-dimensional inverse problem, trying to describe the eccentricities of a solution through a few hypothetical

tests is rather like blind men describing an elephant. Our modest goal is to test the performance of the method in a few exemplary earth models, and attempt to draw conclusions from the results. The earth models discussed are a broad, low velocity slab (BLVS), a thin, high velocity slab (THVS), and a thin, low velocity slab (TLVS). Other models were also tried, but these three contain examples of all the inferences relevant to the results in the text.

Broad Low Velocity Slab (BLVS)

The broad, low velocity slab model consists of a centrally located, vertical, east-west oriented region of low velocity flanked at discrete boundaries by higher velocities (figure B1). The slab is 100 kilometers wide and has 14 percent (for P) and 7% (for S) lower velocities than the surrounding regions (7 km/sec vs. 8 km/sec for P waves, and 4.4 vs. 4.7 for S waves). The 130 events used in the inversion are at depths of 75 and 125 kilometers and are all within the low velocity region. To imitate the real data, the activity is concentrated in the east and there are no events at shallow depths.

The model for the one-dimensional inversion is comprised of two, fifty kilometer thick layers over a half space. In the three-dimensional inversion, the blocks are aligned so that they conform to the southern boundary of the anomaly, and are bisected by the northern boundary.

As shown in figure B1, some mislocation occurs in the

eastern part of the zone when the events are relocated in the one-dimensional model. The velocities inferred in the one-dimensional results (Table B1) are close to the velocities of the seismically active (low velocity) region.

The block inversion (Table B1, figures B1, B2) shows a high contrast, centrally located, low velocity region bounded by higher velocities. The boundaries predicted by the inversion correspond approximately to the actual boundaries.

A couple of inferences can be drawn from this inversion. First, it is possible to locate sudden changes in velocity if these changes are approximated by boundaries in the model. Such a determination is possible even if all the events are confined to one side of the boundary, and even though the one-dimensional model is powerless to lessen the effect of the anomaly by averaging. Second, the solution can underestimate the anomaly in regions with numerous sources, and can exaggerate it in regions with few sources. Such exaggeration is particularly evident at the edges of the velocity solution in event-free layers. For instance, the solution for the P velocities shows a maximum anomaly in the first (inactive) layer of 20 percent, and in the second (active) layer of 12 percent (nothing is resolved in the third layer). Disregarding the extreme values at the edges of the first layer, however, the maximum anomaly is the correct answer of 14 percent. Therefore, in layers with few sources, it may be wise to disregard any extreme values

which occur along the edges.

Thin High Velocity Slab (THVS)

The thin, high velocity slab model used in this test is essentially the same as that used by Spencer and Gubbins (1980) for the inversion of New Zealand data. The model consists of a background velocity which increases with depth, superimposed upon which is a 50 kilometer thick slab-like region of higher velocity. The slab is centrally located, strikes at 60° , and dips 85° to the north. The velocity in the interior of the slab (v) is related to the background velocity (v_0) by the relation

$$v = v_0 / [1-F]$$

where

$$F = H(\pi^2 - b^2 y^2) A \exp(cz) (1 + \cos(by)) / 2.0$$

In this formula for F , y is the distance from the center of the slab, z the depth from the surface, A is the maximum anomaly (0.05), c is the inverse decay length of the slab ($-1/200 \text{ km}^{-1}$), b is related to the half width ($w = 25 \text{ km}$) by $b = \pi/w$, and H is a gate which makes F zero outside of the slab region. A plot of the F function, along with the background velocity profile, is shown in figure B3.

Data was generated by tracing rays through this medium from 93 sources to most of the stations (KHO not included)

using the three-dimensional ray tracing routine of Julian and Gubbins [1977]. The inverse solutions were set up by first dividing the medium into four layers of 50 kilometers thickness overlying a half space, relocating the events, and then solving for a best-fitting layered structure. The layered structure was then divided into blocks of 30 or 40 kilometers length and width for the three-dimensional inversion. Note that the high velocity region has smaller dimensions than the blocks, since, although the velocity increases 25 kilometers from the slab axis, most of the anomaly is concentrated within 15 kilometers of the axis (figure B3). Therefore, slab's effective width is only about 30 kilometers.

The one-dimensional inversion (Table B1) results in velocities that are slightly higher than the background velocity. To first order, the three-dimensional solution (figures B4 and B5) shows a centrally located region of high velocity flanked by lower velocities. The boundaries of the high velocity region are approximately correct, and the S and P solutions correlate.

As in the previous test (BLVS), an exaggeration of the velocity in the anomalous region occurs at the edges of the layers with few sources. Finally, the THVS solution shows that a poorly parameterized, small scale anomaly can be resolved if there is a reasonable distribution of sources in the medium.

Thin Low Velocity Slab (TLVS)

The thin, low velocity slab model consists of a centrally located, vertical slab that is 30 kilometers thick and strikes at 77° . There is a 14% velocity contrast between the interior and exterior of the slab (6.5 km/sec vs. 8.0 km/sec for P waves, 3.8 km/sec vs. 4.7 km/sec for S waves). The 130 events used in the inversion occur at depths of 75 and 125 kilometers and are located within a wedge that thins to the west. The northern part of the wedge borders the southern edge of the slab.

The TLVS model may be considered to be a "worst case" for inversion: the slab width is less than the block dimensions, the slab is oriented obliquely to the block configuration, there are neither sources nor receivers within the slab, and there are no sources in the first layer.

For the one-dimensional inversion, the medium was divided into two, fifty kilometer thick layers overlying a half space. These layers are then divided into blocks with 40 kilometer lengths and widths for the three-dimensional inversion.

The velocities inferred from the one-dimensional inversion (Table B1) are close to the velocities of the seismically active region outside the slab. To first order, the three-dimensional results reveal a low velocity anomaly in the general region of the thin slab.

On closer inspection, the three-dimensional solution

(figure B6) seems to create more misgivings than it alleviates. First, there is a significant reversal of the velocity in the southern and northern ends of the first layer. The lesson from this result is similar to the rule inferred in the previous tests: be suspicious of variations near the edges of layers with few sources. Second, the inferred low velocity region in both layers is wider than one might expect, and extends even into the seismically active regions. It is difficult to classify this result simply, however, since it influences the interpretation of the inferred velocities in the seismic regions. The ramifications of the second result on the real solution is discussed in more detail below.

General Rules

The rule of interpretation inferred from the above tests is that large variations in velocities that occur near the edges of layers with few sources are suspect. By comparing some of the characteristics of erroneous solutions in several tests, the following additional rules were found to apply to reliable solutions:

(1) A reasonable cutoff value for resolution is about 0.6 for P solutions and 0.5 for S solutions, lower for S because the S data is weighted less.

(2) Only those variations greater than two percent can be regarded as significant. This estimate is independent of

the size of the linear error estimate.

(3) Solutions should be contourable, even if they seem well resolved. Trends should persist for several blocks, instead of a being defined by fluctuations in velocity in a single blocks. This rule applies to variations between layers as well as to variations within a layer.

Classifying the Effects of Smoothing

The results using real data show a broad, centrally located, low velocity region enveloping the seismic zone. The obvious interpretation is that a broad, low velocity region actually exists. One may wonder, however, if some vastly different situation could provide the same solution, owing to some shortcoming inherent in the method.

Two fundamental questions concerning the existence of the low velocity region can be answered unequivocally. First, if the medium actually does contain a broad, low velocity region, would we be able to detect it? The answer is yes, as is shown in the BLVS test. Second, since one normally expects higher velocities in the seismic region of a subduction zone, could such a high velocity region be detected? The answer provided by the THVS test is that we would see the high velocities, even if they are confined to a narrow region. The conclusion from these two tests is that if the velocity in the Pamir-Hindu Kush is truly smoothly varying and is approximately parameterized by the block structure (i.e. that the basic assumptions are

justified), then the solutions are believable.

More difficult questions address the violation of basic assumptions, primarily in cases where large changes in velocity occur over short distances. One would expect that inferred velocities are smoothed estimates of sudden velocity changes. The question is how much smoothing can one expect, and how does it affect our interpretation of the results?

Generally speaking, we can classify two effects of smoothing: averaging and misrepresentation. Averaging means that the inferred velocity in a block represents an average of the actual velocities, which is really the most one can expect from the solution. Misrepresentation means that the inferred velocity in a block is in no way a reflection of the actual velocity. In the following, we use the results of the hypothetical tests to suggest some of the characteristics of averaging and misrepresentation.

The results of the BLVS test show some examples of averaging. At the southern edge of the slab, the real boundary and the model boundary are the same. In the results for the blocks near the boundary there is a sudden change in the inferred velocity that is similar to the actual change. In the north, where the slab boundary bisects the model boundary, the blocks on the slab boundary show velocity changes near zero, which is the average change of velocity within the blocks. As a result of averaging, the boundary between high and low velocities appears to be

broader than it actually is. While averaging may be important to some aspects of the interpretations, it is not in most cases a significant drawback because it is the expected behavior of the method. The important lesson from the BLVS test is that a reasonably accurate description of the actual velocity structure can be obtained even in less than ideal conditions (e.g. poor distribution of events, strong lateral heterogeneity, and misplaced boundaries).

Some of the blocks in the TLVS test, on the other hand, provide examples of misrepresentation. The solution for the low velocity slab spreads to blocks north and south of the slab, assigning completely erroneous velocities to those blocks.

Note that the BLVS and TLVS tests are alike in most respects. The significant difference between them is that the regions around sudden changes in velocities are separated into broad zones of lower and higher velocity in the BLVS test, while they appear as small scale features in the TLVS test. We infer from this observation that misrepresentation occurs primarily in the presence of small scale heterogeneities.

The medium in the THVS test also has a small scale heterogeneity, but the results show practically no misrepresentation. The significant difference between the TLVS and THVS models is that the THVS model uses a reasonable distribution of events (inside and outside the anomaly), whereas the events are located to one side of the

TLVS anomaly.

Combining our observations, we infer that although averaging occurs under most conditions, misrepresentation occurs only in the presence of small scale, isolated anomalies.

Misrepresentation of velocities in the Pamir-Hindu Kush may occur as a result of small, isolated anomalies in the inactive regions of the lower crust (35-70 kilometers depth) and in those regions of the mantle to the north and south of the seismic zone.

Since the seismic zone begins abruptly near the base of the crust, any anomaly that broadens vertically into the zone must be confined to the aseismic lower crust. To have a significant effect, such an anomaly must be thin (~20 kilometers), and of much lower velocity (by ~10%) than the average crustal velocities. Note also that the anomaly must be horizontally broad; otherwise it would not be traversed by a sufficient number of rays to be detected.

Perhaps the only reason for doubting the existence of such an anomaly is that it is difficult to think of physical arguments for the existence of a horizontally broad, vertically narrow sheet of low velocity material in the lower crust. Still, it seems reasonable, even in tectonic regions, to assume that the crust and mantle can be separated into broadly defined regions of lower and higher velocity, for which case the inversion scheme is well suited. This is not to say that the Moho needs to be

perfectly horizontal; indeed, the BLVS test shows that the position of such a boundary sharp may lie within half a block dimension without significant misrepresentation of the velocities in the blocks. Fluctuations of the Moho to depths greater than 70 kilometers could lower the estimated velocities in the upper mantle, but this is a question of averaging, not of misrepresentation.

Another source of misrepresentation could be the vertical protrusion of a narrow piece of crustal material to great depths. If this protrusion lies outside of the seismic zone, it is possible that the low velocities of the protrusion could broaden into the zone. Let us assume that these protrusions occur to the north or south of the seismic zone, since these regions are free of sources and receivers.

An argument against an isolated anomaly to the north of the zone is that the boundary between high and low velocity occurs right along the northern edge of the seismic zone. The TLVS test shows that misrepresentation should occur on both sides of the anomaly, which implies that the low velocity boundary would extend northwards of the seismic zone.

A similar argument may be made against an isolated low velocity anomaly occurring to the south of the zone, although not as convincingly. The southern boundary is poorly resolved, and fewer events are located near the border. Note, however, that of the four stations (PEN, DOS, KHO, and GOU) with predominantly positive residuals, three

(PEN, KHO, and DOS) lie north of the inferred southern boundary of the low velocity region. Further, if an isolated anomaly did exist to the south of the seismic zone, one might expect positive residuals at all of the southern stations (SAL, CHS, KUY, and GOU), whereas only one (GOU) has predominantly positive residuals (see Appendix C for a discussion of residuals).

Averaging of the Pamir-Hindu Kush velocities may affect our interpretation of the solution in regions of abrupt velocity changes, such as at the Moho or possibly on the edges of the low velocity region in the mantle. It could be, for instance, that the gradual, lateral changes in velocity in the eastern part of the region are an average of an abrupt change in velocity occurring somewhere in the middle of the slope. Such an effect does not change the interpretation that a low velocity zone in the mantle exists, however.

If the Moho dips below the inferred depth of 70 kilometers, the average velocity for some of the blocks lying between 70 and 110 kilometers will be less than that of the surrounding blocks. In such an event, we may wrongly conclude that the low velocities extend to depths of 110 kilometers. The only way that the effect of averaging can be estimated is by changing the boundaries of the solution with real data. A discussion of averaging effects on the real solution can be found in Appendix C.

We infer from this discussion that the velocity changes

propounded by the real data solution are most likely to be averages of the actual velocities. We are not simply forcing a round-peg reality to fit into a square-hole model.

Applying the Interpretation Rules

Even if the solution is approximately correct, the rules of interpretation inferred from the hypothetical tests still apply. It remains to review how these rules effect our interpretation of the solution using real data.

(1) Contouring

The contour rule was the first filter applied to the inverse solutions, with those violating the rule being dismissed outright. In only one case was contouring a problem: when the block dimensions were decreased from 40 kilometers to 20 kilometers. Velocities deduced from inversions using these smaller blocks oscillated from block to block and from layer to layer. One solution that used smaller blocks in only one layer (AF4, see text) fared better, although this solution did not differ significantly from the inversions with 40 kilometer blocks.

(2) Resolution and Covariance

Blocks classified as spurious because of poor resolution were almost always on the edge of the region or at great depth. Most were also suspect through the application of other rules of interpretation. In any event,

exclusion of poorly resolved blocks had little influence on the interpretation, although removing these blocks frequently made for smoother contours.

Owing to the large variations in the velocities deduced from real data, the two percent rule does not gloss over any interpretable variations in the solution. On the contrary, two percent turns out to be a convenient contouring interval.

These resolution and covariance rules are the only ones applied in screening the solutions before drawing the contours.

(3) Variations away from the source regions

The rule that classifies large variations away from source regions as spurious applies particularly to blocks near the edges of layers with few sources. In the AF2 solution (Table 3, figures 10 and 11 in the text) the low velocities in the northernmost part of layer 2 fall into this category, as do the large variations around station KHO in layer one. Also, because there are fewer events in the western part of the array, the large low velocity changes (-6% to -8%) in layers 2 and 3 may be exaggerated. More likely, these changes are in the -4% range, which are found in the more active, eastern part of the array. These assessments are necessarily qualitative, however, and serve only to give an impression of the uncertainty involved.

Captions

Figure B1. Results of an inversion for the three-dimensional velocity structure of the broad, low velocity slab (BLVS) test. Solid east-west lines define the limits of the BLVS. The solid circles indicate the station locations. Presentation of results is the same as in figure 10 of the text.

Figure B2. Contour plots of inferred percent changes in velocity for the BLVS test, along with epicenters of the events used. The first two rows are contour plots for the upper two layers (nothing is resolved in layer 3). The last row shows the original locations of events (left) and the relocation of the same events after determining the best-fitting layered structure (right). The thick east-west lines in the last row define the limits of the BLVS, and the solid triangles indicate the station locations.

Figure B3. The background velocity profile of the thin, high velocity slab (THVS) test. Inserted in the figure is a plot of the percent anomaly of the THVS as a function of the distance from the center of the slab, and a plot of the decay of the maximum anomaly (in the center of the slab) with depth.

Figure B4. Results of an inversion for the three-dimensional velocity structure of the thin, high velocity slab (THVS) model. The parallel lines obliquely oriented to the block configuration indicate the boundary of the slab region. Presentation of results is the same as in figure 10 of the text.

Figure B5. Contour plots of the inferred velocity changes in the THVS test, along with epicenters of events used. The parallel lines striking at 60° correspond to the boundary of the slab. Solid triangles give the locations of the recording stations. Presentation of results is the same as in figure 11 of the text.

Figure B6. Location of hypothetical events in the TLVS test before (right) and after (left) the one-dimensional velocity inversion. Stars indicate events, solid circles indicate stations. The configuration of the blocks used in the three-dimensional inversion is superimposed on the map on the left. Parallel lines striking obliquely across the maps delimit the position of the TLVS.

Figure B7. Results of an inversion for the three-dimensional velocity structure of the thin, low velocity slab (TLVS) model. The parallel lines obliquely oriented to the block configuration

indicate the boundary of the slab region.

Presentation of results is the same as in figure 10 of the text.

BLVS

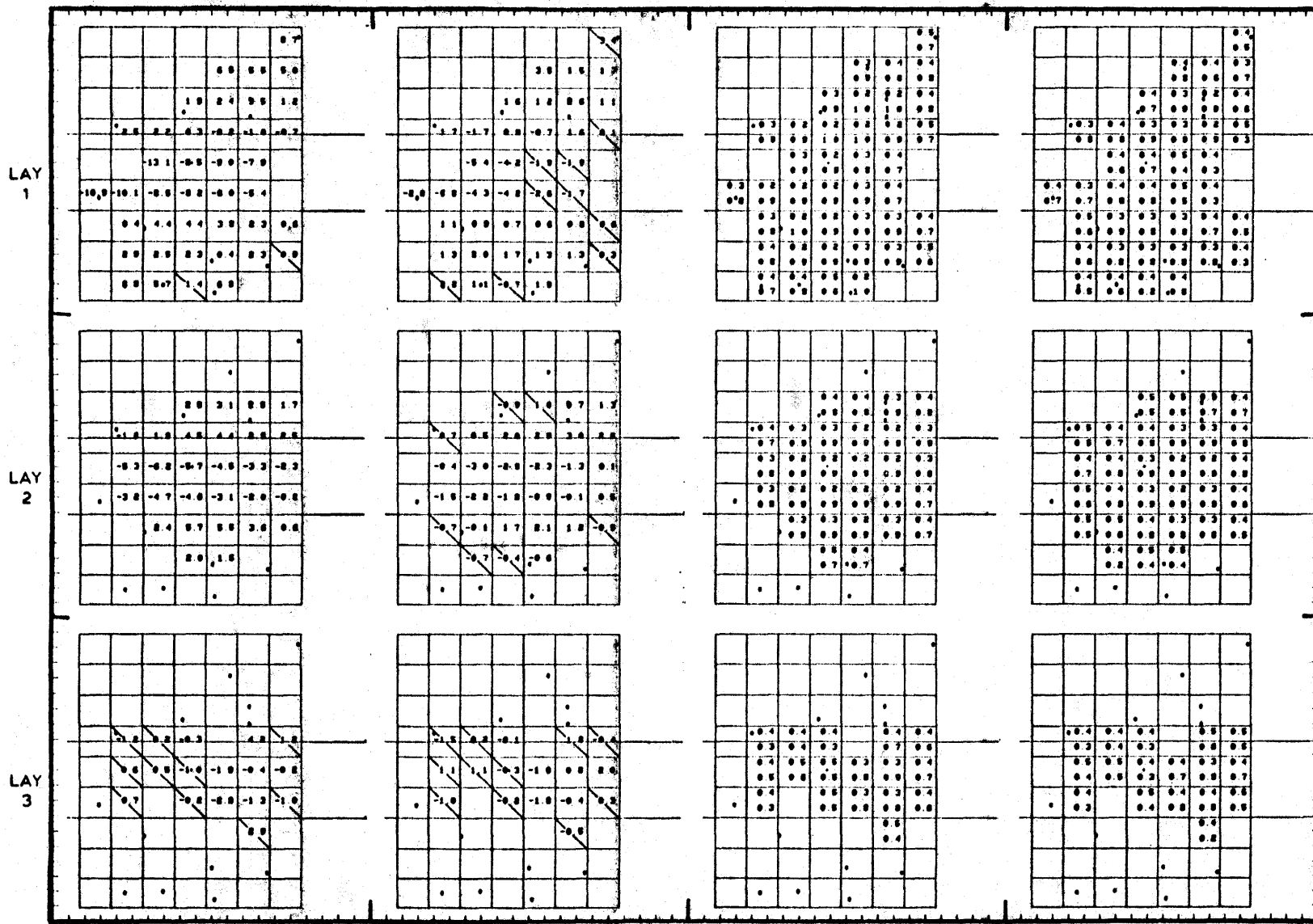


Figure B1.

Figure B2.

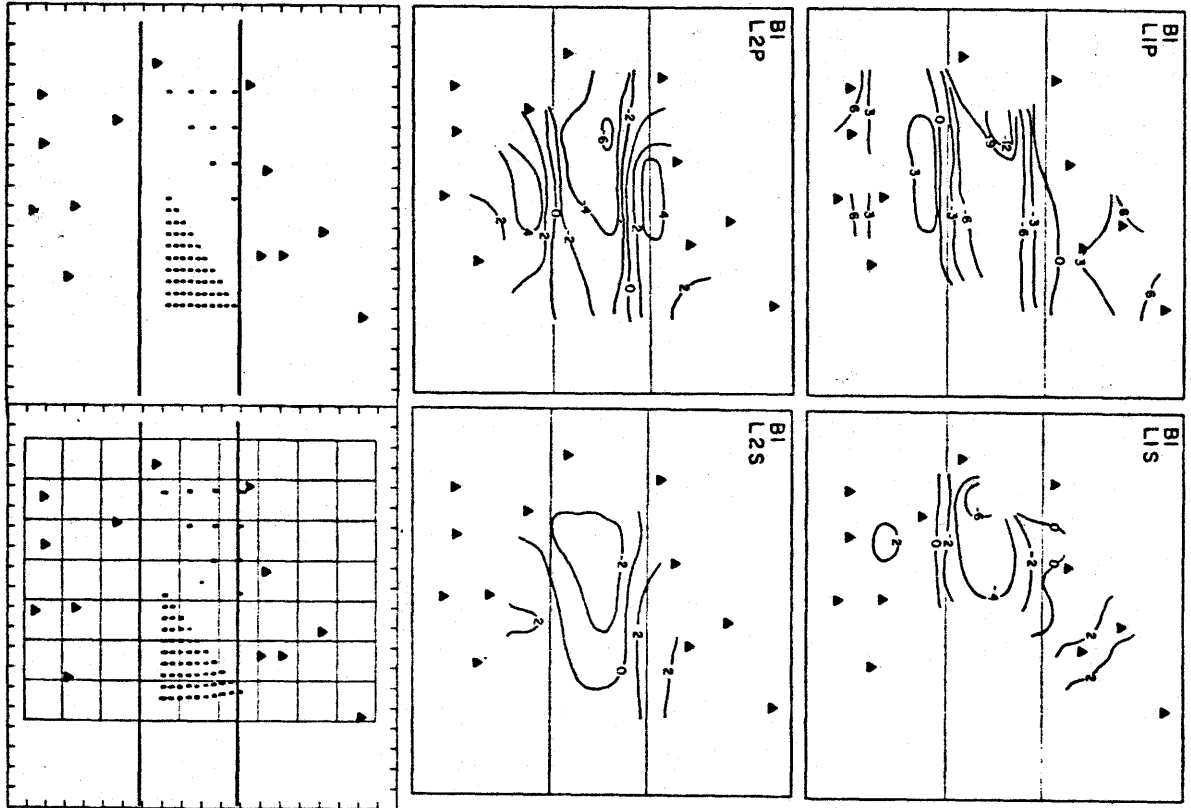


Figure B3.

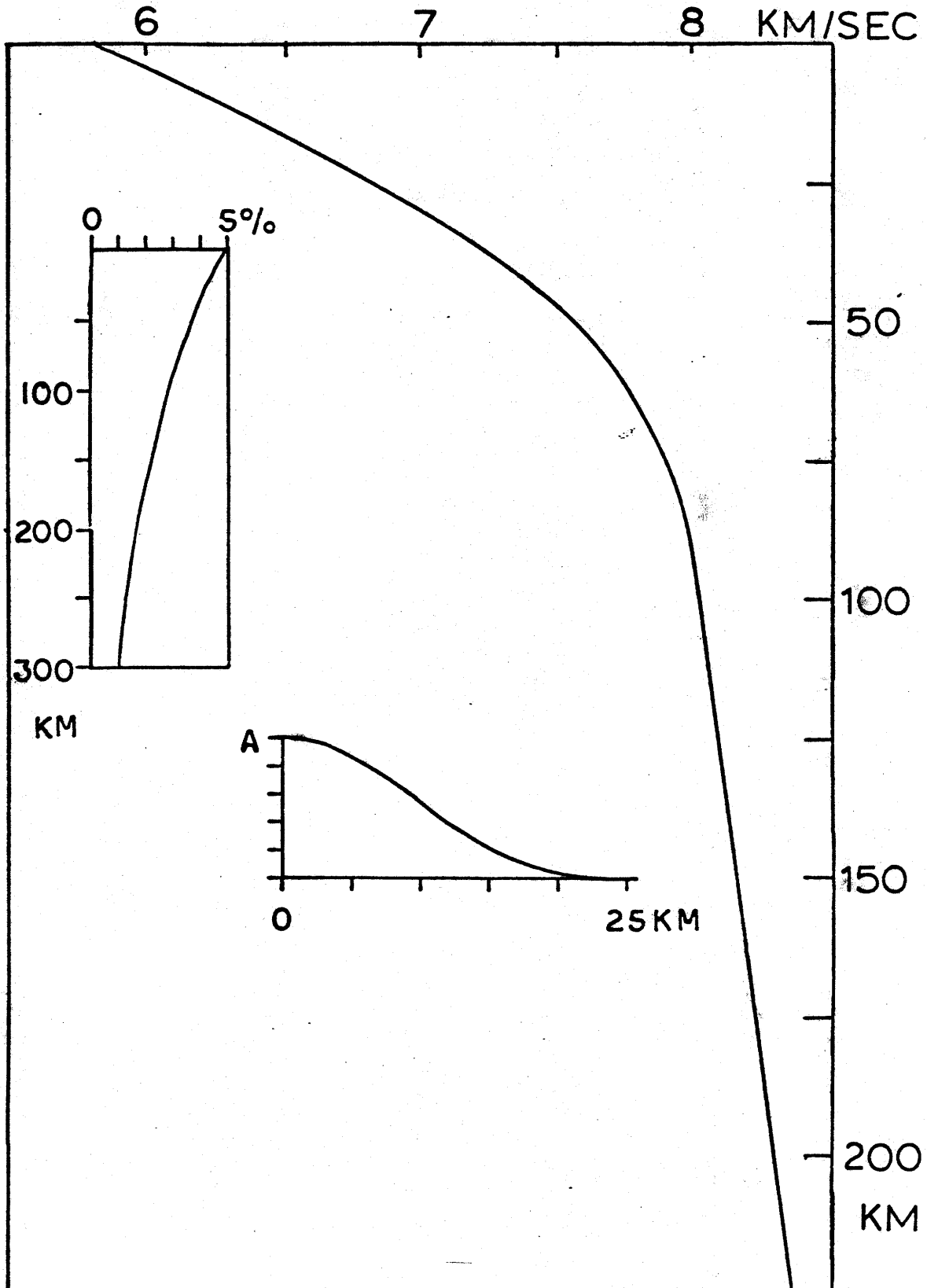


Figure B4. (cont.)

THVS

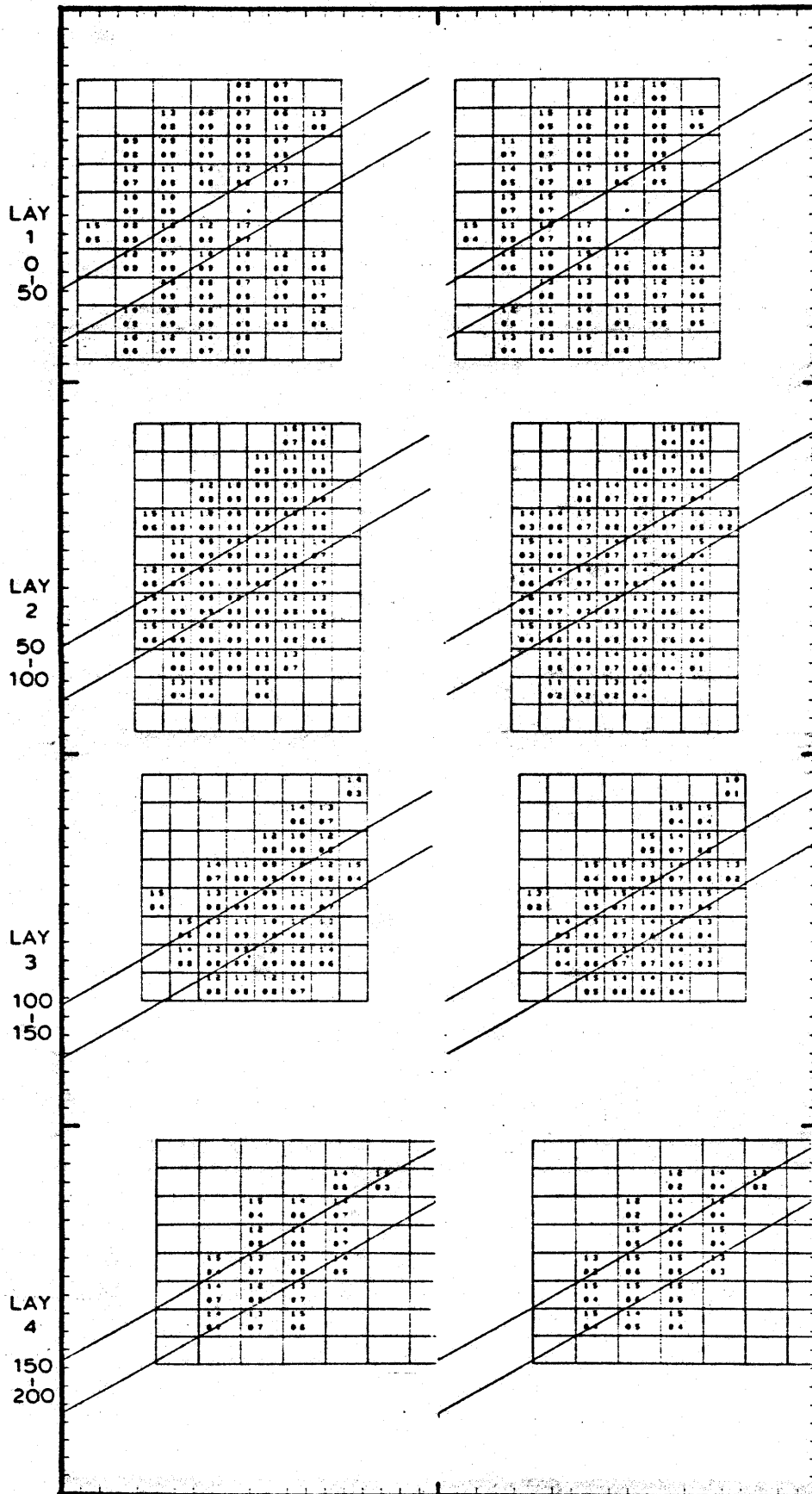
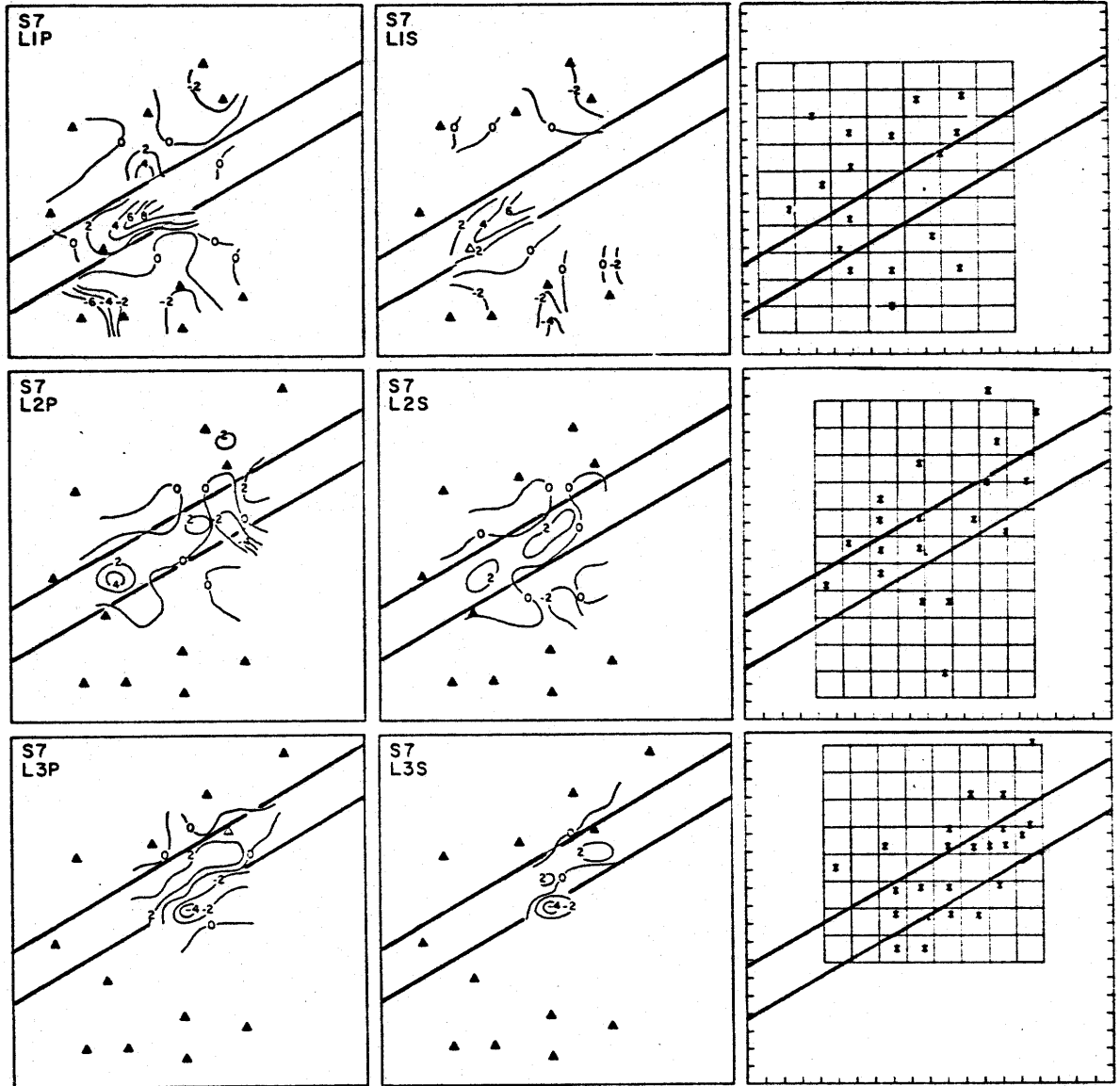
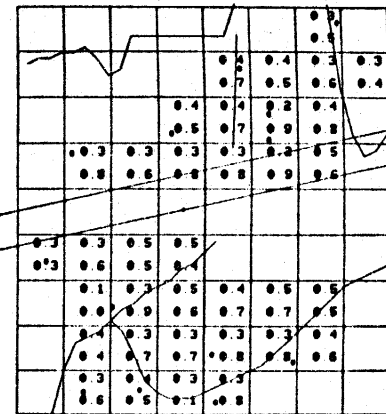
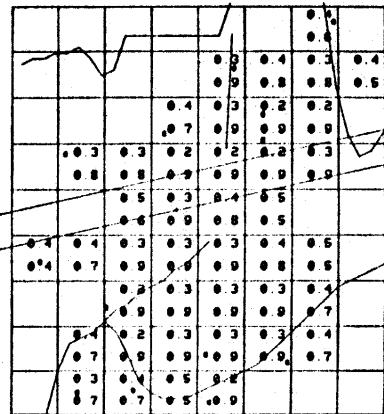
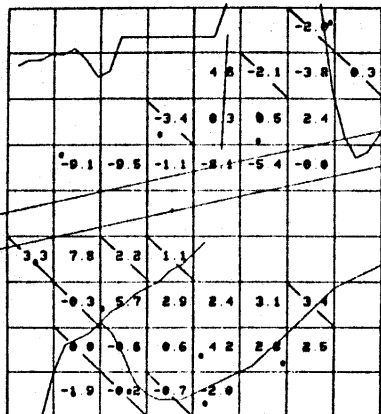
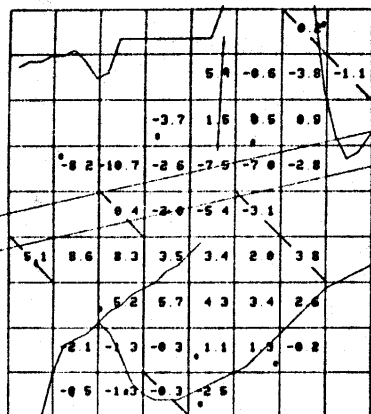


Figure B5.

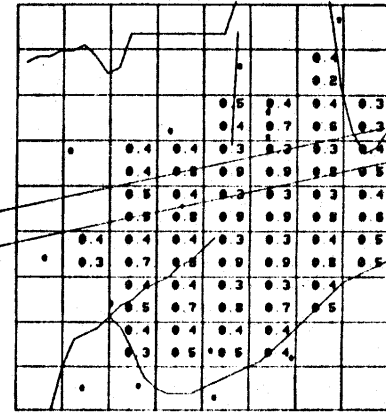
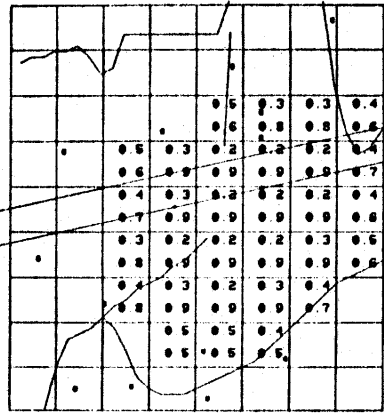
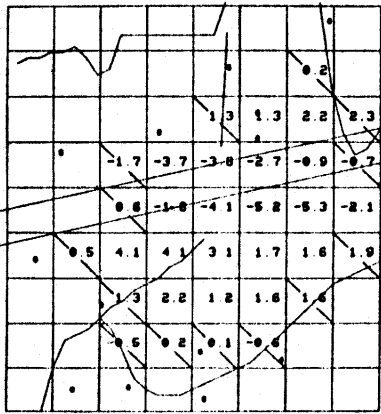
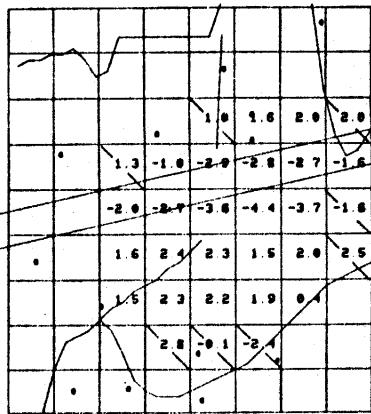


TLVS

LAY
1



LAY
2



LAY
3

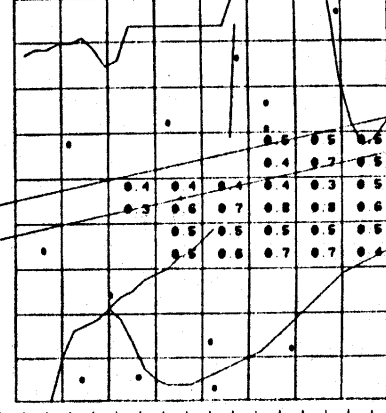
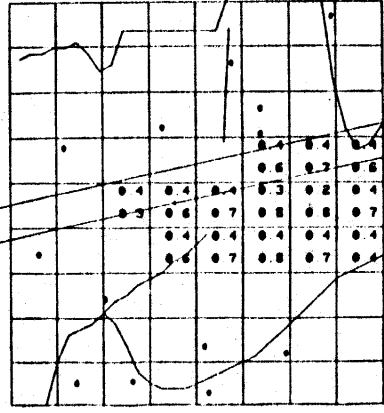
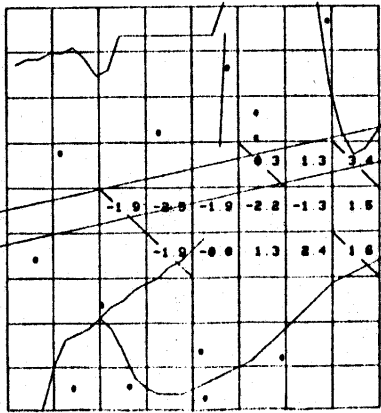
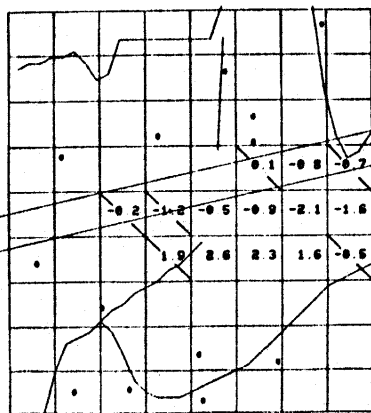


Figure B7.

Table Captions

Table B1. Specifications of the starting models used in the three-dimensional inversions, along with the variance in the data before and after the inversions.

Table B1.

BLVS Inversion				
130	Events			
1950	P Arrivals			
1950	S Arrivals			
Starting Model				
Layer	Depth	P Velocity	S Velocity	
1	-1.0	7.24	4.45	
2	50.0	6.99	4.42	
3	100.0	7.27	4.50	
Original Variance			0.449	
Final Variance			0.007	
Percentage Improvement			98.260	
THVS Inversion				
93	Events			
1090	P Arrivals			
1089	S Arrivals			
Starting Model				
Layer	Depth	P Velocity	S Velocity	
1	-2.0	7.01	4.09	
2	50.0	8.02	4.71	
3	100.0	8.53	4.98	
4	150.0	8.47	5.04	
5	200.0	8.51	5.02	
Original Variance			0.159	
Final Variance			0.065	
Percentage Improvement			59.097	
TLVS Inversion				
110	Events			
1650	P Arrivals			
1650	S Arrivals			
Starting Model				
Layer	Depth	P Velocity	S Velocity	
1	-1.0	7.93	4.30	
2	50.0	8.00	5.11	
3	100.0	7.69	4.65	
Original Variance			0.340	
Final Variance			0.007	
Percentage Improvement			97.748	

APPENDIX C

TESTS WITH REAL DATA

The hypothetical tests in Appendix B attempt to classify the symptoms of nonlinearity and poor modeling, the miscreants that threaten to rob our simple solutions of reliability. Despite their usefulness, however, every hypothetical solution is in some way peculiar to the model that created it. One may invert synthetic data for hundreds of preordained solutions without being completely convinced of their applicability to the real medium.

The only data truly relevant to the real medium is, of course, the real data. To gain a full appreciation for the stability and lack of bias in the real solution, the performance of several inversions with the real data (using various starting models and subsets of data) is necessary. Besides allowing a gross justification for the solution, the tests with real data are intended to provide some insight into the problems of coupling between layers and of averaging the irregularities in the Moho.

Residuals

Honest velocity inversion routines perform no magic; they simply try to explain residuals more precisely than can eyeballs and graph paper. For this reason, a large scale anomaly, such as the low velocity region in the Pamir-Hindu Kush, should produce substantial residuals at appropriate

stations, or else the solution is suspicious.

A plot of percent residuals ($100 \times \text{residual}/\text{travel time}$ = - percent velocity change required along path) at 4 stations (KHO, FRA, PEN, KUY) is shown in figures C1 and C2. The events used are all those between 70 and 110 kilometers depth (layer 3 of inversion AF2). At the stations to the east (KHO) and west (PEN) of the seismic zone, the percent residuals are positive from events throughout the region. Positive residuals require lower velocities (i.e. lower than the model velocities) along the rays to these stations. Likewise, the predominately negative residuals at stations to the north (FAR) and south (KUY) require higher velocities.

These simple patterns in the percent residuals are consistent with a centrally located, east-west trending low velocity zone, flanked to the north and south by higher velocities. (Of course, these few residuals are consistent with other models as well; one needs to examine more stations before drawing definite conclusions). The same patterns are also evident in residuals from deeper (down to 150 kilometer) events.

Coupling and Stability

The resolution matrix provides an estimate of the linear independence (or, conversely, the coupling) of the model parameters. Because certain assumptions made in formulating the general inverse (such as linearity and proper modeling) are implicit in the resolution formulation,

the reliability of the resolution estimates may be suspect.

If the parameters are completely uncoupled, the same solution should be recovered regardless of whether a parameter is determined by itself or jointly with others. Therefore, a straightforward test of coupling is to compare solutions using different subsets of parameters. Further, for stability reasons, a solution should be independent of a specific combination of data. A test of such dependences can be made by comparing inversions using different subsets of data, and determining which data contribute the most to the solution.

Solution AF2 (Table 2, figures 10 and 11 of the text) is an inversion for the entire seismic zone, from the surface to approximately 300 kilometers depth, which makes use of the approximately 580 events that passed the selection criteria. In the following discussion, AF2 provides a basis of comparison for the test runs.

Solution AF8 (Table C1, figures C3 and C4) includes data from only those events shallower than 160 kilometers, and, as a starting model, uses only the first 4 of the 7 layers used in AF2. The results are essentially the same, except that more blocks in AF8 fail the resolution cutoff. This comparison shows that deeper events do not make a significant contribution to the solution for the velocities in the upper layers, and also that the solutions for velocities in deeper and shallow layers are acceptably uncoupled.

Inversions AF7 and AF5 (Table C1, and figures C5 through C8) fix the velocities in layer 1 and in layers 1 and 2, respectively, by excluding them from the normal equations. Events in these layers are also excluded. The velocities inferred in the AF5 inversion agree with those in layers 4 and 5 of AF2, and the reduction in data variance (~25%) is approximately half that of AF2. These results imply that there is no significant coupling between the solutions for the layers above and below 70 kilometers depth. The velocities inferred in the layers that were allowed to vary in the AF7 inversion also compare favorably with AF2, with the exception of the solution for layer 2. The major variations obtained in layer 1 of AF2 appear to be superimposed on layer 2 of AF7. Further, the reduction in data variance is essentially the same (~50%) for AF2 and AF7. The results of the AF5 and AF7 inversions suggest that while layer 3 is independent of the variations in the upper layers, some coupling exists between the relatively event-free first and second layers. It is difficult, therefore, to know the extent of the apparent variations in these two layers. Finally, as with the AF8 solution, the AF7 and AF5 solutions suggest that the events in a layer are primarily responsible for discerning the velocity variations in that layer.

(4) Station corrections

As discussed in the text, it is necessary to have some

estimate of the scale of the heterogeneity to which station corrections apply. On the basis of a priori evidence, it was argued that there were no obvious small scale anomalies near the stations, and so the corrections were not applied. This evidence may not be totally convincing, however, and one may wonder how crucial the decision not to use corrections is.

Run AF11 (Table C1, figures C9 and C10) uses the same data and starting model as AF2, except that station corrections are applied. The most notable difference between the two inversions is that most of the variation in layer 1 of AF2 has disappeared in AF11. Variations in layer 2 are also lessened, owing most likely to the coupling between layers 1 and 2 discussed above. Below layer 2, however, the inferred velocities are essentially the same. Therefore, while variations in the crustal velocities must be defended with some a priori information, the central low velocity zone in the mantle does not.

Averaging

The hypothetical tests of Appendix B suggest that the complete misrepresentation of velocities in the seismic zone by an isolated anomaly in the lower crust is unlikely. Still, one might imagine that fluctuations of 10 or 20 kilometers in the depth of the Moho below 70 kilometers depth would lower the average velocity in the upper mantle blocks, thereby artificially "transporting" a low velocity

anomaly to depths of 110 kilometers.

Even if such fluctuations did occur, it is unlikely that they could explain the central low velocity zone completely. Layer 4 in AF2 also shows lower velocities in the seismic zone, which would require a broad fluctuation in the Moho to depths in excess of 110 kilometers. Such a condition would imply that the crust in the Pamir-Hindu Kush is extraordinarily thick in places, being some 50% thicker than an already thick 70 kilometers.

There remains a question of the extent to which fluctuations in the Moho might alter our perception of the velocity anomaly. An estimate may be provided by inverting the one-dimensional models with deep Mohos of 80 and 90 kilometers, as is done in solutions AF10 and AF9 (Table 3, figures 12-15 of text). Comparing these solutions with AF2, a picture is created of a low velocity region varying smoothly and continuously from somewhere in the lower crust to depths possibly in excess of 150 kilometers.

The continuity of the low velocity region from the lower crust to depths well into the mantle, regardless of the change in boundaries, is hard to explain with a few fluctuations in the Moho. More likely, the solutions represent exactly what they appear to be - a continuous, nearly vertical, centrally located, low velocity region which extends from somewhere near the surface to some unresolved depth.

Captions

Figure C1. Plots of percent residuals ($100 \times (T_o - T_c)/T_c$) at stations to the northeast (KHO) and southwest (PEN) of the seismic zone for P (left) and S (right). Each percent residual is an average over all of the data from events in a 40 km cube located between 70 and 110 kms depth. In each block, the lower number is the average percent residual, and the upper number is the number of arrivals over which the average is taken. The solid triangle in each figure indicates the location of the station named in the upper left corner of the figure. The open triangles indicate the locations of other stations in the array.

Figure C2. Plots of percent residuals at stations to the north (FAR) and south (KUY) of the seismic zone. Presentation of results is the same as in figure C1.

Figure C3. Results of run AF8, an inversion for a three-dimensional velocity structure using only the upper 4 layers of the one-dimensional results of figure 3 as a starting model and only data from event shallower than 150 km. Presentation of results is the same as in figure 10 of the text.

Figure C4. Contour maps of the resolvable percent changes

in P and S wave velocities in the AF8 inversion. Presentation of the results is the same as in figure 11 of the text.

Figure C5. Results of run AF7, an inversion for a three-dimensional velocity structure using the same starting model as run AF8, but with the velocities in the uppermost layer held fixed. Presentation of results is the same as in figure 10 of the text.

Figure C6. Contour maps of the resolvable percent changes in P and S wave velocities in the AF7 inversion. Presentation of the results is the same as in figure 11 of the text.

Figure C7. Results of run AF5, an inversion for a three-dimensional velocity structure using the same starting model as run AF8, but with the velocities in the upper two layer held fixed. Presentation of results is the same as in figure 10 of the text.

Figure C8. Contour maps of the resolvable percent changes in P and S wave velocities in the AF5 inversion. Presentation of the results is the same as in figure 11 of the text.

Figure C9. Results of run AF11, an inversion for a three-dimensional velocity structure using the same

starting model and data as AF2, with the exception that station corrections are subtracted from the arrival times.

Figure C10. Contour maps of the resolvable percent changes in P and S wave velocities in the AF11 inversion. Presentation of the results is the same as in figure 11 of the text.

Figure C1.

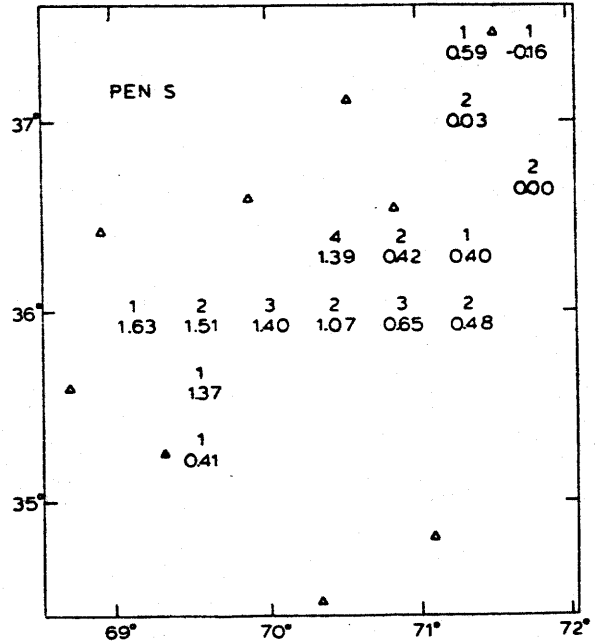
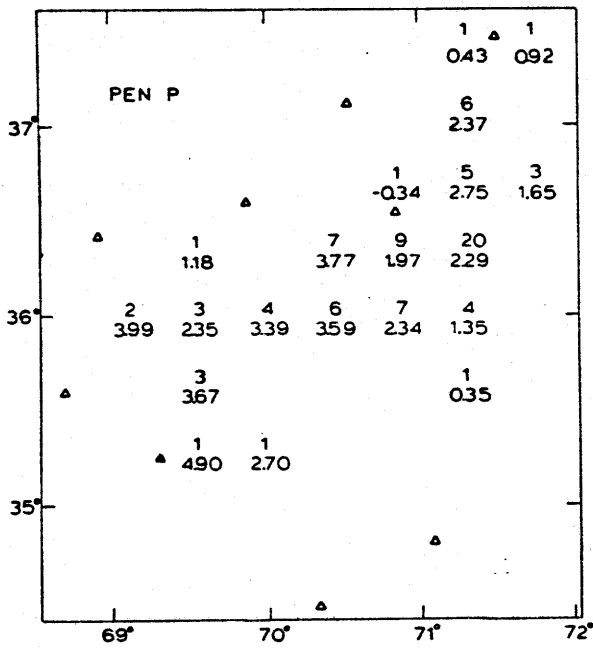
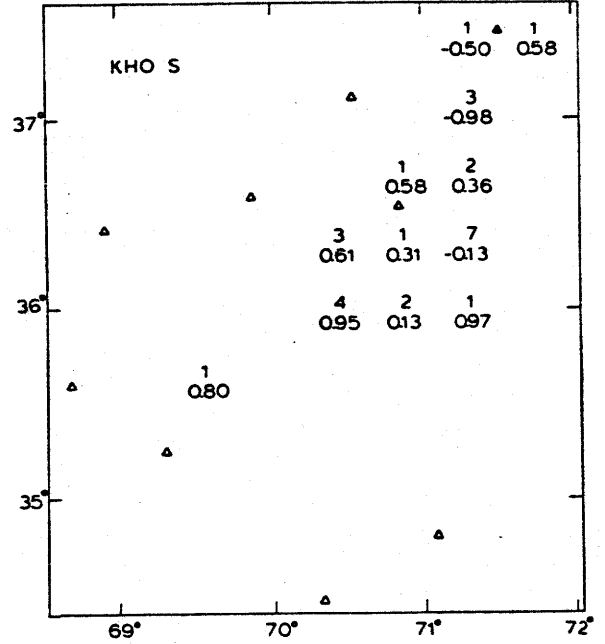
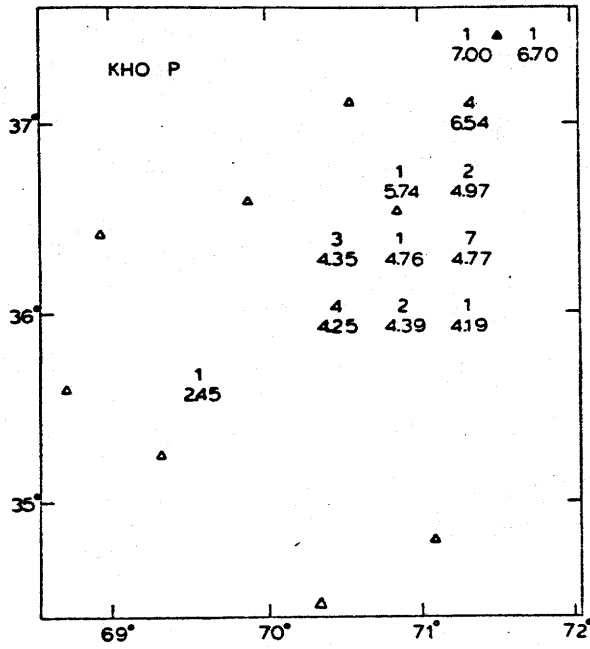


Figure C2.

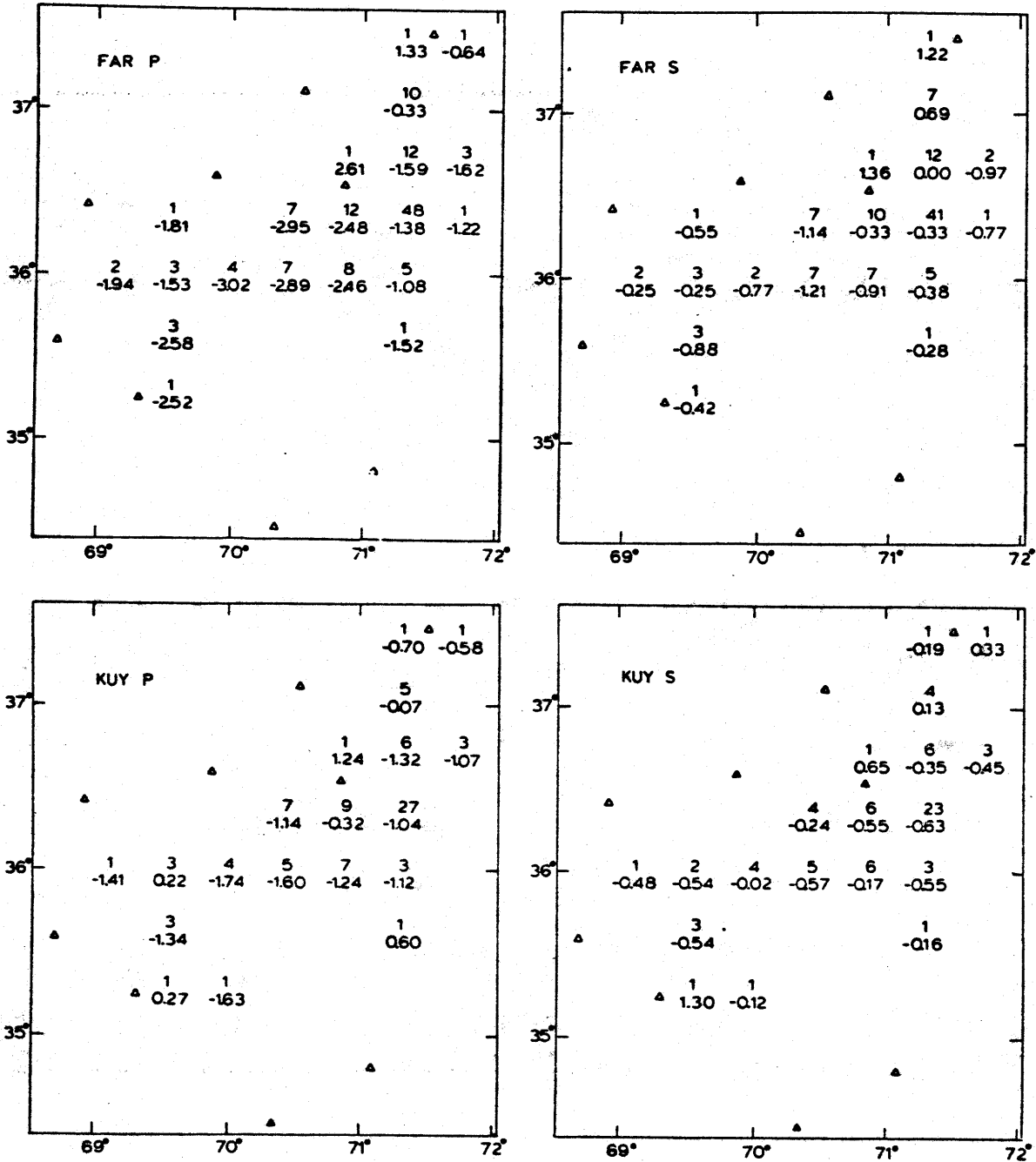


Figure C3.

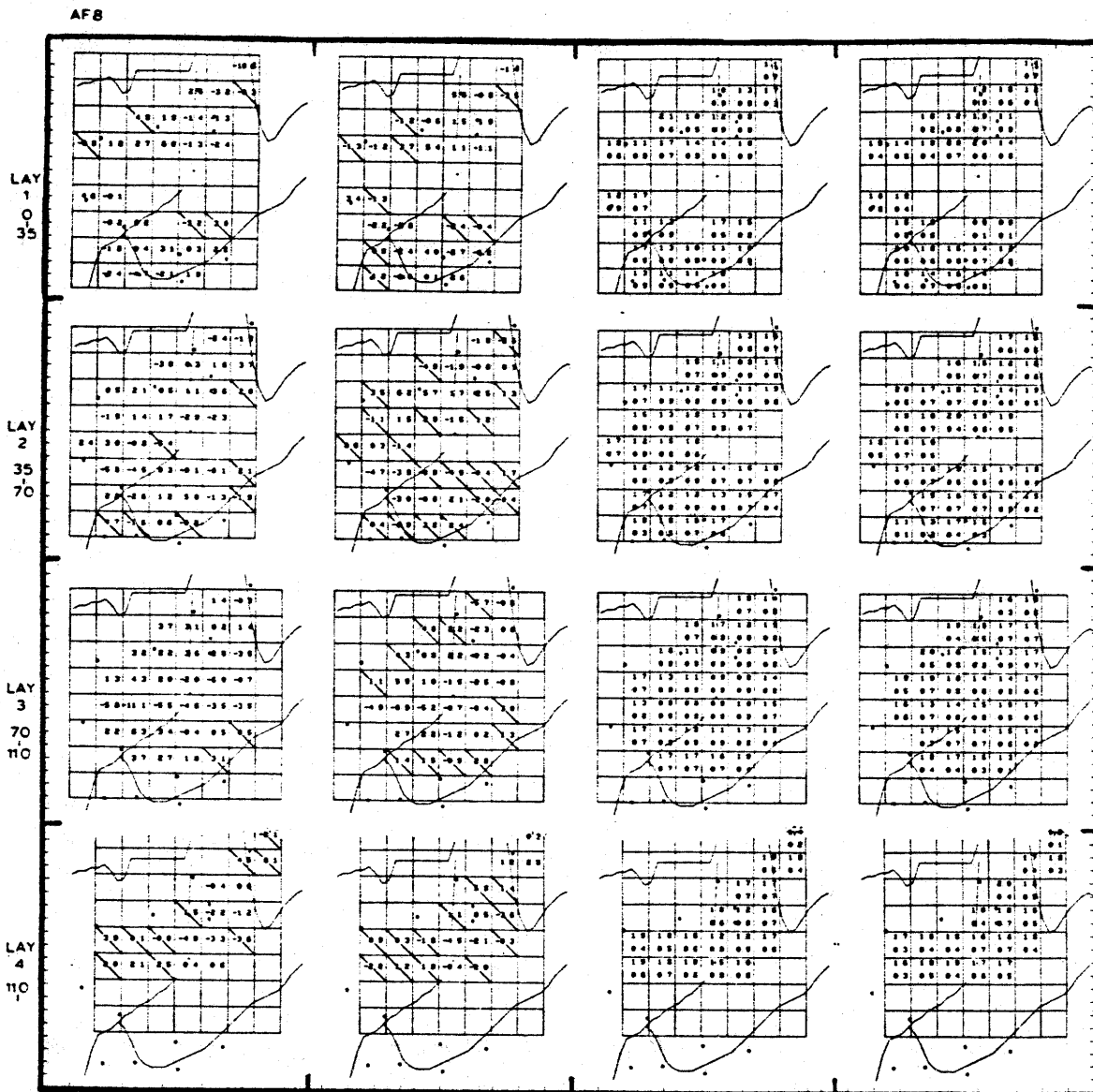
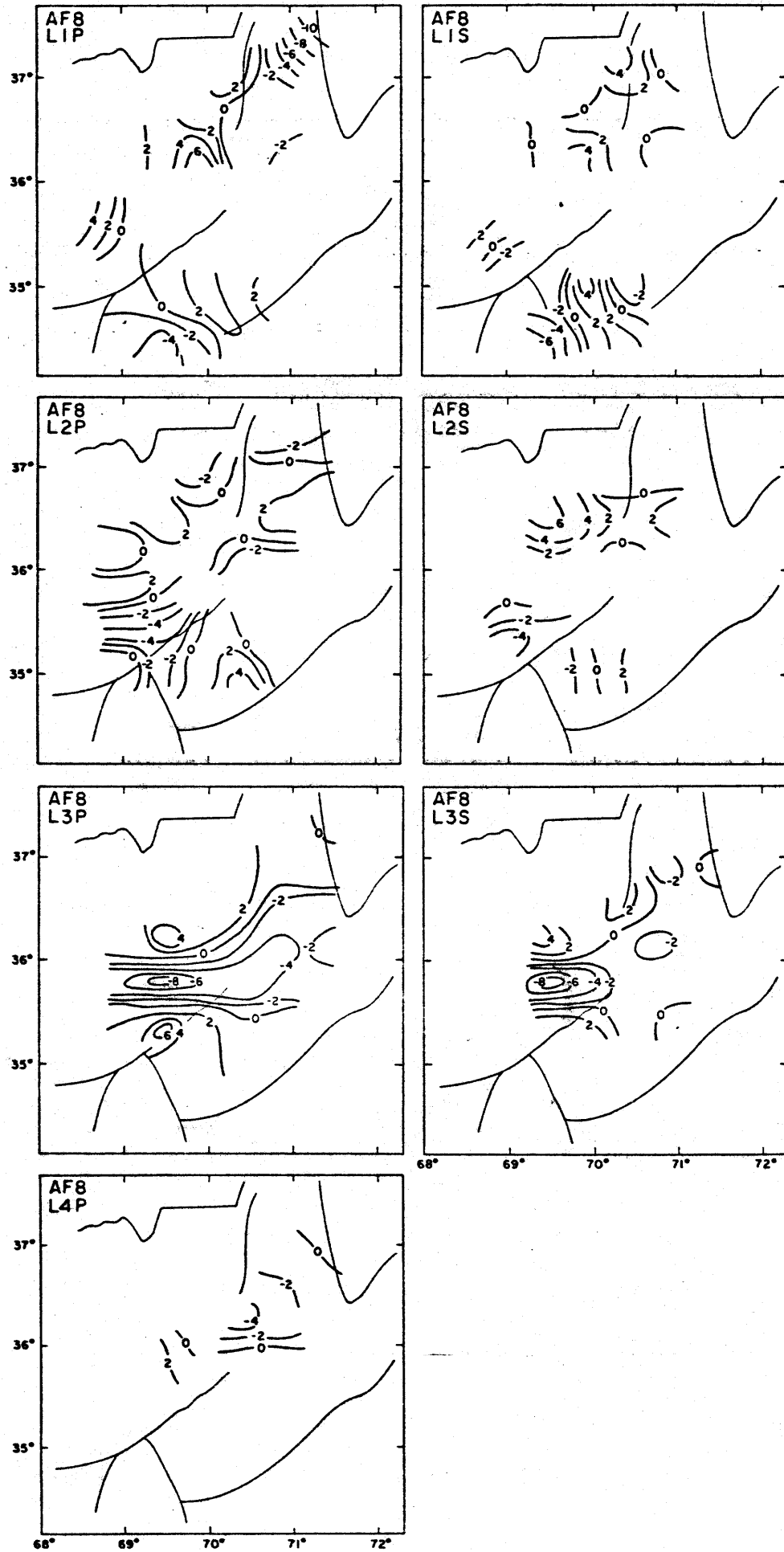


Figure C4.



AF7

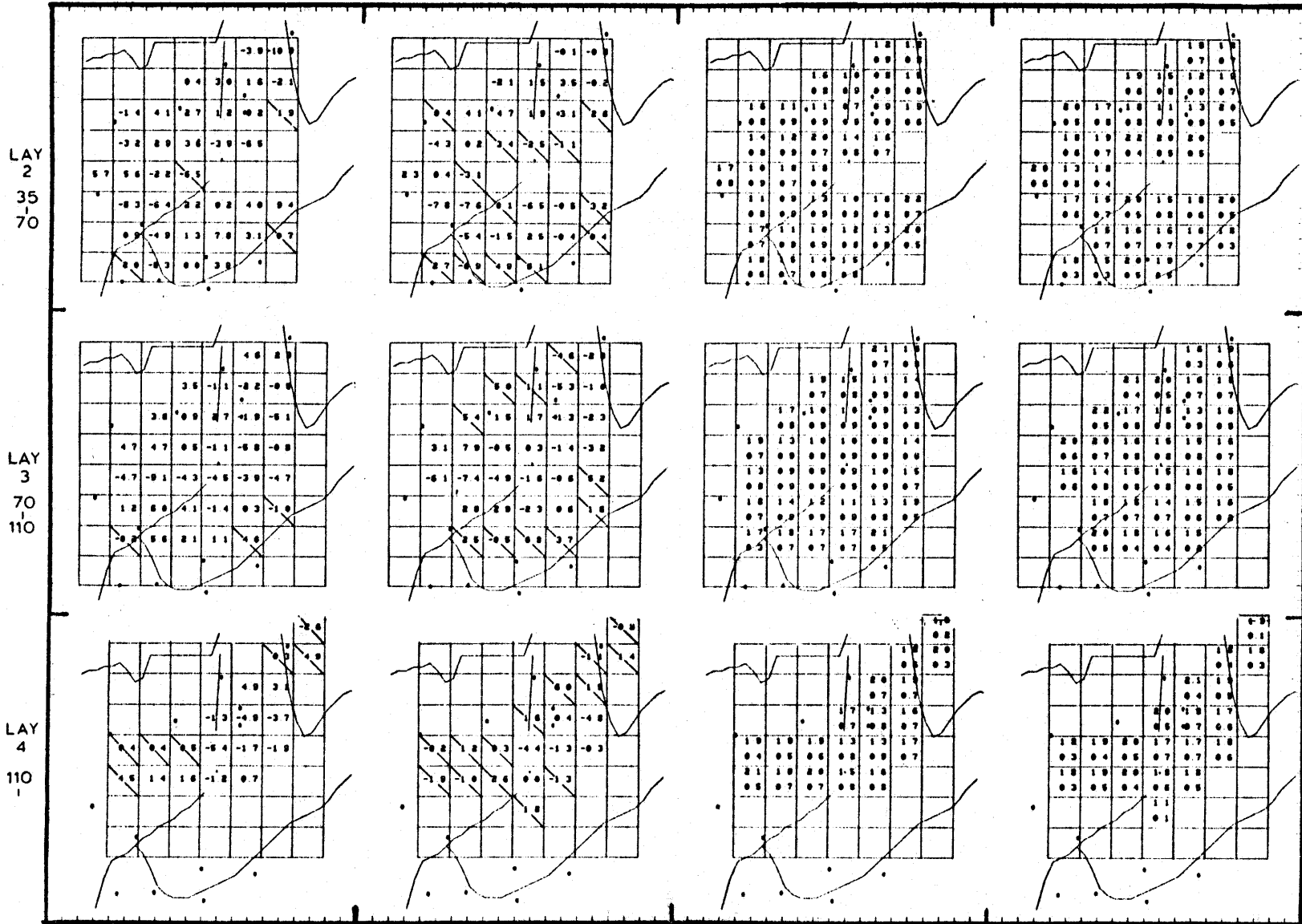
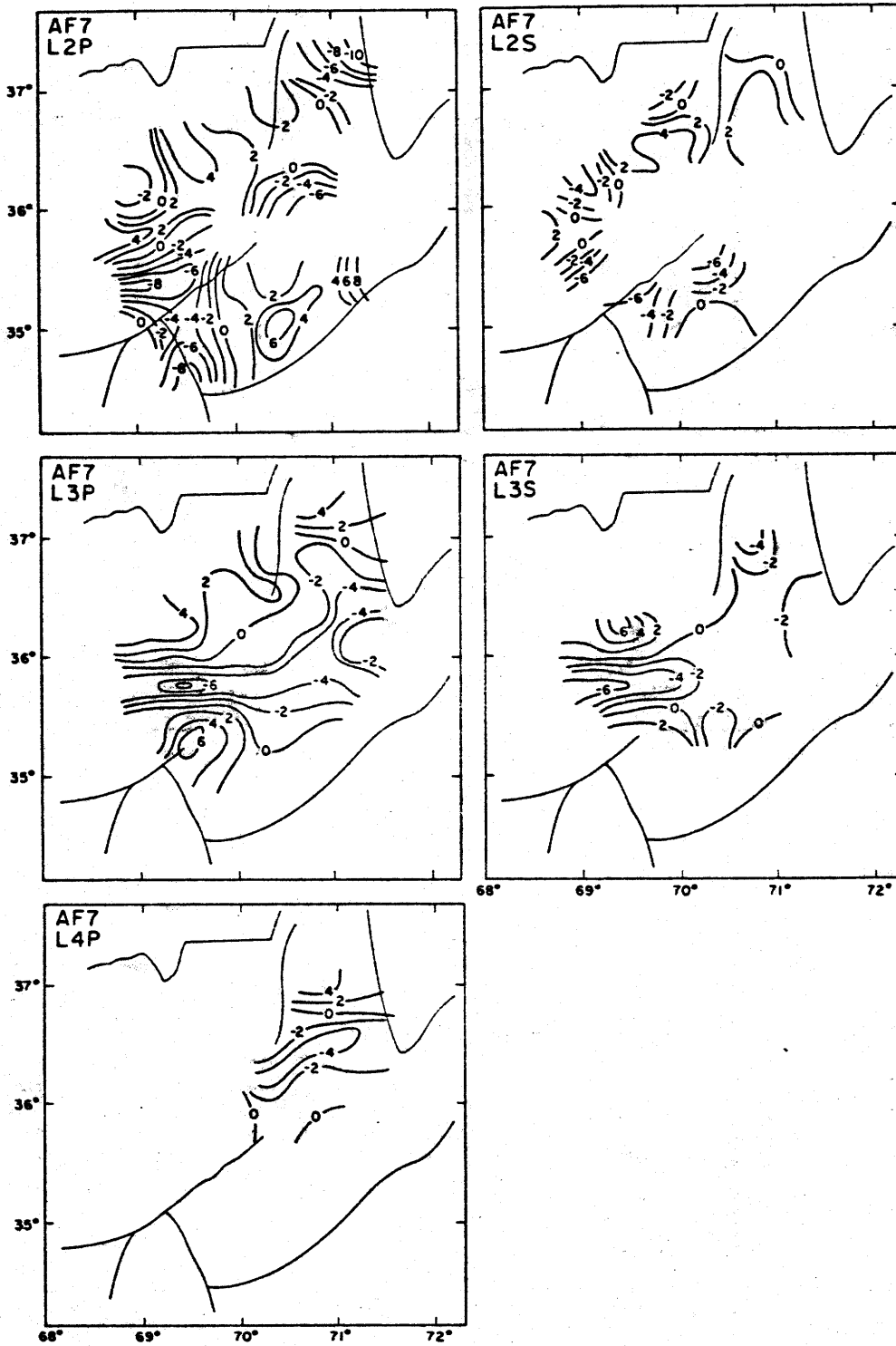


Figure C5.

Figure C6.



AF5

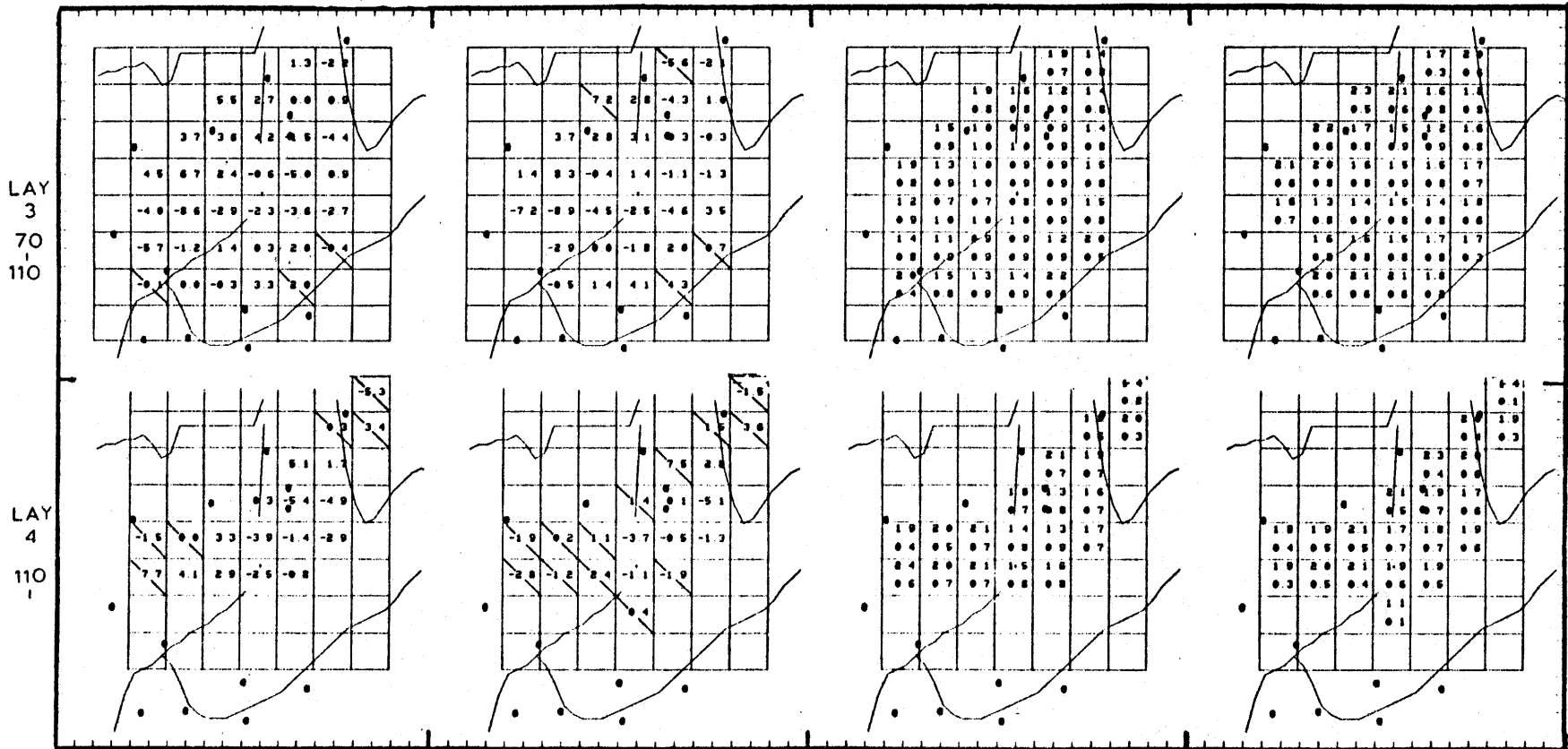


Figure C7.

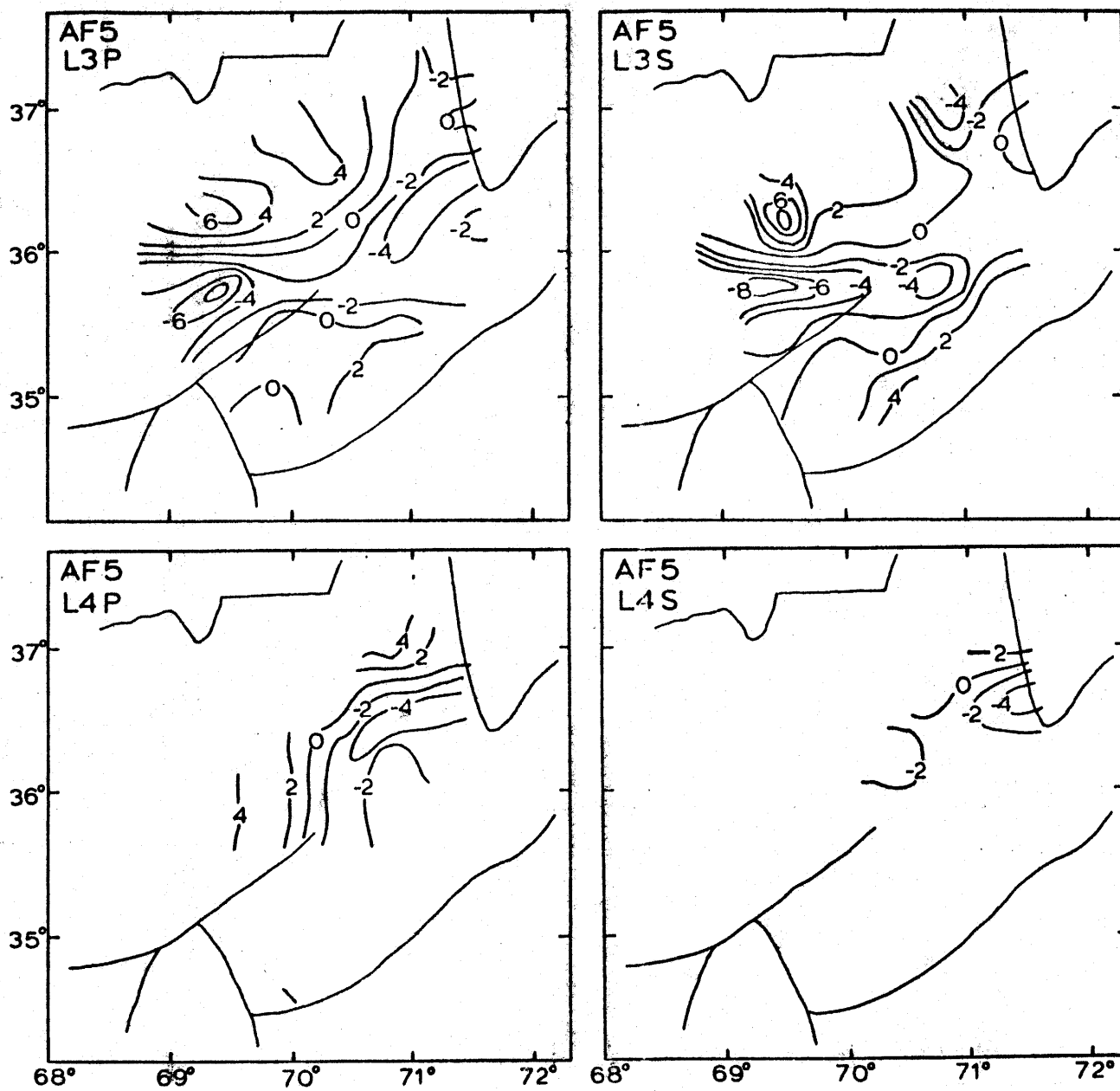


Figure C8.

Figure C9.

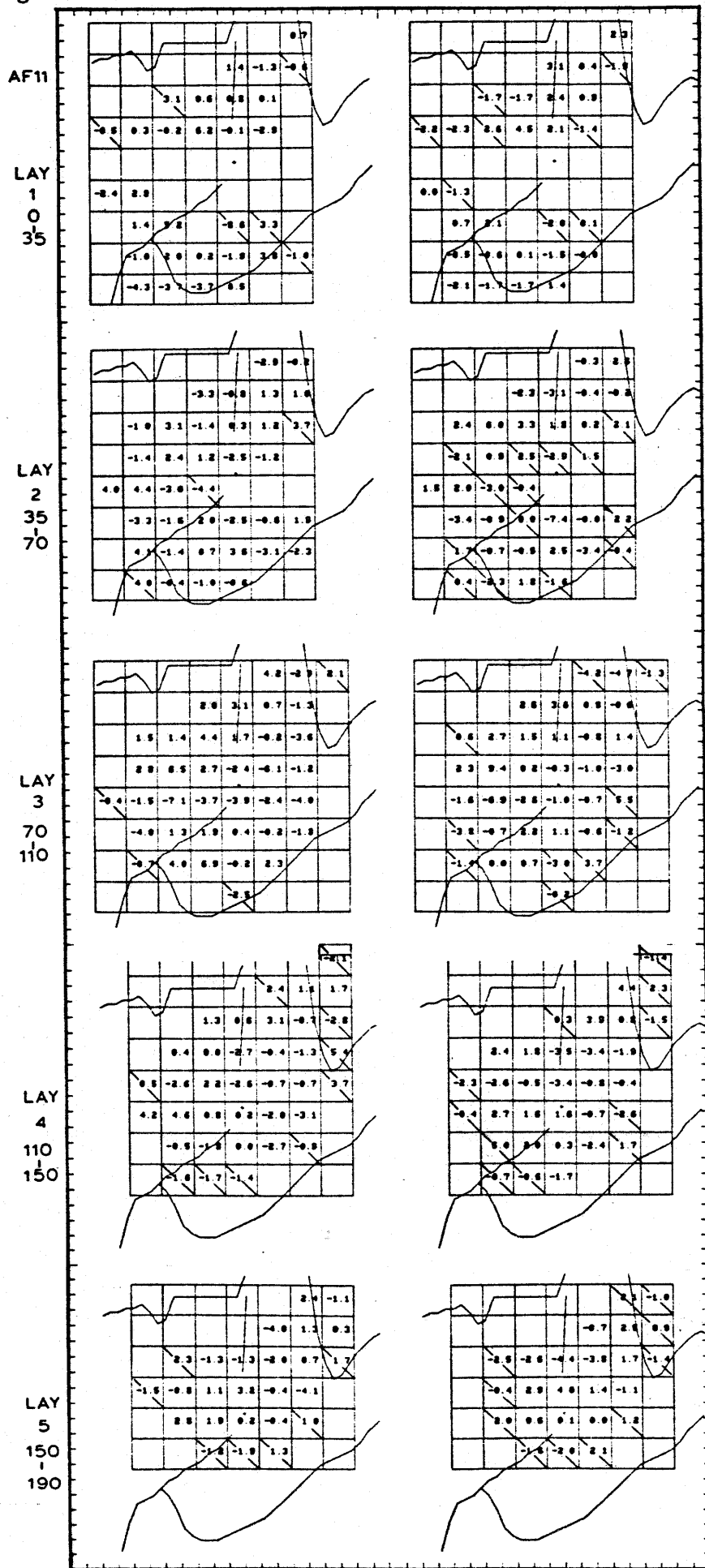


Figure C10.

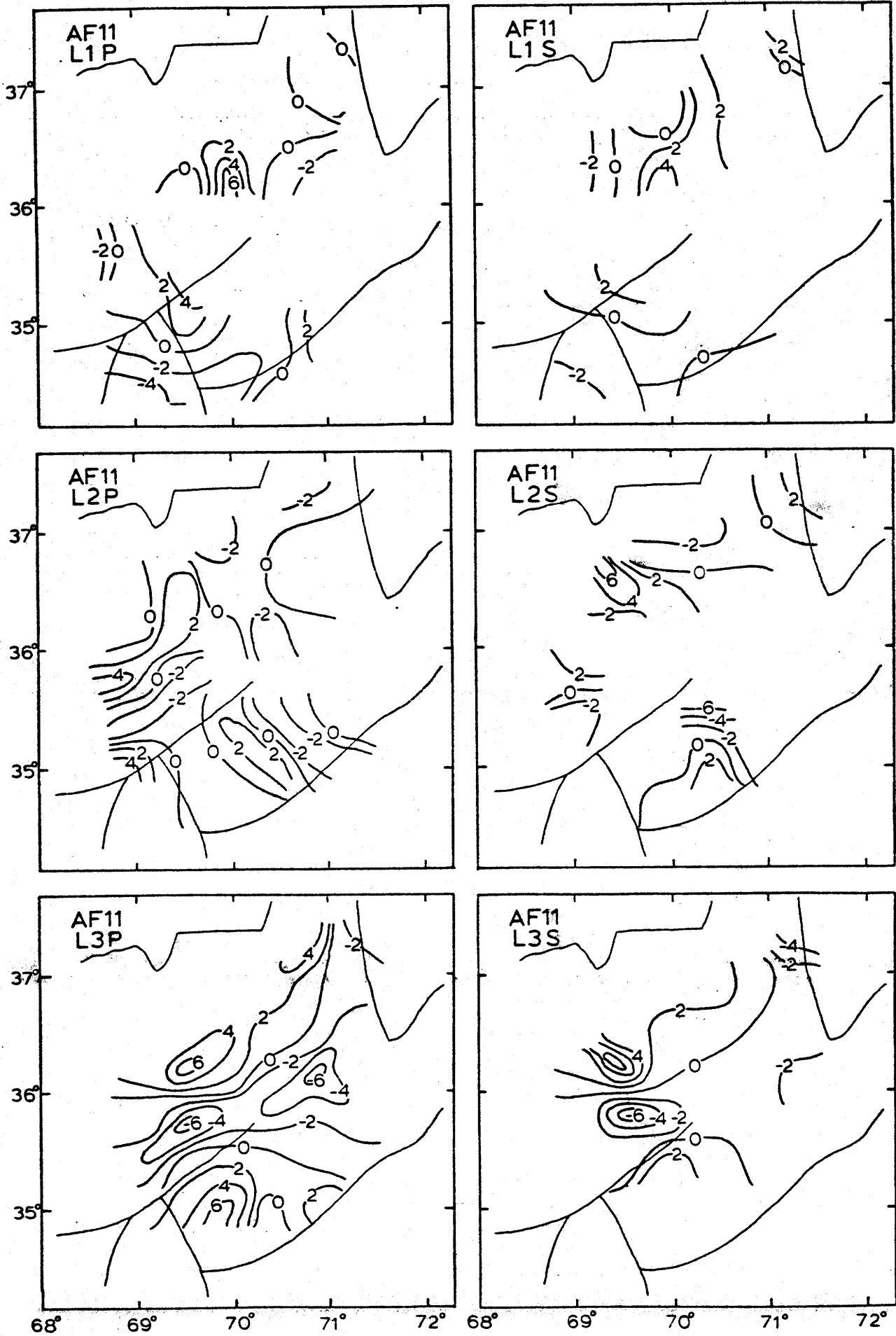


Figure C10. (cont.)

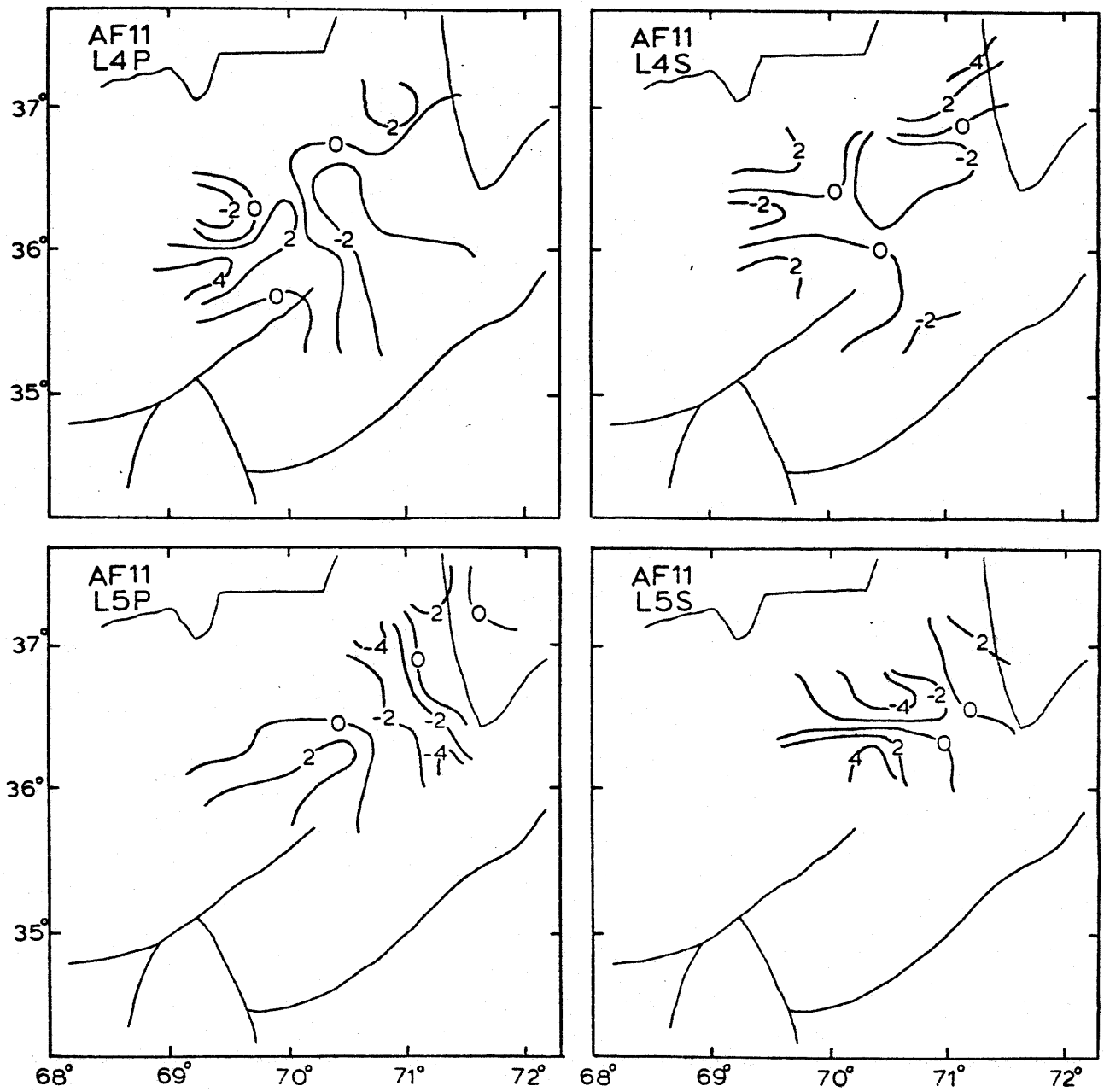


Table Captions

Table C1. Specifications of the starting models used in the three-dimensional inversions, along with the variance in the data before and after the inversions.

Inversion AF5			
241	Events		
2094	P Arrivals		
1535	S Arrivals		
Starting Model			
Layer	Depth	P Velocity	S Velocity
1	-2.0	5.93	3.48
2	35.0	6.41	3.71
3	70.0	8.08	4.63
4	110.0	8.55	4.99
Original Variance		0.191	
Final Variance		0.141	
Percentage Improvement		26.039	

Inversion AF8			
271	Events		
2269	P Arrivals		
1674	S Arrivals		
Starting Model			
Layer	Depth	P Velocity	S Velocity
1	-2.0	5.93	3.48
2	35.0	6.41	3.71
3	70.0	8.08	4.63
4	110.0	8.55	4.99
Original Variance		0.275	
Final Variance		0.126	
Percentage Improvement		54.171	

Inversion AF7			
245	Events		
2118	P Arrivals		
1554	S Arrivals		
Starting Model			
Layer	Depth	P Velocity	S Velocity
1	-2.0	5.93	3.48
2	35.0	6.41	3.71
3	70.0	8.08	4.63
4	110.0	8.55	4.99
Original Variance		0.286	
Final Variance		0.139	
Percentage Improvement		51.295	

Inversion AF11			
585	Events		
5115	P Arrivals		
3840	S Arrivals		
Starting Model			
Layer	Depth	P Velocity	S Velocity
1	-2.0	5.93	3.48
2	35.0	6.41	3.71
3	70.0	8.08	4.63
4	110.0	8.55	4.99
5	150.0	8.41	4.77
6	190.0	9.14	5.40
7	210.0	9.09	5.25
Original Variance		0.139	
Final Variance		0.100	
Percentage Improvement		28.219	

Table C1.

292

APPENDIX D

GRAVITY ANOMALY PRODUCED BY A BURIED,
TWO DIMENSIONAL, INFINITE SLAB

In this appendix we derive an expression for the gravity anomaly produced by an infinite rectangular prism. We start with an expression for the gravity anomaly (Δg) produced by a line source at a depth z and distance x from the observer:

$$(D1) \quad \Delta g = \frac{2G\Delta_m z}{(x^2 + z^2)^{1/2}}$$

where Δ_m is the anomalous line density (mass/unit length), and G is the gravitational constant. An expression for the anomaly produced by a vertical sheet can be found by integrating equation (D1) over chosen depth limits:

$$(D2) \quad \Delta g = G\Delta\sigma \log \left| \frac{x^2 + z_1^2}{x^2 + z_2^2} \right|$$

where z_1 and z_2 are the depths of the top and bottom of the sheet, $\Delta\sigma$ is the anomalous area density (mass/unit area). Finally, the gravity anomaly produced by an infinite rectangular prism is deduced by integrating equation (D2) over chosen distance limits:

$$(D3) \quad \Delta g = G\Delta\rho \left[x \log \left[\frac{x^2 + z_1^2}{x^2 + z_2^2} \right] + 2 \left[z_1 \tan^{-1} \left(\frac{x}{z_1} \right) - z_2 \tan^{-1} \left(\frac{x}{z_2} \right) \right] \right] \Bigg|_{x=l_1}^{x=l_2}$$

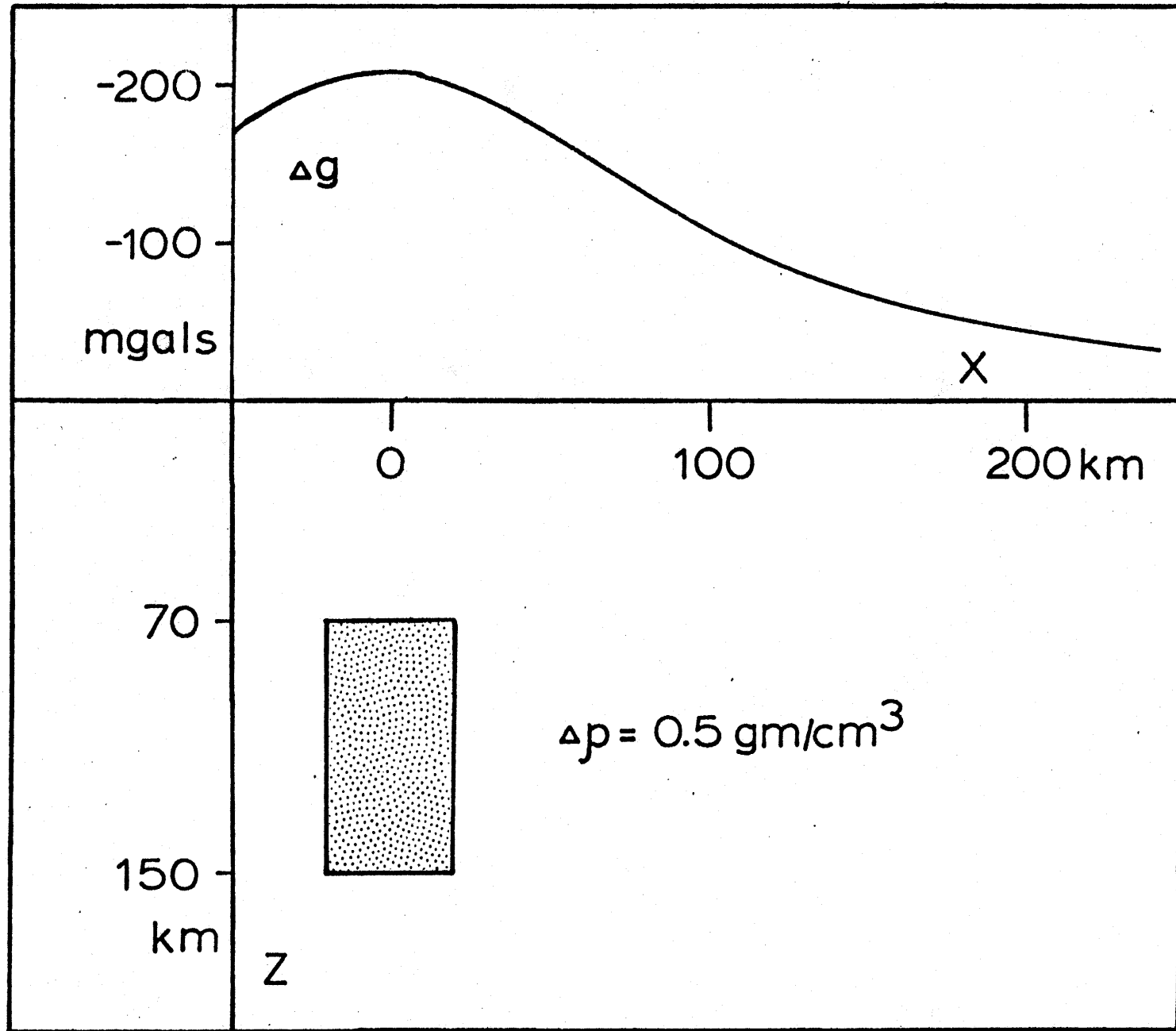
where l_1 and l_2 are the distances from the observation point to the edges of the anomalous region and $\Delta\rho$ is the anomalous volume density (mass/unit volume).

Figure D1 shows the geometry used in this calculation and a plot of the anomaly produced for $\Delta\rho = 0.5 \text{ gm/cm}^3$, $z_1 = 70$ kilometers, $z_2 = 150$ kilometers, and $l_2 - l_1 = 40$ kilometers. This example is intended to imitate a situation where the inferred low velocity region discussed in the text is caused by subducted crust that retains its original density contrast with the respect to the surrounding mantle.

Captions

Figure D1. Gravity anomaly produced by a buried, infinite rectangular prism, as a function of distance away from the point directly above the center of the prism. The density in the prism is 0.5 gm/cm^3 less than that of the surrounding regions.

Figure D1.



BIOGRAPHICAL NOTE

The author was born in Cambridge, England, on November 22, 1954. Before having a chance to ingest his first Spotted-Dick-in-a-Rag, he and his parents flew across the Atlantic to settle in the promised land of Columbus, Ohio. After sixteen years of corn, football, and state fairs, he moved to Atlanta, Georgia and enrolled in the Georgia Institute of Technology. Four years and one B.S. degree in Physics later, he returned to the frozen north to attend graduate school at M.I.T.

During his first year at M.I.T., he was lucky enough to run into Peter Molnar, who asked the young innocent if he would like to do field work in Afghanistan. The fires ignited by that question rage on five years and five field trips later. Memories of full moons over caravanserats, Afghan ballons, Tadjik yogurt, bomb-blasts in a coup d'etat, a dawn on an Aegean shore strewn with recently emptied Retsina bottles, and the mystical properties of a glaciated valley near Huaytapayana will remain with him forever.

The author plans to stay on at M.I.T. as a post-doc for a while. After all, it's a good life, isn't it?